

โครงสร้างเฉพาะบริเวณและสมบัติไดอิเล็กทริกของวัสดุรีแลกเซอร์
เฟอร์โรอิเล็กทริกตระกูลแบเรียมไททานต



นายอติพงศ์ บุตรชานนท์

วิทยานิพนธ์นี้เป็นส่วนหนึ่งของการศึกษาตามหลักสูตรปริญญาวิทยาศาสตรดุษฎีบัณฑิต

สาขาวิชาฟิสิกส์

มหาวิทยาลัยเทคโนโลยีสุรนารี

ปีการศึกษา 2557

**LOCAL STRUCTURE AND DIELECTRIC PROPERTIES
OF BARIUM TITANATE-BASED RELAXOR
FERROELECTRICS**

Atipong Bootchanont



A Thesis Submitted in Partial Fulfillment of the Requirements for the

Degree of Doctor of Philosophy in Physics

Suranaree University of Technology

Academic Year 2014

LOCAL STRUCTURE AND DIELECTRIC PROPERTIES OF BARIUM TITANATE-BASED RELAXOR FERROELECTRICS

Suranaree University of Technology has approved this thesis submitted in partial fulfillment of the requirements for the Degree of Doctor of Philosophy.

Thesis Examining Committee

(Prof. Dr. Santi Maensiri)

Chairperson

(Assoc. Prof. Dr. Rattikorn Yimnirun)

Member (Thesis Advisor)

(Dr. Saroj Rujirawat)

Member

(Assoc. Prof. Dr. Prayoon Songsiriritthigul)

Member

(Asst. Prof. Dr. Thiti Bovornratanaraks)

Member

(Dr. Wantana Klysubun)

Member

(Prof. Dr. Sukit Limpijumnong)

Vice Rector for Academic Affairs
and Innovation

(Assoc. Prof. Dr. Prapun Manyum)

Dean of Institute of Science

อทิพงษ์ บุตรชานนท์ : โครงสร้างเฉพาะบริเวณและสมบัติไดอิเล็กทริกของวัสดุรีแลกเซอร์
เฟอร์โรอิเล็กทริกตระกูลแบเรียมไททานेट (LOCAL STRUCTURE AND DIELECTRIC
PROPERTIES OF BARIUM TITANATE-BASED RELAXOR FERROELECTRICS).
อาจารย์ที่ปรึกษา : รองศาสตราจารย์ ดร.รัตติกร์ ยี่มนิรันฎ, 211 หน้า.

วิทยานิพนธ์นี้มุ่งศึกษาความสัมพันธ์ของโครงสร้างเฉพาะบริเวณที่นำไปสู่การเปลี่ยนสมบัติทางไดอิเล็กทริกของวัสดุ เพื่อให้สามารถเข้าใจกระบวนการการเปลี่ยนสมบัติทางไดอิเล็กทริกได้ดียิ่งขึ้น ในงานนี้วัสดุที่สนใจคือวัสดุประเภทรีแลกเซอร์ตระกูลแบเรียมไททานेटคือ วัสดุแบเรียมเซอร์โคเนียมไททานेट (BZT) วัสดุแบเรียมสแตนเนียมไททานेट (BST) และวัสดุผสมระหว่างแบเรียมไททานेटกับบิสมัทซิงค์ไททานेट (BT-BZnT) เพราะมีการนำไปประยุกต์ใช้อย่างแพร่หลาย เช่น ตัวเก็บประจุ ทรานซิสเตอร์ ตัวแปลงสัญญาณ เป็นต้น

ในระบบของวัสดุแบเรียมเซอร์โคเนียมไททานेट (BZT) ได้ตรวจสอบโครงสร้างผลึกด้วยเทคนิคการเลี้ยวเบนรังสีเอกซ์ (XRD) และการดูดกลืนรังสีเอกซ์ (XAS) ผลการตรวจสอบจากเทคนิคการเลี้ยวเบนรังสีเอกซ์ไม่พบการเปลี่ยนโครงสร้างเฟสของผลึกที่ชัดเจน ส่วนผลการตรวจสอบจากเทคนิคการดูดกลืนรังสีเอกซ์ในขอบ L_3 ของเซอร์โคเนียม พบว่าเซอร์โคเนียมเข้าไปแทนที่ไทเทเนียมในแบเรียมไททานेटและพบโครงสร้างเฉพาะบริเวณค่อยๆ เปลี่ยนรอบๆ อะตอมเซอร์โคเนียม ผลการดูดกลืนรังสีเอกซ์ในขอบ K ของไทเทเนียม พบว่าการเพิ่มขึ้นของเซอร์โคเนียมในแบเรียมไททานेटส่งผลต่อการเปลี่ยนพฤติกรรมแบบรีแลกเซอร์ (Relaxor) ไปสู่พฤติกรรมแบบกลุ่มขั้ว (Polar cluster) แบบฉับพลัน ซึ่งสอดคล้องกับการคำนวณสเปกตรัมโดยโปรแกรม FEFF8.2 และการหาแนวโน้มของกราฟ EXAFS ซึ่งสามารถยืนยันด้วยผลของการวัดสมบัติไดอิเล็กทริก

ในระบบของวัสดุแบเรียมสแตนเนียมไททานेट (BST) ได้ตรวจสอบโครงสร้างผลึกด้วยเทคนิคการเลี้ยวเบนรังสีเอกซ์และการดูดกลืนรังสีเอกซ์ ผลการตรวจสอบจากเทคนิคการเลี้ยวเบนรังสีเอกซ์ไม่พบการเปลี่ยนโครงสร้างเฟสของผลึกที่ชัดเจน ส่วนผลการตรวจสอบจากเทคนิคการดูดกลืนรังสีเอกซ์ในขอบ L_3 ของสแตนเนียมพบว่าสแตนเนียมเข้าไปแทนที่ไททานเนียมในแบเรียมไททานेटและพบ โครงสร้างเฉพาะบริเวณค่อยๆ เปลี่ยนรอบๆ อะตอมของสแตนเนียม ผลการ

ดูคดกลืนรังสีเอกซ์ในขอบ K ของไทเทเนียมพบว่า การเพิ่มขึ้นของสแตนเนียมในแบเรียมไททานเตด ส่งผลต่อการเปลี่ยนพฤติกรรมแบบรีแลกเซอร์ (Relaxor) ไปสู่พฤติกรรมแบบกลุ่มขั้ว (Polar cluster) อย่างฉับพลัน ซึ่งสอดคล้องกับเทคนิคการรวมกันเชิงเส้นและการคำนวณสเปกตรัมโดยโปรแกรม FEFF8.2 ซึ่งสามารถยืนยันด้วยผลของการวัดสมบัติไดอิเล็กทริก

ในระบบของวัสดุผสมระหว่างแบเรียมไททานเตดกับบิสมัทซิงค์ไททานเตด (BT-BZnT) ได้ตรวจสอบโครงสร้างผลึกด้วยเทคนิคการเลี้ยวเบนรังสีเอกซ์และการดูคดกลืนรังสีเอกซ์ ผลการตรวจสอบจากเทคนิคการเลี้ยวเบนรังสีเอกซ์พบการเปลี่ยนโครงสร้างเฟสของผลึกที่ชัดเจนจากโครงสร้างแบบเตตระโกนอลไปสู่โครงสร้างแบบรอมโบฮีดรอล ส่วนผลการตรวจสอบจากเทคนิคการดูคดกลืนรังสีเอกซ์ในขอบ K ของซิงค์ พบว่าซิงค์เข้าไปแทนที่ไทเทเนียมในบิสมัทไททานเตดและผลการดูคดกลืนรังสีเอกซ์ในขอบ K ของไทเทเนียม พบว่า การเพิ่มขึ้นของบิสมัทซิงค์ไททานเตดในแบเรียมไททานเตดส่งผลต่อการเปลี่ยนพฤติกรรมแบบเฟอร์โรอิเล็กทริกไปสู่พฤติกรรมแบบรีแลกเซอร์ (Relaxor) แต่การดูคดกลืนรังสีเอกซ์ในขอบ K ของซิงค์พบการเปลี่ยนแปลงเล็กน้อยของโครงสร้างเฉพาะบริเวณ ซึ่งสามารถยืนยันด้วยผลของการวัดสมบัติไดอิเล็กทริก

กล่าวโดยสรุป ในวัสดุทั้ง 3 ระบบจะแสดงการเปลี่ยนสมบัติไดอิเล็กทริกจากพฤติกรรมรีแลกเซอร์ไปสู่พฤติกรรมแบบกลุ่มขั้วและพฤติกรรมแบบเฟอร์โรอิเล็กทริก ซึ่งสอดคล้องกับโครงสร้างเฉพาะบริเวณของอะตอมไททานเตดจากโครงสร้างแบบคิวบิกเทียม (pseudo-cubic) หรือเกือบจะเป็นโครงสร้างรอมโบฮีดรอล เมื่อจะเปลี่ยนไปสู่พฤติกรรมแบบกลุ่มขั้ว อะตอมไททานเตดจะเคลื่อนที่กลับไปอยู่บริเวณตรงกลางของโครงสร้างเพอรอสไพไรต์ และโครงสร้างจะเข้าสู่โครงสร้างแบบคิวบิกที่สมบูรณ์ นอกจากนี้การเปลี่ยนสมบัติไดอิเล็กทริกไปสู่พฤติกรรมแบบเฟอร์โรอิเล็กทริก จะสอดคล้องกับโครงสร้างรอมโบฮีดรอลเปลี่ยนไปเป็นโครงสร้างเตตระโกนอล

สาขาวิชาฟิสิกส์

ปีการศึกษา 2557

ลายมือชื่อนักศึกษา _____

ลายมือชื่ออาจารย์ที่ปรึกษา _____

ลายมือชื่ออาจารย์ที่ปรึกษาร่วม _____

ATIPONG BOOTCHANONT : LOCAL STRUCTURE AND DIELECTRIC
PROPERTIES OF BARIUM TITANATE-BASED RELAXOR
FERROELECTRICS. THESIS ADVISOR : ASSOC. PROF. RATTIKORN
YIMNIRUN, Ph.D. 211 PP.

LOCAL STRUCTURE/XANES/BaTiO₃/RELAXOR/FERROELECTRIC

The relationship between local structure and phase information of dielectric materials has been studied in this thesis for understanding the process of phase transition. In this work, the materials of interest are BaTiO₃-based relaxor ferroelectrics; i.e., BaTi_{1-x}Zr_xO₃ (BZT), BaTi_{1-x}Sn_xO₃ (BST) and (1-x)BaTiO₃-xBiTi_{0.5}Zn_{0.5}O₃ (BT-BZnT) systems because they are used widely in electronic devices, such as capacitor, transistor and actuator.

In BZT system, the phase information was investigated by XRD and XAS. XRD technique did not clearly show the phase transition in BZT. The Zr L₃-edge XANES spectra showed that Zr atoms substituted in Ti sites in BaTiO₃ and local structure gradually changed around Zr atoms. The Ti K-edge XANES spectra showed that an increase of Zr content in BaTiO₃ affected suddenly the phase transition from relaxor ferroelectrics to polar cluster behavior which corresponded well with simulated spectrum by FEFF8.2 program and EXAFS fitting. The phase transition was also confirmed by the dielectric measurements.

In BST system, the phase information was investigated by XRD and XAS. XRD technique did not clearly show the phase transition in BST. The Sn L₃-edge XANES spectra indicated that Sn atoms substituted in Ti sites in BaTiO₃ and local structure gradually and linearly changed around Sn. The Ti K-edge XANES spectra

showed that an increase of Sn content in BaTiO₃ affected suddenly the phase transition from relaxor ferroelectrics to polar cluster behavior which corresponded well with the linear combination fit and simulated spectrum by FEFF8.2 program, and the phase transition was confirmed by the dielectric measurements.

In BT-BZnT system, the phase information was investigated by X-ray Diffraction and X-ray Absorption Spectroscopy. The results of X-ray diffraction technique clearly showed the phase transition from tetragonal to rhombohedral perovskite structure. The results of Zn K-edge XANES spectra indicated that Zn atoms substituted in Ti sites in BiTi_{0.5}Zn_{0.5}O₃ and the local structure around Zn atoms changed very little. The Ti K-edge XANES spectra showed that an increase of BiTi_{0.5}Zn_{0.5}O₃ content in BaTiO₃ affected gradually the phase transition from normal to relaxor ferroelectric behavior which corresponded well with the dielectric measurements.

In conclusion, the 3 systems exhibited the phase transition of dielectric properties from relaxor to polar cluster and normal ferroelectric behavior, which corresponded to the local structure of Ti atoms from pseudo-cubic or almost rhombohedral. In the change to polar cluster behavior, the Ti atoms gradually moved to central perovskite and the crystal structure changed to almost perfect cubic phase. Moreover, the change to normal ferroelectric behavior corresponded to the transition from pseudo-cubic or rhombohedral to tetragonal structure.

School of Physics

Student's Signature_____

Academic Year 2014

Advisor's Signature_____

Co-advisor's Signature_____

ACKNOWLEDGEMENTS

There are many people, to whom I would like to express my sincere words of acknowledgments:

I thank Assoc. Prof. Dr. Rattikorn Yimnirun, my thesis advisor, for introducing me to the field of synchrotron x-ray absorption spectroscopy. He supervised this work in all steps, from the very first experiments, new ideas, data processing as well as the final proof reading of the manuscript. Not only his scientific expertise, but also his optimism and trust were a great help and motivation throughout my work.

I thank Prof. Dr. Amar Bhalla and Prof. Dr. Ruyan Guo, my thesis co-advisor abroad, for giving me the opportunity to be a member of their multifunctional electronic materials and devices research lab (MeMDRL) group at Department of Electrical and Computer Engineering, College of Engineering, University of Texas at San Antonio (UTSA), Texas, USA and for providing me an excellent experience research condition. I thank them not only for the professional support but also for the good time that they offered me during my visit at UTSA.

I am grateful to Dr. Saroj Rujirawat for his contribution in my work and for accepting me to be a member of his group.

I am grateful to Dr. Wantana Klysuban for her management of beam time in my work at BL-8, Synchrotron Light Research Institute and for accepting to be a member of the examination committee.

my work at BL-5, Synchrotron Light Research Institute. I thank him for his great contribution in bringing up new questions and ideas of X-ray Absorption technique.

I am also grateful to Dr. Narit Triamnak from Department of Materials Science and Engineering, Faculty of Engineering and Industrial Technology, Silpakorn University and Prof. Dr. David P. Cann from Materials Science, School of Mechanical, Industrial, and Manufacturing Engineering, Oregon State University for providing BT-BZnT ceramics.

Special thanks to Mr. Jaru Jutimoosik, Dr. Sujitra Unruan, Dr. Muangjai Unruan and Mr. Santi Phomying for their kind assistance in materials synthesis, XAS measurements, and data analysis and Miss Pitchaya Ponghong for her love and encouragement.

I am grateful to the Science Achievement Scholarship Programme of Thailand (SAST) from Thai Government for financial support.

It is impossible to list all of my fellow graduate students, who were a great support during my Ph.D. study, for all the great times we had together.

Finally, this thesis is dedicated to my parents: my father, Nitipong Bootchanont; my mother, Poonsin Bootchanont and my sister, Sureewan Bootchanont for their love and everything in my life.

Atipong Bootchanont

CONTENTS

	Page
ABSTRACT IN THAI.....	I
ABSTRACT IN ENGLISH	III
ACKNOWLEDGEMENTS	V
CONTENTS.....	VII
LIST OF TABLES	XI
LIST OF FIGURES	XIII
LIST OF ABBEVIATIONS	XXIV
CHAPTER	
I INTRODUCTION	26
1.1 Background.....	26
1.2 Review of literatures.....	27
1.4 Scope and Limitations of the Study	35
1.5 References.....	36
II THEORY	38
2.1 Dielectric properties.....	38
2.2 Relaxor ferroelectrics.....	53
2.3 Hysteresis	57
2.4 X-ray Diffraction (XRD)	61
2.5 X-ray Absorption Spectroscopy (XAS).....	62

CONTENTS (Continued)

	Page
2.6 References	76
III RESEARCH METHODOLOGY	79
3.1 Solid State Solution Synthesis	79
3.2 X ray diffraction setup	84
3.3 X-ray absorption spectroscopy setup	87
3.3.1 X-ray absorption spectrum calculation	87
3.3.2 Ti K pre-edge XANES analysis.....	90
3.3.3 X-ray Absorption Spectroscopy Experimental setup	91
3.5 P-E Hysteresis setup	99
3.6 References	100
IV STUDY OF PHASE INFORMATION AND DIELECTRIC PROPERTIES IN BARIUM ZIRCONATE TITANATE	101
4.1 Introduction.....	101
4.2 Experimental	102
4.3 X-ray Diffraction	103
4.4 XANES results.....	106
4.4.1 Identification of Zr site in BaTiO ₃	106
4.4.2 XANES studies of Ti K pre-edge.....	108
4.4.3 XANES studies of phase transition.	110
4.5 EXAFS results	115

CONTENTS (Continued)

	Page
4.6 Dielectric permittivity	121
4.7 Hysteresis	131
4.8 References	133
V STUDY OF PHASE INFORMATION AND DIELECTRIC PROPERTIES IN BARIUM STANNATE TITANATE	136
5.1 Introduction	136
5.2 Experimental	137
5.3 X-ray diffraction	138
5.4 XANES results	139
5.4.1 Identification of Sn site in BaTiO ₃	139
5.4.2 XANES studies of Ti K pre-edge	141
5.4.3 XANES studies of phase transition.	143
5.5 EXAFS results	151
5.6 Dielectric permittivity	154
5.7 Hysteresis	167
5.8 References	169
VI STUDY OF PHASE INFORMATION AND DIELECTRIC PROPERTIES IN BARIUM TITANATE - BISMUTH ZINC TITANATE.....	171
6.1 Introduction	171

CONTENTS (Continued)

	Page
6.2 Experimental	172
6.3 X-ray Diffraction	173
6.4 XANES results.....	176
6.4.1 Identification of Zn site in BiTiO ₃	176
6.4.2 XANES study on phase transition.....	178
6.5 EXAFS results	182
6.6 Dielectric permittivity.....	184
6.7 Hysteresis.....	199
6.8 References.....	201
VII STRUCTURE-PROPERTY RELATIONSHIP	204
7.1 Global structure.....	205
7.2 Local structure	207
7.3 Dielectric properties.....	208
7.4 References.....	210
VIII CONCLUSIONS AND SUGGESTION	211
APPENDIX.....	213
CURRICULUM VITAE.....	239

LIST OF TABLES

Table		Page
1.1	Some pone piece 677 subthairoperties of BaTiO ₃ -based perovskite structure (Gražulis <i>et al.</i> , 2012).....	35
2.1	The symbol of the electron transition in function as quantum number.....	64
4.1	The structural parameters coordination numbers N , interatomic distances R and DW factors σ^2 obtained by fitting the EXAFS data for the BaTi _{1-x} Zr _x O ₃ (x=0,0.25,0.5 and 0.75).....	120
4.2	Caculated Curie constant and measured T_c from dielectric properties of Ba(Zr _x Ti _{1-x})O ₃ compositions.....	122
4.3	Degree of relaxation γ , dielectric maxima temperature and diffusivity of Ba(Zr _x Ti _{1-x})O ₃ compositions.....	131
5.1	Calculated Curie constant and measured T_c from dielectric properties of Ba(Ti,Sn)O ₃ compositions.....	166
5.2	Degree of relaxation γ , dielectric maxima temperature and diffusivity of Ba(Ti,Sn)O ₃ compositions.....	166
6.1	Caculated Curie constant and measured T_c from dielectric properties of (1-x)BaTiO ₃ - xBi(Zn _{0.5} Ti _{0.5})O ₃ compositions.....	195
6.2	Degree of relaxation γ , dielectric maxima temperature and diffusivity of (1-x)BaTiO ₃ - xBi(Zn _{0.5} Ti _{0.5})O ₃ compositions.....	196

LIST OF TABLES (Continued)

Table		Page
6.3	Vogel-Fulcher temperature, activation energy E_a and exponent τ_0 as calculated from the Arthenius plots of various (1-x)BT-xBZnT compositions.....	199



LIST OF FIGURES

Figure	Page
1.1	Crystal structure of tetragonal perovskite BaTiO_328
1.2	Crystal structure of cubic perovskite BaZrO_329
1.3	Phase diagram of $\text{Ba}(\text{Ti}_{1-x}\text{Zr}_x)\text{O}_3$ compound as a function of Zr content. (Maiti <i>et al.</i> , 2008).31
1.4	Crystal structure of cubic perovskite BaSnO_332
1.5	The phase diagram of $\text{Ba}(\text{Ti}_{1-x}\text{Sn}_x)\text{O}_3$ compound as a function of Sn content/% (Wei and Yao, 2007).33
1.6	The structure of tetragonal perovskite $\text{Bi}(\text{Zn},\text{Ti})\text{O}_3$34
1.7	The phase diagram of $x\text{BaTiO}_3-(1-x)\text{Bi}(\text{Zn}_{1/2}\text{Ti}_{1/2})\text{O}_3$ compound (Huang, 2008).34
2.1	Parallel-plate capacitor of area A and separation d in vacuum attached to a voltage source.39
2.2	Parallel-plate capacitor except that now a dielectric is placed between the plates and attached to a voltage source.41
2.3	Electronic polarization of electron cloud surrounding a nucleus. a). At equilibrium, without an applied electric field b). In the presence of an applied electric field. c). Schematic of model assumed in text. S_0 represent the stiffness of bond between the electrons and the nucleus.44

LIST OF FIGURES (Continued)

Figure		Page
2.4	Ionic polarization. a). Ion positions at equilibrium $E=0$. b). When an applied electric field, the center of positive charge is no longer coincident with the center of negative charge, i.e., polarization occurs.....	47
2.5	Dipolar polarization; (a) energy versus distance diagram in absence of applied field; the two sites are equally populated. (b) The application of an electric field will bias on site relative to the other (Barsoum, 1997).....	48
2.6	Variation of polarization with frequency (Khamkongkaeo, 2013).	53
2.7	Comparisons of normal ferroelectric and relaxor ferroelectric (Huang, 2008).....	56
2.8	Hysteresis loop for polarization. (b) Domain microstructure without electric field. (c) Domain growth in direction of an applied electric field (Barsoum, 1997).....	59
2.9	Mechanism of X-ray diffraction beam path (Peyronel and Marangoni, 2013).	61
2.10	Schematic view of x-ray absorption measurement in transmission mode.	63
2.11	Diagram of the electron transition in inner shells (Thompson <i>et al.</i> , 2001).....	65

LIST OF FIGURES (Continued)

Figure	Page
2.12	Mechanism of the x-ray absorption (a) X-ray absorption (b) Fluorescent X-ray emission and (c) Auger emission (Klysubun, 2006).....66
2.13	The absorbance Fe K-edge spectra in compound iron oxide (Larsen <i>et al.</i> , 2014).67
2.14	The muffin-tin potential consist of non-overlapping spherical regions (Kodre, 2002).....69
2.15	Single scattering (left), double scattering from different atoms (middle), and double scattering from the same atom (right). (b) Graphical representation of the <i>T</i> -operator (Kodre, 2002).....71
2.16	The EXAFS mechanism of photo electron scattering.74
3.1	Flow chart of the synthesis of Ba(Ti _{1-x} M _x)O ₃ powders (M=Zr and Sn).80
3.2	Flow chart of the synthesis of Ba(Ti _{1-x} M _x)O ₃ ceramics (M=Zr and Sn).81
3.3	Flow chart of the synthesis of (1-x)BaTiO ₃ -xBi(Zn _{0.5} Ti _{0.5})O ₃ powders.83
3.4	Flow chart of the synthesis of (1-x)BaTiO ₃ -xBi(Zn _{0.5} Ti _{0.5})O ₃ ceramics.....84
3.5	Schematic illustration of θ -2 θ x-ray diffraction experiment (Jutimoosik, 2010).....86

LIST OF FIGURES (Continued)

Figure		Page
3.6	Schematic representation of X-ray diffractometer D5005(Jutimoosik, 2010).....	86
3.7	Detail of an atoms.inp input file to generate “feff.inp” for FEFF calculation.	87
3.8	Detail of a “feff.inp” input file of BaTiO ₃ with Ti as center atom for FEFF calculation.....	89
3.9	The Ti K pre-edge XANES of BaTiO ₃ , showing the calculated area under the spectral peak denoted by X (Hench and West, 1990).	90
3.10	The three modes of XAS measurement (a) transmission mode, (b) fluorescence mode and (c) electron yield [adapted from (Kawai, 2000)].	92
3.11	Schematic illustration of the experimental setup of transmission-mode X-ray absorption spectroscopy (Jutimoosik, 2010).....	93
3.12	XAS experimental set up at the Siam Photon Laboratory, Synchrotron Light Research Institute (Jutimoosik, 2010).....	94
3.13	The excited state (a) x-ray fluorescence and (b) the Auger effect (Jutimoosik, 2010).....	96
3.14	Vacuum pump and sample holder.	97
3.15	Temperature control (A) and Frequency generator (B) (Arrows indicate the number of equipment).....	98
3.16	The HP4284 LCR meter for dielectric measurement.	98

LIST OF FIGURES (Continued)

Figure	Page
3.17	The oscilloscope and power supply with frequency generator (b) sample holder for P-E hysteresis measurement.....99
4.1	X-ray diffraction patterns of $\text{Ba}(\text{Zr}_x\text{Ti}_{1-x})\text{O}_3$ powders.....104
4.2	Phase diagram of $\text{Ba}(\text{Ti}_{1-x}\text{Zr}_x)\text{O}_3$ compound as a function of Zr content.105
4.3	The phase fraction of $\text{Ba}(\text{Ti}_{1-x}\text{Zr}_x)\text{O}_3$ from XRD patterns.....105
4.4	Model Perovskite crystals structure of BaTiO_3 . b–c Schematic illustrations of Zr on Ti site, Zr on Ba site, respectively. Regions shown in c are shifted from that in a).107
4.5	Zr L_3 -edge XANES spectra of $\text{BaTi}_{1-x}\text{Zr}_x\text{O}_3$ And calculation of Zr site for Zr on Ti site (Zr_{Ti} -red line), Zr on Ba site (Zr_{Ba} -black line)107
4.6	Normalized X-ray absorption Ti K pre-edge spectra of $\text{Ba}(\text{Zr}_x\text{Ti}_{1-x})\text{O}_3$ powders.....109
4.7	a) Present δ_{Ti} determined from the intensity of the pre-edge peak as a function of the unit-cell. The value of δ_{Ti} for $\text{Ba}(\text{Zr}_x\text{Ti}_{1-x})\text{O}_3$ was determined using the spectrum reported in Ref. (Levin <i>et al.</i> , 2013). b) The local Zr/Ti ratio around the absorbing Ti.....109
4.8	Normalized X-ray absorption Ti K-edge spectra of $\text{Ba}(\text{Zr}_x\text{Ti}_{1-x})\text{O}_3$ powders.112
4.9	The perovskite model of cubic distortion with perfect cubic.....112

LIST OF FIGURES (Continued)

Figure	Page
4.10	Comparison of Normalized X-ray absorption Ti K-edge spectra of $\text{Ba}(\text{Zr}_x\text{Ti}_{1-x})\text{O}_3$ ($x=0.25$ and 0.75) with simulated features of Sn L_3 -edge XANES spectra of $\text{Ba}(\text{Zr,Ti})\text{O}_3$ -rather perfect rhombohedral (red-line), a nearly perfect cubic (black line), rhombohedral (dash-line), tetragonal perovskite (dot-line).....113
4.11	The normalized Zr L_3 edge XANES spectra of $\text{Ba}(\text{Zr}_x\text{Ti}_{1-x})\text{O}_3$ powders.114
4.12	The phase fraction of Zr L_3 -edge XANES spectra and Ti K-edge EXAFS in k -space of $\text{Ba}(\text{Zr}_x\text{Ti}_{1-x})\text{O}_3$ crystals.115
4.13	The Normalized Ti K-edge EXAFS spectra of $\text{Ba}(\text{Ti,Zr})\text{O}_3$ powders.117
4.14	The EXAFS Fourier transform in k -space of $\text{Ba}(\text{Ti,Zr})\text{O}_3$ powders.117
4.15	The EXAFS Fourier transform in R -space of $\text{Ba}(\text{Ti,Zr})\text{O}_3$ powders.118
4.16	Experimental and calculated (solid/red) magnitude of EXAFS Fourier transform for a). BaTiO_3 , b). $\text{BaTi}_{0.75}\text{Zr}_{0.25}\text{O}_3$, c). $\text{BaTi}_{0.50}\text{Zr}_{0.50}\text{O}_3$, and d). $\text{BaTi}_{0.25}\text{Zr}_{0.75}\text{O}_3$. The k range used in the FT is from 2 to 5.7 \AA^{-1} for all data sets.119
4.17	Temperature dependence of dielectric constant and loss tangent ($\tan \delta$) at various frequencies for $\text{Ba}(\text{Zr}_x\text{Ti}_{1-x})\text{O}_3$123

LIST OF FIGURES (Continued)

Figure		Page
4.18	The inverse dielectric constant $1/\epsilon$ as a function of temperature at 100 kHz for $\text{Ba}(\text{Zr}_x\text{Ti}_{1-x})\text{O}_3$, symbols denote experimental data and solid line denotes fitting to the Curie-Weiss law. The insets show the plot of $\ln(1/\epsilon - 1/\epsilon_m)$ vs $\ln(T - T_m)$ for $\text{Ba}(\text{Zr}_x\text{Ti}_{1-x})\text{O}_3$ ceramics.	127
4.19	<i>P-E</i> hysteresis measurements on $\text{Ba}(\text{Zr}_x\text{Ti}_{1-x})\text{O}_3$ ceramics obtained at room temperature.	132
5.1	X-ray diffraction patterns of $\text{Ba}(\text{Sn}_x\text{Ti}_{1-x})\text{O}_3$ powders.	138
5.2	The phase fraction of $\text{Ba}(\text{Sn}_x\text{Ti}_{1-x})\text{O}_3$ from XRD patterns.	139
5.3	A Model perovskite crystal structure of BaTiO_3 . b–c schematic illustrations of Sn on Ti site, Sn on Ba site, respectively. Regions shown in c are shifted from that in a).	140
5.4	Sn L_3 -edge XANES spectra of $\text{Ba}(\text{Ti}_{1-x}\text{Sn}_x)\text{O}_3$ and calculation of Sn site for Sn on Ti site (Sn_{Ti} -red line), Sn on Ba site (Sn_{Ba} -black line).	141
5.5	Normalized X-ray absorption Ti K pre-edge spectra of $\text{Ba}(\text{Sn}_x\text{Ti}_{1-x})\text{O}_3$ powders.	142
5.6	a) δ_{Ti} determined from the intensity of the pre-edge peak as a function of the unit-cell. The value of δ_{Ti} for $\text{Ba}(\text{Sn}_x\text{Ti}_{1-x})\text{O}_3$ was determined using the spectrum reported in (Levin <i>et al.</i> , 2013). b) The local Sn/Ti ratio around absorbing Ti.	143
5.7	The normalized X-ray absorption Ti K-edge spectra of $\text{Ba}(\text{Sn}_x\text{Ti}_{1-x})\text{O}_3$ powders.	145

LIST OF FIGURES (Continued)

Figure		Page
5.8	The normalized X-ray absorption Sn L ₃ -edge spectra of Ba(Sn _x Ti _{1-x})O ₃ powders.....	145
5.9	The phase fraction of Sn L ₃ -edge XANES spectra and Ti K-edge EXAFS in k-space of Ba(Ti _{1-x} Sn _x)O ₃ crystals.	147
5.10	Comparison of normalized X-ray absorption Ti K-edge spectra of Ba(Sn _x Ti _{1-x})O ₃ (x=0.25 and 0.75), with the simulated features of Ti K-edge XANES spectra of Ba(Sn,Ti)O ₃ - <i>pseudo cubic</i> (red-line), a nearly perfect cubic (black line), rhombohedral (dash-line) and tetragonal perovskite (dot-line).	149
5.11	Comparison of normalized X-ray absorption Sn L ₃ -edge spectra of Ba(Sn _x Ti _{1-x})O ₃ (x=0.25 and 0.75), with the simulated features of Sn L ₃ -edge XANES spectra of Ba(Sn,Ti)O ₃ -rather perfect rhombohedral (red-line), a nearly perfect cubic (black line), rhombohedral (dash-line), tetragonal perovskite (dot-line).	150
5.12	The normalized EXAFS signal of Ba(Ti,Sn)O ₃ powders.....	152
5.13	The EXAFS Fourier transform in k-space of Ba(Ti,Sn)O ₃ powders.	153
5.14	The EXAFS Fourier transform in R-space of Ba(Ti,Sn)O ₃ powders.....	153
5.15	Temperature dependence of dielectric constant and loss tangent (tan δ) at various frequencies for Ba(Ti,Sn)O ₃ (Arrows indicate the direction of increasing frequency).....	155

LIST OF FIGURES (Continued)

Figure		Page
5.16	The inverse dielectric constant $1/\epsilon$ as a function of temperature at 100 kHz for $\text{Ba}(\text{Ti},\text{Sn})\text{O}_3$ symbols denote experimental data and solid line denotes fitting to the Curie-Weiss law. The insets show the plot of $\ln(1/\epsilon - 1/\epsilon_m)$ vs $\ln(T - T_m)$ for $\text{Ba}(\text{Ti},\text{Sn})\text{O}_3$ ceramics.	161
6.1	X-ray diffraction patterns of $(1-x)\text{BaTiO}_3-x\text{Bi}(\text{Zn}_{0.5}\text{Ti}_{0.5})\text{O}_3$ ceramics (a) all conditions (b) around phase transition $x=0.08$ and 0.09.	174
6.2	The lattice constant and unit cell volume as a function of x content of $(1-x)\text{BaTiO}_3-x\text{Bi}(\text{Zn}_{0.5}\text{Ti}_{0.5})\text{O}_3$ compositions.	175
6.3	The phase fraction of $(1-x)\text{BaTiO}_3-x\text{Bi}(\text{Zn}_{0.5}\text{Ti}_{0.5})\text{O}_3$ from XRD patterns.	175
6.4	Model Perovskite crystal structure of $\text{Bi}(\text{Ti},\text{Zn})\text{O}_3$. b–c schematic illustrations of Zn on Ti site, Zn on Bi site, respectively. Regions shown in c are shifted from that in a).	177
6.5	Present Zn K -edge XANES spectra of $(1-x)\text{BaTiO}_3-x\text{Bi}(\text{Ti}_{0.5}\text{Zn}_{0.5})\text{O}_3$ and calculation of Sn site for Sn on Ti site (Sn_{Ti} -red line), Sn on Bi site (Sn_{Bi} -black line).	178
6.6	The normalized X-ray absorption Ti K -edge spectra of $(1-x)\text{BaTiO}_3-x\text{Bi}(\text{Zn}_{0.5}\text{Ti}_{0.5})\text{O}_3$, with $x= 0.05, 0.07, 0.09, 0.1, 0.11,$ and 0.13.	180

LIST OF FIGURES (Continued)

Figure		Page
6.7	The normalized X-ray absorption Ti K pre-edge spectra of $(1-x)\text{BaTiO}_3-x\text{Bi}(\text{Zn}_{0.5}\text{Ti}_{0.5})\text{O}_3$, with $x = 0.05, 0.06, 0.07, 0.08, 0.09, 0.1, 0.11,$ and 0.13	180
6.8	The normalized X-ray absorption Zn K-edge spectra of $(1-x)\text{BaTiO}_3-x\text{Bi}(\text{Zn}_{0.5}\text{Ti}_{0.5})\text{O}_3$, with $x= 0.05, 0.07, 0.09, 0.1, 0.11,$ and 0.13	181
6.9	The phase fraction of Ti and Zn K-edge EXAFS in k-space in $(1-x)\text{BaTiO}_3-x\text{Bi}(\text{Zn}_{0.5}\text{Ti}_{0.5})\text{O}_3$ crystal.	181
6.10	The EXAFS Fourier transform in E-space of $(1-x)\text{BaTiO}_3-x\text{Bi}(\text{Zn}_{0.5}\text{Ti}_{0.5})\text{O}_3$ ceramics.	183
6.11	The EXAFS Fourier transform in k-space of $(1-x)\text{BaTiO}_3-x\text{Bi}(\text{Zn}_{0.5}\text{Ti}_{0.5})\text{O}_3$ ceramics.	183
6.12	The EXAFS Fourier transform in R-space of $(1-x)\text{BaTiO}_3-x\text{Bi}(\text{Zn}_{0.5}\text{Ti}_{0.5})\text{O}_3$ ceramics.	184
6.13	Temperature dependence of dielectric constant and loss tangent ($\tan \delta$) at various frequencies for $(1-x)\text{BaTiO}_3-x\text{Bi}(\text{Zn}_{0.5}\text{Ti}_{0.5})\text{O}_3$	186
6.14	The inverse dielectric constant $1/\epsilon$ as a function of temperature at 100 kHz for $\text{Ba}(\text{Zr}_x\text{Ti}_{1-x})\text{O}_3$, symbols denote experimental data and solid line denotes fitting to the Curie-Weiss law. The insets show the plot of $\ln(1/\epsilon-1/\epsilon_m)$ vs $\ln(T-T_m)$ for $(1-x)\text{BaTiO}_3-x\text{Bi}(\text{Zn}_{0.5}\text{Ti}_{0.5})\text{O}_3$ ceramics.	190

LIST OF FIGURES (Continued)

Figure		Page
6.13	Temperature dependence of relaxation time for ceramics at 100 kHz, with $x = 0.05, 0.06, 0.07, 0.08, 0.09, 0.1, 0.11,$ and 0.13 . Symbols denote experimental data and solid curve denotes fitting to the Vogel-Fulcher relation.	198
6.14	<i>P-E</i> hysteresis measurements on $(1-x)\text{BaTiO}_3 - x\text{Bi}(\text{Zn}_{0.5}\text{Ti}_{0.5})\text{O}_3$ ceramics obtained at room temperature.....	200
7.1.	The XRD patterns at around phase transition (a) BZT (b) BST and (c) BT-BZnT.....	206
7.2.	The normalized Ti K-edge XANES spectra (a) BZT (b) BST and (c) BT-BZnT.....	208

LIST OF ABBEVIATIONS

°C	Degree Celsius
BL5.2	Beamline 5.2
BL8	Beamline 8
BST	Barium Stannate Titanate
BT	Barium Titanate
BZT	Barium Zirconate Titanate
BZnT	Bismuth Zinc Titanate
EXAFS	Extended X-ray Absorption Fine Structure
DFT	Density Functional Theory
DOS	Density of State
E_0	Absorption edge
E_B	Binding energy
eV	Electron-volt
FMS	Full Multiple Scattering
K	Kelvin
h	Plank's constant
i	Current density
I_e	Electron current
I_p	Photon current

LIST OF ABBEVIATIONS (Continued)

J	Total Angular Momentum
L	Angular Momentum
LDA	Local Density Approximation
MPB	Morphotropic Phase Boundary
S	Spin
SCF	Self Consist Field
SLRI	Synchrotron Light Research Institute
XANES	X-ray Absorption Near Edge Structure
XAS	X-ray Absorption Spectroscopy
XRD	X-ray Diffraction
λ	Wavelength
λ_i	Photoelectron mean free path
σ^2	Debye-Waller factor
S_0^2	Scale factor

CHAPTER I

INTRODUCTION

1.1 Background

Over the years since the discovery of their dielectric properties, extensive research works on relaxor ferroelectric behavior of barium titanate materials have been carried out because they are attractive candidates for dynamic random access memories, transducers, actuators, capacitors and electronic devices (Maiti *et al.*, 2008; Maiti *et al.*, 2006). Barium titanate (BaTiO_3), discovered in 1941 (Yu *et al.*, 2007), exhibits ferroelectric behavior with high dielectric constant. It is also an environmental friendly material to replace the disadvantages of lead-based materials with volatility and toxicity.

In the recent years, researchers have found that increasing Zr or Sn substitution into Ti site in BaTiO_3 crystals can change the material to exhibit relaxor ferroelectric behavior (Maiti *et al.*, 2008; Cerneaw and Manea, 2007). The same behavior can also happen in $\text{BaTiO}_3\text{-Bi}(\text{Ti,Zn})\text{O}_3$ composite (Raengthon and Cann, 2011). The relaxor ferroelectric behavior is classified with strong frequency dependent dielectric properties. It is of particular interest because barium zirconate exhibits non polar or paraelectric behavior, which cannot have spontaneous polarization; i.e. non ferroelectric.

The structure of relaxor ferroelectric materials is generally known to be rather complex. Various groups attempted to create models to explain the relaxor behavior such as, superparaelectric model, dipolar glass model, compositional heterogeneity model and random field model. Therefore, phase transition behavior of relaxor ferroelectric materials has been extensively studied (Mouraa *et al.*, 2008).

1.2 Review of literatures

1.2.1 Background of barium titanate

Barium titanate is a dielectric material with the chemical formula BaTiO_3 . The structure of BaTiO_3 is tetragonal perovskite-like structure, which is a network of corner-linked oxygen octahedra, with the Ti atoms within the octahedral hole and the Ba atoms filling the dodecahedral hole, as shown in Figure 1.1. The BaTiO_3 was first developed as piezoelectric ceramic, and it still is widely studied in the family of perovskite-like dielectric materials (Wei and Yao, 2007). Moreover, it has been mostly applied in multilayer ceramic capacitors.

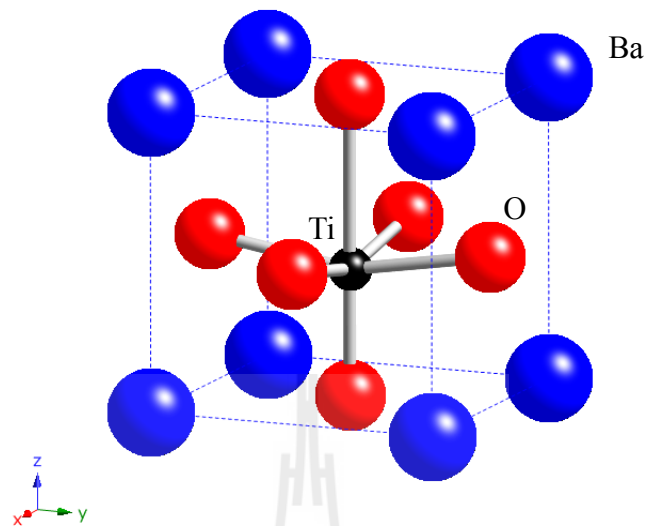


Figure 1.1 Crystal structure of tetragonal perovskite BaTiO₃.

Barium titanate is known to exhibit phase transition in bulk forms with various temperatures (T). At $T \leq -90$ °C, the structure of BaTiO₃ is trigonal or rhombohedral, between -90 °C to 5 °C, the rhombohedral structure change to orthorhombic. Above 5 °C, the orthorhombic cell changes to tetragonal and then to the cubic cell at Curie temperature (T_C) about 120 °C (Maiti *et al.*, 2008). In addition, at room temperature the structure of BaTiO₃ is tetragonal, the position of the titanium ion becomes off-center resulting in the distortion of TiO₆ octrahedra as the temperature is lowered from the high temperature cubic form. The distorted octrahedra create a very large spontaneous polarization, and in tune dielectric constant. Moreover, the distorted octrahedra can be reversed by applying a suitable electric field E .

In addition, researchers have found that doping or element substitution into titanium site in BaTiO₃ lattice induces the relaxor ferroelectric behavior or the relaxation effect in this prototypic ferroelectric material (Yu *et al.*, 2007).

1.3 Relaxor ferroelectrics of barium titanate-based Materials

1.3.1 Barium Titanium Zirconate

Barium zirconate titanate is a lead-free ferroelectric with the chemical formula $\text{Ba}(\text{Ti,Zr})\text{O}_3$. BaZrO_3 is known to exhibit paraelectric behavior because of its crystal symmetry no spontaneous polarization (Figure. 1.2). When Ti suitably substitutes for Zr, relaxor ferroelectric behavior is observed. Its structure becomes pseudocubic or the cubic distortion of perovskite.

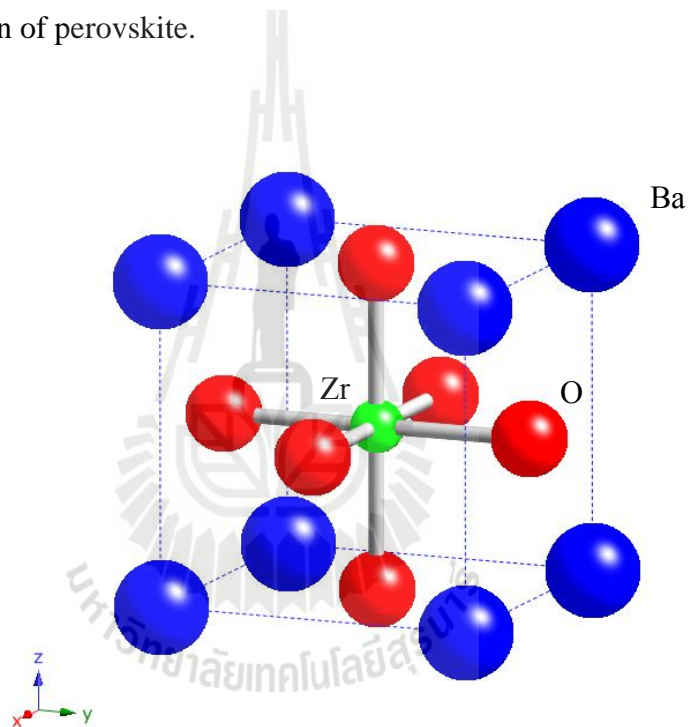


Figure 1.2 Crystal structure of cubic perovskite BaZrO_3 .

Barium zirconate titanate is known to exhibit relaxor behavior in bulk materials with increasing Zr content. Substitution of Zr^{4+} (atomic weight of 91.2, ionic radius of 0.086 nm) with Ti^{4+} (atomic weight of 47.9, ionic radius of 0.0745 nm) exhibits several interesting features in the dielectric behavior of BaTiO_3 . It has been reported that with the incorporation of Zr in BaTiO_3 , the rhombohedral to

orthorhombic (T_1) and orthorhombic to tetragonal (T_2) phase transition temperatures corresponding to pure BaTiO_3 increase. In contrast, the tetragonal to cubic (T_C) phase transition temperature decreases (Maiti *et al.*, 2008; Yu *et al.*, 2007). Thus when Zr concentration is less than 10 mol%, these $\text{BaZr}_x\text{Ti}_{1-x}\text{O}_3$ systems exhibit pinched phase transition; i.e., all the above three phase transition temperatures (T_1 , T_2 , and T_C) correspond to pure BaTiO_3 are merged or pinched into a single diffuse phase transition. At around 27 mol%, Zr-doped BaTiO_3 ceramics exhibit typical diffuse paraelectric to ferroelectric phase transition behavior, whereas Zr-riched compositions exhibit typical relaxor-like behavior in which T_c shifts to higher temperature with increase of frequency (Moura *et al.*, 2008; Mouraa *et al.*, 2008).

Recently, researchers have found that $\text{Ba}(\text{Ti}_{1-x}\text{Zr}_x)\text{O}_3$ with $x = 0$ and $x = 0.005$ contained the tetragonal BaTiO_3 phase. The $x = 0.02$ sample contained a mixture of the tetragonal and orthorhombic structures, whereas the $x = 0.04$ sample contained primarily the orthorhombic phase. For $x = 0.12$, the structure was cubic (Levin *et al.*, 2010). In that work, the local structure information of Ti in $\text{Ba}(\text{Ti}_{1-x}\text{Zr}_x)\text{O}_3$ powders and its characteristics as a function of Zr concentration were obtained. The results showed that increasing of Zr content in BaTiO_3 affected the local structure of BZT, as shown in Figure 1.3.

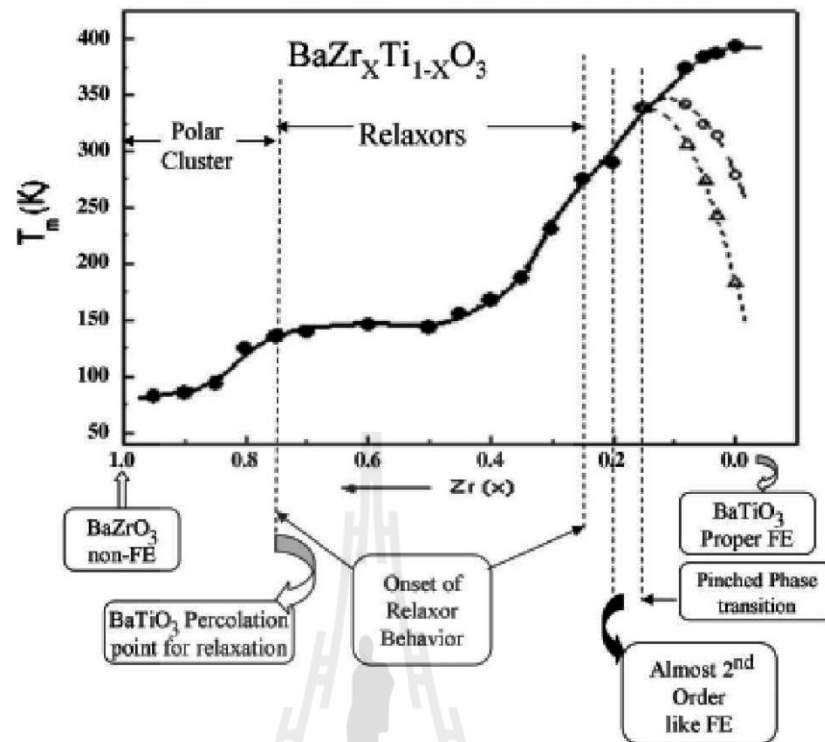


Figure 1.3 Phase diagram of $\text{Ba}(\text{Ti}_{1-x}\text{Zr}_x)\text{O}_3$ compound as a function of Zr content. (Maiti *et al.*, 2008).

1.3.2 Barium Titanium Stannate

Barium titanium stannate is lead-free ferroelectric with the chemical formula $\text{Ba}(\text{Ti},\text{Sn})\text{O}_3$ which can exhibit relaxor ferroelectric behavior when Sn replaces Ti about 30% or $x=0.3$ for $\text{Ba}(\text{Ti}_{1-x}\text{Sn}_x)\text{O}_3$. By comparison between Zr^{4+} (atomic weight of 91.2, ionic radius of 0.086 nm) and Sn^{4+} (atomic weight of 118.7, ionic radius of 0.083 nm), Zr^{4+} has larger ionic radius less than Sn^{4+} but it has less atomic weight. However, substitution of either Zr or Sn (or both) into Ti atom in BaTiO_3 about 30 mol% exhibits relaxor-like ferroelectric behavior (Wei and Yao, 2007; Cerneaw and Manea, 2007). In addition, at $x > 0.13$, Sn-doped BaTiO_3 structure changes to cubic phase as shown in Figure 1.5.

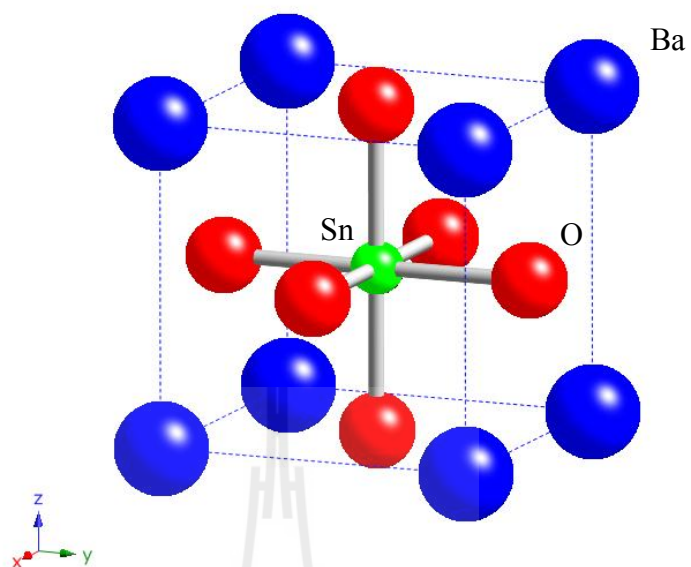


Figure 1.4 Crystal structure of cubic perovskite BaSnO_3 .

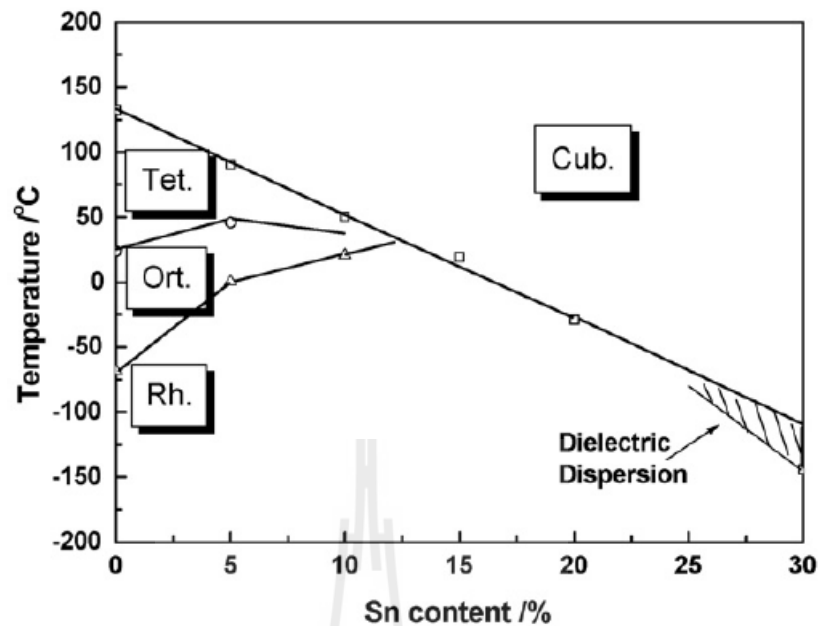


Figure 1.5 The phase diagram of Ba(Ti_{1-x}Sn_x)O₃ compound as a function of Sn content/% (Wei and Yao, 2007).

1.3.3 Bismuth Zinc Titanate

Bismuth zinc titanate is a new lead-free polar compound with the chemical formula Bi(Zn,Ti)O₃. The crystal structure is tetragonal perovskite, with Ti and Zn occupied in B site by ratio 0.5:0.5 (black ball in Figure 1.6) and the highest reported lattice constant *c/a* ratio of 1.211. However, Bi(Zn,Ti)O₃ is unstable in its pure form and can only be stabilized under high pressures or in solid solutions with other perovskite end members (Huang, 2008), but the composite of BaTiO₃ with Bi(Zn,Ti)O₃ is stable and can exhibit relaxor ferroelectric behavior. At around 10 mol% of Bi(Zn_{1/2}Ti_{1/2})O₃ in BaTiO₃-Bi(Zn_{1/2}Ti_{1/2})O₃, phase transition from tetragonal to pseudocubic or rhombohedral is observed (Huang and Cann, 2008; Raengthon and Cann, 2011).

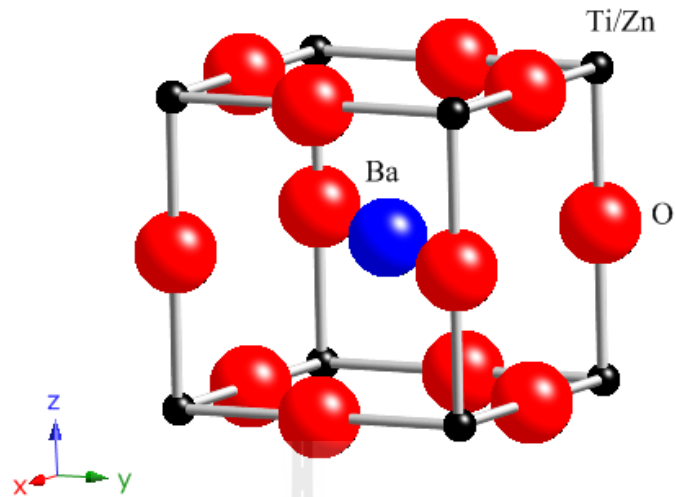


Figure 1.6 The structure of tetragonal perovskite $\text{Bi}(\text{Zn},\text{Ti})\text{O}_3$.

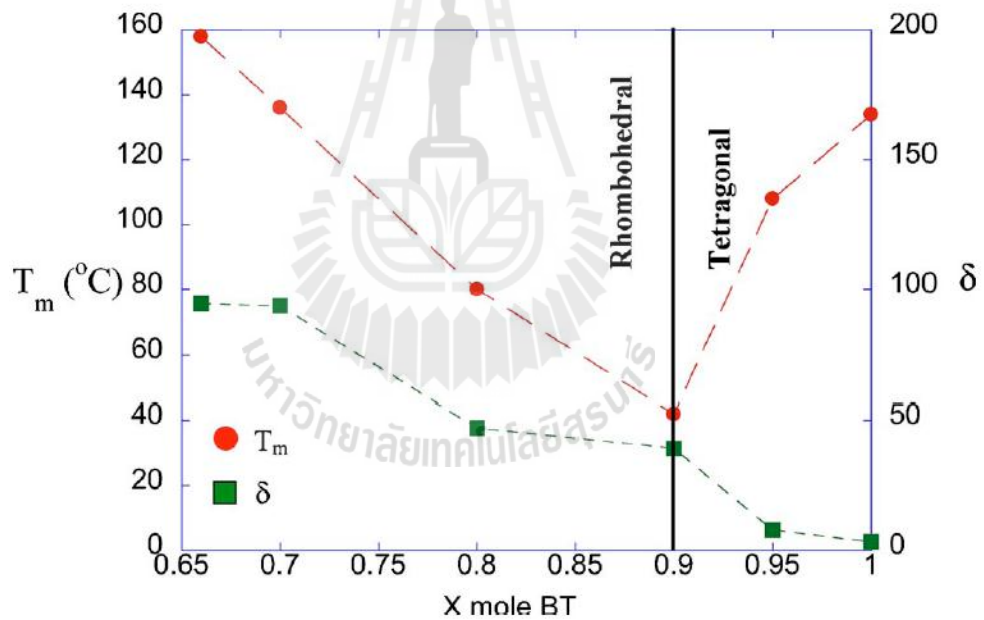


Figure 1.7 The phase diagram of $x\text{BaTiO}_3-(1-x)\text{Bi}(\text{Zn}_{1/2}\text{Ti}_{1/2})\text{O}_3$ compound (Huang, 2008).

Table 1.1 Some properties of BaTiO₃-based perovskite structure (Gražulis *et al.*,2012).

	BaTiO ₃	BaZrO ₃	BaSnO ₃	Bi(Zn,Ti)O ₃
Perovskite type	Tetragonal	Cubic	Cubic	Tetragonal
Lattice parameter	a = 3.998Å c = 4.018Å	a = 4.157Å	a = 4.116Å	c/a = 1.211 Å
Dielectric behavior	ferroelectric	paraelectric	paraelectric	unstable in its pure form

1.4 Scope and Limitations of the Study

This study aims to synthesize Ba(Ti_{1-x}Zr_x)O₃, Ba(Ti_{1-x}Sn_x)O₃ and xBaTiO₃-(1-x)Ba(Ti_{1-x}Zn_x)O₃ materials. The standard XRD will be used to determine global structure of the prepared materials. The local structure of Ba(Ti_{1-x}Zr_x)O₃, Ba(Ti_{1-x}Sn_x)O₃ and xBaTiO₃-(1-x)Ba(Ti_{1-x}Zn_x)O₃ materials will be characterized by XAS. FEFF 8.2 code will be used to simulate the x-ray absorption near edge structure (XANES) of Ba(Ti_{1-x}Zr_x)O₃, Ba(Ti_{1-x}Sn_x)O₃ and xBaTiO₃-(1-x)Ba(Ti_{1-x}Zn_x)O₃ to compare with experiment. Athena and Artemis programs will be used for data analysis and fitting respectively. In addition, dielectric properties of Ba(Ti_{1-x}Zr_x)O₃, Ba(Ti_{1-x}Sn_x)O₃ and xBaTiO₃-(1-x)Ba(Ti_{1-x}Zn_x)O₃ will also be investigated.

1.5 References

- Cerneaw, M. and Manea, A. (2007). Ba(Ti_{1-x}Sn_x)O₃ (x=0.13) Dielectric Ceramics Prepared by Coprecipitation. **J. Am. Ceram. Soc.** 90: 1728.
- Gražulis, S. (2012). Crystallography Open Database (COD) (online) Available: <http://www.crystallography.net>.
- Huang, C.-C. and Cann, D. P. (2008). Phase transitions and dielectric properties in Bi(Zn_{1/2}Ti_{1/2})O₃-BaTiO₃ perovskite solid solutions. **J. Appl. Phys.** 104: 024117.
- Huang, C. C. (2008). **Structure and Piezoelectric Properties of Lead-Free Bismuth-Based Perovskite Solid Solutions**. Doctor of Philosophy, Oregon State University, Oregon.
- Levin, I., Krayzman, V., Woicik, J. C., Tkach, A. and Vilarinho, P. M. (2010). X-ray absorption fine structure studies of Mn coordination in doped perovskite SrTiO₃. **Appl. Phys. Lett.** 96: 052904.
- Maiti, T., Guo, R. and Bhalla, A. S. (2006). The evolution of relaxor behavior in Ti⁴⁺ doped BaZrO₃ ceramics. **J. Appl. Phys.** 100: 114109.
- Maiti, T., Guo, R. and Bhalla, A. S. (2008). Structure-Property Phase Diagram of BaZr_xTi_{1-x}O₃ System. **J. Am. Ceram. Soc.** 91: 1769.
- Moura, F., Simões, A. Z., Stojanovic, B. D., Zaghete, M. A., Longo, E. and Varela, J. A. (2008). Dielectric and ferroelectric characteristics of barium zirconate titanate ceramics prepared from mixed oxide method. **J. Alloys Comp.** 462: 129.
- Mouraa, F., Simões, A. Z., Stojanovic, B. D., Zaghete, M. A., Longoa, E. and Varela, J. A. (2008). Dielectric and ferroelectric characteristics of barium zirconate titanate ceramics prepared from mixed oxide method. **J. Alloys Comp.** 462: 129.

- Raengthon, N. and Cann, D. P. (2011). Dielectric Relaxation in $\text{BaTiO}_3\text{-Bi}(\text{Zn}_{1/2}\text{Ti}_{1/2})\text{O}_3$ Ceramics. **J. Am. Ceram. Soc.** 95: 1604.
- Wei, X. and Yao, X. (2007). Preparation, structure and dielectric property of barium stannate titanate ceramics. **Mater. Sci. Eng. B.** 137: 184.
- Yu, Z., Ang, C., Guo, R. and Bhalla, A. S. (2007). Dielectric properties of $\text{Ba}(\text{Ti}_{1-x}\text{Zr}_x)\text{O}_3$ solid solutions. **J. Appl. Phys.** 61: 326.



CHAPTER II

THEORY

2.1 Dielectric properties

2.1.1 Basic theory (Hench and West, 1990; Barsoum, 1997)

According to Gause's law for two metal parallel plates of area A separated by a distance d in vacuum, shown in Figure 2.1. Assume the area of two metal parallel A larger than distance d and electric field is constant within two metal parallel plates.

$$\varepsilon_0 \oint \vec{E} \cdot d\vec{A} = Q \quad (2.1)$$

For two metal parallel plates ($d \ll A$),

$$\varepsilon_0 EA = Q \quad (2.2)$$

and

$$v = Ed \quad (2.3)$$

From definitions of capacitance

$$C = \frac{Q}{v} \quad (2.4)$$

Therefore, the capacitance for two metal parallel plates of area A separated by a distance d in vacuum, given by

$$C_{vac} = \frac{\varepsilon_0 A}{d} \quad (2.5)$$

where ε_0 is the permittivity of free space, which is a constant equal to $8.85 \times 10^{-12} \text{ C}^2/(\text{J} \cdot \text{m})$. The units of capacitance are farads (F), where $1F = 1 \text{ C}/V = 1 \text{ C}^2/\text{J}$.

In case of within two metal parallel plates is dielectric material, shown in Figure 2.1.

In other words, equation (2.5) is now modified to read

$$C = \frac{\epsilon A}{d} \quad (2.6)$$

where ϵ is the dielectric constant of material of between the plates. In addition, the relative dielectric constant of a material k' is defined as

$$C = \frac{k' \epsilon_0 A}{d} = k' C_{vac} \quad (2.7)$$

Comparing equation (2.6) to equation (2.7) yields

$$k' = \frac{\epsilon}{\epsilon_0} \quad (2.8)$$

Sine ϵ is always greater than ϵ_0 , the minimum value for the relative dielectric constant is 1.

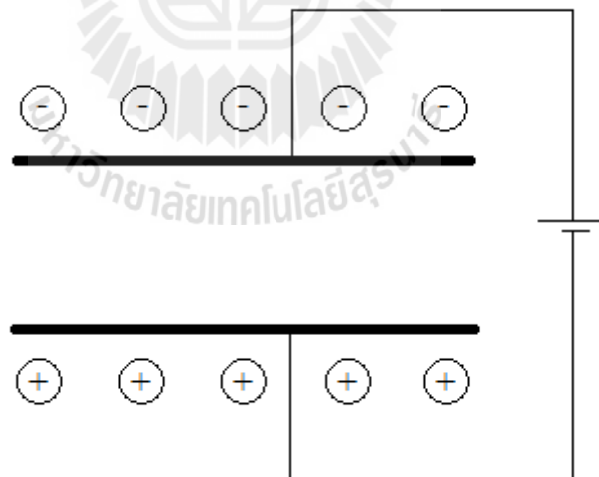


Figure 2.1 Parallel-plate capacitor of area A and separation d in vacuum attached to a voltage source.

Electromagnetic theory defines the **dielectric displacement D** as the surface charge density on the metal plates, in figure 2.2 that is

$$D = \sigma_{vac} + \sigma_{pol} \quad (2.9)$$

By combining equation (2.3), (2.4) and (2.5), the surface charge density in vacuum σ_{vac} is

$$\sigma_{vac} = \left[\frac{Q}{A} \right]_{vac} = \frac{\epsilon_0 V}{d} = \epsilon_0 E \quad (2.10)$$

where E is the applied electric field. For σ_{pol} is surface charge density were induced by dipole moment. Also σ_{pol} is numerically equal to the **polarization P** of dielectric, i.e.. Therefore, equation (2.9) can be written is

$$D = \epsilon_0 E + P \quad (2.11)$$

If $P = 0$, D is simply same equation (2.10), which is mean metal parallel plates in vacuum. Moreover, the **dielectric displacement D** is still defined by

$$D = k' \epsilon_0 E \quad (2.12)$$

If combining equation (2.11) and (2.12), that is

$$P = (k' - 1) \epsilon_0 E = \chi_{die} \epsilon_0 E \quad (2.13)$$

where

$$\chi_{die} = k' - 1$$

and χ_{die} is the dielectric susceptibility of material, which directly related with dielectric constant.

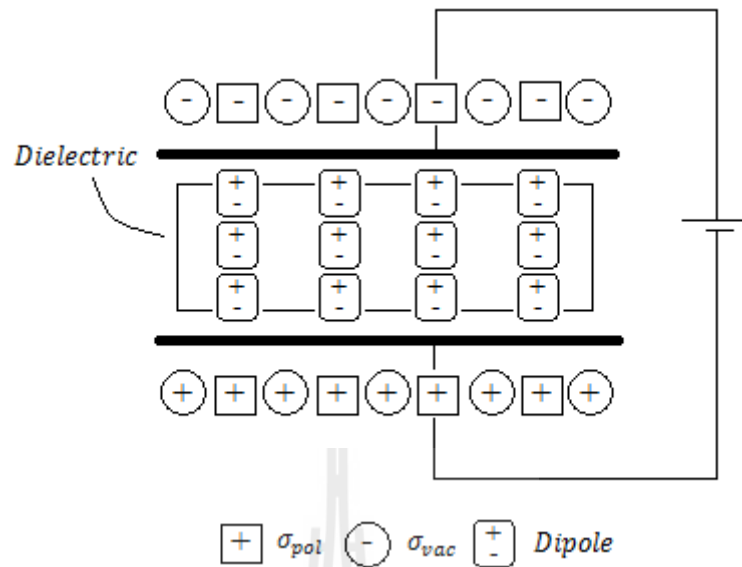


Figure 2.2 Parallel-plate capacitor except that now a dielectric is placed between the plates and attached to a voltage source.

2.1.2 Polarization mechanisms

Consider polarization in microscopic, which can be determined by multiplying the number of atoms per unit volume N with dipole moment μ , that is

$$\vec{P} = N\vec{\mu} \quad (2.14)$$

and

$$\vec{\mu} = \alpha\vec{E}_L \quad (2.15)$$

where α is polarizability, the SI units are $C \cdot m^2/V$ or Fm^2 and E_L is the local electric field to which the atom is subjected. To estimate the local electric field, which will stem from four sources :

- E_1 is the free charges due to the applied electric field E .
- E_2 is the field that arises from the free ends of the dipole chains that

line the cavity.

- E_3 is the field due to atoms or molecules in the near vicinity of the reference molecule.

- E^* is the external electric field.

$$E_L = E_1 + E_2 + E_3 + E^* \quad (2.16)$$

E_1 is depolarization field and related geometry of material for the dielectric material is infinite slab, that is

$$\vec{E}_1 = -\left(\frac{1}{\epsilon_0}\right) \vec{P} \quad (2.17)$$

E_2 is caused from polarize charge of Lorentz cavity. Electric field at center point on sphere radius R is

$$E_2 = \int_0^R \left(\frac{-P \cos \theta}{4\pi\epsilon_0 R^2}\right) \cos \theta (2\pi R^2 \sin \theta d\theta)$$

$$E_2 = \frac{1}{3\epsilon_0} P \quad (2.18)$$

E_3 is total dipoles moment of molecule on cavity sphere

$$E_3 = \left(\frac{1}{4\pi\epsilon_0}\right) \left[\frac{3(\vec{p}\cdot\vec{r})\vec{r}-r^2\vec{p}}{r^5}\right] \quad (2.19)$$

The cubic crystals is highly symmetric crystals, it can be assumed that the additional individual effect of the surrounding atoms mutually cancel, or

$$E_3 = 0 \quad (2.20)$$

Substitution equation (2.17), (2.18) and (2.20) to (2.16)

$$E_L = E^* - \frac{2}{3\epsilon_0} P \quad (2.21)$$

According to Lorentz relation, given by

$$E = E^* - \frac{1}{\epsilon_0} P \quad (2.22)$$

Therefore, combining equation (2.22) with (2.23), that is

$$E_L = E + \frac{1}{3\epsilon_0}P \quad (2.23)$$

If consider polarizability α , it is properties of each atom or molecule. But dielectric constants depend on atom or molecule in crystals. Therefore, polarization of crystals is

$$P = \sum N_i \alpha_i E_{L(i)} \quad (2.24)$$

where N_i is number of atom i per unit volume.

α_i is polarizability of atom i .

$E_{L(i)}$ is the local electric field at position atom i .

Substitution equation (2.23) to (2.24), that is

$$P = \frac{\sum N_i \alpha_i E}{1 - \frac{\sum N_i \alpha_i}{3\epsilon_0}} \quad (2.25)$$

Combining to equation (2.13), that is

$$k' = \frac{1 + \frac{2}{3\epsilon_0} \sum N_i \alpha_i}{1 - \frac{1}{3\epsilon_0} \sum N_i \alpha_i} \quad (2.26)$$

or

$$\frac{k'-1}{k'+2} = \frac{\sum N_i \alpha_i}{3\epsilon_0} \quad (2.27)$$

Equation (2.27) shows relation of dielectric constant with polarizability, it is called Clausius-Mosotti relation. In addition, the total polarizability is the sum of the contributions from the various mechanisms, or

$$\frac{k'-1}{k'+2} = \frac{1}{3\epsilon_0} [N_e \alpha_e + N_{ion} \alpha_{ion} + N_{dip} \alpha_{dip} + N_{space\ chg} \alpha_{space\ chg}] \quad (2.28)$$

where N_i represents the number of polarizing species per unit volume. In the remainder of this section, electronic, ionic and ion jump polarization or dipolar are discussed in some detail.

2.1.2.1 Electronic polarization (Barsoum, 1997; Hench and West, 1990)

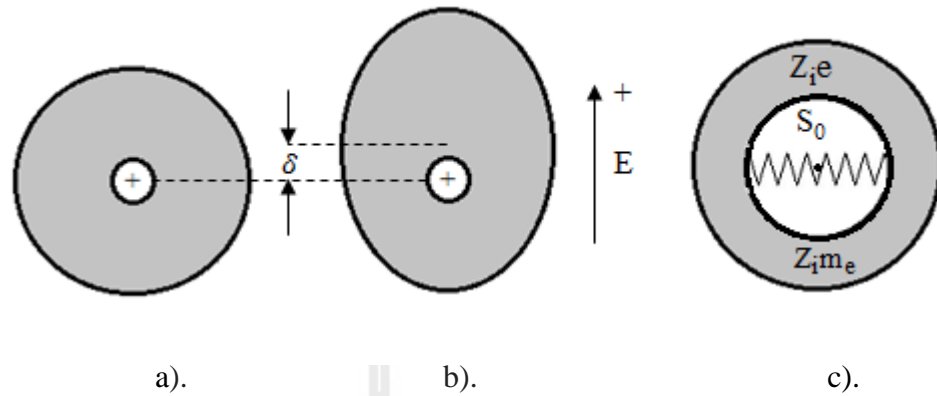


Figure 2.3 Electronic polarization of electron cloud surrounding a nucleus. a). At equilibrium, without an applied electric field b). In the presence of an applied electric field. c). Schematic of model assumed in text. S_0 represent the stiffness of bond between the electrons and the nucleus.

In schematic figure 2.3a and b it is shown that electronic polarization occurs when an applied electric field, exhibits electron displacement relative to the nucleus it is surrounding. It is operative at highest frequencies and drops off only at high frequencies ($\approx 10^{15}$ Hz). In classical theory assumed model, which electron is coupled to nucleus by stiff bonding S_0 , shown in figure 2.3c. If natural frequency of system is ω_0 , the restoring force can be written that

$$F_{restor} = M_r \omega^2 \delta \quad (2.29)$$

where M_r is the reduced mass of oscillation system, defined as

$$M_r = \frac{Z_i^2 m_e m_n}{Z_i m_e + Z_i m_n} \quad (2.30)$$

where m_e and m_n is mass of electron and nucleus respectively, But $m_n \gg m_e$.

Therefore, the reduce mass of oscillation system approximate is

$$M_r \approx Z_i m_e \quad (2.31)$$

If an applied electric field is AC current, a driving force is

$$F = Z_i e E = Z_i e E_0 \exp(i\omega t) \quad (2.32)$$

With a restoring force and a damping constant or friction factor, f . Therefore, the equation of motion is

$$Z_i m_e \left(\frac{d^2 \delta}{dt^2} + f \frac{d\delta}{dt} + \omega_0^2 \delta \right) = Z_i e E_0 \exp(i\omega t) \quad (2.33)$$

Solution of equation (2.33) is

$$\delta = \frac{e E_0}{m_e \sqrt{(\omega_0^2 - \omega^2)^2 + f^2 \omega^2}} \exp i(\omega t - \Phi) \quad (2.34)$$

And
$$\delta = \frac{e E_0}{m_e \{(\omega_0^2 - \omega^2)^2 + i\omega f\}} \exp i\omega t \quad (2.35)$$

where Φ represents the phase difference between the forced vibration and the resulting polarization, take the value

$$\tan \Phi = \frac{f\omega}{\omega_0^2 - \omega^2} \quad (2.36)$$

Consider the dipole moment of electronic polarization μ_e , that is $\mu_e = \sum N_i e \delta_i$ to combine equation (2.13), (2.34) and (2.35), the real (k'_e) and imaginary parts (k''_e) of the relative dielectric constant are, respectively,

$$k'_e(\omega) = 1 + \frac{Z_i e^2 N (\omega_0^2 - \omega^2)}{\epsilon_0 m_e \{(\omega_0^2 - \omega^2)^2 + f^2 \omega^2\}} \quad (2.37)$$

$$k''_e(\omega) = \frac{Z_i e^2 N \omega f}{\epsilon_0 m_e \{(\omega_0^2 - \omega^2)^2 + f^2 \omega^2\}} \quad (2.38)$$

Moreover, for $\omega \gg \omega_0$, the ions no longer follow the applied electric field and drop out, that is $k'_{ion} \rightarrow 1$, as

$$k'_e(\omega) = 1 + \frac{Z_i e^2 N_e}{\epsilon_0 m_e \omega_e^2} \quad (2.39)$$

Therefore, electronic polarization will be sensitive in the high frequencies (10^{16} to 10^{18} Hz).

2.1.2.2 Ionic polarization (Barsoum, 1997)

Ionic polarization is defined as the displacement of positive and negative ions, as shown schematically in Figure. 2.4. Ionic resonance is sensitive in the infrared frequency range (10^{12} to 10^{13} Hz). The expansion of ionic polarization can derive same electronic polarization. Similarity, the positive ions are assumed to be attached to negative ions by a spring having a natural frequency of vibration ω_{ion} . The reduced mass of the system is given by $M_r = m_c m_a / (m_c + m_a)$, where m_c and m_a is masses of cation and anion, respectively. In the structure of materials may be the friction of motion which was defined as f_{ion} . The final result is very similar electronic polarization and is given by

$$\text{For real part} \quad k'_{ion}(\omega) = 1 + \frac{(Ze)^2 N_{ion} (\omega_{ion}^2 - \omega^2)}{\epsilon_0 M_r \{(\omega_{ion}^2 - \omega^2)^2 + f_{ion}^2 \omega^2\}} \quad (2.40)$$

$$\text{And imaginary part} \quad k''_{ion}(\omega) = \frac{(Ze)^2 N_{ion} \omega f_{ion}}{\epsilon_0 M_r \{(\omega_{ion}^2 - \omega^2)^2 + f_{ion}^2 \omega^2\}} \quad (2.41)$$

where N_{ion} is the number of ion pairs per cubic meter. Moreover, for $\omega \gg \omega_{ion}$, the ions no longer follow the applied electric field and drop out, that is $k'_{ion} \rightarrow 1$, as

$$k'_{ion}(\omega) = 1 + \frac{(Ze)^2 N_{ion}}{\epsilon_0 M_r \omega_{ion}^2} \quad (2.42)$$

From Eqs. (2.42), Ionic polarization will be sensitive in the infrared frequency range or high frequencies (10^{12} to 10^{13} Hz).

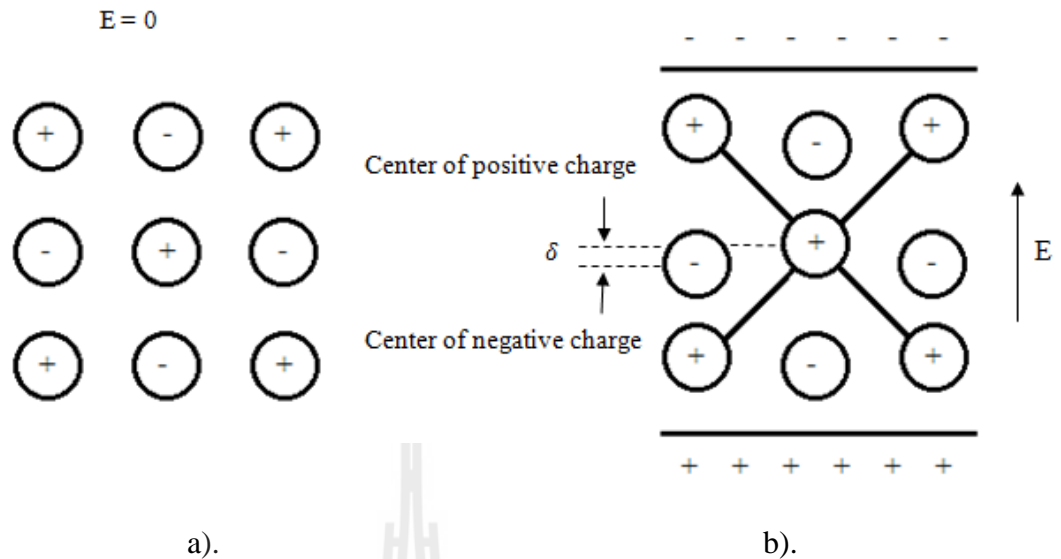


Figure 2.4 Ionic polarization. a). Ion positions at equilibrium $E=0$. b). When an applied electric field, the center of positive charge is no longer coincident with the center of negative charge, i.e., polarization occurs.

2.1.2.3 Dipolar polarization

Dipolar polarization or orientation polarization is important because it occurs at frequencies lower 10^{10} Hz and greatly affects the capacitive and insulative properties of glass and ceramics. Difference with in case of electronic polarization and ionic polarization because it occurs at high frequencies ($\omega > 10^{10}$ Hz).

In case of dipolar polarization, the effect of the applied electric fields occurs the ion jump polarization which is the referential occupation of equivalent or near-equivalent lattice site. In the absence of an electric field, each site has an equal probability of being occupied and no net dipolar polarization, as shown in Figure 2.5(a). While, the applied electric field, the two sites are no longer equivalent. The situation of an ion is localized in deep energy well, within two equivalent sites, labeled A and B in Figure 2.5(b), exist. With applied electric field, the sites are

separated from each other by a distance λ_s and an energy barrier ΔH_m , resulting in a net polarization.

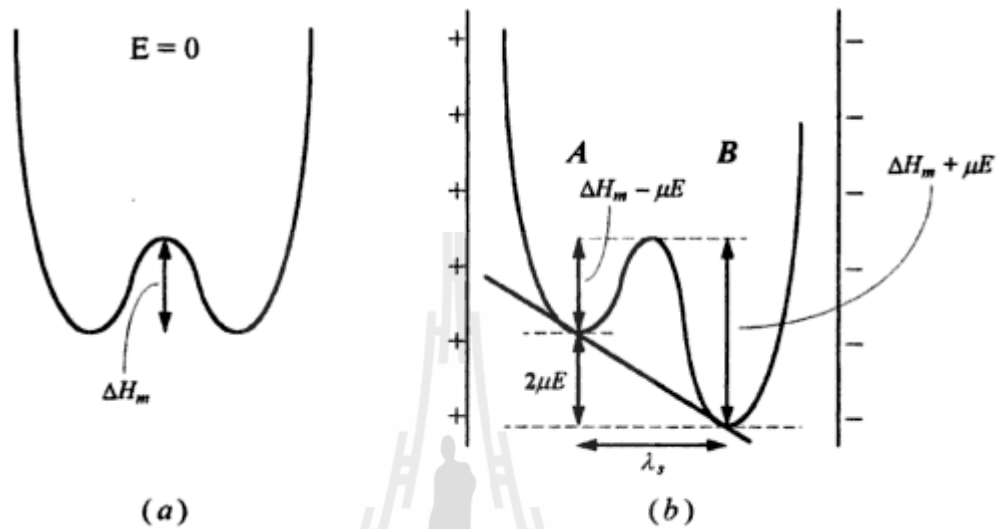


Figure 2.5 Dipolar polarization; (a) energy versus distance diagram in absence of applied field; the two sites are equally populated. (b) The application of an electric field will bias on site relative to the other (Barsoum, 1997).

The Boltzmann factor can be explained the probability of an ion's making a jump in case of no external electric field, as

$$P = K \exp\left(-\frac{\Delta H_m}{kT}\right) \quad (2.43)$$

where P is the probability of an ion's making a jump, k is Boltzmann constant about 1.38×10^{-23} J/K and T is temperature. The potential energy of dipolar depends on the orientation of dipole moment μ_{dip} and the applied electric field E , is

$$U = -\vec{\mu}_{\text{dip}} \cdot \vec{E} = -\mu_{\text{dip}} E \cos \theta \quad (2.44)$$

where U is the potential energy of dipolar and θ is the angle between dipole moment with the applied electric field. The moment aligns with or against the field, the potential energy is simply $\pm\mu_{\text{dip}}E$ at $\theta = 0^\circ$ or 180° . Therefore, the potential energy difference between the two locations is $2\mu_{\text{dip}}E$. Assuming N_{dip} amount of dipoles per unit volume, the jump probability $A \rightarrow B$ is

$$P_{A \rightarrow B} = K \exp\left(-\frac{\Delta H_m - \mu_{\text{dip}}E}{kT}\right) \quad (2.45)$$

For this case, the applied electric fields are small enough that $\mu_{\text{dip}}E/kT \ll 1$ and this equation simplifies to

$$P_{A \rightarrow B} = \left(1 + \frac{\mu_{\text{dip}}E}{kT}\right)P \quad (2.46)$$

Similarity, the jump probability $B \rightarrow A$ is

$$P_{B \rightarrow A} = \left(1 - \frac{\mu_{\text{dip}}E}{kT}\right)P \quad (2.47)$$

At steady state,

$$N_A P_{A \rightarrow B} = N_B P_{B \rightarrow A} \quad (2.48)$$

where N_A and N_B are the number of ions in each well. Combining Eq. (2.46) with (2.47) into (2.48), yield is

$$N_B - N_A = (N_B + N_A) \frac{\mu_{\text{dip}}E}{kT} = N_{\text{dip}} \frac{\mu_{\text{dip}}E}{kT} \quad (2.49)$$

The **static polarization per unit volume** P_s is defined as

$$P_s = (N_B - N_A)\mu_{\text{dip}} = N_{\text{dip}} \frac{\mu_{\text{dip}}^2 E}{kT} \quad (2.50)$$

from the relationship of Eq. (2.13) into (2.50), obtains

$$k'_{\text{dip}} = 1 + N_{\text{dip}} \frac{\mu_{\text{dip}}^2}{\epsilon_0 kT} \quad (2.51)$$

2.1.3 Temperature dependent dielectric loss

Eq. (2.27) shows relationship of the dielectrics constant with polarizations (Khamkongkao, 2013). In this section, we consider the effect of temperature. The experiment results show that dielectric constants are highest at Curie Temperature (T_C). Therefore, according to Eq. (2.26), dielectric constant will be infinite while at

$$\sum N_i \alpha_i = 3\epsilon_0 \quad (2.52)$$

In fact, the dielectric constant cannot be infinite, but is highly temperature dependent.

We can assign $\Delta \ll 1$, very small.

$$\frac{1}{3\epsilon_0} \sum N_i \alpha_i = 1 - \Delta \quad (2.53)$$

Substitution Eq. (2.53) into (2.27),

$$k' = \frac{3-2\Delta}{\Delta} \quad (2.54)$$

But $\Delta \ll 1$,

$$k' \approx \frac{3}{\Delta} \quad (2.55)$$

If consider the region around Curie temperature, Δ can be assigned as

$$\Delta \approx \frac{3(T-T_C)}{C} \quad (2.56)$$

Therefore,

$$k' = \frac{C}{T-T_C} \quad (2.57)$$

where C is Curie constant and Eq. (2.57) was called “Curie-Weiss law” which explains the dielectric constant in case of paraelectrics behavior.

In addition, dielectric loss will be increasing while temperature is increasing. Dielectric loss is caused by leakage currents (I_R). However, dielectric loss is caused by leakage currents only but all cause as

- ▶ Loss from dielectric constant not have infinite.
- ▶ Loss from dipole relaxation.

- ▶ Loss from electron polarization.
- ▶ Loss from ionic vibration.

Dielectric loss from dielectric constant cannot be infinite and dipole relaxation will be the effect of various frequencies. Dielectric loss from electron polarization and ionic vibration will be the effect of high frequencies only.

2.1.4 Frequency dependence and Dielectric loss

The process of polarization will be relaxation when applied electric field with dielectric materials (Khamkongkao, 2013). The relaxation will depend on frequency of applied electric field which can be described by Debye equation. We consider the relaxation during frequencies about 10^2 - 10^{11} Hz or dipolar polarizations. Define the dielectric constant of dipolar polarization at zero frequency a

$$k(\omega) = k_{\infty} + f(\omega) \quad (2.58)$$

where k_{∞} is optical dielectric constant or dielectric constant respond high frequency ($k_{\infty} = k_e + k_{ion}$). At zero frequency,

$$f(0) = k_s - k_{\infty} \quad (2.59)$$

where k_s is static dielectric constant. With applied electric field, dielectric materials exhibit of polarization relaxation and will be decreasing when applied field is removed.

$$P(t) = P_0 e^{-t/\tau} \quad (2.60)$$

where τ is relaxation time constant. We can use Fourier transform Eq. (2.60) into frequency space is

$$f(\omega) = \int_0^{\infty} P(t) e^{i\omega t} dt$$

$$f(\omega) = \frac{P_0}{-i\omega\tau + \frac{1}{\tau}} \quad (2.61)$$

at zero frequency,

$$f(0) = P_0\tau \quad (2.62)$$

according to the relationship of Eq. (2.59), (2.61) and (2.62),

$$f(\omega) = \frac{k_s - k_\infty}{1 - i\omega\tau} \quad (2.63)$$

substitute Eq. (2.63) into (2.58),

$$k(\omega) = k_\infty + \frac{k_s - k_\infty}{1 - i\omega\tau} \quad (2.64)$$

in electrical AC can be written as

$$k = k' - ik'' \quad (2.65)$$

Consider Eq. (2.64) and (2.65),

$$k'(\omega) = k_\infty + \frac{k_s - k_\infty}{1 + \omega^2\tau^2} \quad (2.66)$$

and

$$k''(\omega) = \frac{(k_s - k_\infty)\omega\tau}{1 + \omega^2\tau^2} \quad (2.67)$$

definition of dielectric loss is

$$\tan \delta = \frac{k''}{k'} \quad (2.68)$$

$$\tan \delta = \frac{(k_s - k_\infty)\omega\tau}{k_s + k_\infty + \omega^2\tau^2} \quad (2.69)$$

Equation of (2.66), (2.67) and (2.69) are Debye's equation which k' is related the dielectric constant and k'' is related the dielectric loss.

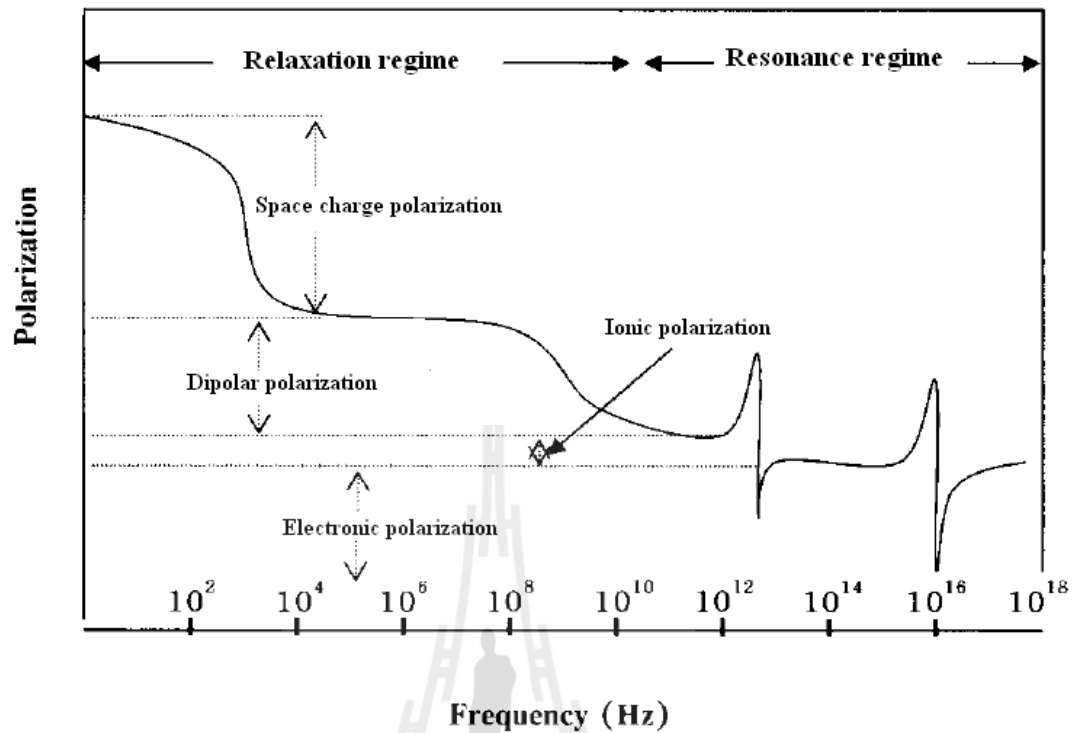


Figure 2.6 Variation of polarization with frequency (Khamkongkaeo, 2013).

2.2 Relaxor ferroelectrics (Huang, 2008)

In the 1950's, Smolenskii *et al.* first discovered relaxor ferroelectrics. The difference between a normal ferroelectric and a relaxor were discussed by the behavior around the Curie point which is illustrated in Figure. 2.7.

Considering the dielectric behavior of normal ferroelectric, when the temperature is above Curie temperature, T_c , the dielectric constant can be obtained by Curie-Weiss law which is shown in Eq. (2.64). Normal ferroelectric exhibits the sharp first order dielectric transition peak as a function of temperature. In relaxor ferroelectrics exhibit a broad and strong frequency dependent maximum dielectric permittivity. Moreover, the dielectric constant of relaxor ferroelectrics does not follow

Curie-Weiss law. But, it can be described by quadratic Curie-Weiss law, as shown in Eq. (2.65).

$$\text{Normal Ferroelectric:} \quad \frac{1}{\varepsilon} = \frac{T-T_C}{C} \quad (2.64)$$

$$\text{Relaxor Ferroelectric:} \quad \frac{1}{\varepsilon'(\omega, T)} - \frac{1}{\varepsilon'_m} = \frac{(T-T_m(\omega))^\gamma}{2\varepsilon'_m \delta_\gamma^2} \quad (1 \leq \gamma \leq 2) \quad (2.65)$$

where ε_{\max} is the permittivity at T_m , γ is degree of dielectric relaxation, where $\gamma = 1$ corresponds to a normal first-order ferroelectric phase transition. $\gamma > 1$ represent relaxor-ferroelectric behavior transition. The value of δ_γ represents the degree of diffuseness for transition peaks. Both γ and δ_γ are determined from the slope and intercept $\ln(\varepsilon'_{\max}/\varepsilon')$ versus $\ln(T - T_m)$ (Cross, 2011).

At the Curie point, the polarization decreases to zero relatively more rapid in ferroelectric materials compared to relaxor ferroelectric materials. The gradual decrease of the polarization in relaxors can be extended to the temperature above T_m and decays to zero at temperatures exceed T_m . At temperatures below T_m , relaxors can also show non-linear P-E behavior. However, the remnant polarization is much smaller than in normal ferroelectrics when the temperature is close to T_m as shown in Figure 2.7(b).

Generally, these kinds of materials may undergo transitions between the following states. (i) when the temperature above T_m , the paraelectric (PE) state occurs, and (ii) upon cooling they gradually transform into an ergodic relaxor (ER) state with a random distribution of polar nano-regions (PNRs). Generally the transition temperature from PE to ER state is the so-called Burns temperature (TB)

and is lower than T_m . It must not be confused with a structural transformations temperature since at TB there is no macroscopic structure change. (iii) an intermediate non-ergodic state (true relaxor state) with short range ordered polar nano-regions appeared once the temperature is low enough. (iv) when a strong electric field is applied to the nonergodic state, the ferroelectric state appears. On the basis of ordered PNRs, the relaxor ferroelectric shows unique properties from dipolar glasses and normal ferroelectrics (Huang, 2008).



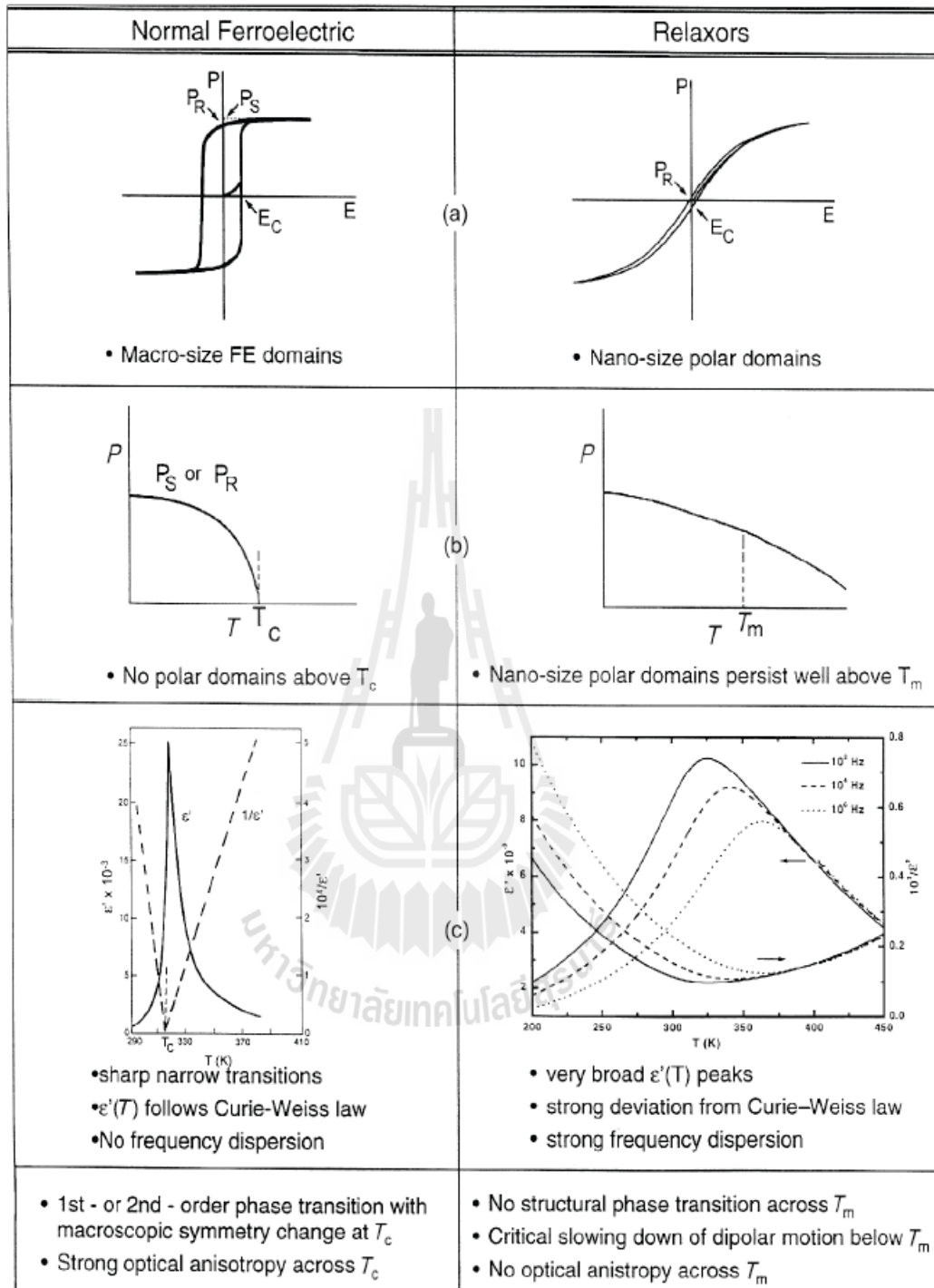


Figure 2.7 Comparisons of normal ferroelectric and relaxor ferroelectric (Huang, 2008).

2.3 Hysteresis

The hysteresis is a result of applied electric field into dielectric material, and it will generate polarization. For paraelectric materials, the polarization will be linearly increasing along electric field. But ferroelectric materials have included spontaneous polarization. The hysteresis loop is due to the presence of crystallographic domains within which there is complete alignment of electric dipoles. At low field strengths in unpolarized material, the polarization \mathbf{P} is initially reversible and will be linearly increasing along electric field follow by Eq. (2.66). In addition, the initial dielectric constant can be found at slope of polarization and electric field, as

$$\tan \alpha = \frac{P}{E} \quad (2.66)$$

$$\tan \alpha = (k'_i - 1)\epsilon_0$$

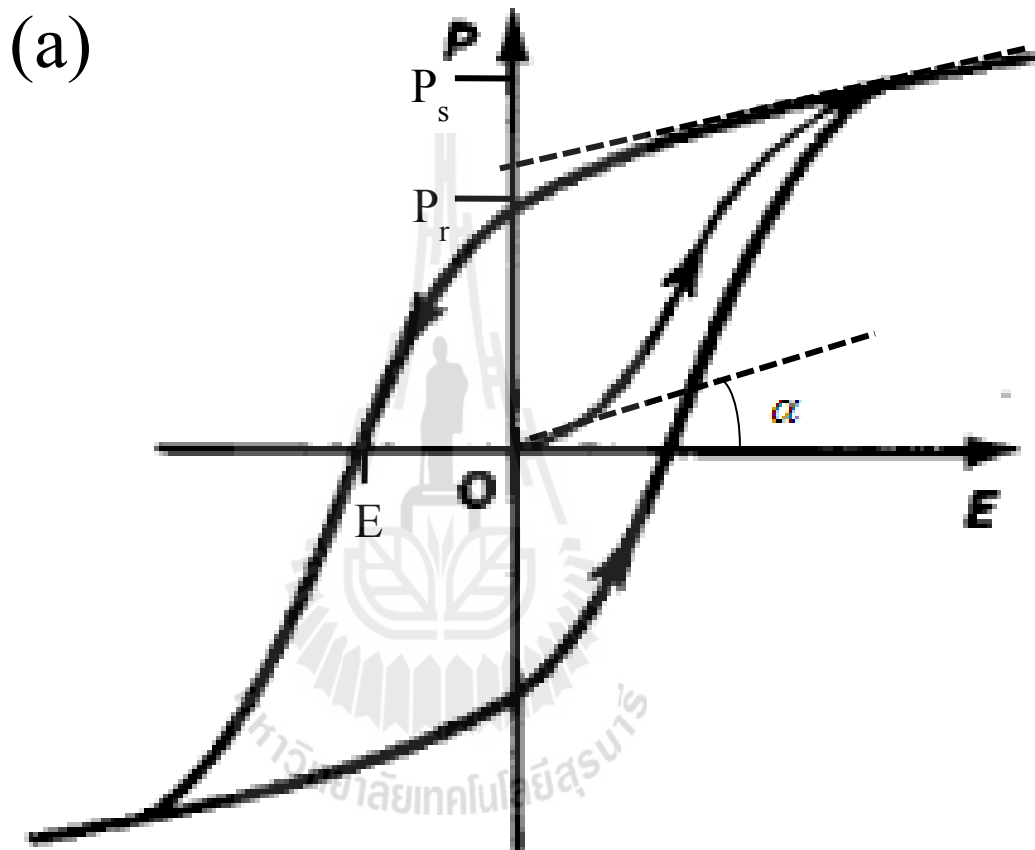
$$\text{or} \quad k'_i = 1 + \tan \alpha / \epsilon_0 \quad (2.67)$$

where k' is the initial dielectric constant.

At higher electric field, the polarization increases cause the switching of the ferroelectric domains which can explain by dipolar polarization or orientation polarization in section 2.1.2.3. The polarization switches so to align with the applied field by means of domain boundaries moving through the crystal. At high field strengths, the polarization will be saturation \mathbf{P}_s that means, all the domain orientation are aligned with the electric field, shown in Figure 2.8(a). The saturation polarization can be found at the high electric field curve back to $\mathbf{E}=0$ and corresponding to the spontaneous polarization with all dipoles aligned in parallel.

When the applied electric field decreases gradually until $\mathbf{E}=0$, the polarization does not go to zero but remains at finite value and called the remnant polarization, \mathbf{P}_r ,

because the oriented domains being unable to return to their random state. However, with the backward applied electric field, the dipole will return into random state until $P=0$ at the coercive field, E_c .



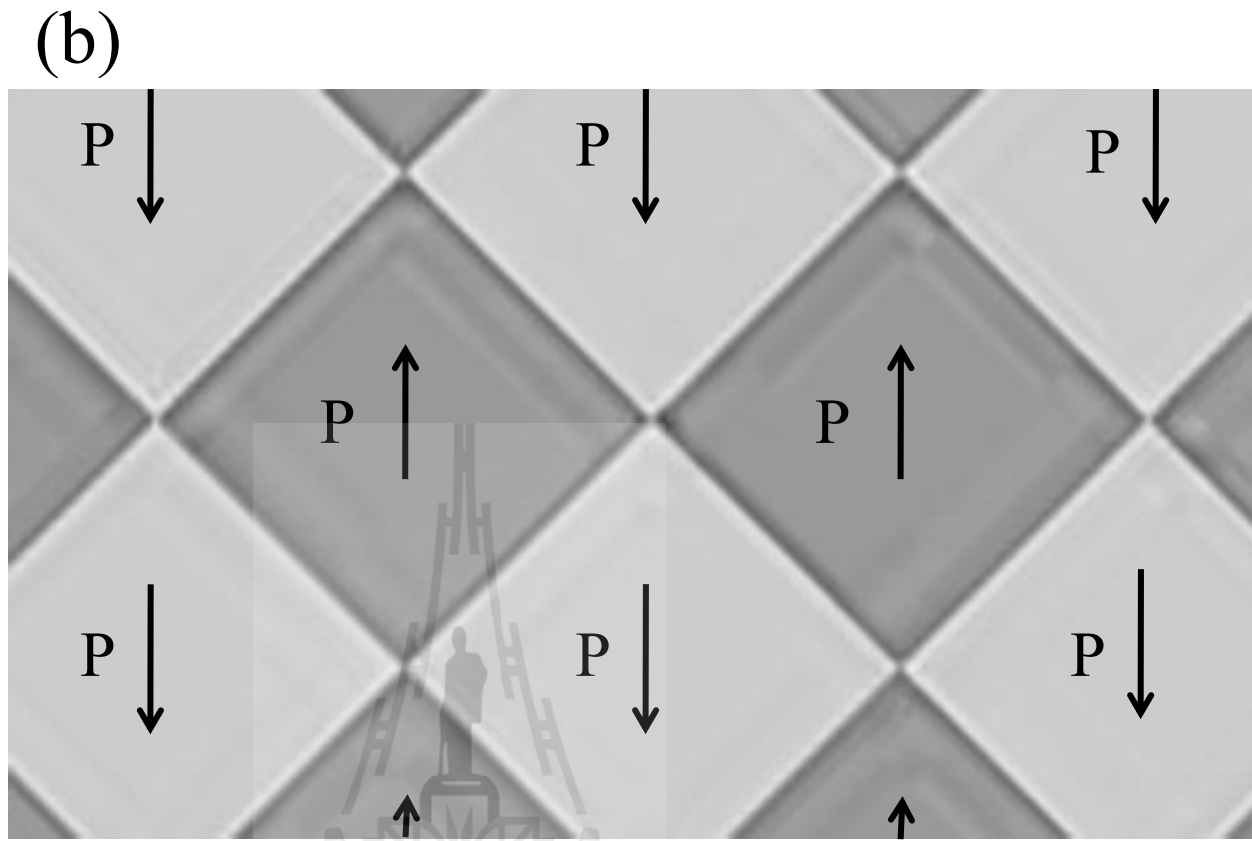


Figure 2.8 Hysteresis loop for polarization. (b) Domain microstructure without electric field, (c) Domain growth in direction of an applied electric field (Barsoum, 1997).

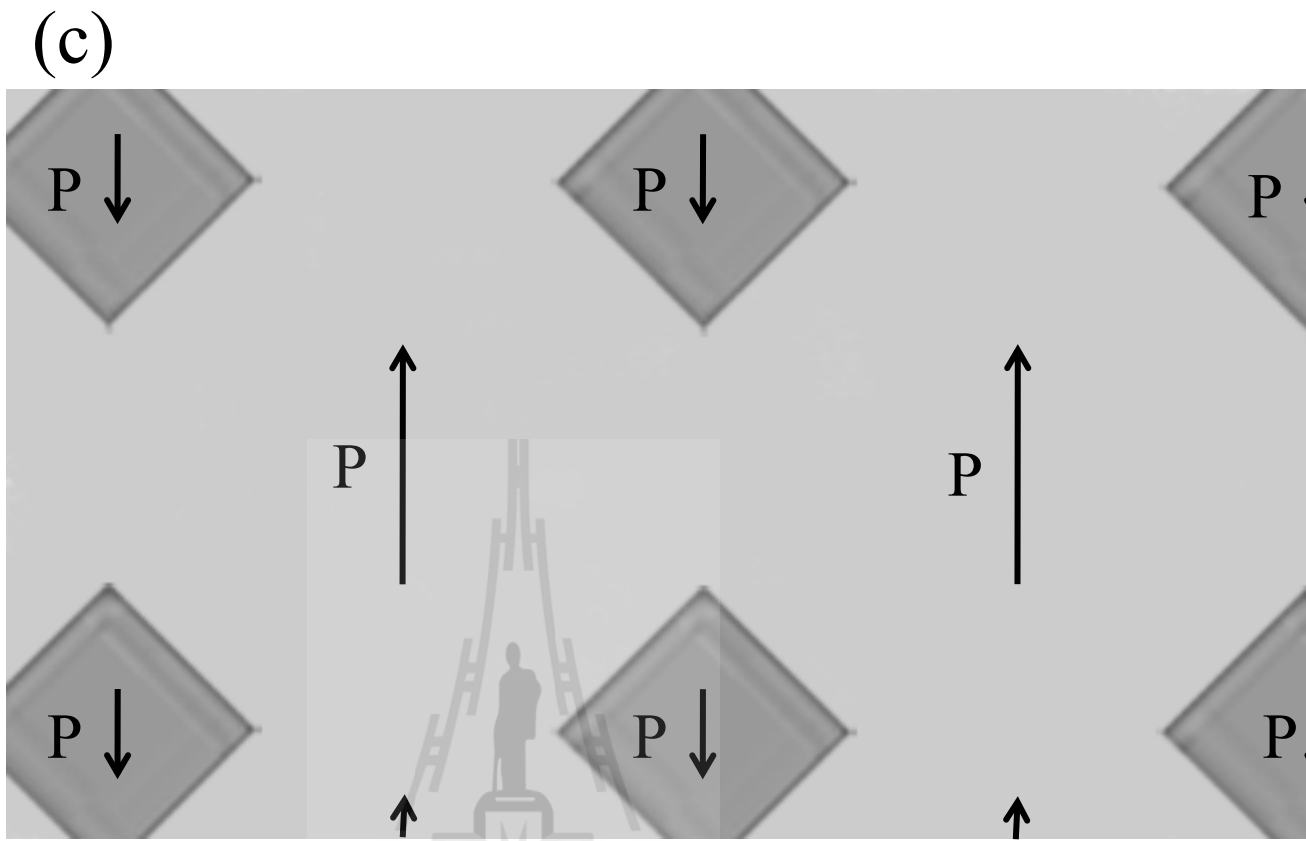


Figure 2.1 (Continued) Hysteresis loop for polarization. (b) Domain microstructure without electric field. (c) Domain growth in direction of an applied electric field (Barsoum, 1997).

2.4 X-ray Diffraction (XRD)

X-ray Diffraction is the standard technique which can identify the crystals structure and crystalline size of material. However, x-ray diffraction cannot measure amorphous materials because fundamental treatment of x-ray diffraction is considering the reflection of x-ray on each plan of crystal. While, the wave nature of x-ray incident on plan of crystal that occur reflection and the path difference of two plan equal amount of wavelength of the x-ray beam, as shown in Figure 2.9. The relationship between d -spacing, the angle of x-ray beam and wavelength of the x-ray obtained by the Bragg's law, as

$$2d \sin \theta = n\lambda \quad (2.68)$$

where d is the distance between adjacent plans of atoms or called “ d -spacing”, θ is the angle of x-ray beam, n is order of the diffracted beam and λ represents the wavelength of the incident x-ray beam.

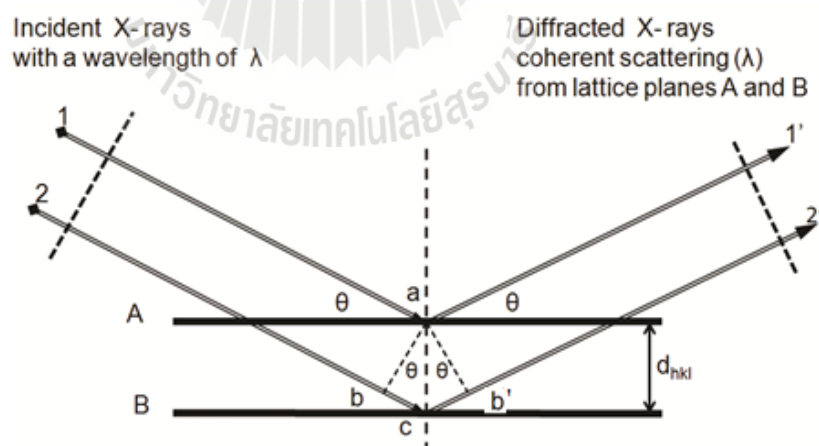


Figure 2.9 Mechanism of X-ray diffraction beam path (Peyronel and Marangoni, 2013).

In Figure 2.9, the path difference of the incident X-ray beam path 1 and path 2, is $\overline{bcb'}$. According to geometry mathematic, $\overline{bcb'}$ is $2d \sin \theta$ and correspond with Bragg's law.

2.5 X-ray Absorption Spectroscopy (XAS)

X-ray Absorption Spectroscopy is the powerful techniques for identifying local structure site of element, formal oxidation state, neighbor atoms and investigate the electronic structure of materials. The XAS experiment is normally carried out at the synchrotron radiation facility, where the energy of x-ray photon can be modified and selected (Shanthakumar, 2008). In addition, the synchrotron radiation facility has high intensity of light sources.

The equation of absorption was explained by the intensity of the beam after pass through the sample decreases according to exponential equation with the intensity of the incoming x-ray beam, as

$$I = I_0 e^{-\mu x} \quad (2.69)$$

where I_0 is the intensity of the incoming x-ray beam, I is the intensity of the beam after pass through the sample, x is the thickness of the sample, μ is the absorption coefficient as shown in Figure 2.10 and the absorption was defined by μx

$$\mu x = \ln\left(\frac{I_0}{I}\right) \quad (2.70)$$

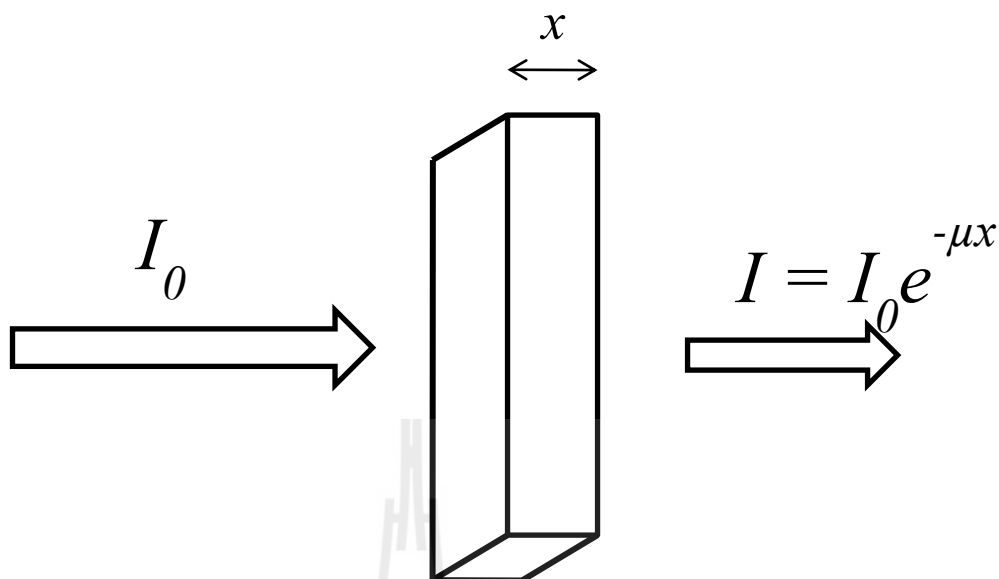


Figure 2.10 Schematic view of x-ray absorption measurement in transmission mode.

In case the electrons transition is followed by the selection rules. The Selection Rules governing transitions between electronic energy levels of transition metal complexes are

1. $\Delta S = 0$; The Spin Rule, the electron's spin must be unchanged from core shell state to excited state.
2. $\Delta l = \pm 1$; The Orbital Rule, the difference of electron's orbital angular momentum must be equal -1 or 1 only.

The total angular momentum was defined as $J = l + S$ or have value $|l - s| \geq J \geq l + s$, where $l = 0, 1, 2 \dots n - 1$ and $S = -\frac{1}{2}, \frac{1}{2}$. Therefore, the spin rule can be consider by $\Delta J = \pm 1$. In addition, the new symbol for electron each shell were

defined for the electron transition, shown in the Table 2.1, and Figure 2.11, shows the electron transition in inner shell.

Table 2.1 The symbol of the electron transition in function as quantum number.

<i>Shell</i>	<i>n</i>	<i>l</i>	<i>J</i>	<i>Symbol</i>
K	1	0	1/2	1s
L1	2	0	1/2	2s
L2	2	1	1/2	2p _{1/2}
L3	2	1	3/2	2p _{3/2}
M1	3	0	1/2	3s
M2	3	1	1/2	3p _{1/2}
M3	3	1	3/2	3p _{3/2}
M4	3	2	3/2	3d _{3/2}
M5	3	2	5/2	3d _{5/2}

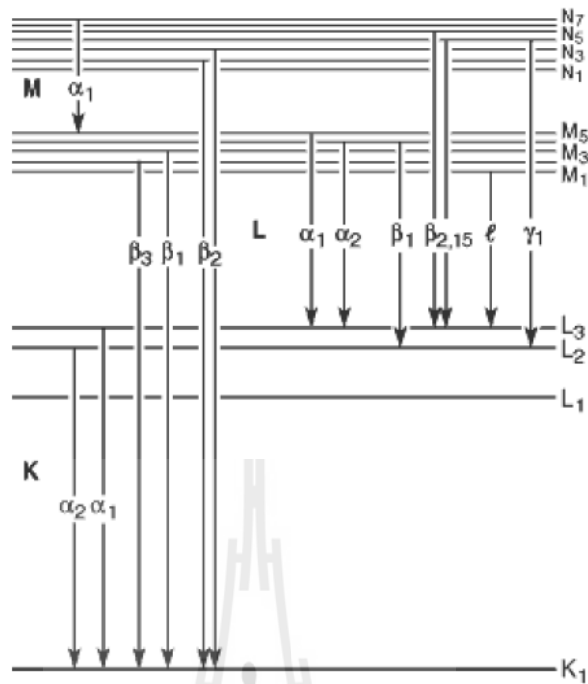


Figure 2.11 Diagram of the electron transition in inner shells (Thompson *et al.*, 2001).

When the X-ray energy is incident through the binding energy of a core shell, there exhibits a sudden increase in absorption cross-section. This spectrum is called absorption edge, with each edge representing a different core-electron binding energy. The name of edges is identified by the principle quantum number: K for $n=1$, L for $n=2$, M for $n=3$, etc. In the x-ray absorption process, a photon energy was absorbed by atom, affect to electron in inner shells: K, L or M shell which is transition to unoccupied valance band above the Fermi level. However, when electron is excited, energy state will not be stable. Therefore, electron in next state will be transition to replace excited electron and fluorescence emission occurs, shown in Figure 2.12. Although, core energy state is stabled but the next state will not be stable.

Therefore, another electron in next state will transit to conduction band and it is called “Auger electron”.

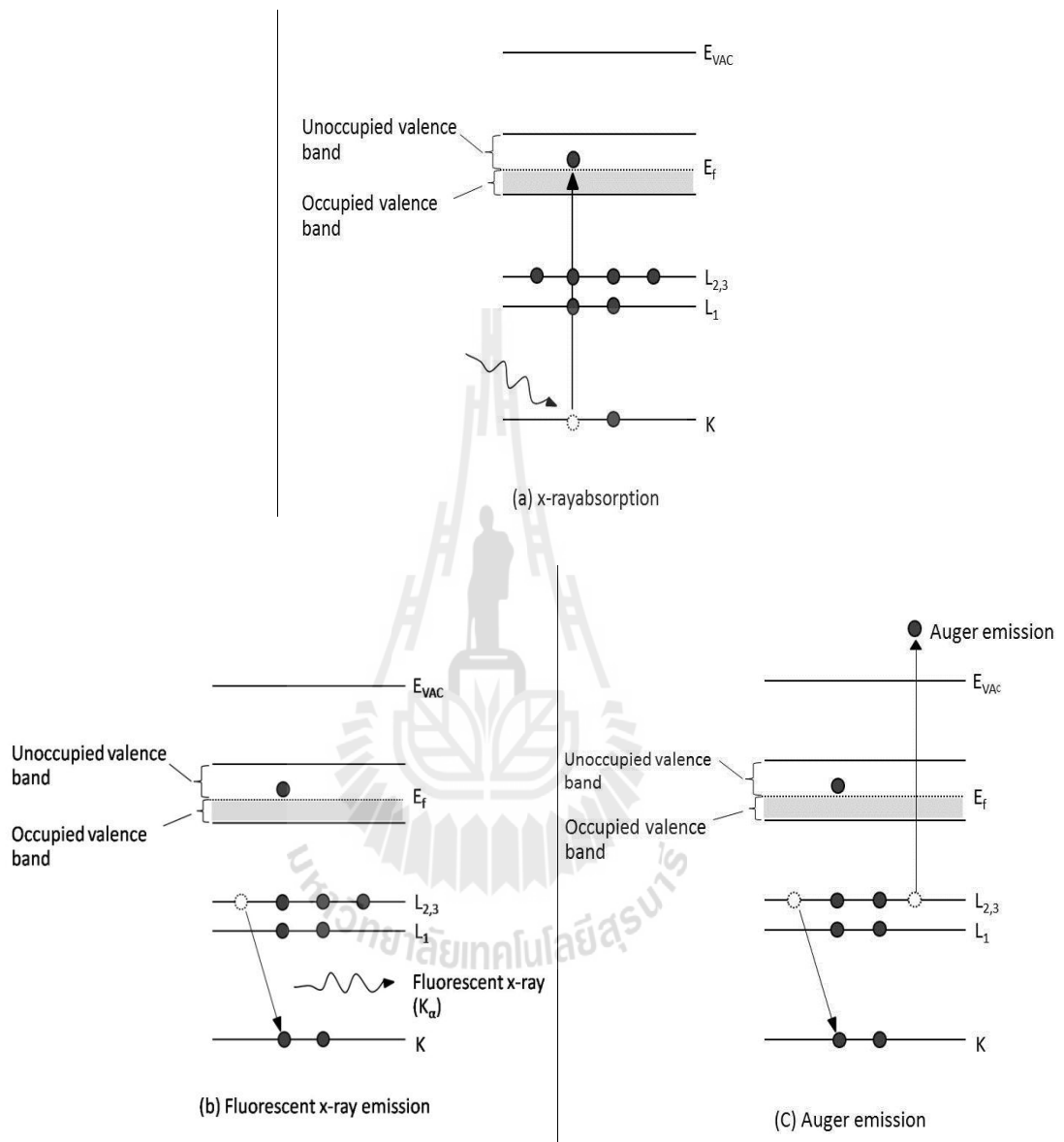


Figure 2.12 Mechanism of the x-ray absorption (a) X-ray absorption (b) Fluorescent X-ray emission and (c) Auger emission (Adapt from Klysubun, 2006).

For example, Fe K-edge refers to transition that excited electron from 1s to 3d orbital but according to the selection rule that is forbidden. However, in the case of compound FeO, the effect of Fe-O bonding affects d-orbital splitting as t_{2g} and e_g , after then occur the mixing d-p orbital from ligand field theory. Therefore, a forbidden transition is partially allowed due to mixing of ligand p-character. While the first line on the main edge is due to the allowed 1s to 4p bound-state transition. The post edge relates to unoccupied state in conduction band and full multiple scattering of spherical wave electron with neighbor atom. Moreover, XAS is classified as XANES, which ends about 80-100 eV above the edge, and EXAFS, which starts about 50 eV above the edge, as shown in Figure 2.13

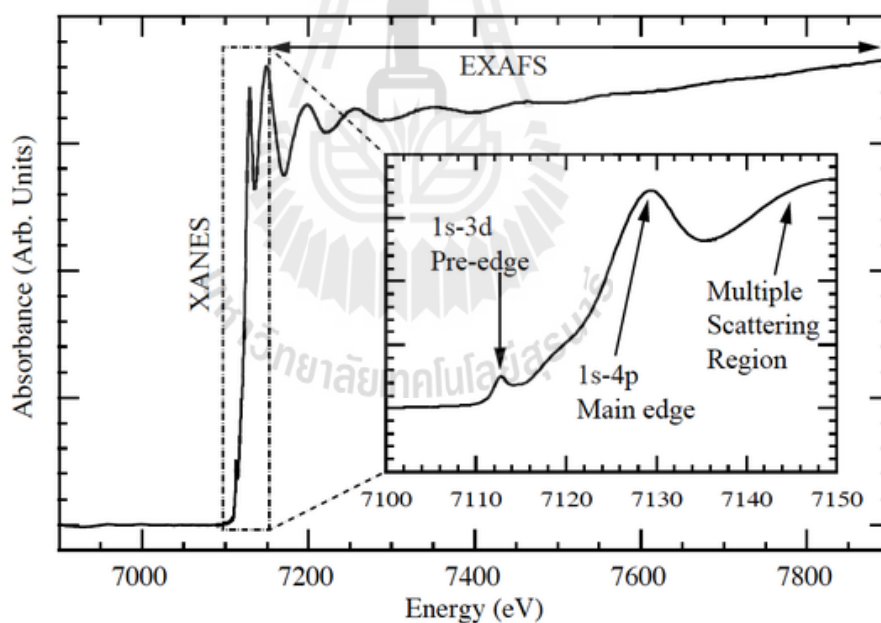


Figure 2.13 The absorbance Fe K-edge spectra in compound iron oxide (Larsen *et al.*, 2014).

2.5.1 X-ray Absorption Near Edge Structure (XANES)

The total absorption cross-section can be calculated by using the Fermi's Golden rule of one electron approximation (Gaussian unit)(Koningsberger and Prins, 1988; Kodre, 2002; Stern *et al.*, 1983; Als-Nielsen and McMorrow, 2001; Newville, 2004; Ravel, 1997; Shanthakumar, 2008),

$$\mu(\omega) = \frac{4\pi^2 e^2 c}{\omega} \sum_{i,f} \left| \langle f | \vec{r} \cdot \hat{\epsilon} e^{i\vec{k} \cdot \vec{r}} | i \rangle \right|^2 \delta(E_i - E_f + \hbar\omega) \quad (2.71)$$

where $|i\rangle, |f\rangle, E_i$ and E_f denote the initial and final states and their energies; k is wave vector, $\hat{\epsilon}$ is unit polarization, ω is frequency of photon energy, c is light velocity, e is electron charge and $\delta(E)$ is the Dirac delta function. Generally, this equation can be write in form the Dipole operator (\mathbf{D}) as

$$\mu(\omega) = \sum_{i,f} |\langle f | \mathbf{D} | i \rangle|^2 \delta(E_i - E_f + \hbar\omega) \quad (2.72)$$

which can easily understand for electron transition from $|i\rangle$ to next $|f\rangle$ state corresponding to the photon energy incident in the Dirac delta function and amplitude relate dipole transition in inner atom. However, when electron was excited by photon energy greater than binding energy, the electron will be transit to unoccupied valance band after then the photon energy is higher which carry out from inner atom and exhibit the propagation of spherical electron wave.

In this case we calculate the spherical electron wave scattering from the muffin-tin approximation. We discuss scattering from muffin-tin potential which is several atoms or ions, each of which makes a non-zero contribution only within a spherically non-overlapping scattering region of finite radius.

$$V = \sum_i v^i \quad (2.73)$$

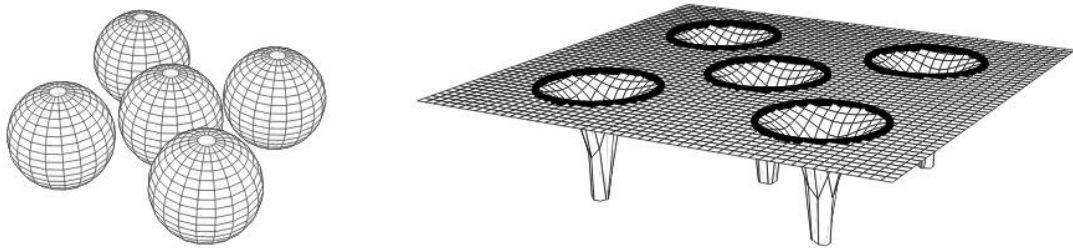


Figure 2.14 The muffin-tin potential consist of non-overlapping spherical regions (Kodre, 2002).

Figure 2.14, shows the muffin-tin potential, which outside the spherical regions or interstitial region, the potential is set to zero. The scattering parameters, consisting of the scattering amplitude and phase shifts, are determined separately for each scatterer and are therefore pure atomic quantities. Propagation of spherical electron wave in such muffin-tin potential V is described by the Hamiltonian

$$H = H_0 + V \quad (2.74)$$

where H_0 is the kinetic-energy operator. According to Schrodinger's equation is

$$H|\varphi\rangle = E|\varphi\rangle \quad (2.75)$$

substitution Eq. (2.74) into (2.75),

$$(E - H_0)|\varphi\rangle = V|\varphi\rangle \quad (2.76)$$

However, we cannot solve to exact solution. Therefore, we can consider to separated terms. The term of $(E - H_0)|\varphi\rangle$ is free-electron wave function and if $\langle \vec{r} | \varphi \rangle$ is the solution of the "homogeneous" part of free-electron wave function

$$(E - H_0)\langle \vec{r} | \varphi \rangle = 0 \quad (2.77)$$

And the free-electron Green's function G_0 is defined with relation

$$(E - H_0)G_0(\vec{r}, \vec{r}'; E) \equiv (\nabla^2 + k^2)G_0(\vec{r}, \vec{r}'; E) = \delta(\vec{r} - \vec{r}') \quad (2.78)$$

Therefore, the general solution of Eq. (2.77) can be written as a sum of the solution of the “homogeneous” part and the Green’s function for the muffin-tin potential part

$$\langle \vec{r} | \varphi \rangle = \langle \vec{r} | \emptyset \rangle + \int d^3r' G_0(\vec{r}, \vec{r}'; E) \langle \vec{r}' | V \varphi \rangle \quad (2.79)$$

It is easily understood, if the spherical electron wave is only weakly scattered by the potential V , the solution $\langle \vec{r} | \varphi \rangle$ is close to the free-electron solution $\langle \vec{r} | \emptyset \rangle$. Generally, the Green’s function can be written in form

$$G_0^\pm(\vec{r}, \vec{r}'; E) = \langle \vec{r} | G_0^\pm | \vec{r}' \rangle = -\frac{1}{4\pi} \frac{\exp(\pm ik|\vec{r}-\vec{r}'|)}{|\vec{r}-\vec{r}'|} = \langle \vec{r} | \frac{1}{E-H_0 \pm i\eta} | \vec{r}' \rangle \quad (2.80)$$

Because of its singularity, an imaginary term is modified in the operator $1/(E - H_0)$ by $\pm i\eta$, where η is infinitesimally small for identify direction of spherical wave electron, G_0^+ and G_0^- describe how outing and coming spherical waves propagate in free space, respectively. Therefore, the formal solution of the operator Eq. (2.79) is given by the Lippman-Schwinger equation

$$\langle \vec{r} | \varphi \rangle = \langle \vec{r} | \emptyset \rangle + \frac{1}{E-H_0 \pm i\eta} V | \varphi \rangle \quad (2.81)$$

To solve Eq. (2.81), one needs to define transition operator (T) are

$$V | \varphi \rangle = T | \emptyset \rangle \quad (2.82)$$

If we define the propagation G of this system as

$$\begin{aligned} G(E) &= (E - H_0 - V + i\eta)^{-1} = ([G_0]^{-1} - V)^{-1} \\ &= (1 - VG_0)^{-1} G_0 \end{aligned} \quad (2.83)$$

According to the Taylor series expression

$$G(E) = G_0 + G_0 V G_0 + G_0 V G_0 V G_0 + \dots = G_0 + G_0 V G \quad (2.84)$$

The following important relationships from Eq. (2.82),

$$G_0 T = G V;$$

$$T = G_0^{-1} G V = V + V G_0 V + V G_0 V G_0 V + \dots = V + V G_0 T \quad (2.85)$$

and $G = G_0 + G_0 T G_0; \quad T = V + V G V$ (2.86)

according to the muffin-tin potentials from Eq. (2.73), we can write the transition operators of individual atoms as

$$t^i = v^i + v^i G_0 t^i \tag{2.87}$$

However, the operator T and t^i is not obvious in the physical meaning, but we are able to explain in the weak-scattering expansions by substituting Eq. (2.87) into (2.85), (2.86), respectively, we obtain

$$G = G_0 + \sum_i G_0 v^i G_0 + \sum_{i,i_1} G_0 v^{i_1} G_0 v^i G_0 + \dots \tag{2.88}$$

$$= G_0 + \sum_i G_0 t^i G_0 + \sum_i \sum_{i_1 \neq i} G_0 t^{i_1} G_0 t^i G_0 + \dots \tag{2.89}$$

$$T = \sum_i t^i + \sum_i \sum_{i_1 \neq i} t^{i_1} G_0 t^i + \sum_i \sum_{i_1 \neq i} \sum_{i_2 \neq i_1} t^{i_2} G_0 t^{i_1} G_0 t^i + \dots \tag{2.90}$$

$$t^i = v^i + v^i G_0 v^i + v^i G_0 v^i G_0 v^i + \dots \tag{2.91}$$

Their series equations are called Dyson’s expansion and Eq. (2.90) can explain the order of scattering process of the spherical electron wave. The first term is an unscattered wave propagation. The second term is single scattering by free propagation G_0 to the i th atom where the wave is scattered once with potential v^i and then heads forward again as shown in Figure. 2.15(a)-left. Similarity, the third term “scatter” describes the incident wave two times as shown in Figure. 2.15(a)-middle and right.

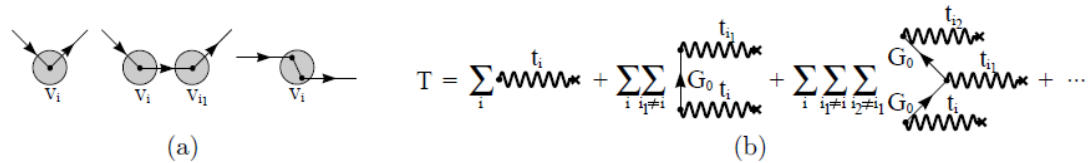


Figure 2.15 Single scattering (left), double scattering from different atoms (middle), and double scattering from the same atom (right). (b) Graphical representation of the T -operator (Kodre, 2002).

2.5.2 Extended X-ray Absorption Fine Structure (EXAFS)

The EXAFS is the effect of back scattering of the spherical electron wave by the neighbors of the central absorbing atom (Groot *et al.*, 1994; Hench and West, 1990), resulting in oscillations in the energy dependence of the absorption coefficient $\mu(E)$ after the energy edge (Rehr and Albers, 2000). The normalized experimental EXAFS signal is obtained by

$$\chi(E) = [\mu(E) - \mu_0(E)]/\Delta\mu_0(E). \quad (2.92)$$

where μ_0 is the background absorption coefficient, $\Delta\mu_0(E)$ is the absorption edge jump, and k is the photoelectron wave number, given by $k = \sqrt{2m_e(E - E_0)/\hbar^2}$ with m_e is the electron mass and E_0 is the edge energy. After that, $\chi(k)$ is obtained from the measured absorption coefficient $\mu(E)$. Also, the E_0 is the energy at the first maximum of the derivative of $\mu(E)$ at the Ti K -edge (S. Limpijumrong *et al.*, 2007). According to Fermi-Golden rule Eq. (2.71), the final state will be affected by the neighboring atom because the photo-electron will be able to see it. If we separate $|f\rangle$ into two state, one that is the “bare atom” portion ($|f_0\rangle$), and one that is the effect of the neighboring atom ($|\Delta f\rangle$) as

$$|f\rangle = |f_0\rangle + |\Delta f\rangle \quad (2.93)$$

Substituting Eq. (2.93) into (2.81),

$$\mu(E) \propto |\langle i|\hat{\epsilon}|f_0\rangle|^2 [1 + \langle i|\hat{\epsilon}|\Delta f\rangle \frac{\langle f_0|\hat{\epsilon}|i\rangle^*}{|\langle i|\hat{\epsilon}|f_0\rangle|^2} + C.C] \quad (2.94)$$

where C.C. means complex conjugate. Comparison Eq. (2.93) and (2.94), we can now assign $\mu_0(E) = |\langle i|\hat{\epsilon}|f_0\rangle|^2$ as the “bare atom absorption”, which depends on the absorbing atom only. Therefore, the signal of EXAFS will be proportion as

$$\chi(E) \propto \langle i|\hat{\epsilon}|\Delta f\rangle \quad (2.95)$$

We can consider (at least roughly) an integral equation easily (at least roughly). The interaction term H is probably the most complicated part, which represents the process of changing between two energy, momentum states. In quantum radiation theory, the interaction term needed is the $p \cdot \mathbf{A}$ term, where \mathbf{A} is the quantized vector potential (the $\mathbf{A} \cdot \mathbf{A}$ term, but this does not contribute to absorption). Therefore, it can be reduced to a term that is proportional to $e^{-i\vec{k} \cdot \vec{r}}$. The initial state is a tightly bound core-level, which we can be approximated by delta function. Finally, the change in final state is the wave-function of the scattered photo-electron, $\varphi_{scatt}(r)$.

$$\chi(E) \propto \int dr \delta(r) e^{ikr} \varphi_{scatt}(r) \quad (2.96)$$

However, the signal of EXAFS scattering occurs at $r=0$,

$$\chi(E) \propto \varphi_{scatt}(0) \quad (2.97)$$

The wave-function of the scattered photo-electron can be considered from the spherical wave electron moving out from absorber atoms and expressed as

$$\varphi_0(k, r) = \frac{e^{ik|R_i-r|}}{|R_i-r|} \quad (2.98)$$

traveling a distance R to the neighboring atom, then scattering from a neighbor atom, and traveling as a spherical wave a distance R back to the absorbing atom.

$$\varphi_{backscatt}(k, r) = \frac{f_i^{eff}(k) e^{ik|R_i-r|} e^{i(\delta_i(k)-\pi/2)}}{|R_i-r|} \quad (2.99)$$

where $f_i^{eff}(k)$ is the scattering amplitude and the term $\delta_i(k) - \pi/2$ is phase shift of photoelectron after scattering from neighbor atoms. Therefore, the total photoelectron wave scattering is obtained by

$$\varphi_{scatt}(k, r) = \varphi_0(k, r) \cdot \varphi_{backscatt}(k, r)$$

$$= \frac{f_i^{eff}(k) e^{2ik|R_i-r| + \delta_i(k) - \pi/2}}{|R_i-r|^2} \quad (2.100)$$

The scattering at absorber atom $r=0$, the real part of Eq. (2.100) is written as,

$$\varphi_{scatt}(k, r) = \frac{f_i^{eff}(k) \sin[2kR + \delta_i(k)]}{R^2} \quad (2.101)$$

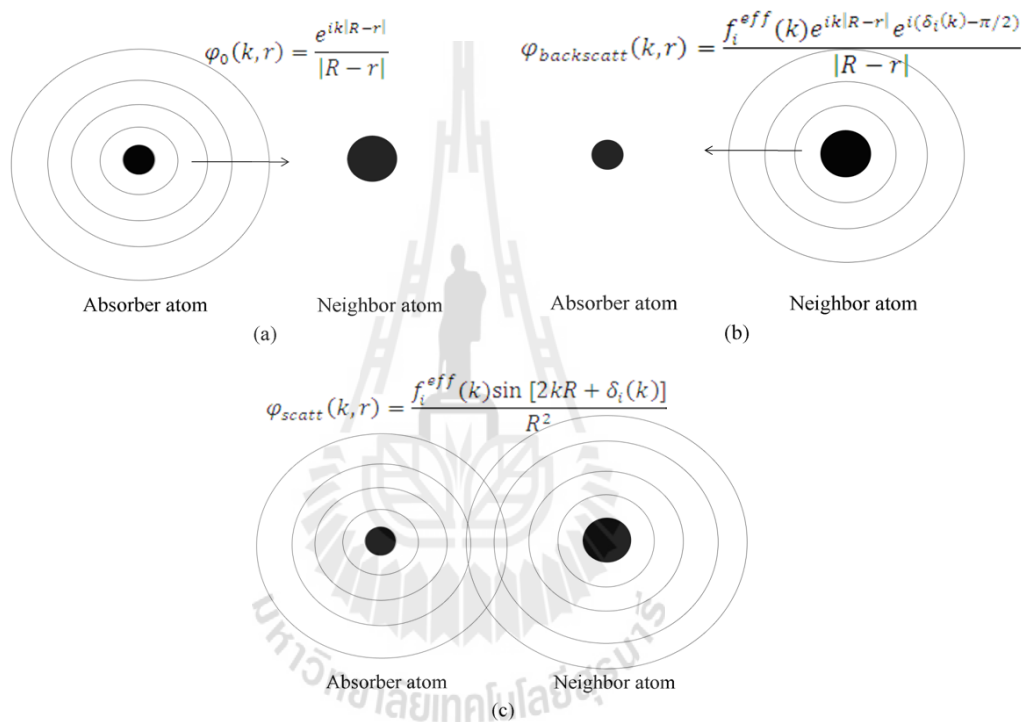


Figure 2.16 The EXAFS mechanism of photo electron scattering.

However, we neglect the effect of the thermal and static disorder in the bond distances will give a range of distances that will affect the XAFS is

$$e^{-2\sigma_i^2 k^2} \quad (2.102)$$

where σ_i^2 is the Debye-Waller (DW) factor which is caused by thermal vibration in subject of the heat capacity, is written as

$$\sigma_i^2(T) = \frac{\hbar^2}{2k_B M_R \theta_E} \coth\left(\frac{\theta_E}{2T}\right) \quad (2.103)$$

where k_B is the Boltzmann constant, M_R is reduce mass of scattering atoms and θ_E is the Einstein temperature.

Moreover, we still neglect the effect of the lifetime of excited photoelectron and core hole. Because in order for backscattering wave to interfere with outgoing wave the two must be coherent as

$$e^{-R_i/\lambda(k)} \quad (2.104)$$

where $\lambda(k)$ is mean-free part of the photoelectron. In addition, we should be neglect the relaxation of unexcited electrons in inner atom, defined as

$$S_0^2 = |\langle \phi_f^{N-1} | \phi_0^{N-1} \rangle|^2 \quad (2.105)$$

where $\langle \phi_f^{N-1} |$ accounts for the relaxation of the other (N - 1) electrons relative to these electrons in the unexcited atom: $|\phi_0^{N-1}\rangle$. Typically, S_0^2 is taken as a constant: $0.7 \leq S_0^2 \leq 1.0$. Therefore, the EXAFS equation can be modified as

$$\chi(k) = \frac{S_0^2}{kR_j^2} |f_j^{eff}(k, R_j)| \sin[2kR_j + \varphi_j(k)] e^{-2\sigma_j^2 k^2} e^{-R_j/\lambda(k)} \quad (2.106)$$

However, real systems usually have more than one type of neighboring atom around a particular absorbing atom. This is easily accommodated in the XAFS formalism, as the measured XAFS will simply be a sum of the contributions from each scattering atom type (or coordination shell, as it is often called – the terms coordination sphere and scattering path are also used), In general, $\chi(k)$ can be expressed by summation of all path, EXAFS equation is

$$\chi(k) = \sum_f \frac{S_0^2 N_j}{kR_j^2} |f_j^{eff}(k, R_j)| \sin[2kR_j + \varphi_j(k)] e^{-2\sigma_j^2 k^2} e^{-R_j/\lambda(k)} \quad (2.107)$$

where N_j is the degeneracy of path j . Note that Eq. (2.107) includes both single scattering (SS) and multiple scattering (MS) processes. For a SS path, N_j is simply the number of chemically identical atoms situated at a given distance R_j from the central atom. However, $\chi(k)$ can be a Fourier transform (FT) in R-space and expressed by

$$\chi(R) = \frac{1}{\sqrt{2\pi}} \int_0^\infty k^2 \chi(k) W(k) e^{i2kR} dk \quad (2.108)$$

To process and enhance the EXAFS with the high k region, the plot $k^2X(k)$ is considered and windowed using a Hanning window $W(k)$.

2.6 References

- Als-Nielsen, J. and McMorrow, D. (2001). **Elements of Modern X-ray Physics**. JohnWiley & Sons.
- Barsoum, W. (1997). **Fundamentals of Ceramics**. McGraw-Hill Companies.
- Cross, L. E. (2011). Relaxor ferroelectrics. **Ferroelectrics**. 76:1: 241.
- Groot, D., F., F. M., Hu, Z. W., Lopez, M. F., Kaindl, G., Guillot, F. and Tronc, M. (1994). Differences between L3 and L2 x-ray absorption spectra of transition metal compounds. **J. Chem. Phys.** 101: 6570.
- Hench, L. L. and West, J. K. (1990). **Principles of electronic ceramics**. Wiley.
- Huang, C.-C. (2008). **Structure and Piezoelectric Properties of Lead-Free Bismuth-Based Perovskite Solid Solutions**. Oregon State University, Oregon State
- Khamkongkao, A. (2013). **Electrical and Magnetic Properties of Cobalt Ferrite and Cobalt Ferrite–Barium Titanate Nanocomposites**. Ph.D. Dissertation, Khon Khen University, Khon Khen.

- Klysubun, W. (2006). **X-ray Absorption Spectroscopy Technique**. Nakhon Ratchasima Synchrotron Light Research Institute.
- Kodre, A. (2002). XANES spectroscopy (online). Available: <http://www.ung.si/~arcon/xas/xanes/xanes-theory.pdf>.
- Koningsberger, D. C. and Prins, R. (1988). **X-ray Absorption: Principles, Applications, Techniques of EXAFS, SEXAFS, and XANES**. John Wiley & Sons Inc.
- Larsen, D. (2014). **XANES : Application** (online). Available : <http://chemwiki.ucdavis.edu.htm>.
- Newville, M. (2004). **Consortium for Advanced Radiation Sources**. Chicago.
- Peyronel, F. and Marangoni, A. G. (2013). **Analytical Methods, Procedures and Theory for the Physical Characterization of Fats** (online). Available: <http://lipidlibrary.aocs.org/physics/xray/index.htm>.
- Ravel, B. D. (1997). **Ferroelectric Phase Transition in Oxide Perovskites Studied by XAFS**. Ph.D. Dissertation, University of Washington, Washington.
- Rehr, J. J. and Albers, R. C. (2000). Theoretical approaches to x-ray absorption fine structure. **Rev. Mod. Phys.** 72: 3.
- Shanthakumar, P. (2008). **X-ray study of two complex oxides, each having octahedral oxygen co-ordination of transition metals**. Ph.D. Dissertation, University of Connecticut, Connecticut.
- Stern, E. A., Heald, S. M. and Koch, E. E. (1983). **Synchrotron Radiation**. North-Holland.
- Thompson, A. C., Attwood, D. T., Gullikson, E. M., Howells, M. R., Jeffrey B. Kortright, Robinson, A. L., Underwood, J. H., Kim, K.-J., Kirz, J., Lindau, I.,

Pianetta, P., Winick, H., Williams, G. P. and Scofield, J. H. (2001). **X-RAY DATA BOOKLET**. Berkeley: Lawrence Berkeley Laboratory.



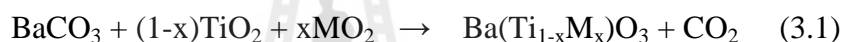
CHAPTER III

RESEARCH METHODOLOGY

3.1 Solid State Solution Synthesis

3.1.1 Ba(Ti,Zr)O₃ and Ba(Ti,Sn)O₃

In these two systems, the solid state reaction or conventional method was employed to synthesize the materials via chemical reactions, shown as



where M is Zr and Sn. The mixing between starting oxide materials was performed by the zirconium ball milling in ethanol solution. After that, the mixed powders were dried by hot plate with stirrer or magnetic bar at temperature about 100 °C. Finally, the yield of powders was calcined in furnace at high temperature suitable for each material (generally determined by TG-DTA). Although, the yield powders is rather inhomogeneous and particle size is large in micron size, this method is easy for basic synthesis.

Ba(Ti,M)O₃ (M=Zr and Sn) powders were prepared via methods of the solid state reaction. The starting materials BaCO₃ (99.98%) TiO₂ (99.98%), SnO₂ (98.7%) and ZrO₂ (98.7%) were weighed according to the *stoichiometric* composition Ba(Ti_{1-x}Zr_x)O₃ with $x = 0, 0.2, 0.25, 0.3, 0.35, 0.5, 0.6, 0.7, 0.75$ and 0.95. For Ba(Ti_{1-x}Sn_x)O₃ with $x = 0, 0.25, 0.3, 0.5, 0.7, 0.75$ and 0.95. The raw materials were weighed and ball milled in ethanol for 24 h. After drying, the powders were calcined

at 1150-1250 °C for 4h (Yu *et al.*, 2007; Cerneaw and Manea, 2007). The procedures are shown in Figure. 3.1.

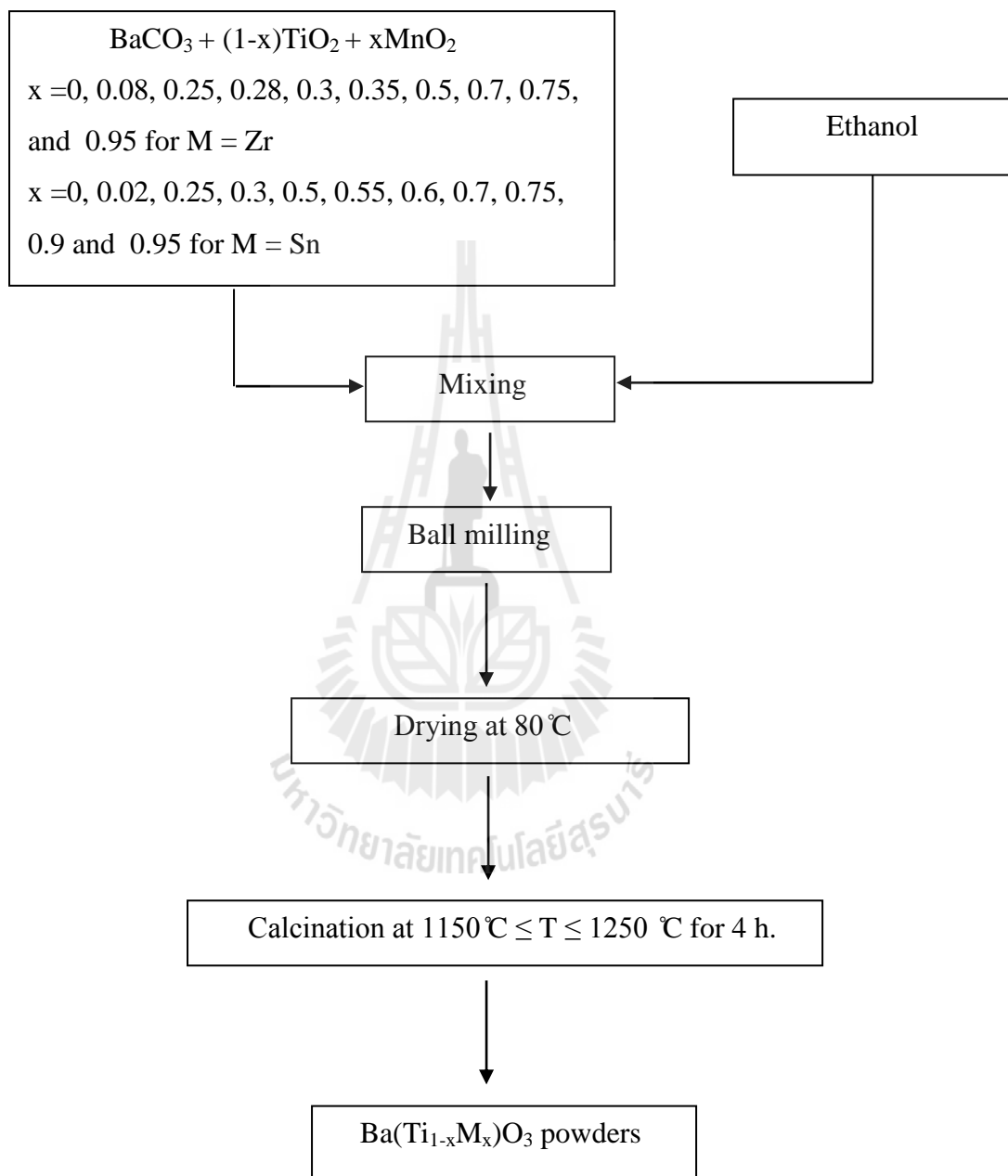


Figure 3.1 Flow chart of the synthesis of $\text{Ba}(\text{Ti}_{1-x}\text{M}_x)\text{O}_3$ powders ($\text{M} = \text{Zr}$ and Sn).

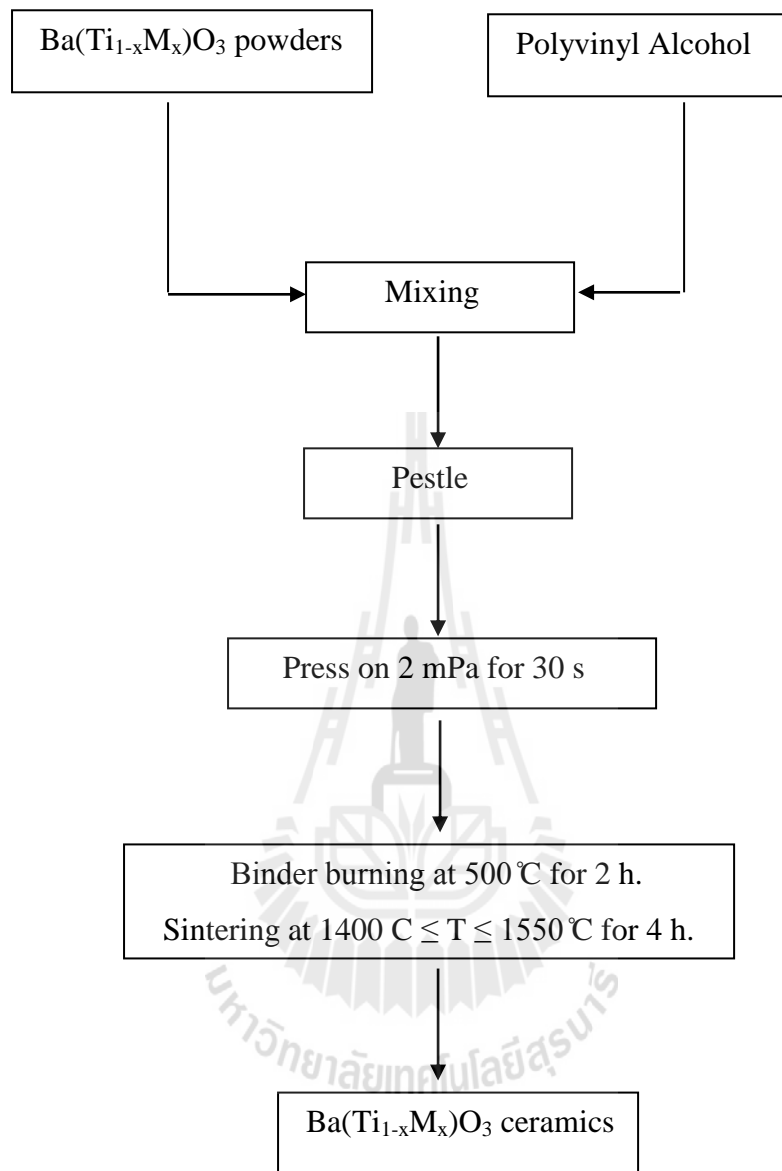
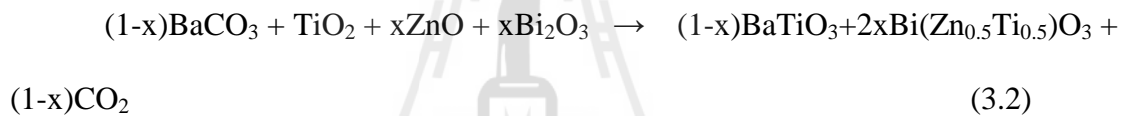


Figure 3.2 Flow chart of the synthesis of Ba(Ti_{1-x}M_x)O₃ ceramics (M=Zr and Sn).

After that, the Ba(Ti,Zr)O₃ powders were mixed with polyvinyl alcohol for homogeneous powders and made to bulk ceramics by pressed in disks holder about 2 mPa, diameter about 10.2 mm and thickness about 1 mm. The pellets were burned the polyvinyl alcohol at 500 °C for 2 h and sintered at 1500–1560 °C for 4–15 h (Maiti *et al.*, 2008). The synthesis flowchart is shown as Figure. 3.2.

3.1.2 BaTiO₃-Bi(Ti_{1/2}Zn_{1/2})O₃ Synthesis

(1-x)BaTiO₃-xBi(Zn_{0.5}Ti_{0.5})O₃ materials were prepared at Oregon State University at USA via the solid state reaction or conventional method with chemical reaction,



(1-x)BaTiO₃-xBi(Zn_{0.5}Ti_{0.5})O₃ powders were prepared by a conventional solid state reaction method. The starting BaCO₃(≥99.9%), TiO₂(≥99.9%), ZnO(≥99%) and Bi₂O₃(≥99.5%) materials were weighed according to the composition (1-x)BaTiO₃-xBi(Zn_{0.5}Ti_{0.5})O₃ (with $x = 0.05, 0.06, 0.07, 0.08, 0.09, 0.10, 0.11$ and 0.13) and mixed in ball mill for 24 h using an ethanol medium. After drying, the mixed powders were calcined at temperature of 950 °C for 12 h with 5°C/min heating/cooling rates. Sintering of the pellets was carried out between 1100-1300 °C for 4 h (Huang and Cann, 2008), as shown in Figure 3.3.

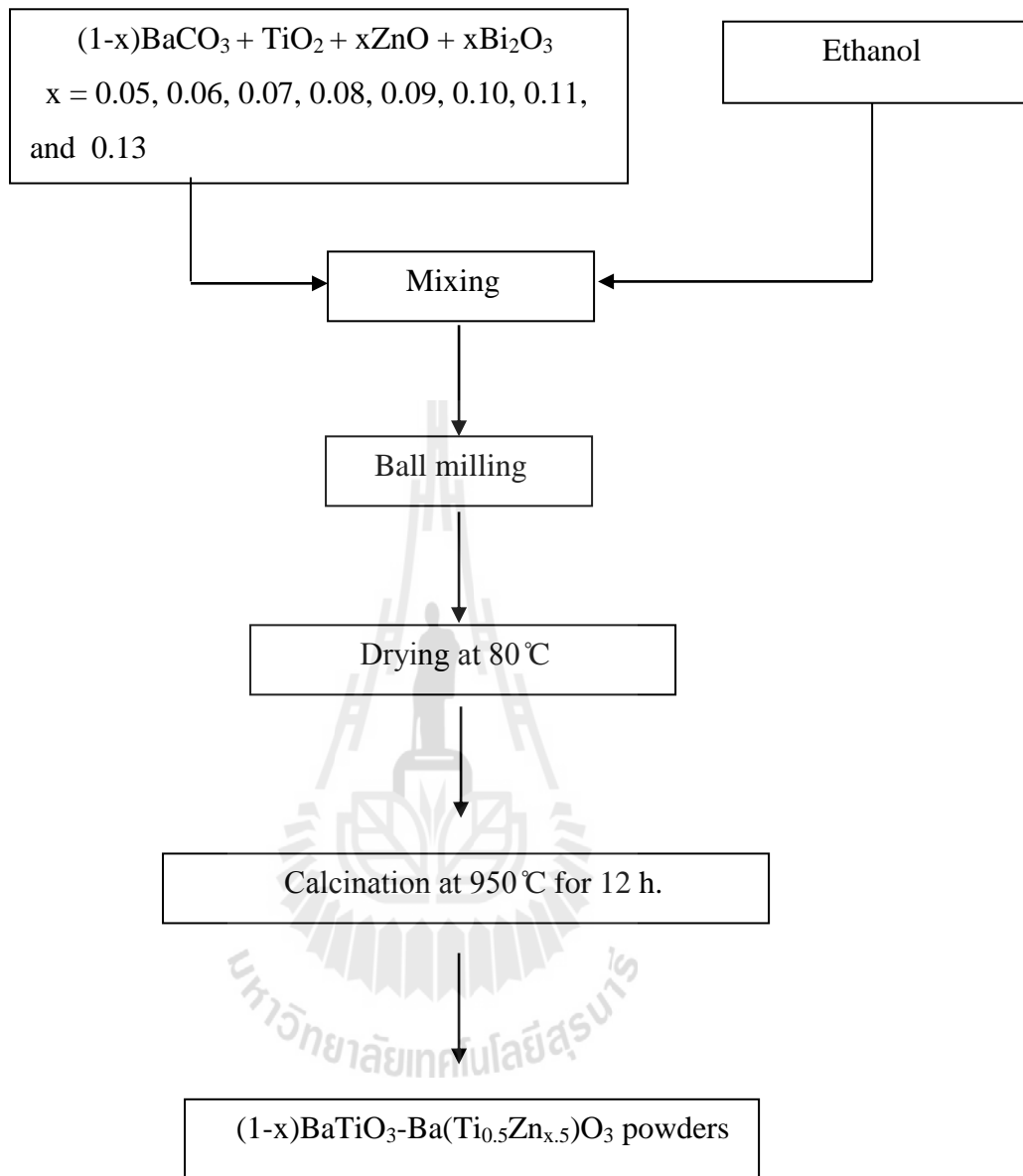


Figure 3.3 Flow chart of the synthesis of $(1-x)\text{BaTiO}_3\text{-xBi}(\text{Zn}_{0.5}\text{Ti}_{0.5})\text{O}_3$ powders.

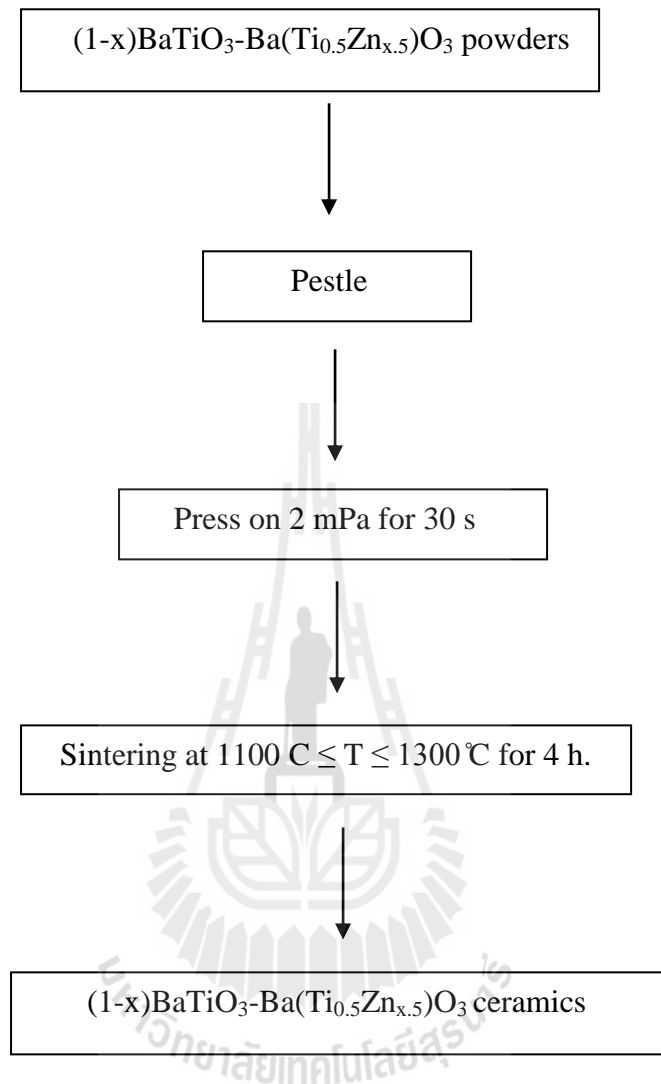


Figure 3.4 Flow chart of the synthesis of $(1-x)\text{BaTiO}_3\text{-xBi}(\text{Zn}_{0.5}\text{Ti}_{0.5})\text{O}_3$ ceramics.

3.2 X ray diffraction setup

The Bragg condition can be suitable for each planes of crystal. The half wavelength of the x-ray is smaller than spacing (if $\lambda/2 < d$, then $\sin\theta > 1$, which is impossible). This condition is a limit on how many orders of diffracted waves can be obtained from a given crystal using an x-ray beam of a given wavelength. The crystal

patterns, indicated in three dimensions and denoted ($h k l$) are required to describe the order of the diffracted waves or called “the Miller indices”, which are used in crystallography, denote the orientation of the reflecting sheets with respect to the unit cell and the path difference in units of wavelength between identical reflecting sheets.

The x-ray diffraction technique is normally carried out by an x-ray diffractometer. The essential components of x-ray diffractometer (Fultz and Howe, 2008) are:

- 1) A source of x-ray, usually a sealed x-ray tube
- 2) A goniometer, which provides precise mechanical motions of the tube specimen and detector
- 3) An x-ray detector
- 4) Electronics for counting detector pulses in synchronization with the positions of the goniometer

There are four practical approaches for observing diffractions and making diffraction measurements: Debye-Scherrer Method, Laue Method, Rotating Crystal Method and θ - 2θ diffractometer Method. All are designed to ensure that Bragg's law is satisfied. The schematic diagram of θ - 2θ x-ray diffractometer used in this work (BRUKER X-ray diffractometer model D5005 equipped with Cu K_{α} sealed tube, wave length 1.54 Å) is shown in Figures 3.5 and 3.6. The θ - 2θ Diffractometer is used for diffraction measurements of unfixed horizontal sample. For this purpose, sample will be rotated to θ and x-ray detector moved to 2θ . The diffraction angle followed on Bragg's equation (2.68). The one-side weight of the tube stand is compensated by a counter weight. Both tube stand and counter weigh are fixed to the outer ring.

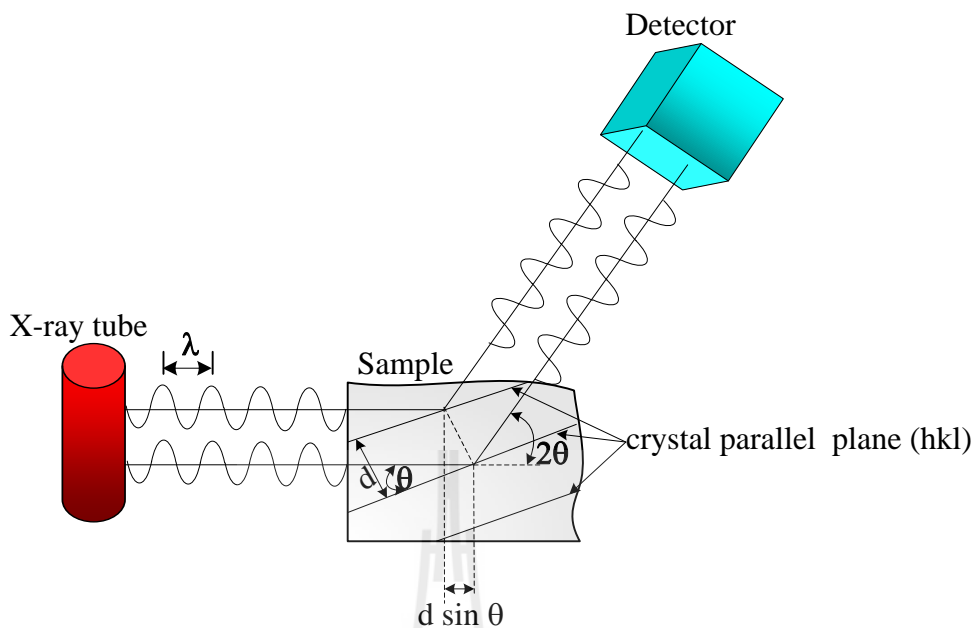


Figure 3.5 Schematic illustration of θ - 2θ x-ray diffraction experiment (Jutimoosik, 2010).

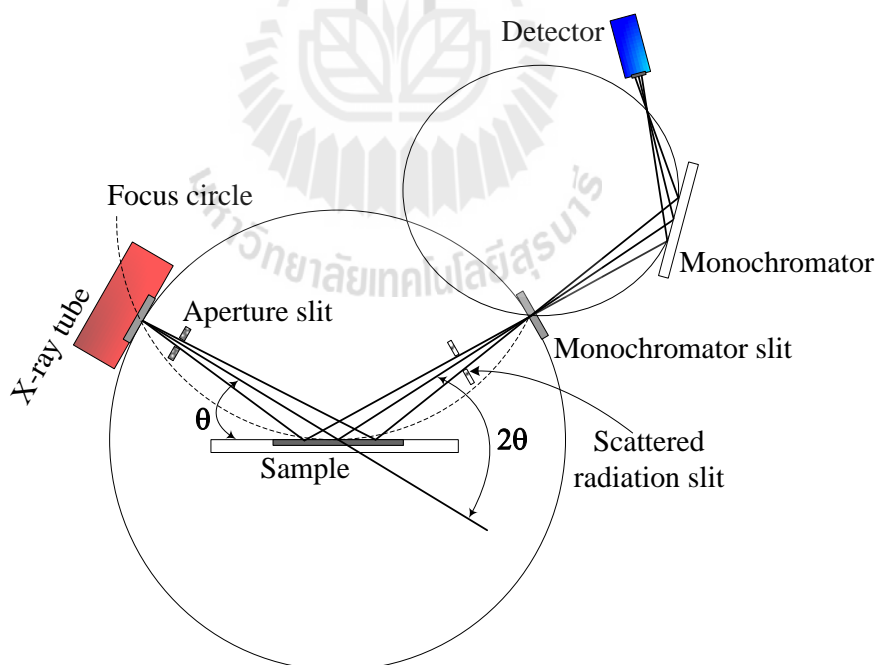


Figure 3.6 Schematic representation of X-ray diffractometer D5005 (Jutimoosik, 2010).

3.3 X-ray absorption spectroscopy setup

3.3.1 X-ray absorption spectrum calculation

In thesis, the principle theoretical calculations are performed based on FEFF 8.2 code. This code is developed to primarily calculate x-ray absorption for the FEFF (f_{eff}) project developed by the Department of Physics, University of Washington, Seattle. USA. Apart from XAS spectra calculation, FEFF code can also calculate x-ray natural circular dichroism (XNCD), spin-dependent calculations of x-ray magnetic dichroism (XMCD), nonresonant x-ray emission (XES) and electronic structure including local densities of states (LDOS). FEFF code is written in ANSI FORTRAN 77 with principle investigator John J. Rehr and co-principle investigator Alexei L. Ankudinov (Rehr and Albers, 2000).

FEFF is ab initio self-consistent real space multiple-scattering (RSMS) code for simultaneous calculations of x-ray absorption spectra and electronic structure. The input file “feff.inp” can be created directly from ATOMS code via “atoms.inp” as shown in Figure 3.7.

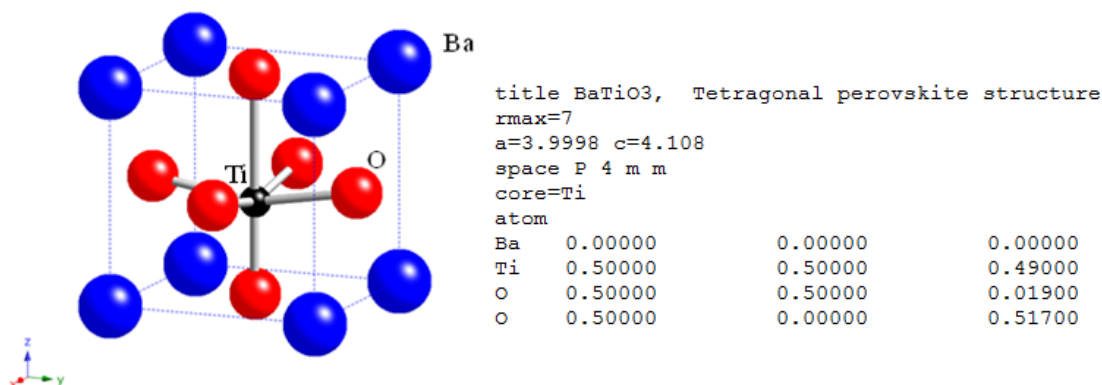


Figure 3.7 Detail of an atoms.inp input file to generate “feff.inp” for FEFF calculation.

The suitable commands, parameter and atomic positions for FEFF-XAS spectrum calculations can be edited within the input file named “feff.inp”, which is shown in Figure 3.8. This file controlled with some details, for instance the generator of input file and the number of atom which contains in the cluster. The followed details describe about various card use to assign the steps of calculation. The type of atomic potentials and defined atomic symbols are presented in the next part, and eventually with the locations of the created atoms in the system where the location of center atom is placed at (0,0,0) in (x,y,z) coordination.



```

TITLE   BaTiO3, Tetragonal perovskite structure

EDGE    K
S02     1.0

*       pot   xsph  fms   paths genfmt ff2chi
CONTROL 1     1     1     1     1     1
PRINT   1     0     0     0     0     0

*       r_scf [ l_scf n_scf ca ]
SCF     4.3   0     20    0.1

*       ixc   [ Vr  Vi ]
EXCHANGE 0     4    0.3

*EXAFS
*RPATH   8.50057

*       kmax  [ delta_k delta_e ]
XANES   7.0   0.05  0.3
*       r_fms   [ l_fms ]
FMS     6.5   0
*
RPATH   0.10000
*       emin  emax  resolution
*LDOS   -20   20   0.1

POTENTIALS
*       ipot  z [ label  l_scmf l_fms stoichiometry ]
        0  22  Ti   -1     -1     0
        1   8   O   -1     -1     3
        2  56  Ba   -1     -1     1
        3  22  Ti   -1     -1     1

ATOMS
0.00000  0.00000  0.00000  0  Ti  0.00000
0.00000  0.00000 -1.93195  1  O  1.93195
0.00000 -1.99990  0.11075  1  O  2.00296
1.99990  0.00000  0.11075  1  O  2.00296
-1.99990 0.00000  0.11075  1  O  2.00296
0.00000  1.99990  0.11075  1  O  2.00296
0.00000  0.00000  2.16985  1  O  2.16985
1.99990  1.99990 -2.00988  2  Ba  3.46970
-1.99990 -1.99990 -2.00988  2  Ba  3.46970
-1.99990  1.99990 -2.00988  2  Ba  3.46970
 1.99990 -1.99990 -2.00988  2  Ba  3.46970
-1.99990 -1.99990  2.09192  2  Ba  3.51786
-1.99990  1.99990  2.09192  2  Ba  3.51786
 1.99990  1.99990  2.09192  2  Ba  3.51786
 1.99990 -1.99990  2.09192  2  Ba  3.51786

```

Figure 3.8 Detail of a “feff.inp” input file of BaTiO₃ with Ti as center atom for FEFF calculation.

3.3.2 Ti K pre-edge XANES analysis

The integrated intensity of Ti K pre-edge, which is associated with both the quadrupole and the dipole $1s \rightarrow 3d$ transition of Ti, reflects the $3d-4p$ hybridization for Ti. This hybridization results from displacement of the Ti atom from centro symmetric position within the oxygen octahedron. Vedrinskii *et al.* have shown that a contribution to the area under peak X is given by

$$A = \left(\frac{\gamma_s}{3}\right) d_s^2 \quad (3.3)$$

In this equation, d_s is the mean-square displacement of Ti atom from center and a is the average displacement of the oxygen octahedral and A is a peak area. An experimental determination of the constant γ_s by Ravel resulted (Shanthakumar, 2008) in values of $11.2 \text{ eV}/\text{Å}^2$ for BaTiO_3 and $13.6 \text{ eV}/\text{Å}^2$ for EaTiO_3 , with an error bar of about $\pm 3 \text{ eV}/\text{Å}^2$, as shown in Figure. 3.9.

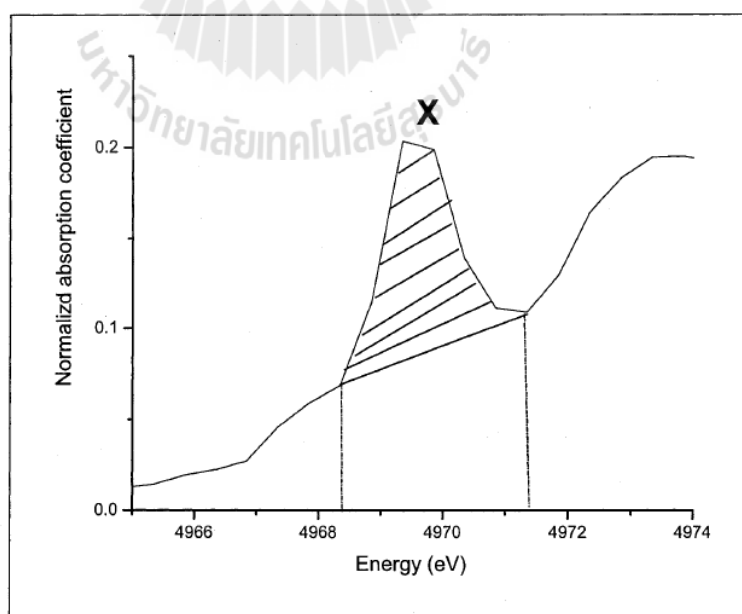
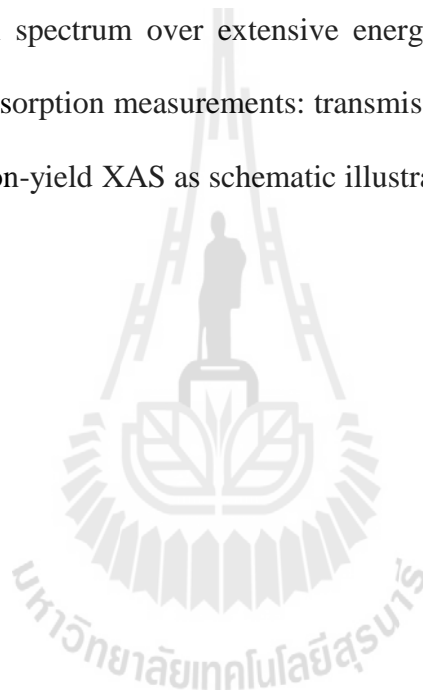


Figure 3.9 The Ti K pre-edge XANES of BaTiO_3 , showing the calculated area under the spectral peak denoted by X (Shanthakumar, 2008).

3.3.3 X-ray Absorption Spectroscopy Experimental setup (Jeon *et al.*, 2010)

The x-ray absorption spectroscopy experiment is commonly accomplished at a synchrotron radiation source, due to high intensity and energy alterable competency of generated x-ray photon, and the competency to obtain the continuous absorption spectrum over extensive energy range. In general, there are three types of x-ray absorption measurements: transmission-mode XAS, fluorescence-mode XAS and electron-yield XAS as schematic illustration shown in Figure 3.10.



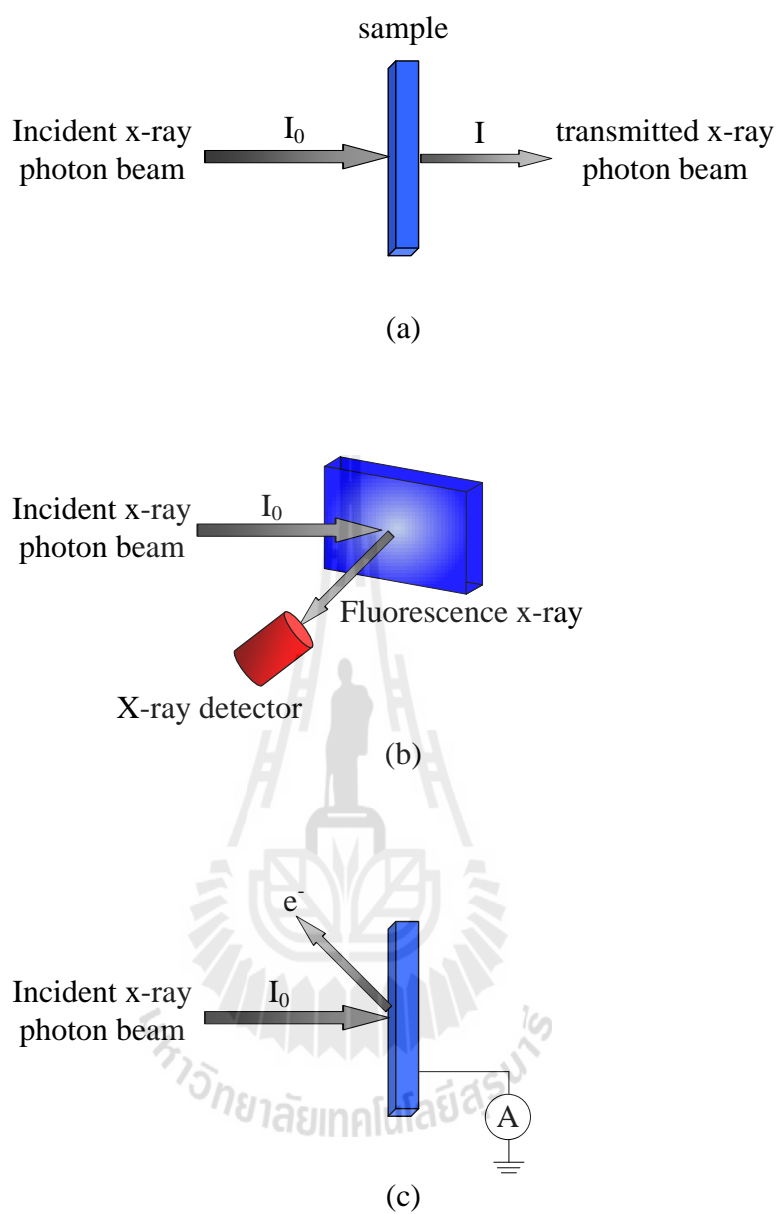


Figure 3.10 The three modes of XAS measurement (a) transmission mode, (b) fluorescence mode and (c) electron yield [adapted from (Kawai, 2000)].

In transmission mode XAS, after the energy of x-ray photons being changed by x-ray double crystals monochromator, the intensities of incident x-ray photon beam (I_0) and the transmitted x-ray photon beam (I) are measured by ionization chambers as shown in Figure 3.11. In this mode, we make sure the x-ray photon beam is well-aligned on the sample. The x-ray absorption can be extracted based on equation (2.69). The experimental set up of XAS experimental station at XAS beam line, Siam Photon Laboratory, SLRI is shown in Figure 3.12.

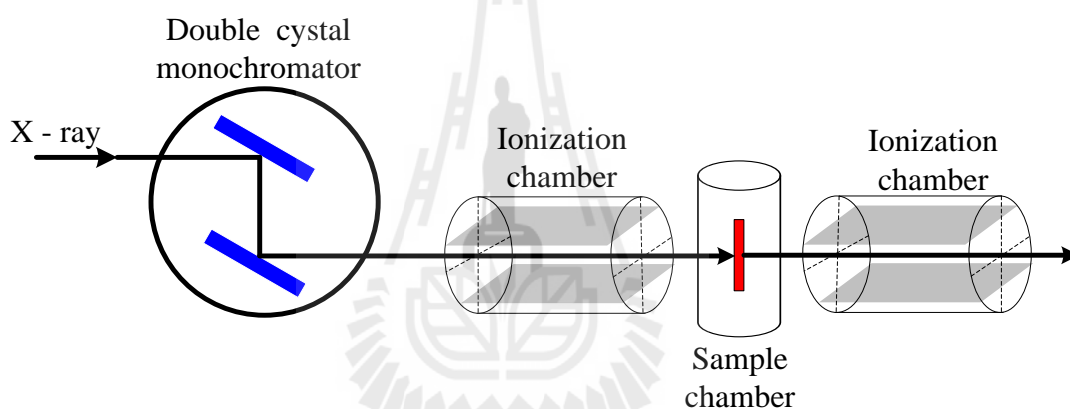


Figure 3.11 Schematic illustration of the experimental setup of transmission-mode X-ray absorption spectroscopy (Jutimoosik, 2010).

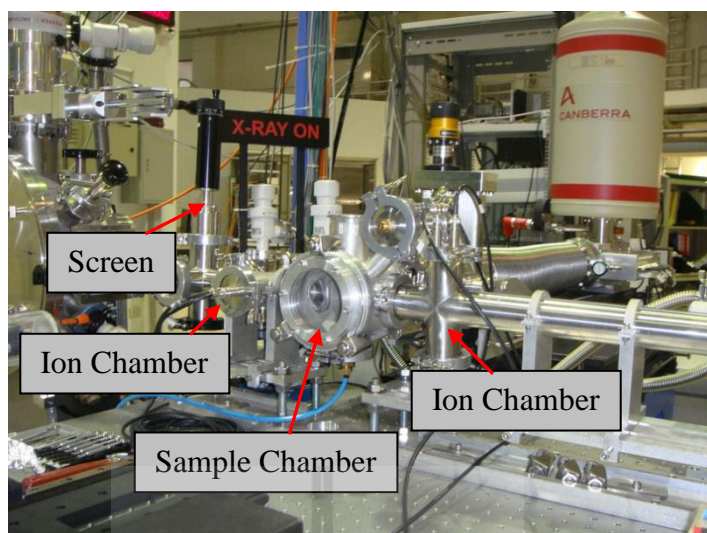
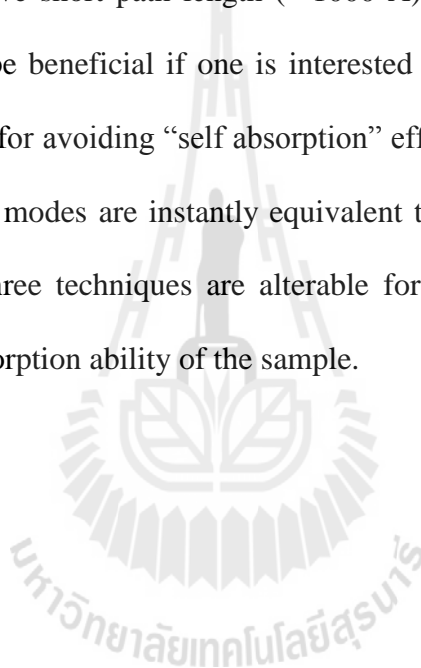


Figure 3.12 XAS experimental set up at the Siam Photon Laboratory, Synchrotron Light Research Institute (Jutimoosik, 2010).

Other than the transmission mode, the fluorescence mode and the electron yield are also competent for the measurement of the absorption coefficient. In the x-ray absorption phenomena, where x-ray photon knock out an electron from the inner shell an electron from higher energy level will cascade down to fill in the hole and discharging radiation of energy, the discharged energy x-ray photon will be released as demonstrated in Figure 3.10(a) and the fluorescence x-ray can be detected. In addition, de-excitation can cause the Auger effect, where the electron reduce to lower energy state, a second electron can be excited to the continuum state and perhaps go out from the sample as shown in Figure 3.10(b), and then it can be detected by using the electron-yield XAS detectors.

For fluorescence mode, we measure the intensities of incident x-ray photon beam and the fluorescence x-ray that are emitted following the x-ray absorption.

Usually the fluorescence detector is placed at 90° to the incident x-ray photon beam in the horizontal plane, with the sample at an angle (usually 45°) with respect to the beam. Fluctuations in the number of elastically scattered x-ray are significant source of noise in fluorescence XAS, so the position of the detector is selected to minimize the elastically scattered radiation by exploiting the polarization of the x-ray beam. In case of electron yield, we measure the electrons that are emitted from the surface of the sample. The relative short path length ($\approx 1000 \text{ \AA}$) makes the technique surface-sensitive, which can be beneficial if one is interested in near-surface phenomena. It also can be beneficial for avoiding “self absorption” effect that occurs in fluorescence mode. However, both modes are instantly equivalent to the absorption ability of the sample. Hence, the three techniques are alterable for the study of the structure of material using the absorption ability of the sample.



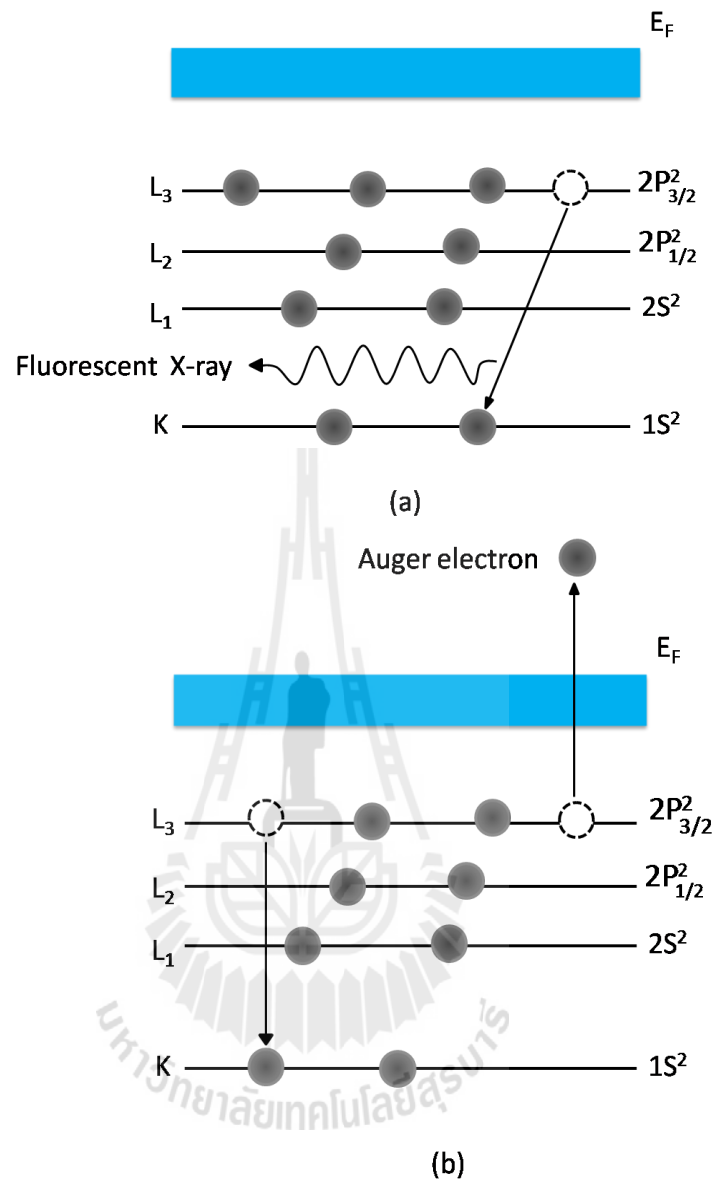


Figure 3.13 The excited state (a) x-ray fluorescence and (b) the Auger effect (Adapt from Jutimoosik, 2010).

3.4 Dielectric measurement setup

The HP4284 LCR meter at Department of Electrical and Computer Engineering, College of Engineering, University of Texas at San Antonio, Texas, USA was employed to measure the dielectric constant and loss tangent on the various frequencies in the temperature range of 30-425 K. The system consist of 5 complement equipment as

1. Vacuum pump.
2. Chiller pump for cooling in the system from liquid nitrogen.
3. Frequency Generator for applying frequencies into sample.
4. Temperature control for controlling cooling and heating rate in the system.
5. The HP4284 LCR meter for measuring the dielectric constant and loss tangent



Figure 3.14 Vacuum pump and sample holder.

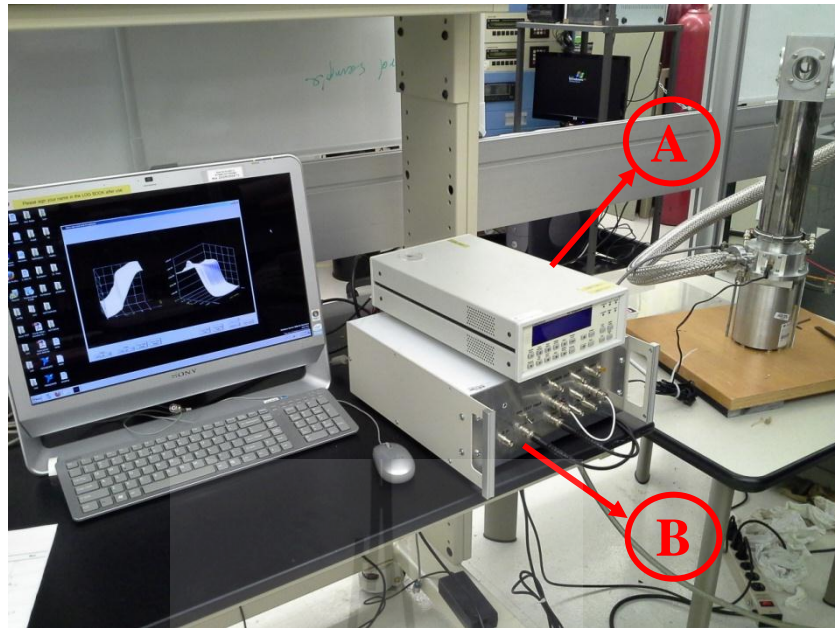


Figure 3.15 Temperature control (A) and Frequency generator (B) (Arrows indicate the number of equipment).

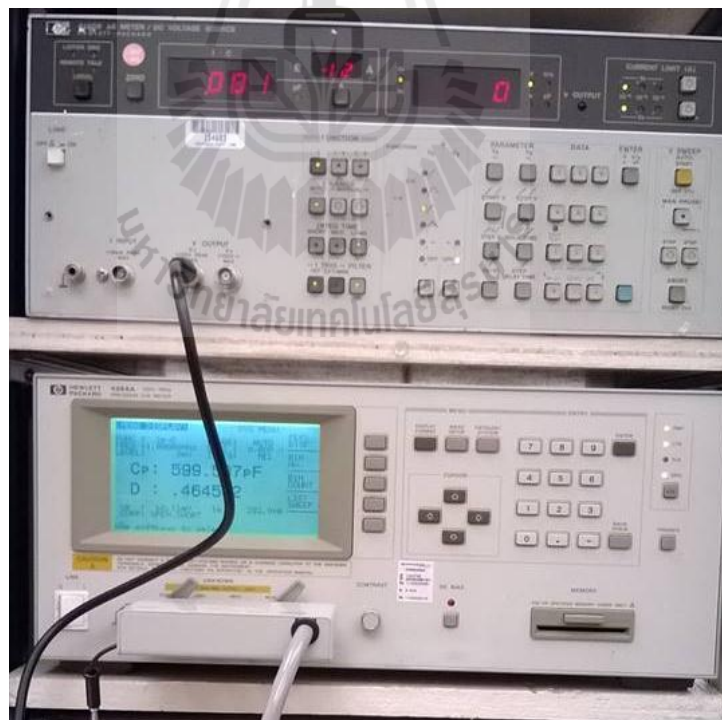


Figure 3.16 The HP4284 LCR meter for dielectric measurement.

3.5 P-E Hysteresis setup

The P-E Hysteresis was provided by the oscilloscope and power supply with frequency generator as shown in Figure. 3.17(a) and sample holder as shown in Figure. 3.17(b) at School of Physics, Institute of Science, Suranaree University of Technology.

1. Power supply with frequency generator was used to the apply electric field and frequency into the sample.
2. The oscilloscope was used for the voltage measurement and the increasing polarizations of sample.



(a)

(b)

Figure 3.17 The oscilloscope and power supply with frequency generator (b) sample holder for P-E hysteresis measurement.

3.6 References

- Cerneaw, M. and Manea, A. (2007). $\text{Ba}(\text{Ti}_{1-x}\text{Sn}_x)\text{O}_3$ ($x=0.13$) Dielectric Ceramics Prepared by Coprecipitation. **J. Am. Ceram. Soc.** 90: 1728.
- Cross, L. E. (2011). Relaxor ferroelectrics. 76:1: 241.
- Hench, L. L. and West, J. K. (1990). **Principles of electronic ceramics**. Wiley.
- Huang, C.-C. and Cann, D. P. (2008). Phase transitions and dielectric properties in $\text{Bi}(\text{Zn}_{1/2}\text{Ti}_{1/2})\text{O}_3\text{-BaTiO}_3$ perovskite solid solutions. **J. Appl. Phys.** 104: 024117.
- Huang, C. C. (2008). **Structure and piezoelectric properties of lead-free bismuth-based perovskite solid solutions**. Ph.D.dissertation, Oregon State University.
- Jeon, J.-S., Kim, B.-H., Park, C.-I., Seo, S.-Y., Kwak, C., Kim, S.-H. and Han, S.-W. (2010). In-situ X-ray Absorption Fine Structure Study of TiO_2 Nanoparticles under Ultraviolet Light. **Jpn. J. Appl. Phys.** 49.
- Jutimoosik, J. (2010). **Local Structure of Magnesium Zinc Oxide Nanocrystals**. M.S. thesis, Suranaree University of Technology, Nakorn Ratchasima.
- Maiti, T., Guo, R. and Bhalla, A. S. (2008). Structure-Property Phase Diagram of $\text{BaZr}_x\text{Ti}_{1-x}\text{O}_3$ System. **J. Am. Ceram. Soc.** 91: 1769.
- Rehr, J. J. and Albers, R. C. (2000). Theoretical approaches to x-ray absorption fine structure. **Rev. Mod. Phys.** 72: 3.
- Shanthakumar, P., (2008). **X-ray study of two complex oxides, each having octahedral oxygen co-ordination of transition metals**. Ph.D. thesis, University of Connecticut, Connecticut.
- Yu, Z., Ang, C., Guo, R. and Bhalla, A. S. (2007). Dielectric properties of $\text{Ba}(\text{Ti}_{1-x}\text{Zr}_x)\text{O}_3$ solid solutions. **J. Appl. Phys.** 61: 326.

CHAPTER IV

STUDY OF PHASE INFORMATION AND DIELECTRIC PROPERTIES IN BARIUM ZIRCONATE TITANATE

4.1 Introduction

The prototypic ferroelectric barium titanate (BaTiO_3 :BT), discovered in 1941 (Thurnauer and Deaderick, 1941), exhibits ferroelectric behavior with high dielectric constant. Moreover, BT is lead-free perovskite material. Therefore, BT is environmental friendly and non-toxic. However, dielectric properties of BT is lower than $\text{Pb}(\text{Zr},\text{Ti})\text{O}_3$ (PZT). In the recent years, it has been found that the substitution of Zr in BT or barium zirconium titanate ($\text{Ba}(\text{Zr},\text{Ti})\text{O}_3$ or BZT) has become one of the attractive candidates for various electronic devices.

The ferroelectric behavior is classified with spontaneous polarization dependent dielectric properties. Particularly, it is of great interest because barium zirconate (BaZrO_3 : BZ) exhibits non-polar or paraelectric behavior, which does not have spontaneous polarization. It has been found that increasing Zr substitution into the Ti site in BaTiO_3 lattice can change the material to exhibit relaxor ferroelectric behavior (Maiti *et al.*, 2008; Mouraa *et al.*, 2008; Maiti *et al.*, 2011; Levin *et al.*, 2011). If Zr is substituted into the Ti site in BaTiO_3 by more than 70 mol%, BZT exhibits polar clusters like behavior (Maiti *et al.*, 2008; Mouraa *et al.*, 2008; Maiti *et al.*, 2011). Moreover, the relaxor ferroelectric behavior is characterized with strong

frequency-dependent dielectric properties. It has been reported that, with the incorporation of Zr in BT, the rhombohedral to orthorhombic (T_1) and orthorhombic to tetragonal (T_2) phase transition temperatures increase, as compared to pure BT (Maiti *et al.*, 2011; Maiti *et al.*, 2008; Cross, 1987).

Recently, it has been reported that the $\text{Ba}(\text{Zr}_x\text{Ti}_{1-x})\text{O}_3$ compositions with $x = 0$ and 0.005 contained the tetragonal BT phase. With $x = 0.02$, the ceramic contained a mixture of the tetragonal and orthorhombic structures, whereas the $x = 0.04$ sample exhibited primarily the orthorhombic phase. For $x = 0.12$, the crystal structure then became cubic (Levin *et al.*, 2011). While it is clearly intuitive to expect the role of locally arranged lattice structure in determining the phase transition behavior and relevant properties of BZT material, the prior investigations usually employed only a global structural determination technique, such as X-ray Diffraction (XRD). In the present study, we employed the local structure sensitive Synchrotron X-ray Absorption Spectroscopy (XAS) technique to obtain the local structure information around the Ti atom in the ferroelectric region of $\text{Ba}(\text{Zr}_x\text{Ti}_{1-x})\text{O}_3$ with hope to better understand how the local structure is related to the properties of ferroelectric transition.

4.2 Experimental

$\text{BaZr}_x\text{Ti}_{1-x}\text{O}_3$ powders were synthesized by a conventional solid state reaction method. The $\text{BaZr}_x\text{Ti}_{1-x}\text{O}_3$ were weighed according to the composition with $x = 0.0, 0.08, 0.2, 0.3, 0.5, 0.6, 0.7, 0.75, 0.95$ and 1 from the starting BaCO_3 , TiO_2 and ZrO_2 materials. The ball milled in ethanol solution for 24 h and then drying, the mixed

powders were calcined at temperature of 1250 °C for 2 h with 5°C/min heating/cooling rates (N.Binhayeeniyi *et al.*, 2010; Yu *et al.*, 2002).

The global structure of $\text{Ba}(\text{Zr}_x\text{Ti}_{1-x})\text{O}_3$ was investigated by X-ray diffraction (XRD) patterns which were scanned in 2θ range of 20° - 60° with 0.02° step and $\text{CuK}\alpha$ radiation was used. In addition, the local structure was investigated by XAS measurements which were conducted at room temperature at BL-8 of the Siam Photon Laboratory, Synchrotron Light Research Institute (SLRI), Thailand (electron energy of 1.2 GeV, beam current 120-80 mA). The synchrotron X-ray beam with energy step of 0.20 eV provides to excite the electrons in the Ti *K*-edge were measured by XANES spectra for all compositions. The data were processed using the ATHENA program. The simulation was carried out using the FEFF8.2 program and qualitatively compared with XANES patterns obtained from the experiment. In addition, EXAFS spectra were obtained for some compositions and processed using the ARTEMIS program (Chandarak *et al.*, 2012).

The silver electrodes were sputtered on the BZT ceramics for dielectric measurement. The HP4284 LCR meter was used to measure the dielectric constant and loss tangent from 100 Hz to 500 kHz in the temperature range of 30-425 K with a cooling rate of 2 K/min.

4.3 X-ray Diffraction

The XRD patterns of $\text{Ba}(\text{Zr}_x\text{Ti}_{1-x})\text{O}_3$ powders are shown in Figure. 4.1. It is seen that the global crystal structure, as determined by XRD, changes from tetragonal to cubic perovskite phases with increasing Zr concentration in BaTiO_3 lattice. The sample with $x = 0$ (pure BT) shows the tetragonal perovskite phase, while the samples

at $0.25 \leq x \leq 0.7$ exhibit the broad XRD peaks. The compositions with $x \geq 0.75$ also exhibit the broad peaks with the cubic perovskite structure. The standard tetragonal perovskite BaTiO_3 phase and cubic perovskite BaZrO_3 are also shown (matched with JCPDS file No. 81-2201 and 74-1299, respectively). The lattice constant of the cubic phase increases continuously with increasing Zr concentration. The XRD results show a noticeable change in the global structure across the compositional range studied. Figure 4.2 displays the change in the lattice parameter with Zr content and corresponding electrical behavior in each region; i.e., normal ferroelectric ($0 \leq x \leq 0.27$), relaxor ferroelectric ($0.27 \leq x \leq 0.75$), and polar clusters ($x \geq 0.75$) (Maiti *et al.*, 2008). In addition, the solid arrow line indicates a region of mixed tetragonal-orthorhombic perovskite phase ($0 < x < 0.12$), and a region of cubic perovskite symmetry ($x \geq 0.12$). However, the exact crystal symmetry is not clearly seen from the XRD study and the cubic structure region could also be identified as “*pseudo-cubic*”.

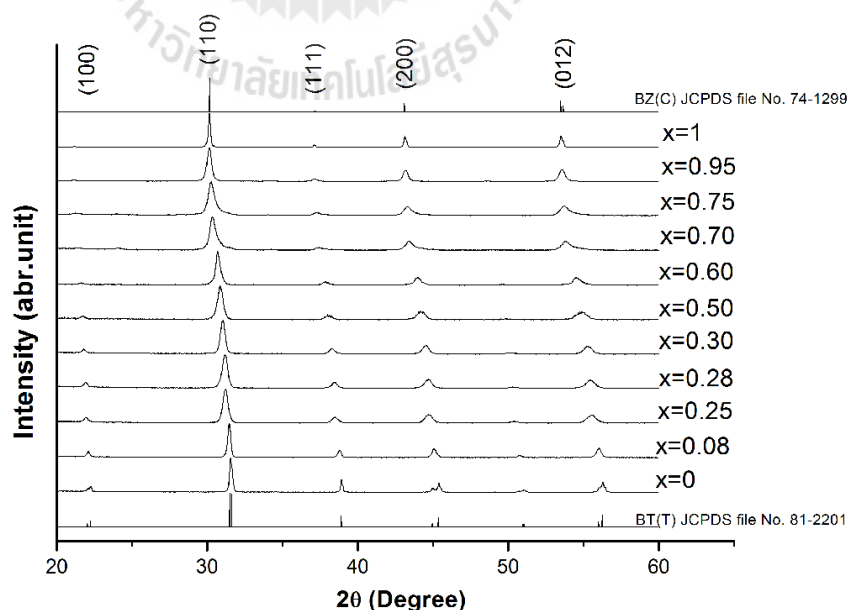


Figure 4.1 X-ray diffraction patterns of $\text{Ba}(\text{Zr}_x\text{Ti}_{1-x})\text{O}_3$ powders.

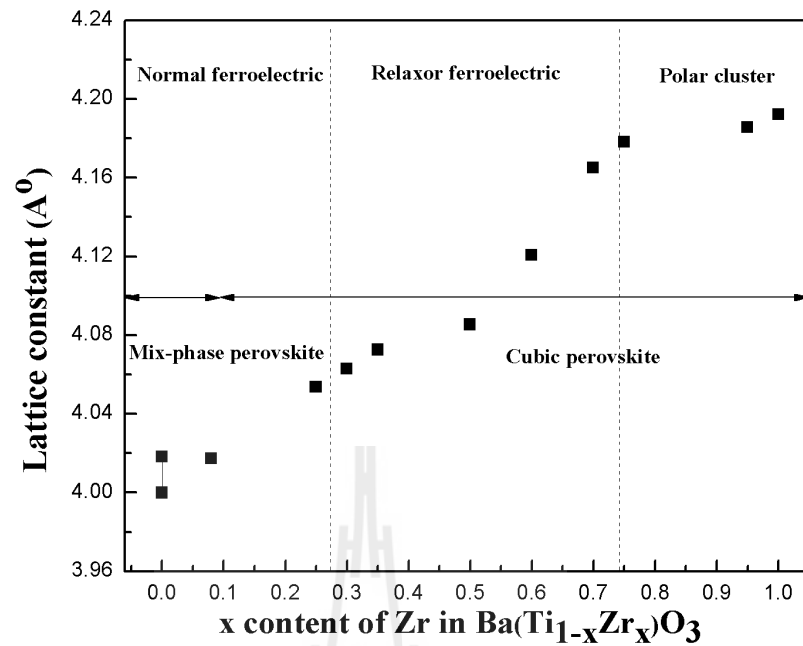


Figure 4.2 Phase diagram of $\text{Ba}(\text{Ti}_{1-x}\text{Zr}_x)\text{O}_3$ compound as a function of Zr content.

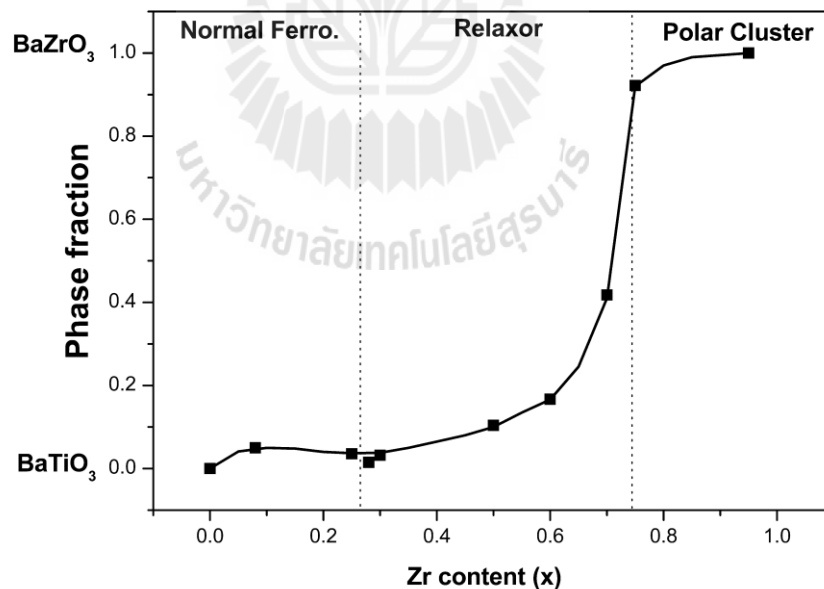


Figure 4.3 The phase fraction of $\text{Ba}(\text{Ti}_{1-x}\text{Zr}_x)\text{O}_3$ from XRD patterns.

In addition, the phase fraction between BaTiO_3 and BaZrO_3 is obtained from linear combination of the integrated intensity of mean peak (110) of XRD patterns.

The results show that the phase fraction suddenly increases around $x=0.7-0.75$ which is rather corresponding with the phase transition from relaxor to polar cluster. However, this result does not provide a complete picture for understanding the phase transition.

4.4 XANES results

4.4.1 Identification of Zr site in BaTiO₃.

Generally, XANES measures the excitation of electrons L_3 -levels to unoccupied bound states and is thus used to obtain information about the local arrangement of atoms around the absorbing atoms and the density of states of unoccupied states.

XANES spectra of Zr L_3 -edge in Zr on Ti site in BaTiO₃ (Ba(Ti,Zr)O₃), Zr on Ba site in BaTiO₃ ((Ba,Zr)TiO₃) and SnO₂ were obtained using the FEFF8.2 codes follow models in Figure 4.3. The FEFF codes is using a full multiple scattering approach based on ab initio overlapping muffin-tin potentials. The muffin-tin potentials used in FEFF codes are self-consistent calculations with Hedin-Lundqvist exchange-correlation function (Hedin and Lundqvist, 1970; Rehr and Albers, 2000). The results show that the measured XANES is clearly consistent with the calculation of Zr on Ti site and inconsistent with Zr at other lattice locations as shown in Figure. 4.4.

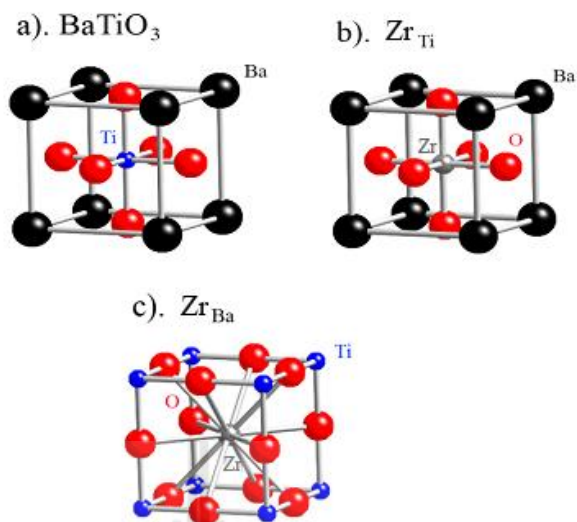


Figure 4.4 Model Perovskite crystals structure of BaTiO_3 . b–c Schematic illustrations of Zr on Ti site, Zr on Ba site, respectively. Regions shown in c are shifted from that in a).

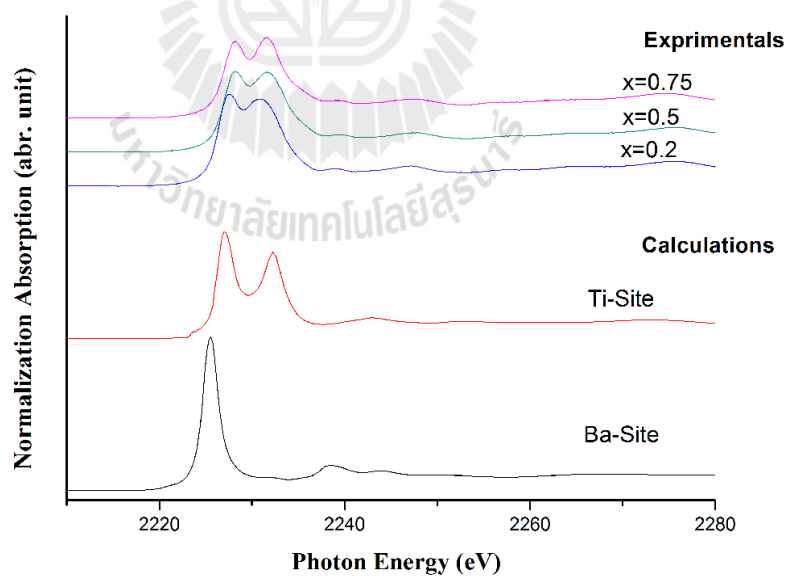


Figure 4.5 Zr L_3 -edge XANES spectra of $\text{BaTi}_{1-x}\text{Zr}_x\text{O}_3$ And calculation of Zr site for Zr on Ti site (Zr_{Ti} -red line), Zr on Ba site (Zr_{Ba} -black line)

4.4.2 XANES studies of Ti K pre-edge

Generally, XANES measures the excitation of core electrons to unoccupied bound states and is thus used to obtain information about the local arrangement of atoms around the absorbing atoms and the density of states of unoccupied states⁵. According to the molecular orbital theory and valence band theory, 3d levels of the octahedral complex split into t_{2g} and e_g level. The integrated intensity of pre-edge is associated with probability of electrons 1s to t_{2g} and e_g level. However, transition of electrons from 1s to 3d levels are forbidden but, if Ti atoms is off center, it will be effect to 3d levels spiting lager until e_g levels overlap 4s levels and electrons 1s can be occupied on e_g levels more. Therefore, the integrated intensity of Ti K pre-edge, which is associated with both the quadrupole and the dipole 1s \rightarrow 3d transition of Ti, reflects the 3d-4p hybridization for Ti and I_A is directly proportional to the displacements of Ti off-center of oxygen octahedra and is indirectly proportional to the lattice constants (Vedrinskii *et al.*, 1998; Levin *et al.*, 2011). The integrated intensity of peak B is associated with both the quadrupole and the dipole 1s \rightarrow 3d transition in molecular orbital related the local Zr/Ti ratio around the absorbing Ti.

The normalized Ti K pre-edge XANES spectra of $\text{Ba}(\text{Zr}_x\text{Ti}_{1-x})\text{O}_3$ powders are shown in Figure. 4.6. According to Eq. (3.3), we adopted this value as a reference for calculating local Ti off-centering from the pre-edge peak intensities in the solid-solution samples (Figure. 4.7a). Clearly, the local value of δ_{Ti} in BZT when x content is increasing, I_A will decrease continuously until $x=0.5$, which is increasing in the relaxor ferroelectrics region. After then, drop at $x=0.75$ in polar cluster region and is also larger than that expected from the relaxor ferroelectrics change to polar cluster,

local Ti off-centering were decreased. Figure 4.7b show the average local Zr/Ti ratio around the absorbing Ti atoms.

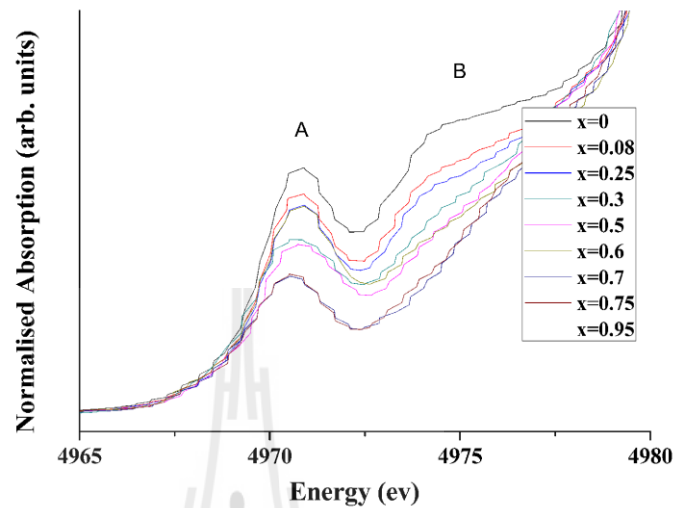


Figure 4.6 Normalized X-ray absorption Ti K pre-edge spectra of $\text{Ba}(\text{Zr}_x\text{Ti}_{1-x})\text{O}_3$ powders.

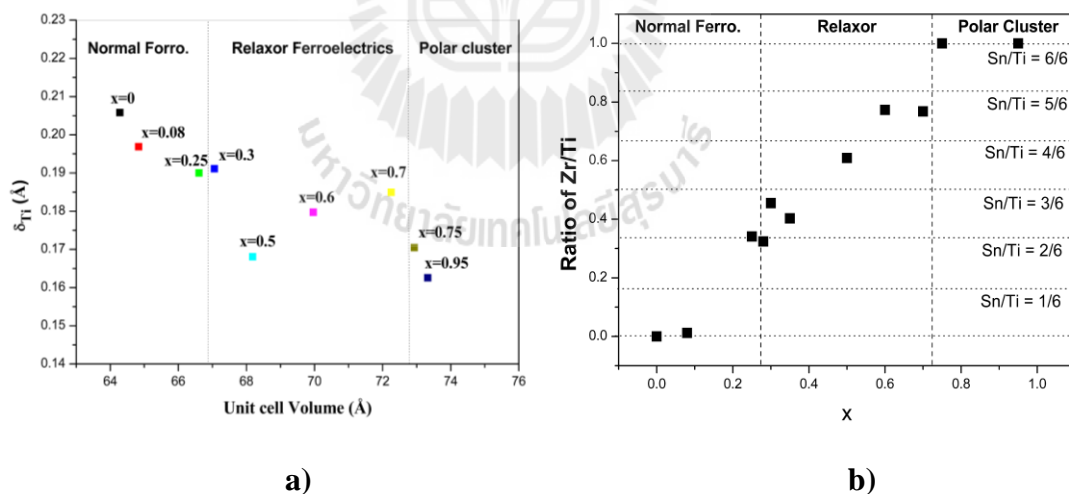


Figure 4.7 a) Present δ_{Ti} determined from the intensity of the pre-edge peak as a function of the unit-cell. The value of δ_{Ti} for $\text{Ba}(\text{Zr}_x\text{Ti}_{1-x})\text{O}_3$ was determined using the spectrum reported in Ref. (Levin *et al.*, 2013). b) The local Zr/Ti ratio around the absorbing Ti.

4.4.3 XANES studies of phase transition.

The normalized Ti *K*-edge XANES spectra of Ba(Zr_xTi_{1-x})O₃ powders are shown in Figure. 4.8. While XANES spectra only show little difference in features for compositions with $0 \leq x \leq 0.7$, at $x \geq 0.75$ the spectra exhibit a clear change in features with the shift in the peak C to the left-hand side; an indication of the change in local structure around Ti absorbing atom. Moreover, according to Maiti et al. [1] it was found that the electrical behavior of Ba(Ti,Zr)O₃ at $x > 0.75$ change from ferroelectric to polar cluster. This means that Ti atoms should locally move toward central of oxygen octahedra. However, this shift in the location of Ti cannot be observed by XRD. The XANES spectrum can be simulated using the unoccupied electronic states of the system, as described below. The x-ray absorbance $\mu(E)$ is given by Fermi's golden rule. Simulated XANES spectra of Ti *K*-edge in Zr-deficient Ba(Ti,Zr)O₃ and Zr-enriched Ba(Ti,Zr)O₃ were obtained using the FEFF8.2 code. The FEFF code employs a full multiple scattering approach based on *ab initio* overlapping muffin-tin potentials. The muffin-tin potentials used in FEFF codes are self-consistent calculations with Hedin-Lundqvist exchange-correlation function (Hedin and Lundqvist, 1970; Rehr and Albers, 2000). It should be noted here first that, to simulate the XANES spectra of Ti, the structural model with Ti-off center in a rather perfect rhombohedral perovskite structure ($\alpha=\beta=\gamma=89.96$) was used for the pseudo-cubic symmetry, while a nearly perfect cubic structural model ($\alpha=\beta=\gamma=89.99$) with Ti moving towards the center was used in the cubic symmetry case, image models shown in Figure. 4.9. The perfect rhombohedral ($\alpha=\beta=\gamma=89.5$) and tetragonal ($\alpha=\beta=\gamma=90$) perovskite structures were also calculated for comparison. The self-consistent calculation was performed in sphere radius of 4.2, 4.3, 4.4 and 4.5 Å, respectively, for

rhombohedral and cubic structure around the absorber Ti *K*-edge in the system and the full multiple scattering calculations include all possible paths within a larger cluster radius of 6.0 Å.

The simulation of the XANES spectra of the BZT phase was subsequently carried out to investigate the feature around Ti absorbing atoms in BZT solid solution with the simulated and experimental results compared in Figure 4.10. It is shown that the simulated spectra of the perfect rhombohedral and tetragonal perovskite structures are not in good agreement with the measurements. However, the simulated spectral features from the pseudo-cubic (or the rather perfect rhombohedral) structure $\text{Ba}(\text{Ti,Zr})\text{O}_3$ and a nearly perfect-cubic $\text{Ba}(\text{Ti,Zr})\text{O}_3$ are in good agreement with the experimental XANES spectra. This agreement between the experimental and simulated spectra indicates that for $\text{Ba}(\text{Ti,Zr})\text{O}_3$ compositions with lower Zr contents the local structure around Ti atom is in the pseudo-cubic symmetry (or the rather perfect rhombohedral model), even though the XRD results exhibit the (*global*) cubic perovskite structure. This new result is also consistent with the electrical properties which for $x \leq 0.7$ $\text{Ba}(\text{Ti}_{1-x}\text{Zr}_x)\text{O}_3$ ceramics exhibit ferroelectric characteristics with spontaneous polarization from *local* ionic distortion of Ti atoms. On the other hand, when $x > 0.7$, $\text{Ba}(\text{Ti}_{1-x}\text{Zr}_x)\text{O}_3$ ceramics show a polar cluster behavior with very small *local* spontaneous polarization; hence, the structure is close to perfect cubic perovskite, as observed in both XAS and XRD measurements.

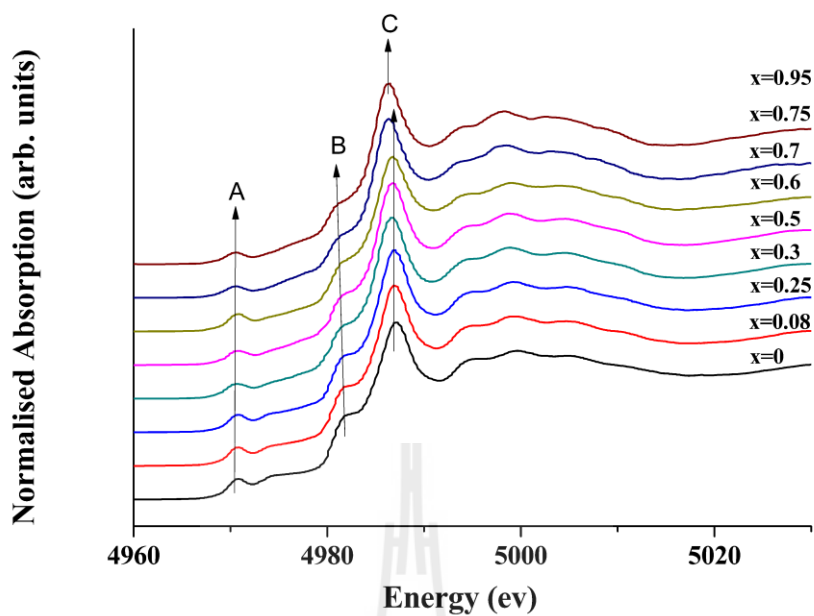


Figure 4.8 Normalized X-ray absorption Ti K-edge spectra of $\text{Ba}(\text{Zr}_x\text{Ti}_{1-x})\text{O}_3$ powders.

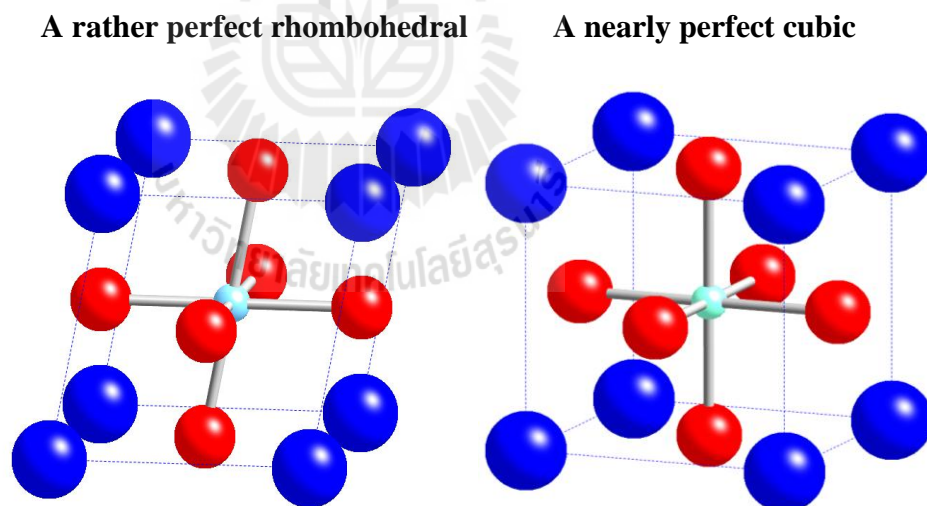


Figure 4.9 The perovskite model of a rather perfect rhombohedral with a nearly perfect cubic.

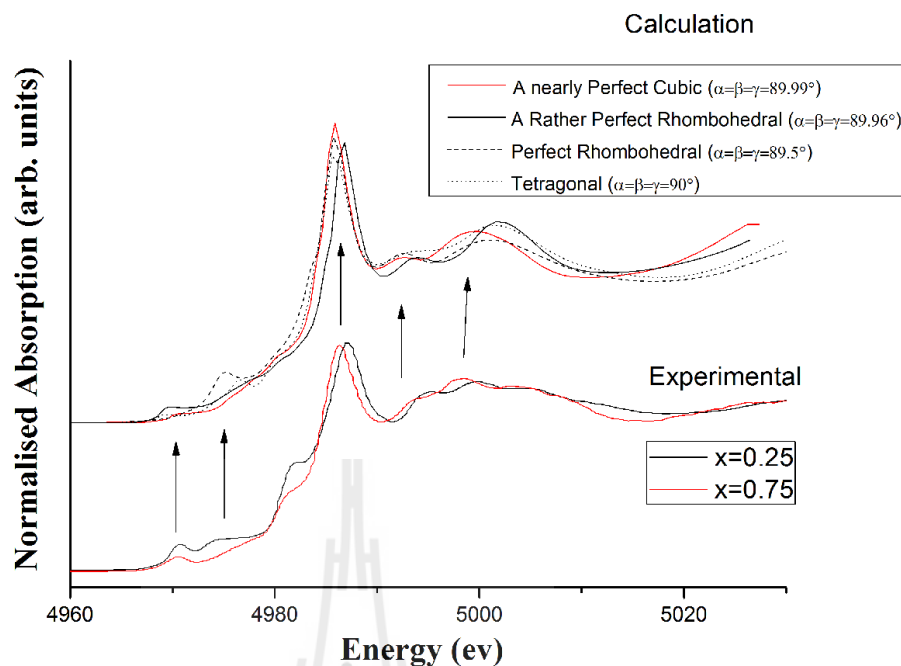


Figure 4.10 Comparison of normalized X-ray absorption Ti K-edge spectra of $\text{Ba}(\text{Zr}_x\text{Ti}_{1-x})\text{O}_3$ ($x=0.25$ and 0.75) with simulated features of Zr L_3 -edge XANES spectra of $\text{Ba}(\text{Zr},\text{Ti})\text{O}_3$ -rather perfect rhombohedral (red-line), a nearly perfect cubic (black line), rhombohedral (dash-line), tetragonal perovskite (dot-line).

The normalized Zr L_3 edge XANES spectra of $\text{Ba}(\text{Zr}_x\text{Ti}_{1-x})\text{O}_3$ powders are shown in Figure. 4.11. The intensity of peak A (I_A) and B (I_B), which are associated with both the quadruple and the dipole $2p_{3/2} \rightarrow 3d$ -orbitals transition of Zr, follow selection rules of electron transition is allowed. Therefore, the intensity of peak A relates to the electrons $2p_{3/2}$ to $3d$ -originated unoccupied t_{2g} -type MO of the absorbing ZrO_6 polyhedron. The intensity of peaks B which appear above the peaks A by about 3 eV are shown to be caused by Zr $2p_{3/2}$ electron transitions to the unoccupied $3d$ -originated e_g -type MO of ZrO_6 polyhedra neighboring the absorbing Zr atom which are weakly affected by the core hole potential (Groot *et al.*, 1994). The peak B area

does not depend strongly on small displacements of the atoms from their sites in a cubic crystal lattice but it changes significantly when 3d-unoccupied atoms appear in the vicinity of the absorbing Zr atom (for instance, Ti atoms in BZT solid solutions). However, the results of Zr XANES spectra is not changed the local structure of Zr atoms in $\text{Ba}(\text{Ti,Zr})\text{O}_3$. Therefore, The Zr atoms have no effect to the phase transition from relaxor to polar cluster behavior of $\text{Ba}(\text{Ti,Zr})\text{O}_3$ materials.

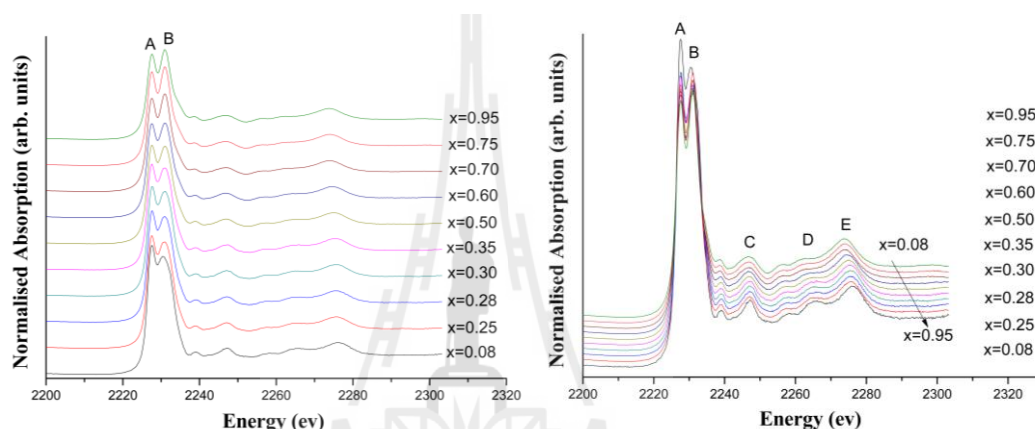


Figure 4.11 The normalized Zr L_3 edge XANES spectra of $\text{Ba}(\text{Zr}_x\text{Ti}_{1-x})\text{O}_3$ powders.

In addition, we assume the mixture phase caused by the phase fraction between BaTiO_3 and BaZrO_3 . Therefore, the phase fraction is obtained from a linear combination fit of BaTiO_3 and $\text{BaTi}_{0.05}\text{Zr}_{0.95}\text{O}_3$ materials, (assumed $\text{BaTi}_{0.05}\text{Zr}_{0.95}\text{O}_3$ is pure BaZrO_3). However, this assumption is not entirely correct, but the tend of change in phase fraction may provide a tool to understand better. The results show that the phase fraction of Zr L_3 -edge linear combination increases faster than the phase fraction of Ti K-edge, meaning Zr atoms attempt to keep nature bonding with oxygen more than Ti atoms (Figure. 4.12). However, the phase fraction indicated the phase transition at intercept of phase fraction of Zr and Ti atoms around $x=0.7-0.75$,

corresponding with local Ti off-centering from the pre-edge peak intensities and Ti K-edge XANES simulation spectra.

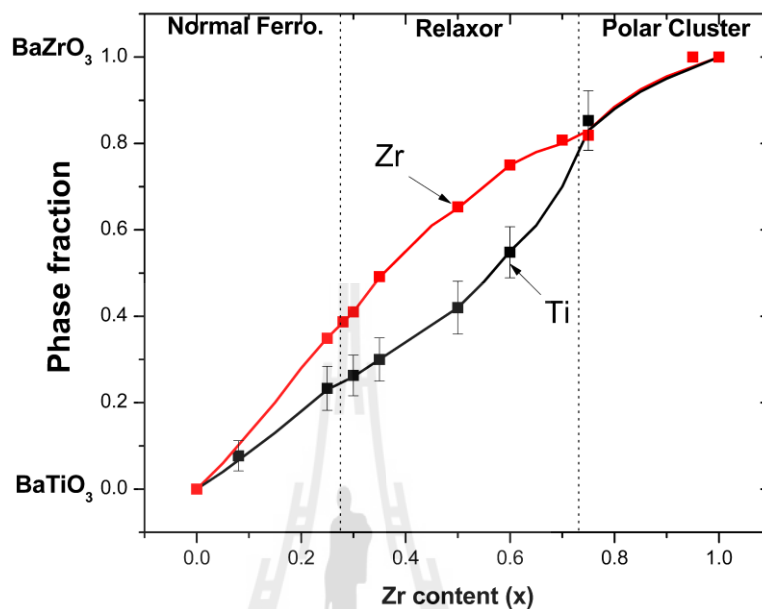


Figure 4.12 The phase fraction of Zr L₃-edge XANES spectra and Ti K-edge EXAFS in k-space of Ba(Zr_xTi_{1-x})O₃ crystals.

4.5 EXAFS results

To process and enhance the EXAFS with the high k region, the plot $k^2X(k)$ is considered and windowed using a Hanning window $W(k)$. The EXAFS spectra were processed, information on local structure of Ti atom via fitting with perovskite models of Ba(Ti,Zr)O₃ in ARTEMIS program. In this work, the Ti K-edge EXAFS spectra can only be obtained up to photon energy of 250 eV above the absorption edge, due to the presence of Ba L₃-edge. Therefore, EXAFS spectral fitting can only be performed up to the second shell; i.e. the first shell-oxygen octahedral and second shell of 8-fold coordinate, shown in Figure. 4.13.

The Ti *K*-edge EXAFS spectra did not show clearly the phase transition at $x = 0.7-0.75$. Therefore, the Ti *K*-edge EXAFS spectra can be changed to the normalized experimental EXAFS signal (χ) in function k follow by Eq. (2.108), shown in Figure 4.14. At $x = 0.7-0.75$, $\chi(k)$ is shown clearly the phase transition of relaxor ferroelectric behavior to polar cluster likely XANES spectra. In addition, $\chi(k)$ can be a Fourier transform (FT) in *R*-space (Figure. 4.15). For $x = 0.7-0.75$, the trend of the peak B features change and correspond with XANES results and phase transition from relaxor to polar cluster. Figure 4.16 shows the EXAFS Fourier Transform and fitting for all the six samples. EXAFS data for $x \leq 0.7$ can be fit assuming the Ti ions occupy octahedrally coordinated *B*-sites in pseudo-cubic structure, the same condition used in XANES simulation. Each fit for the compositions with $x \geq 0.7$ was performed assuming the Ti ions occupy octahedrally coordinated *B*-sites in the perfect cubic structure. The model included single distances and their associated DW factors for the Ti–O and (x6), Ti–Ba (x8) coordination shells, respectively. All single and significant double-scattering paths were also included. The refined structural parameters are summarized in Table 4.1, showing coordination numbers **N**, the bond length of Ti absorbing atoms within oxygen octahedral with 8-fold barium atoms and the Debye-Waller (DW) factor σ^2 . It is observed that with increasing Zr content in Ba(Ti,Zr)O₃ system the local structure is closer to the perfect cubic symmetry, particularly at $x \geq 0.75$ with the pseudo-cubic (almost a perfect cubic) structure observed. This phase transition is likely the effect of temperature dependence in BaTiO₃. While the temperature is increasing, the tetragonal perovskite structure of BaTiO₃ changes to cubic perovskite (Vedrinskii *et al.*, 1998). Similarly, when Zr content in Ba(Ti,Zr)O₃

is increased, the structure at room temperature becomes disordered and when $x > 0.75$ the structure becomes that of BaZrO_3 .

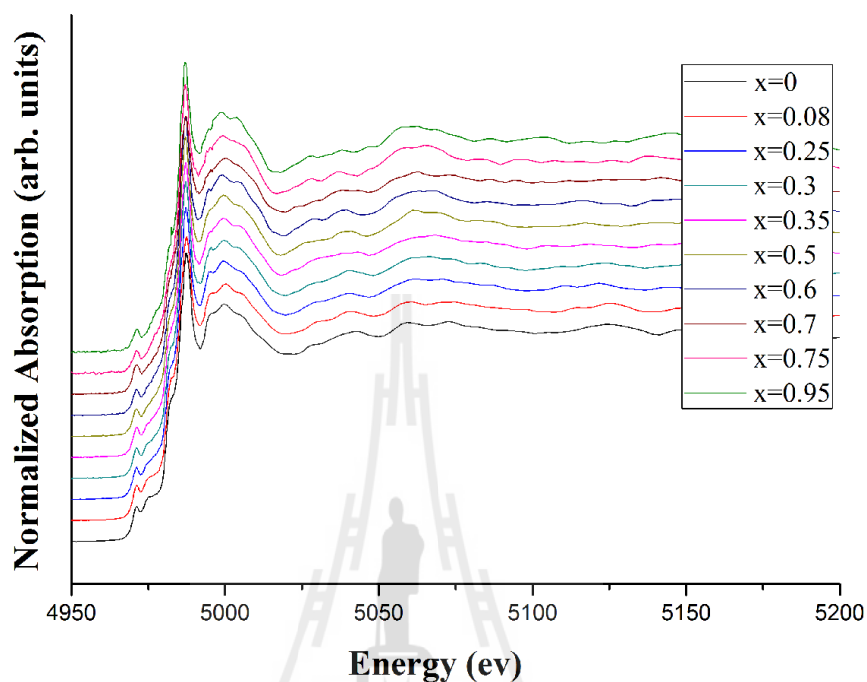


Figure 4.13 The Normalized Ti K-edge EXAFS spectra of $\text{Ba}(\text{Ti},\text{Zr})\text{O}_3$ powders.

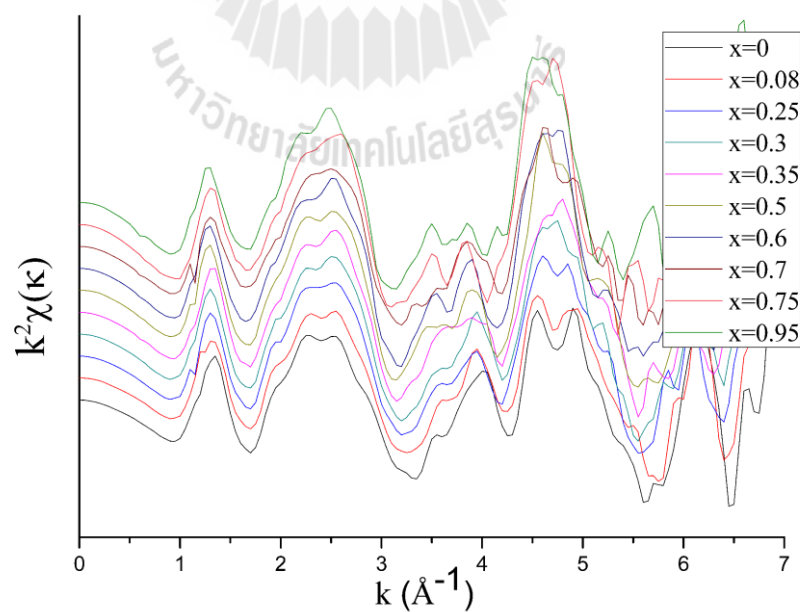


Figure 4.14 The EXAFS Fourier transform in k-space of $\text{Ba}(\text{Ti},\text{Zr})\text{O}_3$ powders.

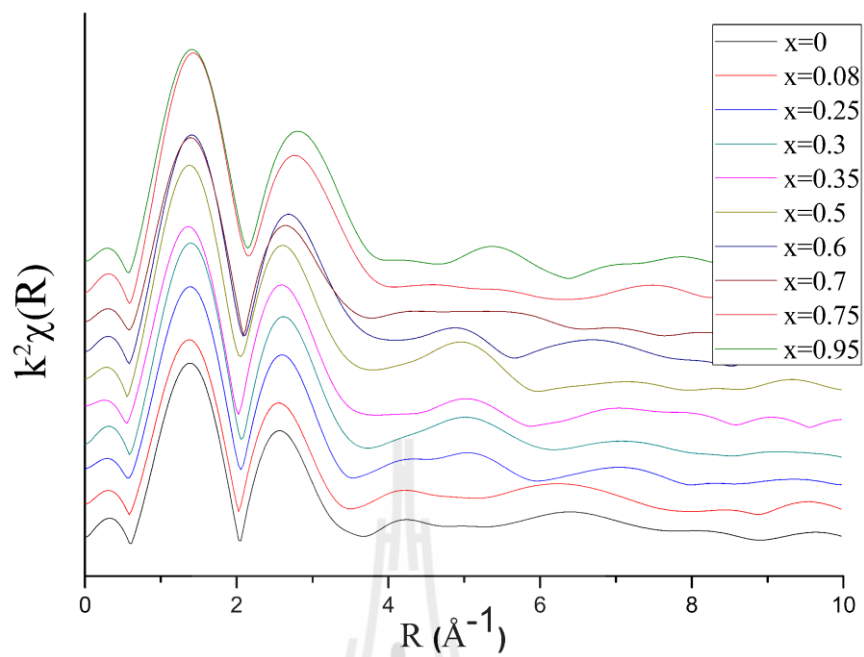


Figure 4.15 The EXAFS Fourier transform in R-space of Ba(Ti,Zr)O₃ powders.

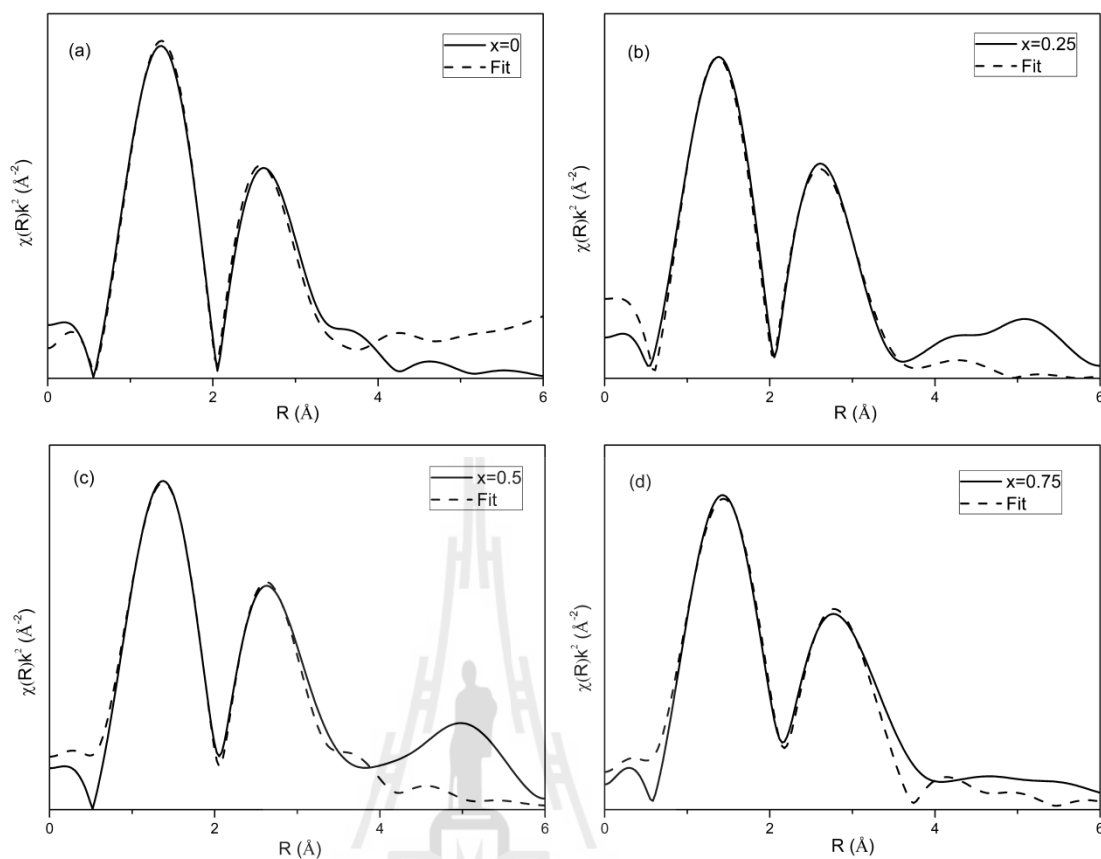


Figure 4.16 Experimental and calculated (solid/red) magnitude of EXAFS Fourier transform for a). BaTiO_3 , b). $\text{BaTi}_{0.75}\text{Zr}_{0.25}\text{O}_3$, c). $\text{BaTi}_{0.50}\text{Zr}_{0.50}\text{O}_3$, and d). $\text{BaTi}_{0.25}\text{Zr}_{0.75}\text{O}_3$. The k range used in the FT is from 2 to 5.7 \AA^{-1} for all data sets.

Table 4.1 The structural parameters coordination numbers N , interatomic distances R and DW factors σ^2 obtained by fitting the EXAFS data for the $\text{BaTi}_{1-x}\text{Zr}_x\text{O}_3$ ($x=0,0.25,0.5$ and 0.75).

Sample	Shell	N	R (Å)	σ^2
BaTiO₃	Ti-O1	1	1.4809(1)	0.003
	Ti-O2	1	2.2190(2)	0.003
	Ti-O3	4	1.8962(2)	0.003
	Ti-Ba1	4	3.3721(2)	0.005
	Ti-Ba2	4	3.4559(2)	0.005
BaTi_{0.75}Zr_{0.25}O₃	Ti-O1	1	1.4675(2)	0.003
	Ti-O2	1	2.2403(2)	0.003
	Ti-O3	4	1.8539(2)	0.003
	Ti-Ba1	4	3.3630(2)	0.003
	Ti-Ba2	4	4.1565(2)	0.003
BaTi_{0.5}Zr_{0.5}O₃	Ti-O1	1	1.9463(2)	0.008
	Ti-O2	1	1.9707(2)	0.008
	Ti-O3	4	1.9585(2)	0.008
	Ti-Ba1	4	3.3533(2)	0.0001
	Ti-Ba2	4	3.3675(2)	0.0001
BaTi_{0.25}Zr_{0.75}O₃	Ti-O	6	1.9718(1)	0.008
	Ti-Ba	8	3.4355(1)	0.0001

4.6 Dielectric permittivity

The dielectric constant and dielectric loss tangent ($\tan \delta$) at various frequencies for Ba(Ti,Zr)O₃ compositions, with $x=0, 0.08, 0.25, 0.28, 0.30, 0.35, 0.50, 0.75$ and 0.95 , are shown in Figure 4.17. The compositions with $0 \leq x \leq 0.25$, exhibit normal ferroelectric behavior and T_m is not change as a function of frequencies. At $x = 0.28$, it starts showing relaxor behavior and the broad peaks of dielectric constant as a function temperature. A strong frequency dispersion is observed around the ϵ' and $\tan \delta$ peaks for $x \geq 0.30$ compositions or so called “relaxor” like behavior. However, at $x \geq 0.75$, it exhibits polar cluster behavior and dielectric constant is dropping with weak frequency dispersion in polar cluster region. With the increase in frequency, ϵ' decreases and the temperature at which the maximum dielectric constant (T_m) is shifted to higher temperatures. In contrast, the dielectric loss tangent is decreasing while the frequencies decreases and similarly, the temperature where the maximum dielectric loss is shifted to higher temperatures. Furthermore, the dielectric constants decrease refer to the composition with x increased. Except at $x = 0.35$, the dielectric constants increase compared with $x = 0.30$.

The Curie-Weiss law can explain a normal ferroelectric in the paraelectric region follow by Eq. (2.64). Figure 4.18, shows the inverse dielectric constant as a function of temperature at 100 KHz. The linear fitting as observe in the paraelectric region or high temperature for all compositions. The fitting parameters Curie-Weiss constant and Curie temperature as calculation are shown in Table 4.2 (Maiti *et al.*, 2006). The results show that the Curie temperature decreases while the composition x increases. It is evident from the value of T_C , that the compositions $x=0.08-0.50$, shows the ferroelectric behavior. However, the values of T_C is negative temperature

for $x=0.75-0.95$. Therefore, they are not normal ferroelectric behavior. Furthermore, the relaxor ferroelectric behavior in the high temperature region follows a modified Curie-Weiss law from Eq. (2.65). The value of δ_γ represents the degree of diffuseness for transition peaks. Both γ and δ_γ are determined from the slope and intercept $\ln(\varepsilon'_{max}/\varepsilon')$ versus $\ln(T - T_m)$, as shown in Figure. 4.18 for $x= 0.08, 0.25, 0.28, 0.30, 0.35, 0.50, 0.75,$ and 0.95 . In the Table 4.3, the value of γ is increasing while the composition x increases, indicate the relaxor behavior. For $x \geq 0.25$, the compositions exhibit the relaxation behavior until $x = 0.50$, close to the ideal relaxor ferroelectric ($\gamma=2$). The value of δ_γ also increases because of the increasing of relaxation. In addition, the transition temperature T_m decreases as x increases.

Table 4.2 Calculated Curie constant and measured T_c from dielectric properties of $\text{Ba}(\text{Zr}_x\text{Ti}_{1-x})\text{O}_3$ compositions.

Composition	C (K)	T_c (K)
$x=0.08$	1.95×10^5	353.75
$x=0.25$	7.44×10^5	181.41
$x=0.28$	1.71×10^5	256.58
$x=0.30$	7.99×10^4	230.83
$x=0.35$	2.61×10^5	162.80
$x=0.50$	9.12×10^4	59.49
$x=0.75$	5.92×10^4	-116.66
$x=0.95$	7.08×10^4	-1095.42

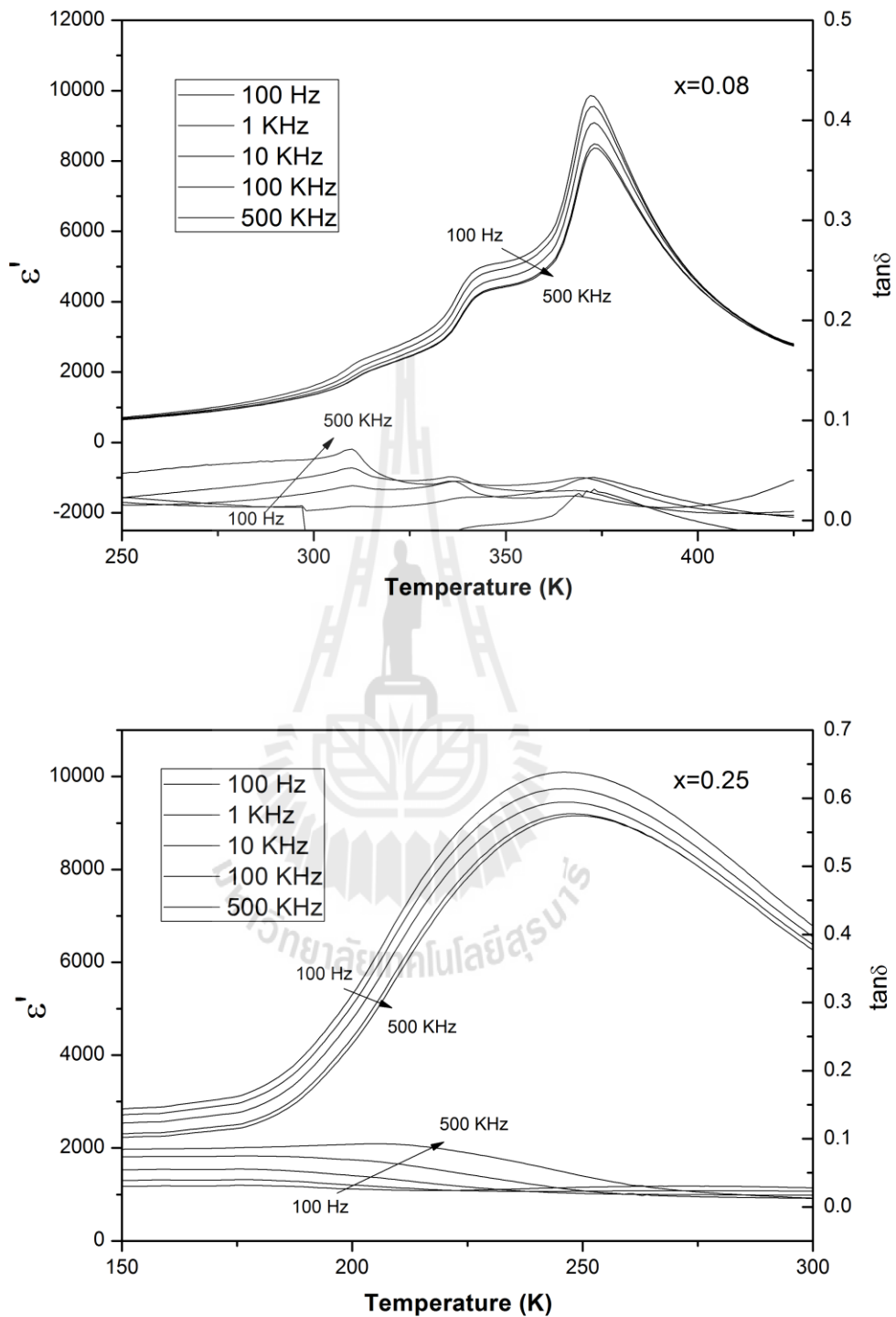


Figure 4.17 Temperature dependence of dielectric constant and loss tangent ($\tan \delta$) at various frequencies for $\text{Ba}(\text{Zr}_x\text{Ti}_{1-x})\text{O}_3$.

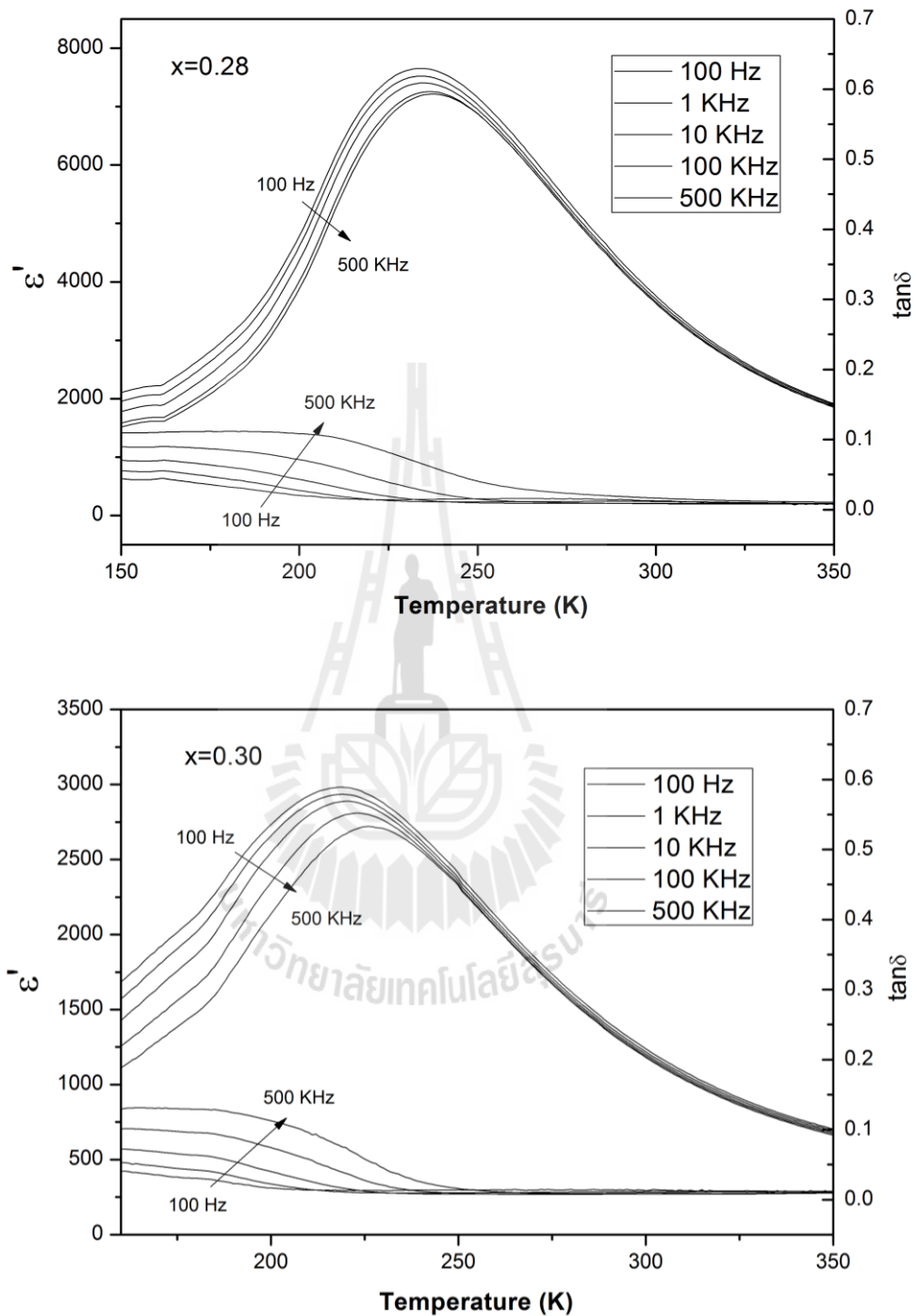


Figure 4.17 (Continued) Temperature independence of dielectric constant and loss tangent ($\tan \delta$) at various frequencies for $\text{Ba}(\text{Zr}_x\text{Ti}_{1-x})\text{O}_3$.

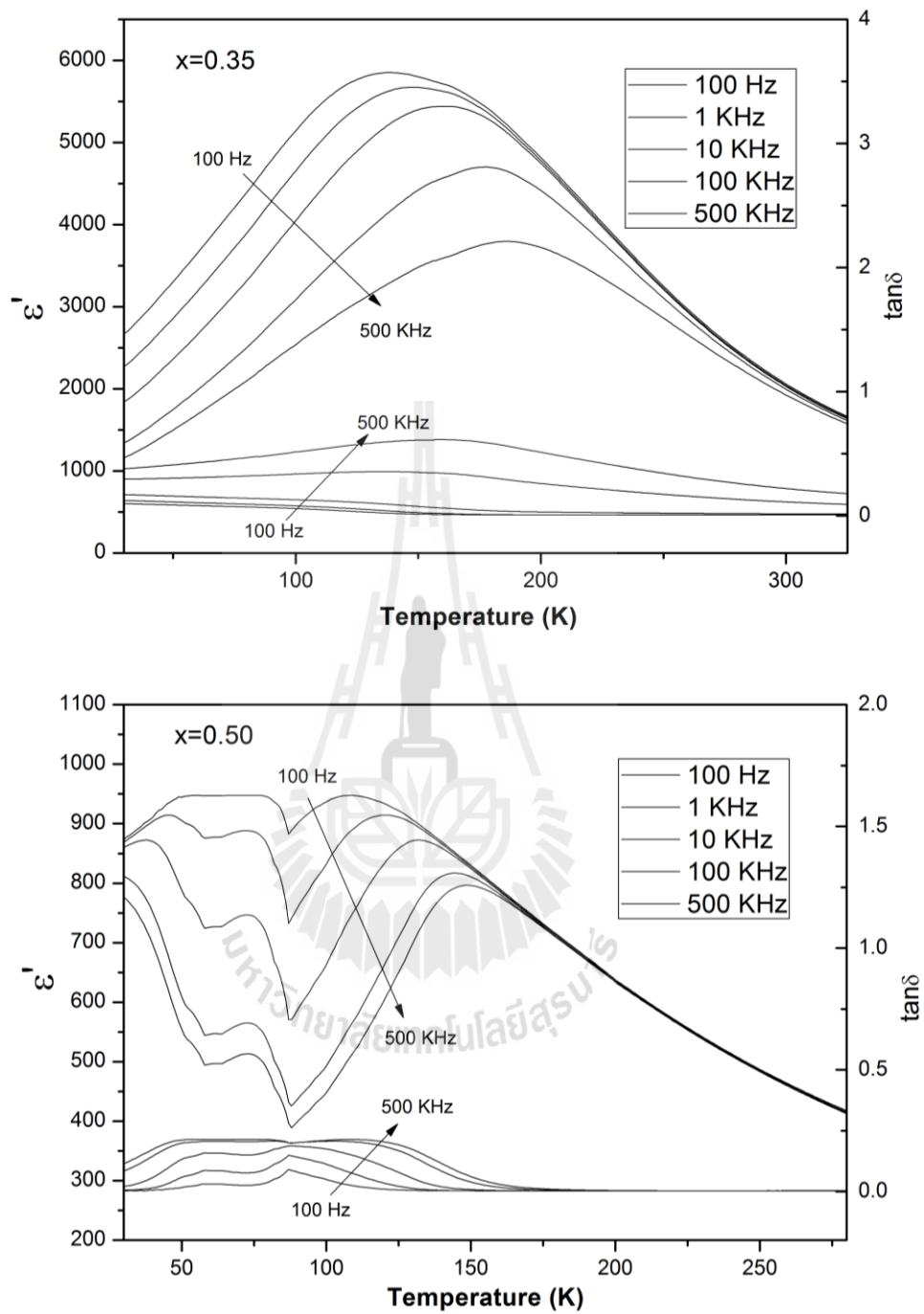


Figure 4.17 (Continued) Temperature independence of dielectric constant and loss tangent ($\tan \delta$) at various frequencies for $\text{Ba}(\text{Zr}_x\text{Ti}_{1-x})\text{O}_3$.

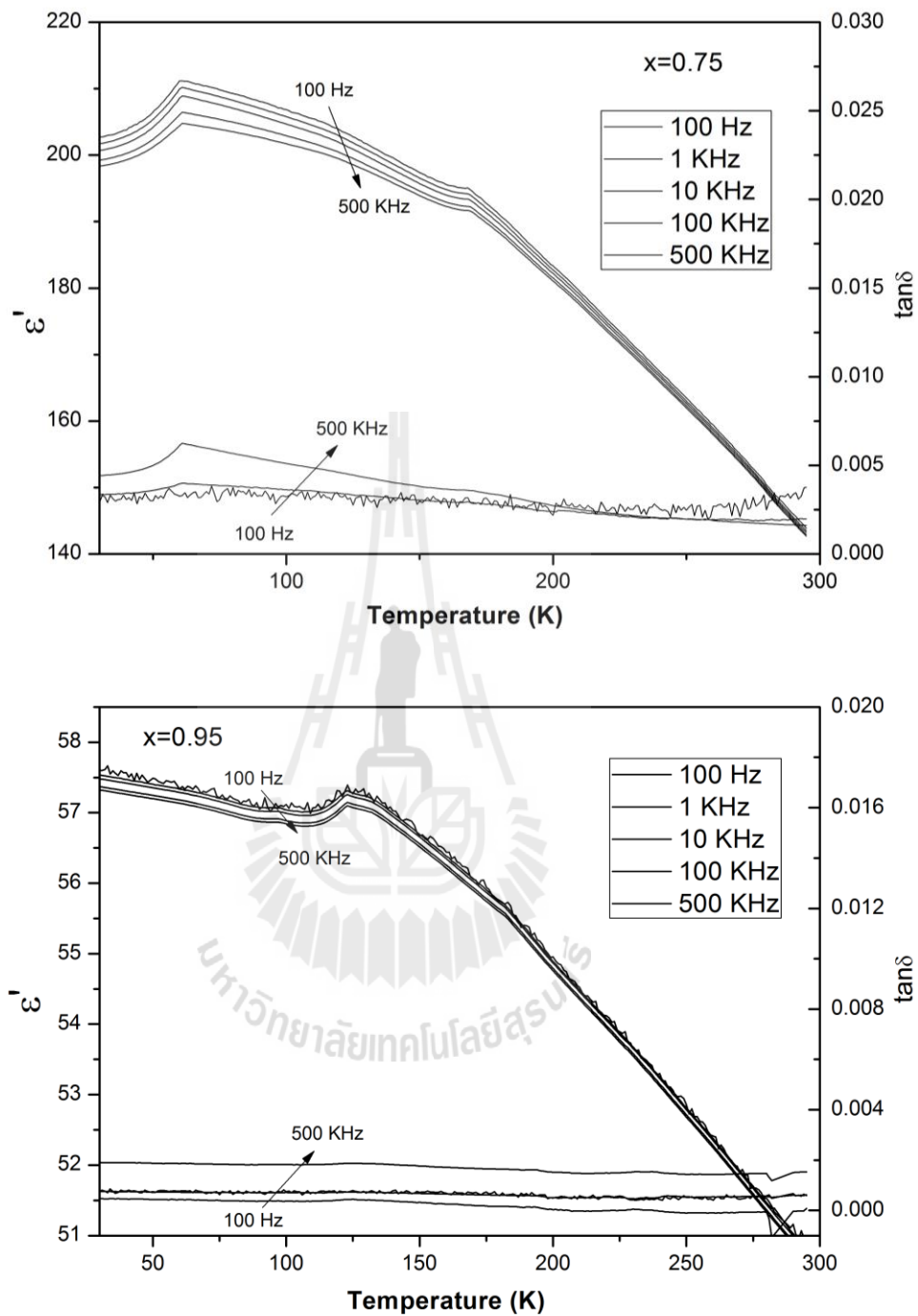


Figure 4.17 (Continued) Temperature independence of dielectric constant and loss tangent ($\tan \delta$) at various frequencies for $\text{Ba}(\text{Zr}_x\text{Ti}_{1-x})\text{O}_3$.

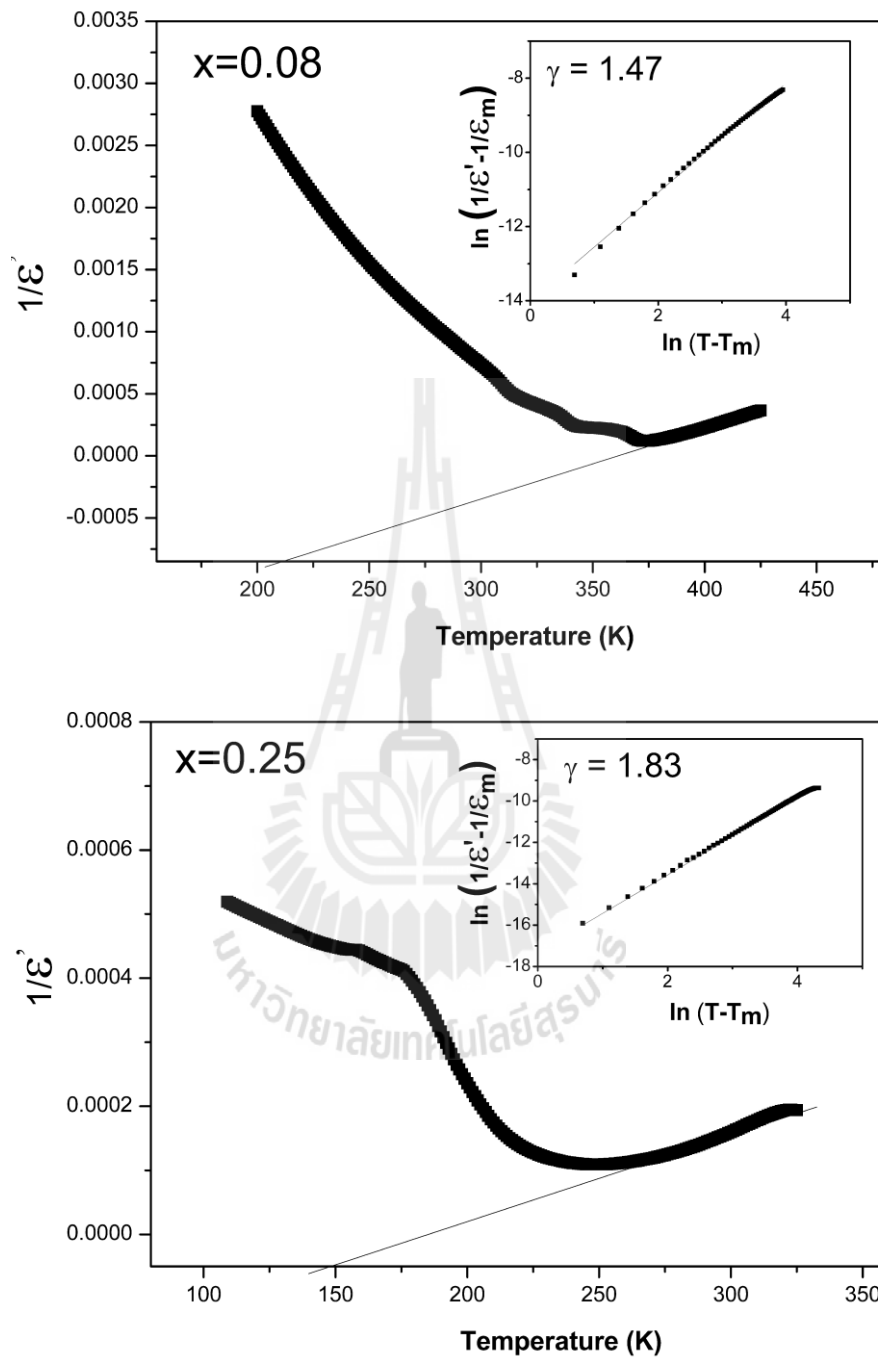


Figure 4.18 The inverse dielectric constant $1/\epsilon$ as a function of temperature at 100 kHz for $\text{Ba}(\text{Zr}_x\text{Ti}_{1-x})\text{O}_3$, symbols denote experimental data and solid line denotes fitting to the Curie-Weiss law. The insets show the plot of $\ln(1/\epsilon - 1/\epsilon_m)$ vs $\ln(T - T_m)$ for $\text{Ba}(\text{Zr}_x\text{Ti}_{1-x})\text{O}_3$ ceramics.

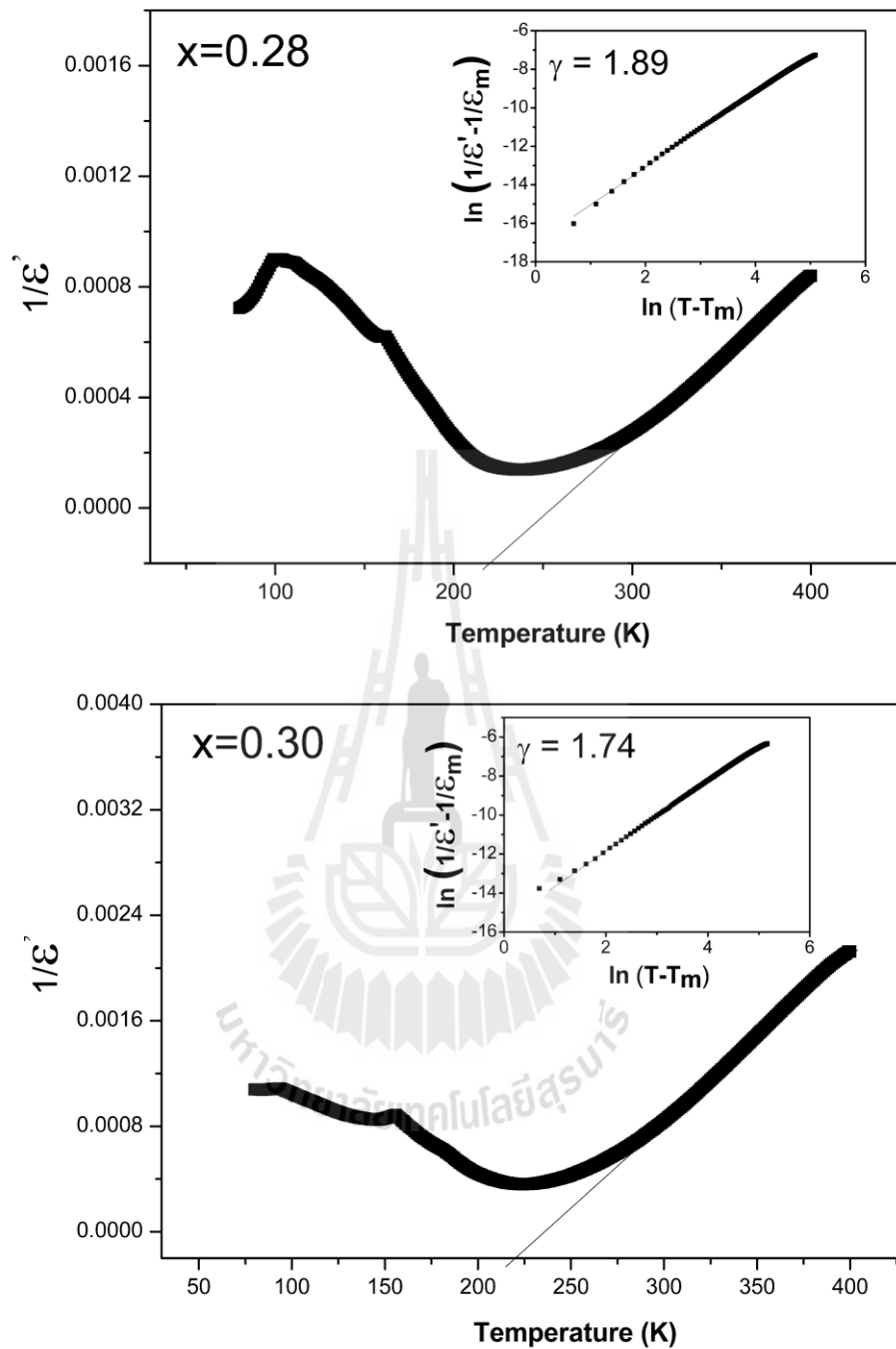


Figure 4.18 (Continued) The inverse dielectric constant $1/\epsilon$ as a function of temperature at 100 kHz for $\text{Ba}(\text{Zr}_x\text{Ti}_{1-x})\text{O}_3$, symbols denote experimental data and solid line denotes fitting to the Curie-Weiss law. The insets show the plot of $\ln(1/\epsilon - 1/\epsilon_m)$ vs $\ln(T - T_m)$ for $\text{Ba}(\text{Zr}_x\text{Ti}_{1-x})\text{O}_3$ ceramics.

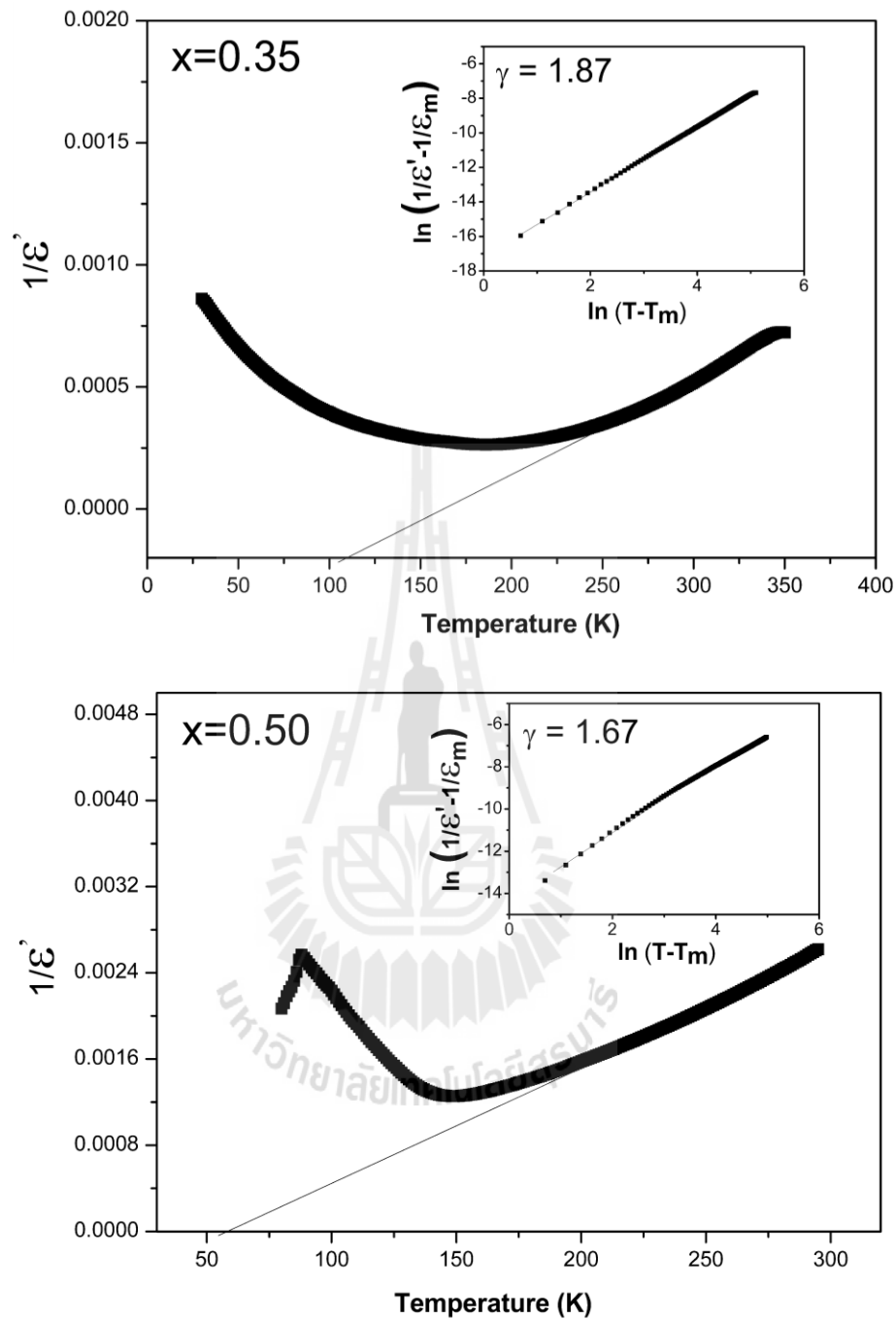


Figure 4.18 (Continued) The inverse dielectric constant $1/\epsilon$ as a function of temperature at 100 kHz for $\text{Ba}(\text{Zr}_x\text{Ti}_{1-x})\text{O}_3$, symbols denote experimental data and solid line denotes fitting to the Curie-Weiss law. The insets show the plot of $\ln(1/\epsilon - 1/\epsilon_m)$ vs $\ln(T - T_m)$ for $\text{Ba}(\text{Zr}_x\text{Ti}_{1-x})\text{O}_3$ ceramics.

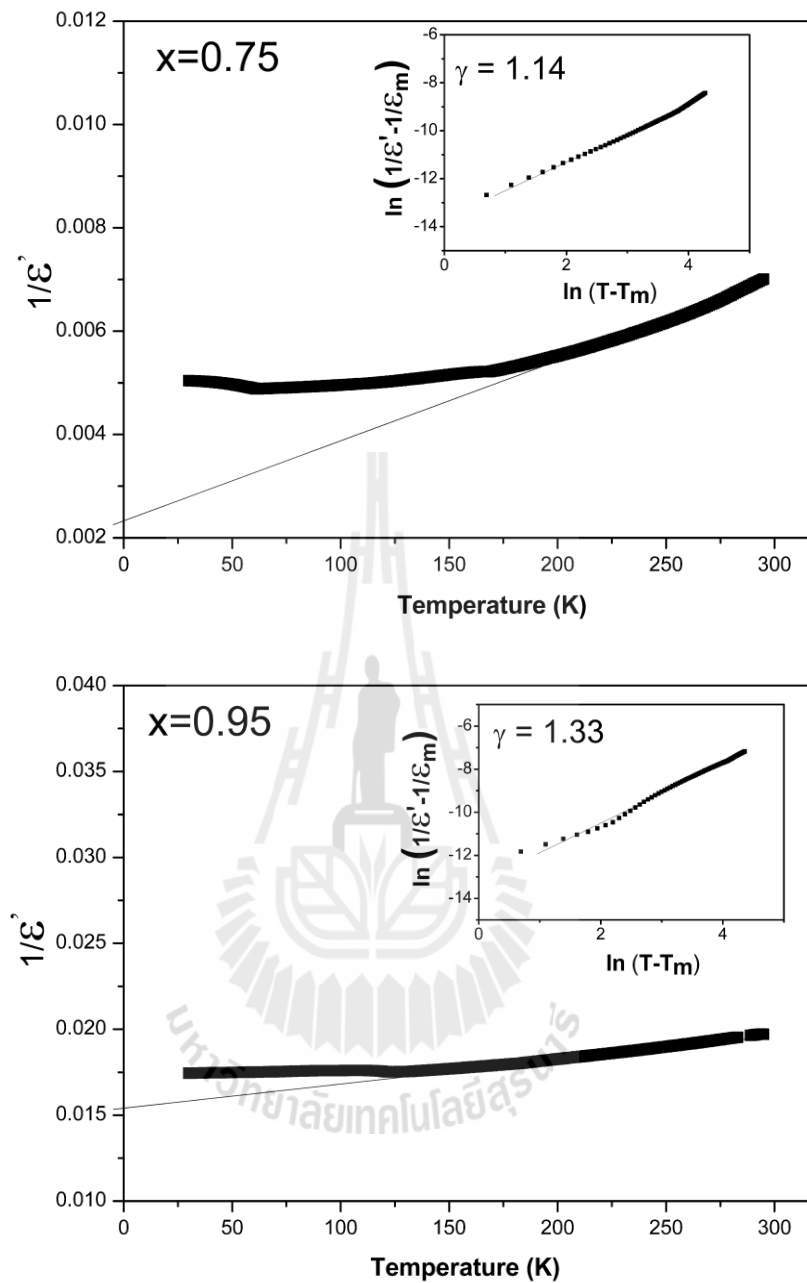


Figure 4.18 (Continued) The inverse dielectric constant $1/\epsilon$ as a function of temperature at 100 kHz for $\text{Ba}(\text{Zr}_x\text{Ti}_{1-x})\text{O}_3$, symbols denote experimental data and solid line denotes fitting to the Curie-Weiss law. The insets show the plot of $\ln(1/\epsilon - 1/\epsilon_m)$ vs $\ln(T - T_m)$ for $\text{Ba}(\text{Zr}_x\text{Ti}_{1-x})\text{O}_3$ ceramics

Table 4.3 Degree of relaxation γ , dielectric maxima temperature and diffusivity of $\text{Ba}(\text{Zr}_x\text{Ti}_{1-x})\text{O}_3$ compositions.

Composition	γ	$T_m(\text{K})$	δ_γ
x=0.08	1.47	373	18.63
x=0.25	1.83	249	54.02
x=0.28	1.89	237	44.94
x=0.30	1.74	224	44.23
x=0.35	1.87	186	80.08
x=0.50	1.67	149	67.78
x=0.75	1.14	61	737.53
x=0.95	1.33	30	549.18

4.7 Hysteresis

The polarization hysteresis data at room temperature for $\text{Ba}(\text{Ti,Zr})\text{O}_3$ are shown in Figure 4.19. The characteristics of hysteresis loops show the ferroelectric properties at $x = 0.05$ and show the slim loop of ferroelectric properties around $0.25 \leq x \leq 0.28$. When $x = 0.30$ and 0.35 , the hysteresis exhibited normal ferroelectric properties again. When $x = 0.50$, the hysteresis exhibited a large dielectric loss. However, this result of dielectric permittivity showed the relaxor ferroelectric. At $x \geq 0.70$, the paraelectric properties were observed which rather corresponded with the polar cluster behavior. However, the results show the properties related with microstructure. It means that the characteristics of the hysteresis loops depend on the synthesis process of the ceramics which is hard to explain with local structure.

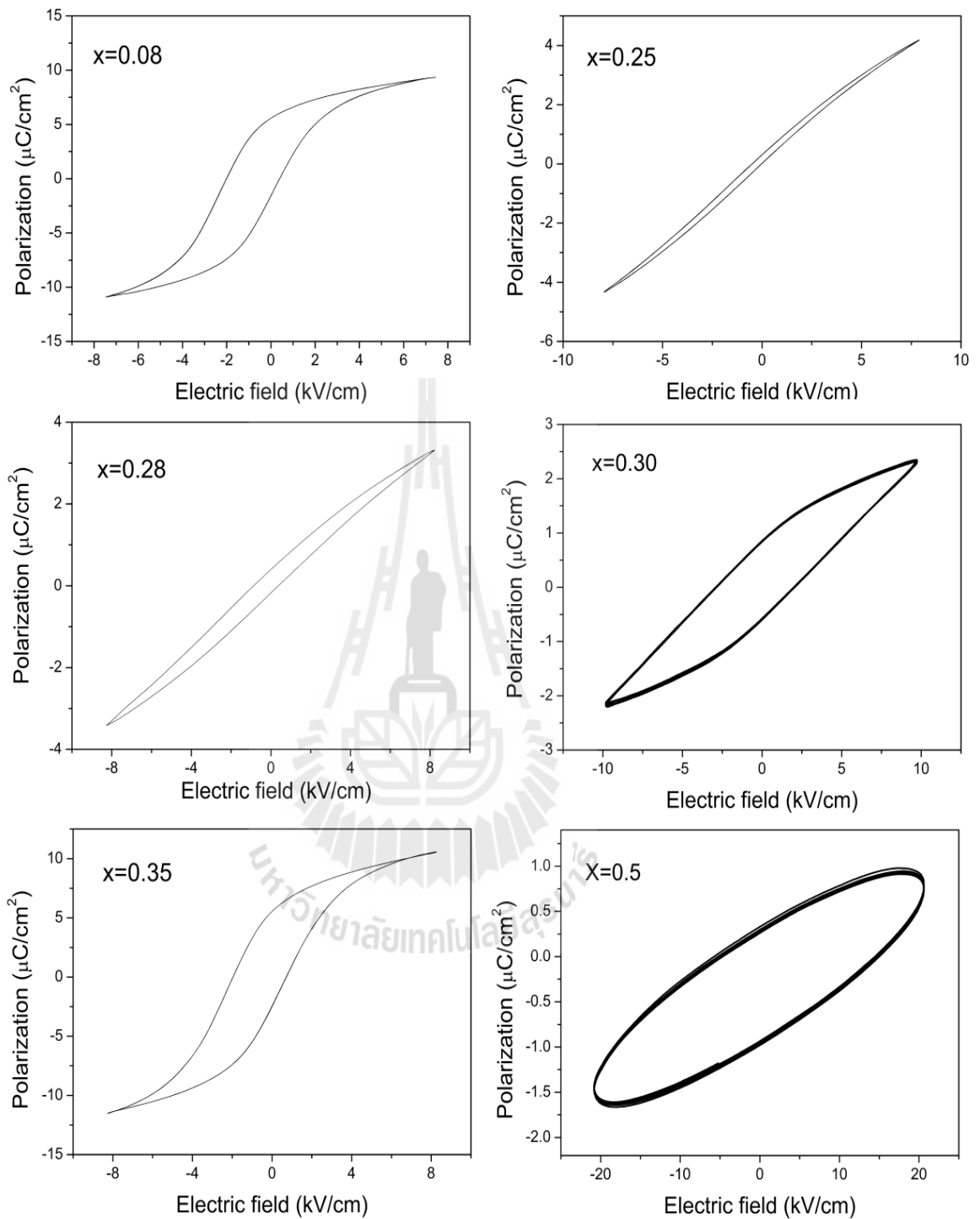


Figure 4.19 *P-E* hysteresis measurements on Ba(Zr_xTi_{1-x})O₃ ceramics obtained at room temperature.

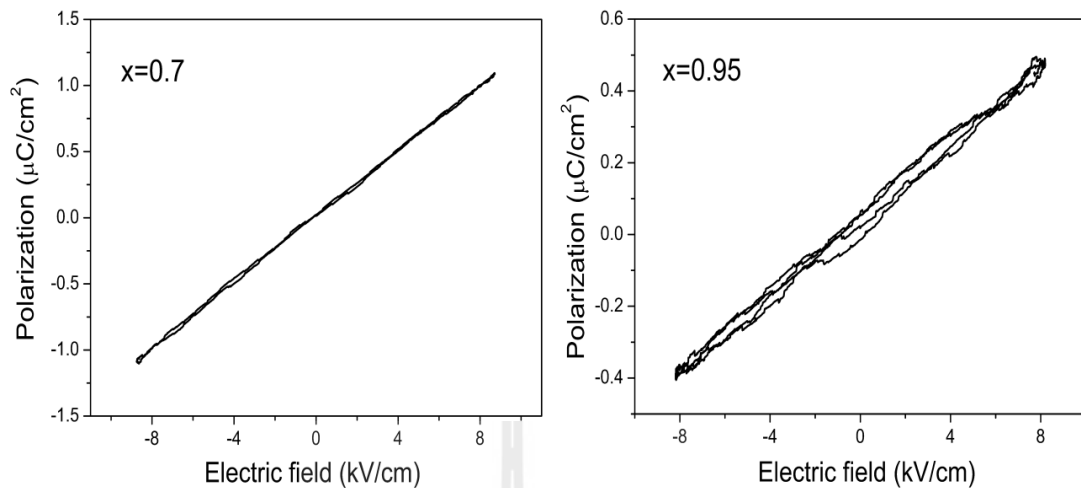


Figure 4.19 (Continued) *P-E* hysteresis measurements on $\text{Ba}(\text{Zr}_x\text{Ti}_{1-x})\text{O}_3$ ceramics obtained at room temperature.

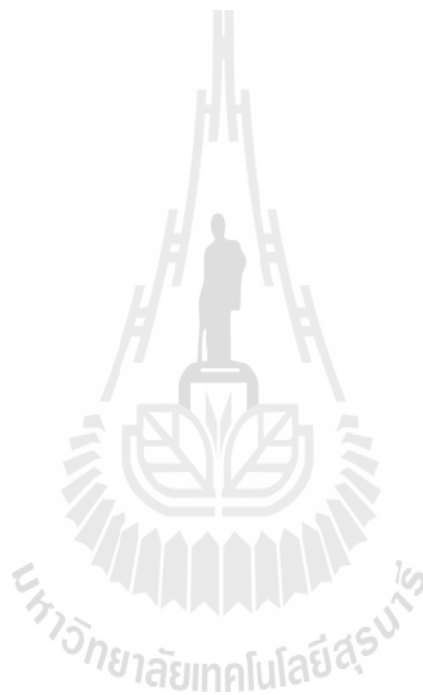
4.8 References

- Chandarak, S., Jutimoosik, J., Bootchanont, A., Unruan, M., Jantaratana, P., Priya, S., Srilomsak, S., Rujirawat, S. and Yimmirun, R. (2012). Local Structure of Magnetolectric $\text{BiFeO}_3\text{-BaTiO}_3$ Ceramics Probed by Synchrotron X-Ray Absorption Spectroscopy. **J. Supercond. Nov. Magn.** 26: 455.
- Cross, L. E. (1987). Relaxor ferroelectrics. **Ferroelectrics.** 76: 241.
- de Groot, F. M. F., Hu, Z. W., Lopez, M. F., Kaindl, G., Guillot, F. and Tronc, M. (1994). Differences between L3 and L2 x-ray absorption spectra of transition metal compounds. **J. Chem. Phys.** 101: 6570.
- Hedin, L. and Lundqvist, S. (1970) Effects of Electron-Electron and Electron-Phonon Interactions on the One-Electron States of Solids. **Sol. Stat. Phys.** 23 (Eds, Frederick Seitz, D. T. and Henry, E.) Academic Press, pp. 1.

- Levin, I., Cockayne, E., Krayzman, V., Woicik, J. C., Lee, S. and Randall, C. A. (2011). Local structure of Ba(Ti,Zr)O₃ perovskite-like solid solutions and its relation to the band-gap behavior. **Phys. Rev. B.** 83: 094122.
- Levin, I., Krayzman, V. and Woicik, J. C. (2013). Local-structure origins of the sustained Curie temperature in (Ba,Ca)TiO₃ ferroelectrics. **Appl. Phys. Lett.** 102: 162906.
- Maiti, T., Guo, R. and Bhalla, A. S. (2006). The evolution of relaxor behavior in Ti⁴⁺ doped BaZrO₃ ceramics. **J. Appl. Phys.** 100: 114109.
- Maiti, T., Guo, R. and Bhalla, A. S. (2008). Structure-Property Phase Diagram of BaZr_xTi_{1-x}O₃ System. **J. Am. Ceram. Soc.** 91: 1769.
- Maiti, T., Guo, R. and Bhalla, A. S. (2011). Evaluation of Experimental Resume of BaZr_xTi_{1-x}O₃ with Perspective to Ferroelectric Relaxor Family: An Overview. **Ferro.** 425: 4.
- Mouraa, F., Simões, A. Z., Stojanovic, B. D., Zaghete, M. A., Longoa, E. and Varela, J. A. (2008). Dielectric and ferroelectric characteristics of barium zirconate titanate ceramics prepared from mixed oxide method. **J. Alloys Comp.** 462: 129.
- N. Binhayeeniyi, P. Sukvisut, C. Thanachayanont and S. Muensit (2010). Physical and electromechanical properties of barium zirconium titanate synthesized at low-sintering temperature. **Matt. Lett.** 64: 305.
- Rehr, J. J. and Albers, R. C. (2000). Theoretical approaches to x-ray absorption fine structure. **Rev. Mod. Phys.** 72: 3.
- Thurnaurer, H. and Deaderick, J. (1941) **In U.S. Patent** Vol. 2,429,588.
- Vedrinskii, R. V., Kraizman, V. L., Novakovich, A. A., Demekhin, P. V. and Urazhdin, S. V. (1998). Pre-edge fine structure of the 3d atom K x-ray

absorption spectra and quantitative atomic structure determinations for ferroelectric perovskite structure crystals. **J. Phys. Condens. Matter.** 10: 9561.

Yu, Z., Ang, C., Guo, R. and Bhalla, A. S. (2002). Piezoelectric and strain properties of $\text{Ba}_{1-x}\text{Ti}_x\text{Zr}_x\text{O}_3$ ceramics. **Matt. Lett.** 92: 3.



CHAPTER V

STUDY OF PHASE INFORMATION AND DIELECTRIC PROPERTIES IN BARIUM STANNATE TITANATE

5.1 Introduction

Barium stannate, BaSnO_3 , is of interest due to its high performance applications, such as gas sensors and capacitors. With substitution of Ti, it becomes a cubic perovskite-like compound and also an environmental friendly material which is unlike lead-based materials with volatility and toxicity. These are some of the advantages for the demand of BaSnO_3 . Moreover, this perovskite-like material is also ceramic capacitors due to the properties of dielectric constant (Cernew and Manea, 2007; Yun Liua *et al.*, 2007; Wei *et al.*, 2004)

The $\text{Ba}(\text{Sn}_x\text{Ti}_{1-x})\text{O}_3$ (BST), $x=0-0.95$, system is most widely studied of such systems. With increasing Sn content, the tetragonal ferroelectric to pseudo cubic relaxor phase transition occurs around $x=0.2-0.25$ (Yun Liua *et al.*, 2007; Cai *et al.*, 2011). In previous work, x-ray diffraction (XRD) technique was used to investigate the crystal structure. However, XRD technique did not show clearly the phase transition from ferroelectric to relaxor behavior. Therefore, we focus on local structure investigation by x-ray absorption spectroscopy (XAS) technique.

5.2 Experimental

The starting materials BaCO_3 , TiO_2 and SnO_2 powders were weighed according to the composition $\text{BaSn}_x\text{Ti}_{1-x}\text{O}_3$ with $x = 0.0, 0.05, 0.25, 0.3, 0.5, 0.55, 0.60, 0.75$ and 0.95 . by a conventional solid state reaction method. The materials were mixed in ball milled using ethanol for 24 h. After drying, the calcinations of the mixed powders was carried out at temperature of $1200\text{ }^\circ\text{C}$ for 4 h with $5^\circ\text{C}/\text{min}$ heating/cooling rates (Wei and Yao, 2007; Wei *et al.*, 2004).

XRD technique was employed to investigate the phase formation and global structure of $\text{Ba}(\text{Sn}_x\text{Ti}_{1-x})\text{O}_3$. XRD patterns were scanned in 2θ range of 20° - 60° with 0.02° step and CuK_α radiation was used. The phase information of local structure was investigated by XAS measurements which were conducted at ambient temperature at BL-5 and BL-8 of the Siam Photon Laboratory, Synchrotron Light Research Institute (SLRI), Thailand (electron energy of 1.2 GeV, beam current 120-80 mA). The experiments were performed in fluorescence mode. XANES spectra for the Ti *K*-edge were measured for all compositions.

The silver electrodes were sputtered on the BST ceramics for dielectric measurement. The HP4284 LCR meter was used to measure the dielectric constant and loss tangent from 100 Hz to 500 kHz in the temperature range of 30-425 K with a cooling rate of 2 K/min.

5.3 X-ray diffraction

In Figure 5.1, XRD patterns of $\text{Ba}(\text{Sn}_x\text{Ti}_{1-x})\text{O}_3$ powders display the characteristic global structure. The result showed the second phase of BaCO_3 starting material at $x=0.95$. However, this result has not affected the dielectric properties because content of BaCO_3 is very small. When Sn substituted Ti in BaTiO_3 , the structure changes from tetragonal to cubic perovskite phases. The composition $x = 0$ (pure BT) shows tetragonal perovskite phase which can be matched with JCPDS file No. 81-2201, while the samples at compositions $x \leq 0.25$ exhibit the broad XRD peaks which can be matched with JCPDS file No. 74-1299. However, the compositions between $0.25 \leq x \leq 0.95$ do not clearly show the phase transition or significant change of the global structure. The broad XRD peaks indicate that the cubic structure could also be identified as “*pseudo-cubic*” or a small distortion of cubic structure, which also affects the change in the dielectric properties.

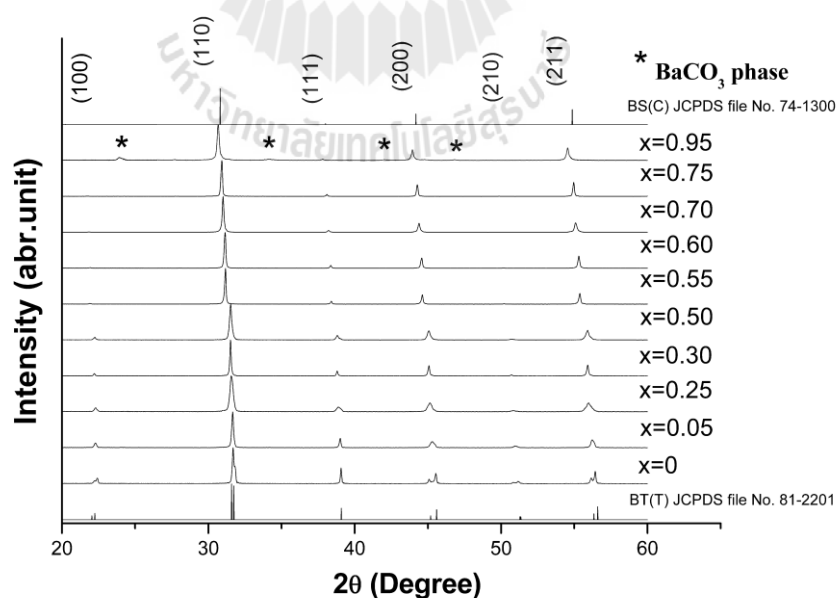


Figure 5.1 X-ray diffraction patterns of $\text{Ba}(\text{Sn}_x\text{Ti}_{1-x})\text{O}_3$ powders.

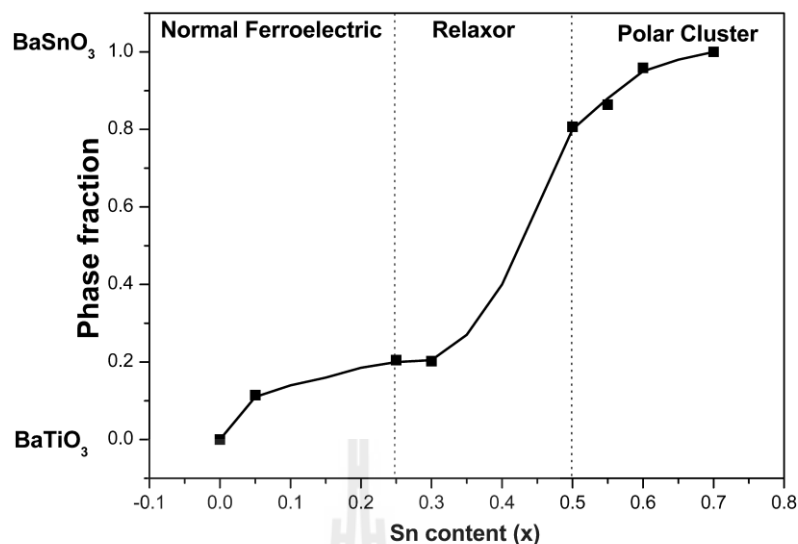


Figure 5.2 The phase fraction of $\text{Ba}(\text{Sn}_x\text{Ti}_{1-x})\text{O}_3$ from XRD patterns.

In addition, the phase fraction between BaTiO_3 and BaSnO_3 is obtained from a linear combination of the integrated intensity of mean peak (110) of XRD patterns, as show in Figure. 5.2. The results show that the phase fraction suddenly increases around $x=0.3-0.5$ which is not corresponding with the phase transition of normal ferroelectric to relaxor and relaxor to polar cluster. Therefore, the phase transition cannot be seen clearly from this result.

5.4 XANES results

5.4.1 Identification of Sn site in BaTiO_3

Generally, XANES measures the excitation of electrons L_3 -levels to unoccupied bound states and is thus used to obtain information about the local arrangement of atoms around the absorbing atoms and the density of states of unoccupied states.

XANES spectra of Sn L_3 -edge in Sn on Ti site in BaTiO_3 ($\text{Ba}(\text{Ti},\text{Sn})\text{O}_3$) and Sn on Ba site in BaTiO_3 ($(\text{Ba},\text{Sn})\text{TiO}_3$) were obtained using the FEFF8.2 codes following models in Figure 5.3. The FEFF codes is using a full multiple scattering approach based on ab initio overlapping muffin-tin potentials (Rehr and Albers, 2000). The muffin-tin potentials used in FEFF codes are self-consistent calculations with Hedin-Lundqvist exchange-correlation function(Hedin and Lundqvist, 1970). The results show that the measured XANES is clearly consistent with the calculation of Sn on Ti site and inconsistent with Sn at other lattice locations, as shown in Figure. 5.4.

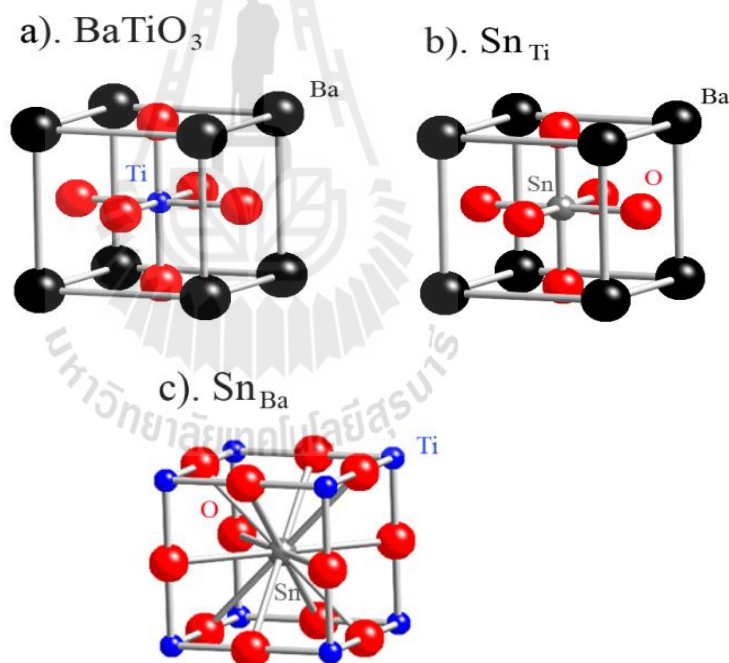


Figure 5.3 A Model perovskite crystal structure of BaTiO_3 . b–c schematic illustrations of Sn on Ti site, Sn on Ba site, respectively. Regions shown in c are shifted from that in a).

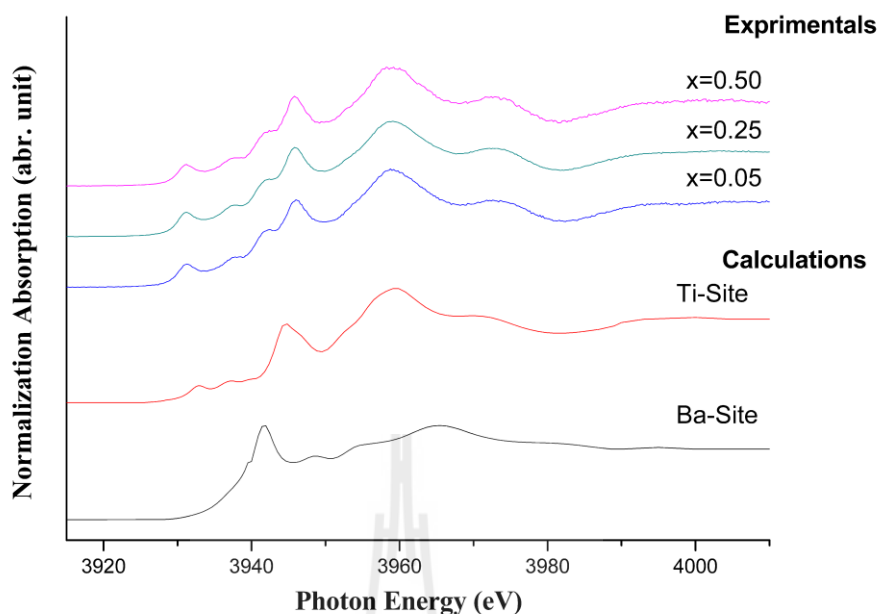


Figure 5.4 Sn L₃-edge XANES spectra of Ba(Ti_{1-x}Sn_x)O₃ and calculation of Sn site for Sn on Ti site (Sn_{Ti}-red line), Sn on Ba site (Sn_{Ba}-black line).

5.4.2 XANES studies of Ti K pre-edge

Generally, XANES measures the excitation of core electrons to unoccupied bound states and is thus used to obtain information about the local arrangement of atoms around the absorbing atoms and the density of states of unoccupied states. According to the molecular orbital theory and valence band theory, 3d levels of the octahedral complex split into t_{2g} and e_g level. The integrated intensity of pre-edge is associated with probability of electrons 1s to t_{2g} and e_g level. However, electrons 1s to 3d levels are forbidden but, if Ti atoms off center will be the effect of 3d levels splitting larger until e_g levels overlap 4s levels and electrons 1s can be occupied on e_g levels more. Therefore, the integrated intensity of Ti K pre-edge, which is associated with both the quadruple and the dipole $1s \rightarrow 3d$ transition of Ti, reflects the $3d-4p$

hybridization for Ti and I_A is directly proportional to the displacements of Ti off-center of oxygen octahedra and is indirectly proportional to the lattice constants (Vedrinskii *et al.*, 1998; Levin *et al.*, 2013; Levin *et al.*, 2011). The integrated intensity of peak B is associated with both the quadrupole and the dipole $1s \rightarrow 3d$ transition in molecular orbital related the local Zr/Ti ratio around the absorbing Ti.

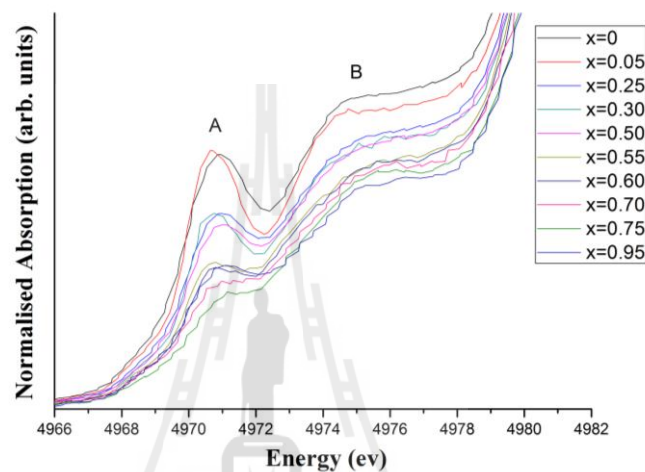


Figure 5.5 Normalized X-ray absorption Ti K pre-edge spectra of $\text{Ba}(\text{Sn}_x\text{Ti}_{1-x})\text{O}_3$ powders.

The normalized Ti K pre-edge XANES spectra of $\text{Ba}(\text{Sn}_x\text{Ti}_{1-x})\text{O}_3$ powders are shown in Figure. 5.5. According to Eq. (3.3), we adopted this value as a reference for calculating local Ti off-centering from the pre-edge peak intensities in the solid-solution samples (Figure. 5.6a). Clearly, the local value of δ_{Ti} in BST when x content is increasing, I_A will decrease continuously until $x=0.5$, which is increasing in the relaxor ferroelectrics region. After then, a drop at $x=0.75$ in polar cluster region is observed and is also larger than that expected from the relaxor ferroelectrics change to polar cluster, hence the local Ti off-centering was decreased. Figure 5.6b shows the average local Sn/Ti ratio around absorbing Ti atoms.

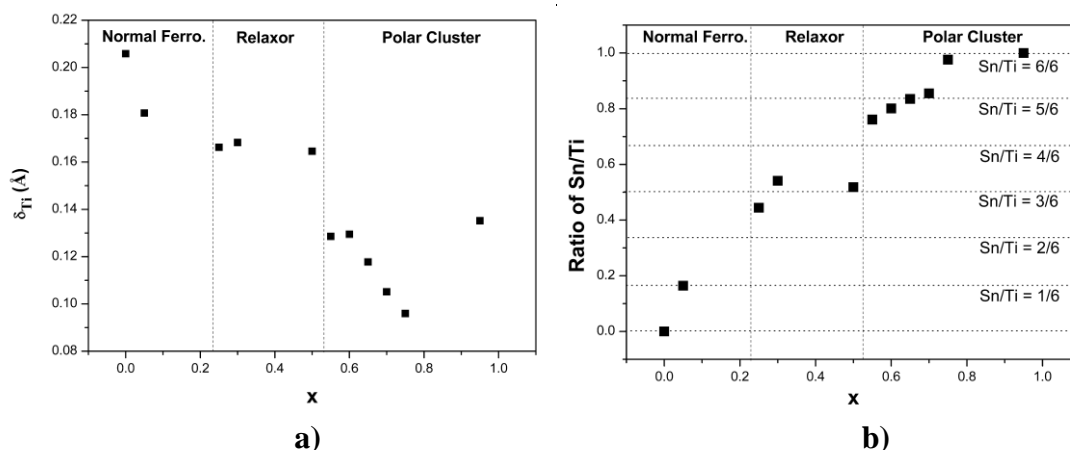


Figure 5.6 a) δ_{Ti} determined from the intensity of the pre-edge peak as a function of the unit-cell. The value of δ_{Ti} for $Ba(Sn_xTi_{1-x})O_3$ was determined using the spectrum reported in (Levin *et al.*, 2013). b) The local Sn/Ti ratio around absorbing Ti.

5.4.3 XANES studies of phase transition.

The normalized Ti K edge XANES spectra of $Ba(Sn_xTi_{1-x})O_3$ powders are shown in Figure. 5.7. While an increases in Sn content affects the average mean-square displacement of Ti ions, which decreases continuously until $x=0.25$, the structure approaches the cubic perovskite, as observed in the XRD results, and there are a few changes in local structure in the relaxor region. However, when $x = 0.55$, the δ_{Ti} decreases again, possibly due to the phase transition of relaxor to polar cluster like- $Ba(Zr_xTi_{1-x})O_3$ behavior (Maiti *et al.*, 2008). In addition, the Ti K pre-edge spectra is caused by the electron $1s$ transit to the hybridization of $3d-4p$ level and relate to the Ti displacement in oxygen octahedral. While the Sn content increasing, the integral intensity of peak A is continuously decreased or the Ti displacement

deceases. But at $x=0.95$, it increases again. However, the Ti displacement of $x=0.95$ is in order of polar cluster region. The substitution in B-site affect the phase transition to relaxor and polar cluster, respectively. On the other hand, the normalized Sn L_3 edge XANES spectra of $\text{Ba}(\text{Sn}_x\text{Ti}_{1-x})\text{O}_3$ powders are shown in Figure. 5.8. The results did not indicate the phase transition around $x=0.05-0.25$. However, the phase information changes gradually. But at around $x=0.5-0.55$, the phase transition like in the Ti K-edge XANES spectra can be seen. It means that the Ti atom in B-site of perovskite structure is a significant key to the dielectric properties.



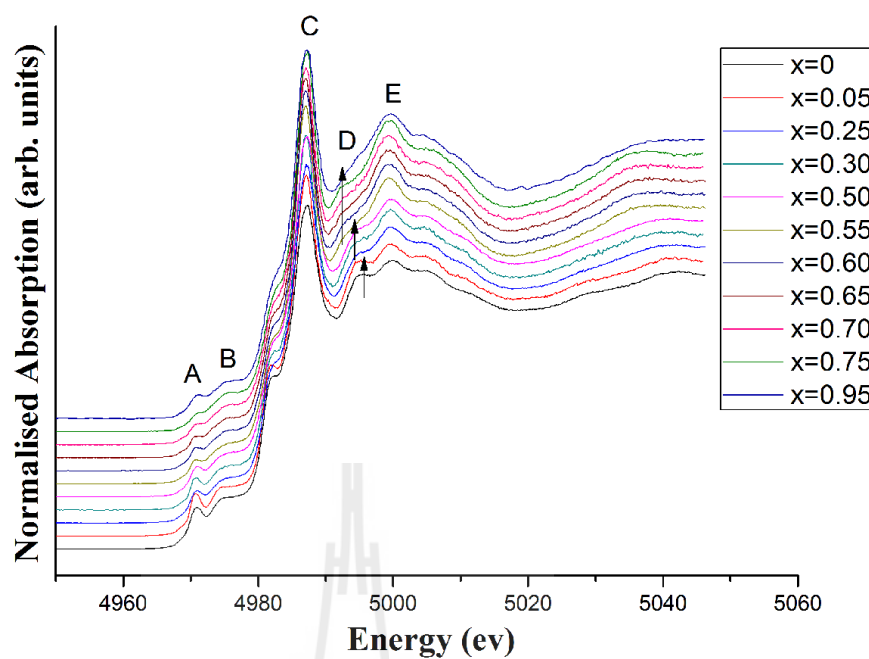


Figure 5.7 The normalized X-ray absorption Ti K-edge spectra of $\text{Ba}(\text{Sn}_x\text{Ti}_{1-x})\text{O}_3$ powders.

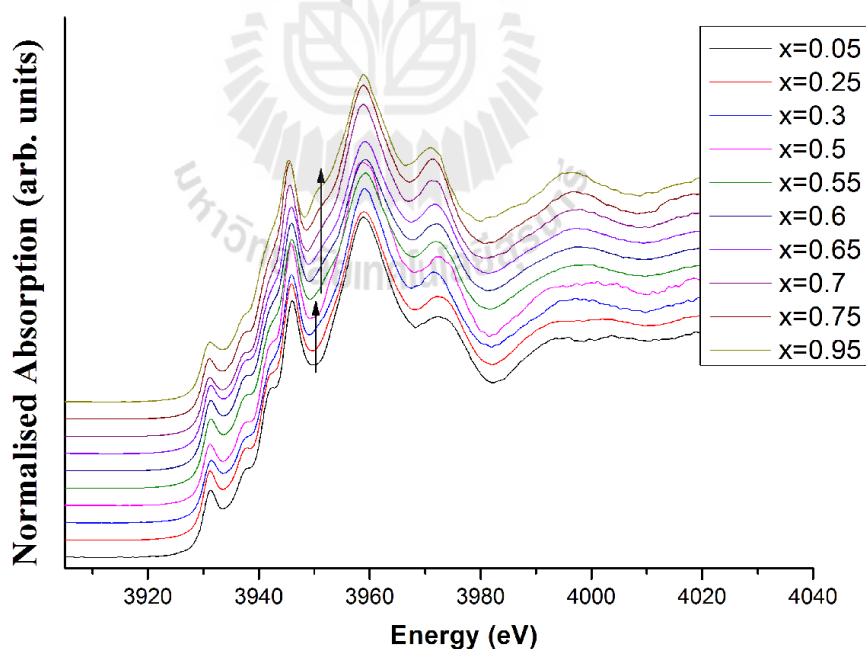


Figure 5.8 The normalized X-ray absorption Sn L_3 -edge spectra of $\text{Ba}(\text{Sn}_x\text{Ti}_{1-x})\text{O}_3$ powders.

In addition, we assume the mixture phase which is caused by the phase fraction between BaTiO_3 and BaSnO_3 . Therefore, the phase fraction is obtained from linear combination fit of BaTiO_3 and $\text{BaTi}_{0.05}\text{Sn}_{0.95}\text{O}_3$ materials, (assuming that $\text{BaTi}_{0.05}\text{Sn}_{0.95}\text{O}_3$ is pure BaSnO_3). However, this assumption rather is not entirely correct but the tend of change in phase fraction may contribute to better understanding. The results show that the phase fraction of Sn L_3 -edge linear combination increases in the same tend as the phase fraction of Ti K-edge for $x \leq 0.5$, and separates when $x > 0.5$, meaning that Sn atoms occult more lattices in BST. Therefore, Ti atoms were pressed from Sn atoms, as shown in Figure. 5.9. However, the phase fraction indicated the phase transformation at changing slope of phase fraction of Sn and Ti atoms around $x = 0.3$ and $x = 0.5$, corresponding to the phase transition of normal ferroelectric to relaxor, and relaxor to polar cluster, respectively.



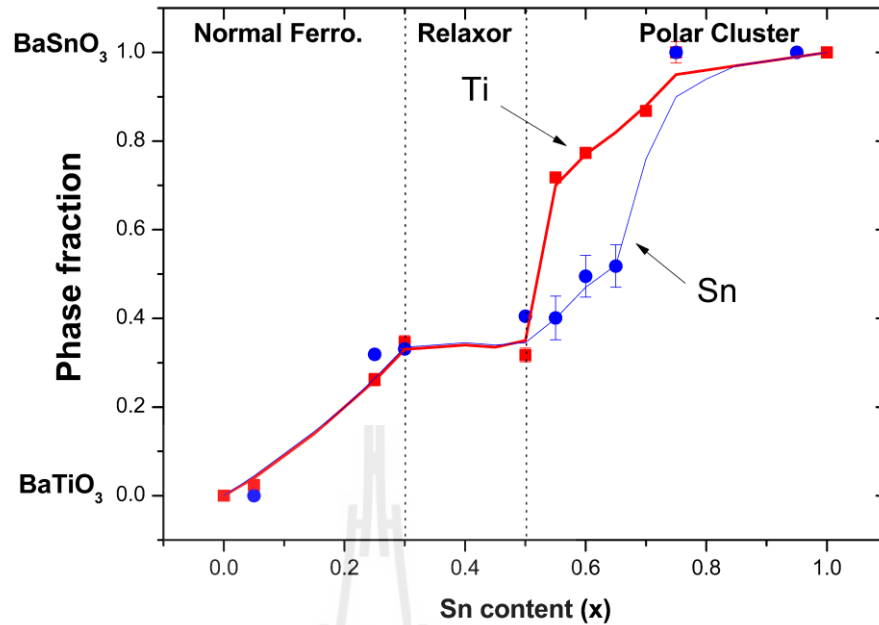
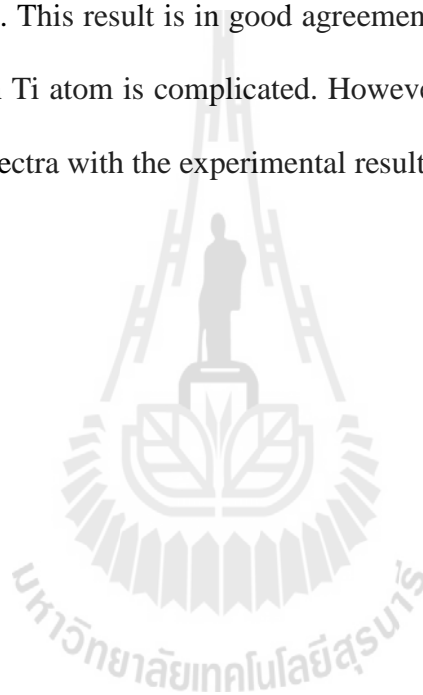


Figure 5.9 The phase fraction of Sn L_3 -edge XANES spectra and Ti K-edge EXAFS in k-space of $\text{Ba}(\text{Ti}_{1-x}\text{Sn}_x)\text{O}_3$ crystals.

The XANES spectra were calculated by FEFF8.2 program. The Ti K -edge XANES spectra in $\text{Ba}(\text{Ti},\text{Sn})\text{O}_3$ pseudo-cubic perovskite and $\text{Ba}(\text{Ti},\text{Sn})\text{O}_3$ perfect cubic perovskite. The full multiple scattering were calculated based on ab initio overlapping muffin-tin potentials. The exchange-correlation functions used in FEFF codes are Hedin-Lundqvist potential (Hedin and Lundqvist, 1970; Rehr and Albers, 2000). To simulate XANES spectra of Ti K -edge, the structural models consist of Ti-off center in rhombohedral perovskite structure ($\alpha=\beta=\gamma=89.98$) or pseudo-cubic symmetry, tetragonal perovskite, rhombohedral perovskite ($\alpha=\beta=\gamma=89.96$) and the pseudo-cubic with almost perfect cubic symmetry ($\alpha=\beta=\gamma=89.99$) structural model with Ti moving to the center (similar to models in Figure. 4.9). The self-consistent field was calculated in sphere radius of 4.2 Å and 4.3 Å for pseudo-cubic, tetragonal, rhombohedral and perfect cubic structure around the absorber Ti K -edge in the

system, respectively, and the full multiple scattering was performed within a larger cluster radius of 7.0 Å. The simulated and experimental results can then be compared. Figure 5.10 shows the comparison between the simulated spectra of Ti *K*-edge XANES spectra of BST with the different structural models. The results of calculation indicate the phase transition between the rhombohedral to perfect cubic which corresponds with the phase transition from relaxor to polar cluster as shown in the black line and red line. This result is in good agreement with some peaks because the electronic transition in Ti atom is complicated. However, we can confirm Sn L_3 -edge simulation XANES spectra with the experimental result.



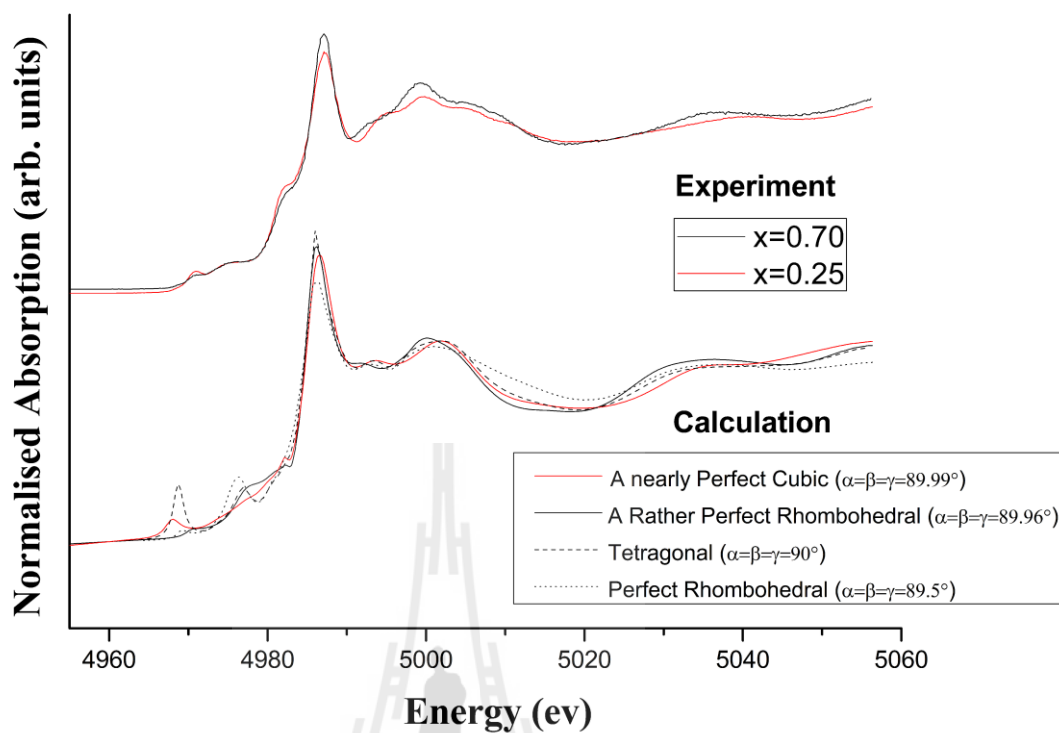


Figure 5.10 Comparison of normalized X-ray absorption Ti K-edge spectra of $\text{Ba}(\text{Sn}_x\text{Ti}_{1-x})\text{O}_3$ ($x=0.25$ and 0.75), with the simulated features of Ti K-edge XANES spectra of $\text{Ba}(\text{Sn},\text{Ti})\text{O}_3$ -a nearly perfect cubic (red-line), a rather perfect rhombohedral (black line), tetragonal (dash-line) and perfect rhombohedral (dot-line).

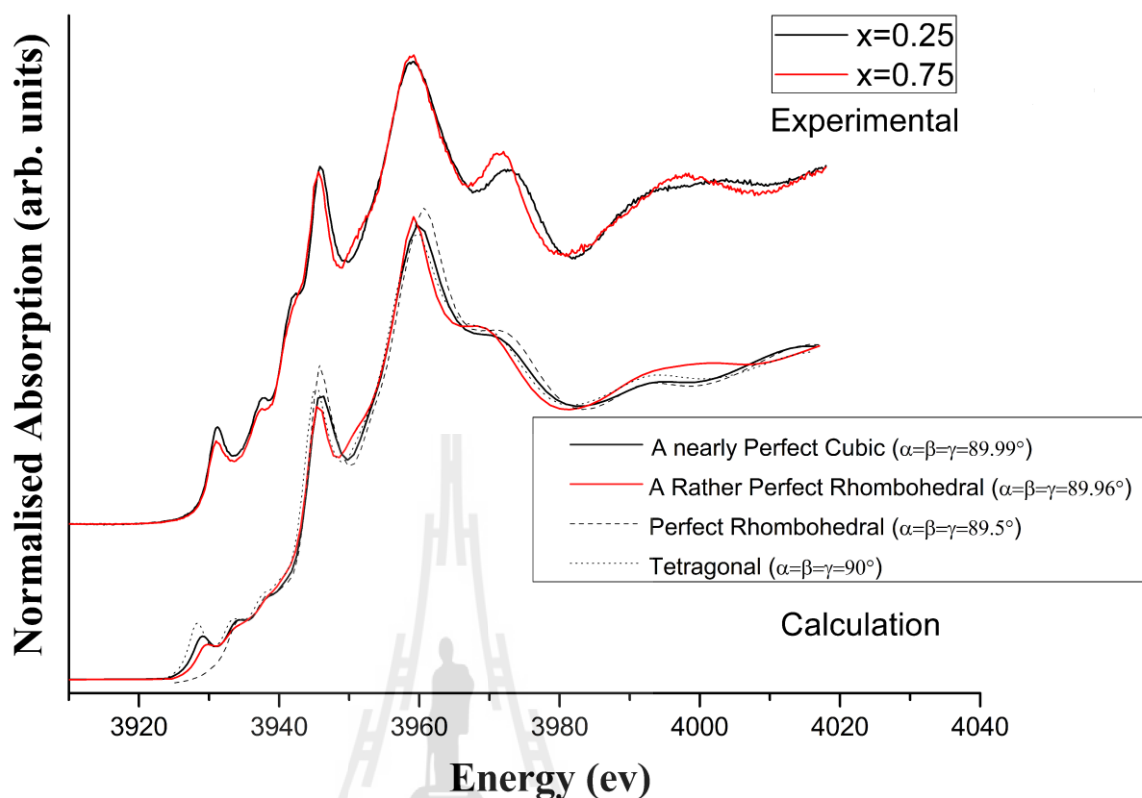


Figure 5.11 Comparison of normalized X-ray absorption Sn L_3 -edge spectra of $\text{Ba}(\text{Sn}_x\text{Ti}_{1-x})\text{O}_3$ ($x=0.25$ and 0.75), with the simulated features of Sn L_3 -edge XANES spectra of $\text{Ba}(\text{Sn},\text{Ti})\text{O}_3$ -a nearly perfect cubic (red-line), a rather perfect rhombohedral (black line), tetragonal (dash-line) and perfect rhombohedral (dot-line).

To simulate Sn L_3 -edge XANES spectra, the structural models were calculated in all cases, similar to the Ti XANES spectra. The self-consistent field was calculated in sphere radius of 4.2 Å and 4.3 Å for pseudo-cubic, tetragonal, rhombohedral and perfect cubic structure around the absorber Ti K -edge in the system, respectively and the full multiple scattering was performed within a larger cluster radius of 7.0 Å. Figure 5.11 shows the comparisons of the simulated and experimental results for Sn

L_3 -edge XANES spectra. $Ba(Ti,Sn)O_3$ -rather perfect rhombohedral and nearly perfect-cubic $Ba(Ti,Sn)O_3$ show very good agreement with the experimental XANES spectra for representative compositions. This excellent agreement between the experimental and simulated spectra means that in the $Ba(Ti,Sn)O_3$ compositions with lower Sn contents the local structure around Ti atom is in the pseudo-cubic symmetry (or almost rhombohedral), even though the XRD results exhibit the broad peaks of (*global*) cubic perovskite structure. This is also in good agreement with the electrical properties because at $x \leq 0.55$ $Ba(Ti_{1-x}Sn_x)O_3$ ceramics still exhibit ferroelectric characteristics with spontaneous polarization from *local* ionic distortion of Ti atoms. On the other hand, when $x > 0.5$, $Ba(Ti_{1-x}Sn_x)O_3$ ceramics show a polar cluster behavior with very small *local* spontaneous polarization; hence the structure is close to perfect cubic perovskite, as observed in both XAS and XRD measurements.

5.5 EXAFS results

The normalized absorption Ti K-edge EXAFS spectra show the phase transition corresponding with XANES results at $x = 0.05-0.25$ and $x = 0.5-0.55$, as shown in Figure. 5.12. To process and enhance the EXAFS with the high k region, the plot $k^2X(k)$ is considered and windowed using a Hanning window $W(k)$. The EXAFS spectra were processed, information on local structure of Ti atom. In this work, the Ti K-edge EXAFS spectra can only be obtained up to photon energy of 250 eV above the absorption edge, due to the presence of Ba L_3 -edge. Therefore, the range of Fourier transform of k space was limited to about $k=7.0$, after which the signal became very noisy, as shown in Figure. 5.13. The Fourier transform in R space showed that the features change suddenly around $x=0.5-0.55$ (Figure.5.14), where the phase transition

between relaxor to polar cluster exists. This result can be confirmed by the XANES and EXAFS.

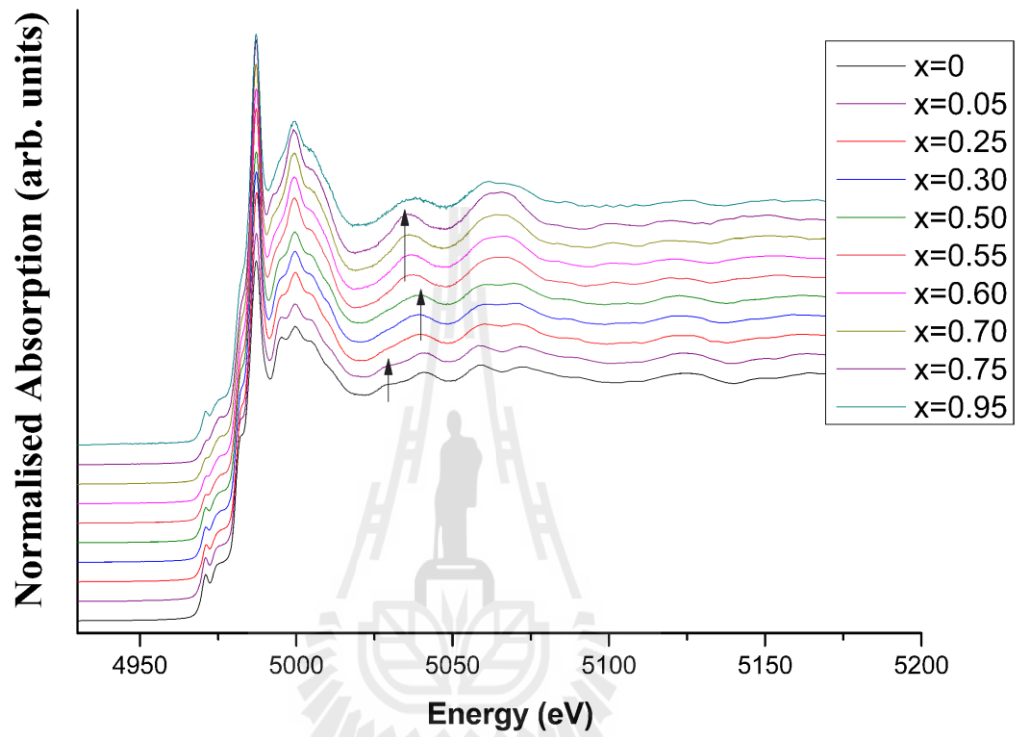


Figure 5.12 The normalized EXAFS signal of Ba(Ti,Sn)O₃ powders.

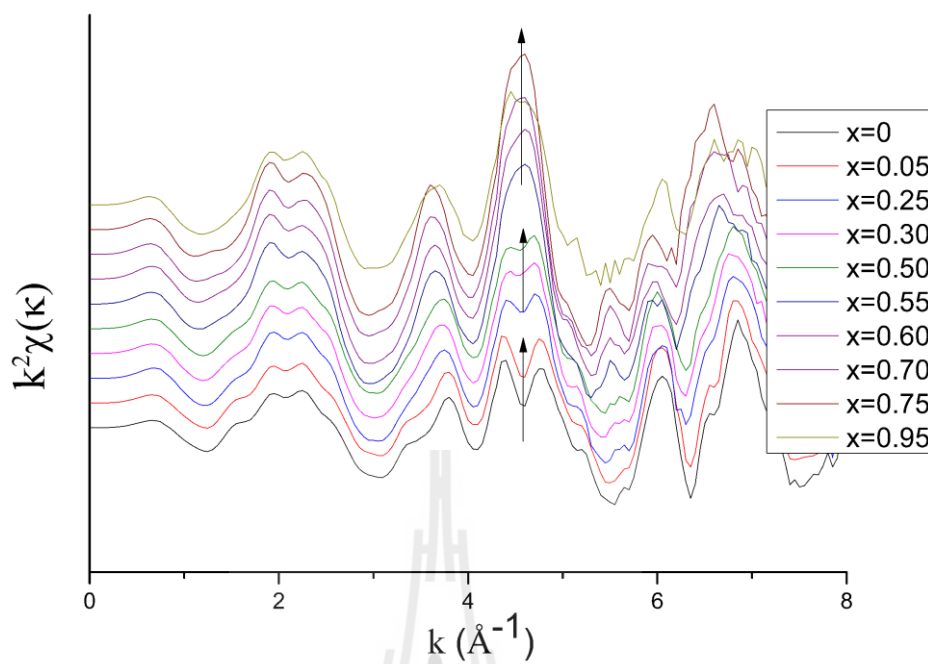


Figure 5.13 The EXAFS Fourier transform in k-space of Ba(Ti,Sn)O₃ powders.

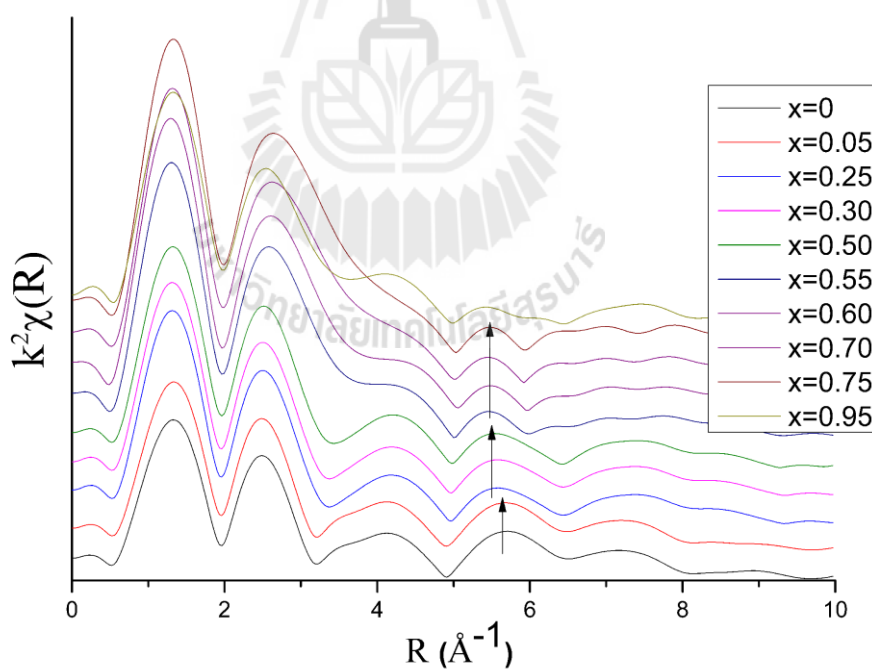


Figure 5.14 The EXAFS Fourier transform in R-space of Ba(Ti,Sn)O₃ powders.

5.6 Dielectric permittivity

The dielectric constant and dielectric loss tangent ($\tan \delta$) at various frequencies for $\text{Ba}(\text{Ti},\text{Sn})\text{O}_3$ compositions, with $x=0, 0.05, 0.25, 0.30, 0.50, 0.55, 0.60, 0.70, 0.75, 0.90$ and 0.95 , are shown in Figure 5.15. The composition with $x = 0.05$ exhibits a normal ferroelectric behavior and sharp peak of dielectric constant as a function of temperature is observed. At $x=0.25$, the relaxor behavior and the broad peaks of dielectric constant as a function temperature start. A strong frequency dispersion is observed around the ϵ' and $\tan \delta$ peaks for $x \geq 0.30$ compositions or so called “relaxor” like behavior. However, at $x \geq 0.55$, it exhibits polar cluster behavior and the dielectric constant is dropping with insignificant frequency dispersion in polar cluster region. With the increase in frequency, ϵ' decreases and the temperatures at which the maximum dielectric constant (T_m) shift to higher temperatures. In contrast, the dielectric loss tangent is decreasing while the frequencies decreases, and similarly, the temperature where the maximum dielectric loss is shifted to higher temperatures. Furthermore, the dielectric constants decrease refer to the composition with x increases. But the dielectric loss tangent increases until $x=0.50$, after then there are only a little change.

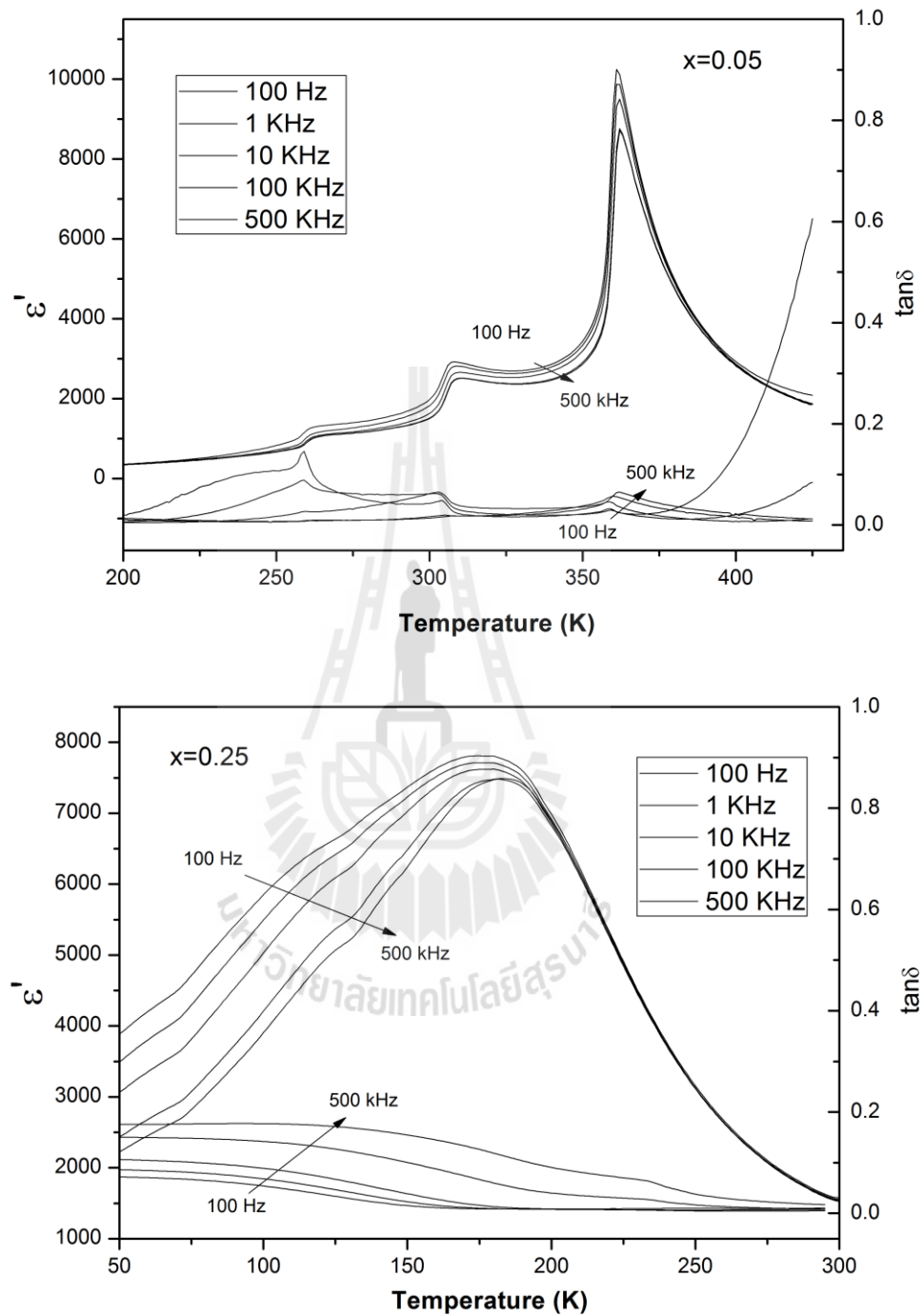


Figure 5.15 Temperature dependence of dielectric constant and loss tangent ($\tan \delta$) at various frequencies for $\text{Ba}(\text{Ti},\text{Sn})\text{O}_3$ (Arrows indicate the direction of increasing frequency).

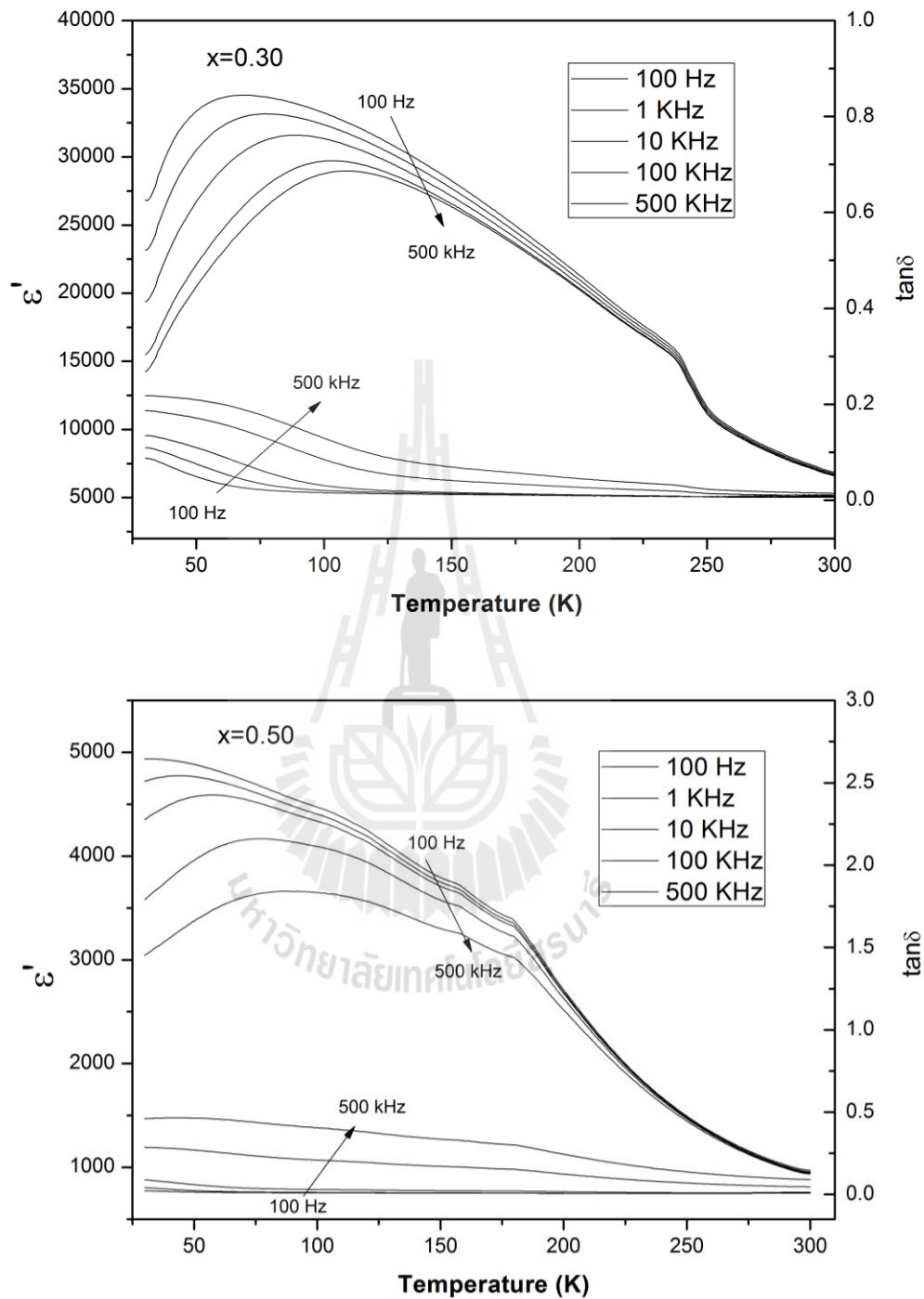


Figure 5.15 (Continued) Temperature dependence of dielectric constant and loss tangent ($\tan \delta$) at various frequencies for $\text{Ba}(\text{Ti},\text{Sn})\text{O}_3$ (Arrows indicate the direction of increasing frequency).

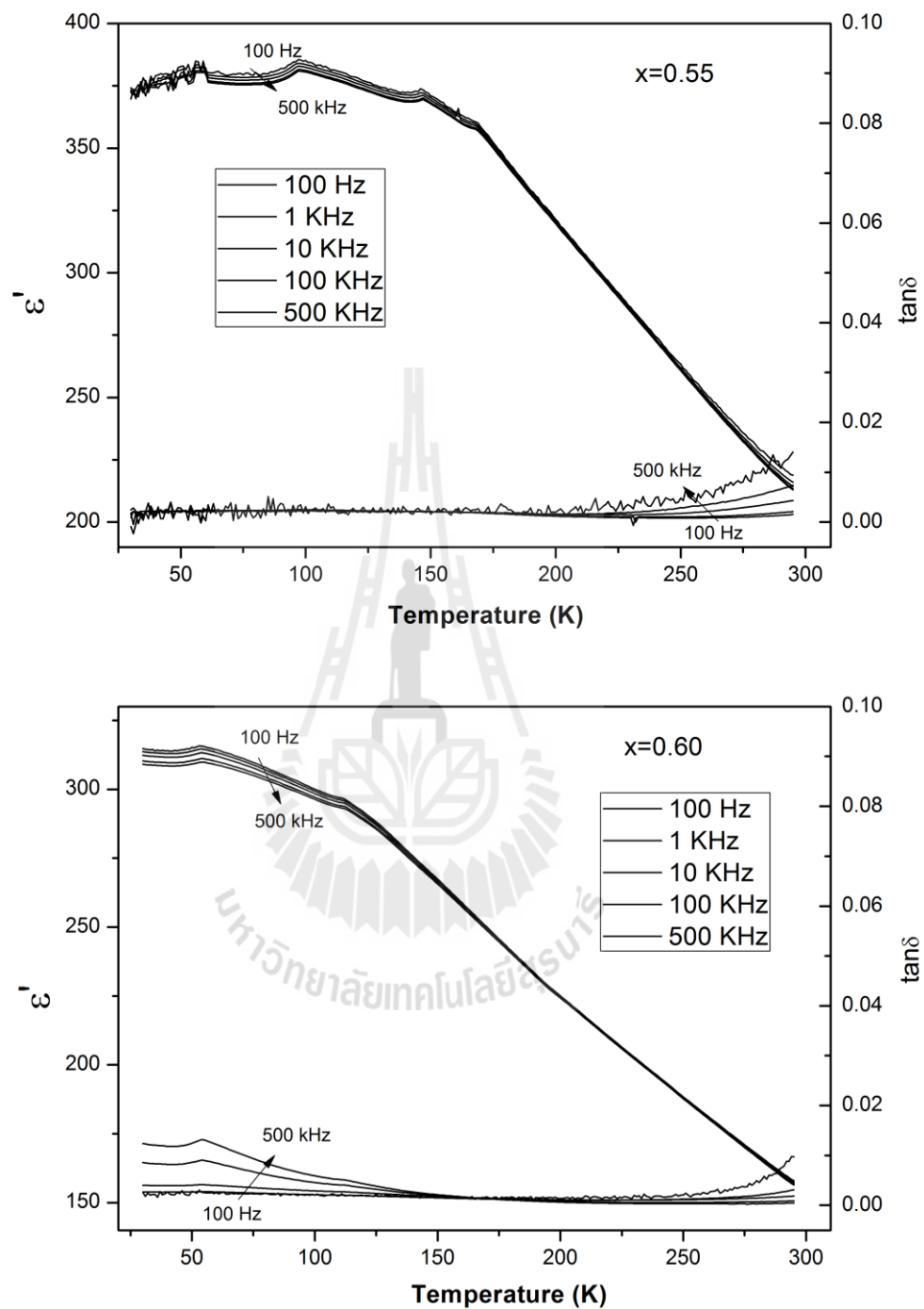


Figure 5.15 (Continued) Temperature dependence of dielectric constant and loss tangent ($\tan \delta$) at various frequencies for $\text{Ba}(\text{Ti},\text{Sn})\text{O}_3$ (Arrows indicate the direction of increasing frequency).

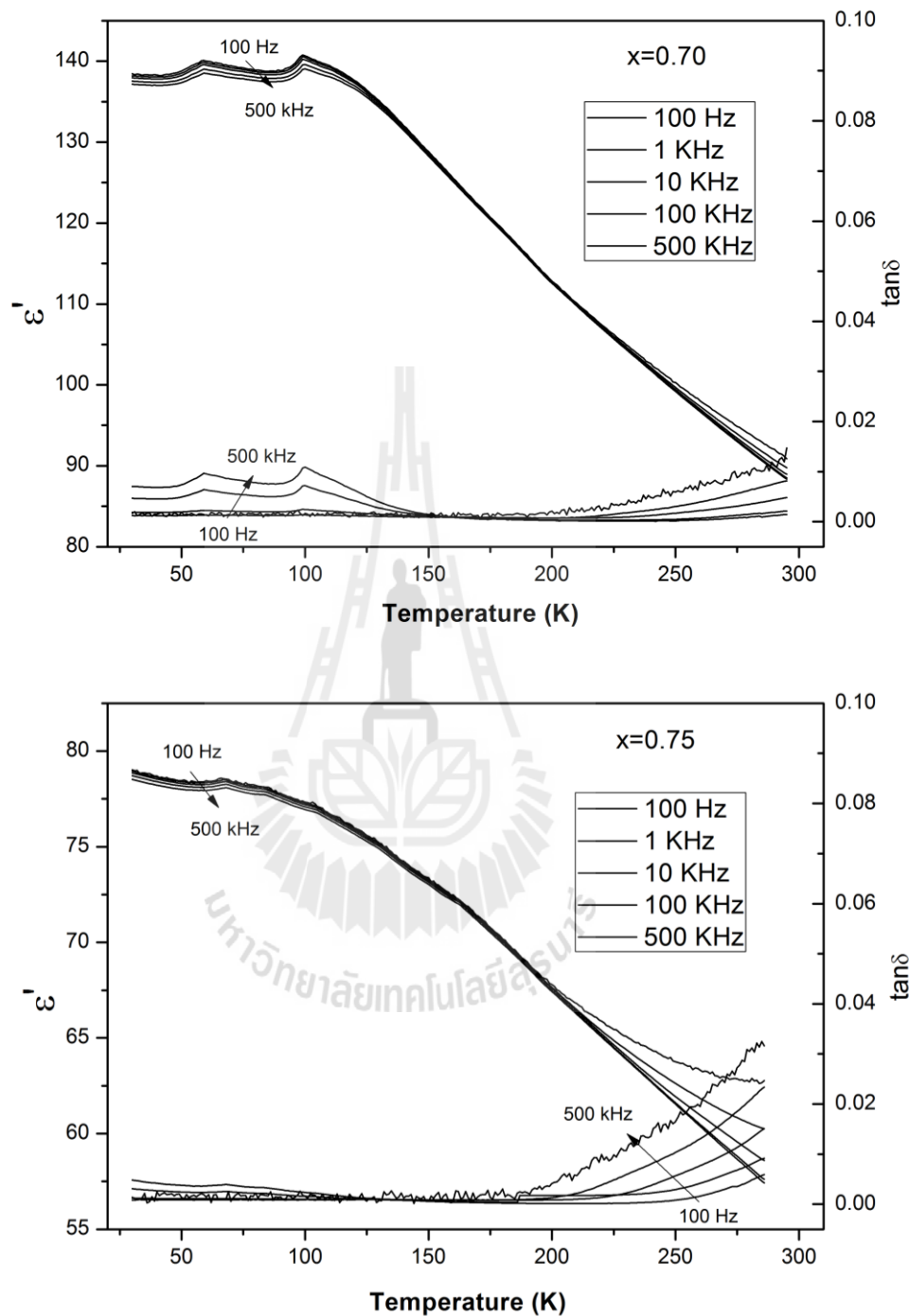


Figure 5.15 (Continued) Temperature dependence of dielectric constant and loss tangent ($\tan \delta$) at various frequencies for $\text{Ba}(\text{Ti},\text{Sn})\text{O}_3$ (Arrows indicate the direction of increasing frequency).

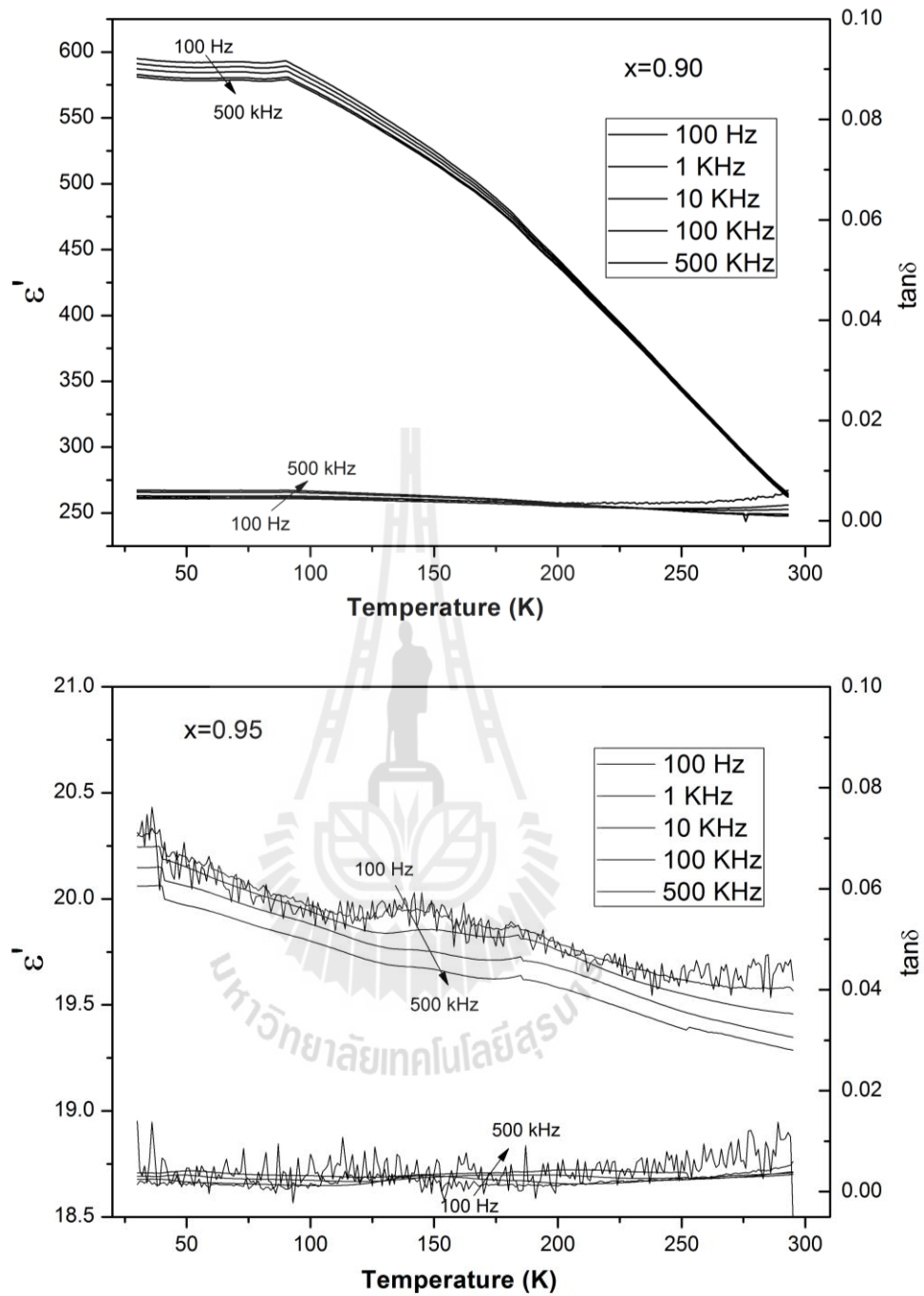


Figure 5.15 (Continued) Temperature dependence of dielectric constant and loss tangent ($\tan \delta$) at various frequencies for $\text{Ba}(\text{Ti},\text{Sn})\text{O}_3$ (Arrows indicate the direction of increasing frequency).

The Curie-Weiss law can explain a normal ferroelectric in the paraelectric region follow by Eq. (2.64). Figure 5.16 shows the inverse dielectric constant as a function of temperature at 100 KHz. The linear fitting is observed in the paraelectric region or high temperature for all compositions. The fitting parameters of Curie-Weiss constant and Curie temperature as calculated are shown in Table 5.1 (Maiti *et al.*, 2006). The results show that the Curie temperature decreases while the composition x increases. It is evident from the value of T_C that the compositions $x=0.05-0.08$ show the normal ferroelectrics behavior. However, the values of T_C indicate nearly the relaxor behavior for $x=0.25-0.50$. Furthermore, the relaxor ferroelectric behavior in the high temperature region follows a modified Curie-Weiss law from Eq. (2.65). The value of δ_γ represents the degree of diffuseness for transition peaks. Both γ and δ_γ are determined from the slope and intercept $\ln(\epsilon'_{max}/\epsilon')$ versus $\ln(T - T_m)$, as shown in Figure 5.16 for $x=0, 0.05, 0.25, 0.30, 0.50, 0.55, 0.60, 0.70, 0.75, 0.90$ and 0.95 (Huang, 2008). In the Table 5.2, the value of γ indicates the relaxor behavior. For $x = 0.25-0.50$, the compositions exhibit the relaxor behavior until $x=0.55$, close to the ideal relaxor ferroelectric ($\gamma=2$). For $x \geq 0.55$, the value of γ decreases nearly showing the normal ferroelectric behavior. The value of δ_γ also increases because of the increasing relaxation.

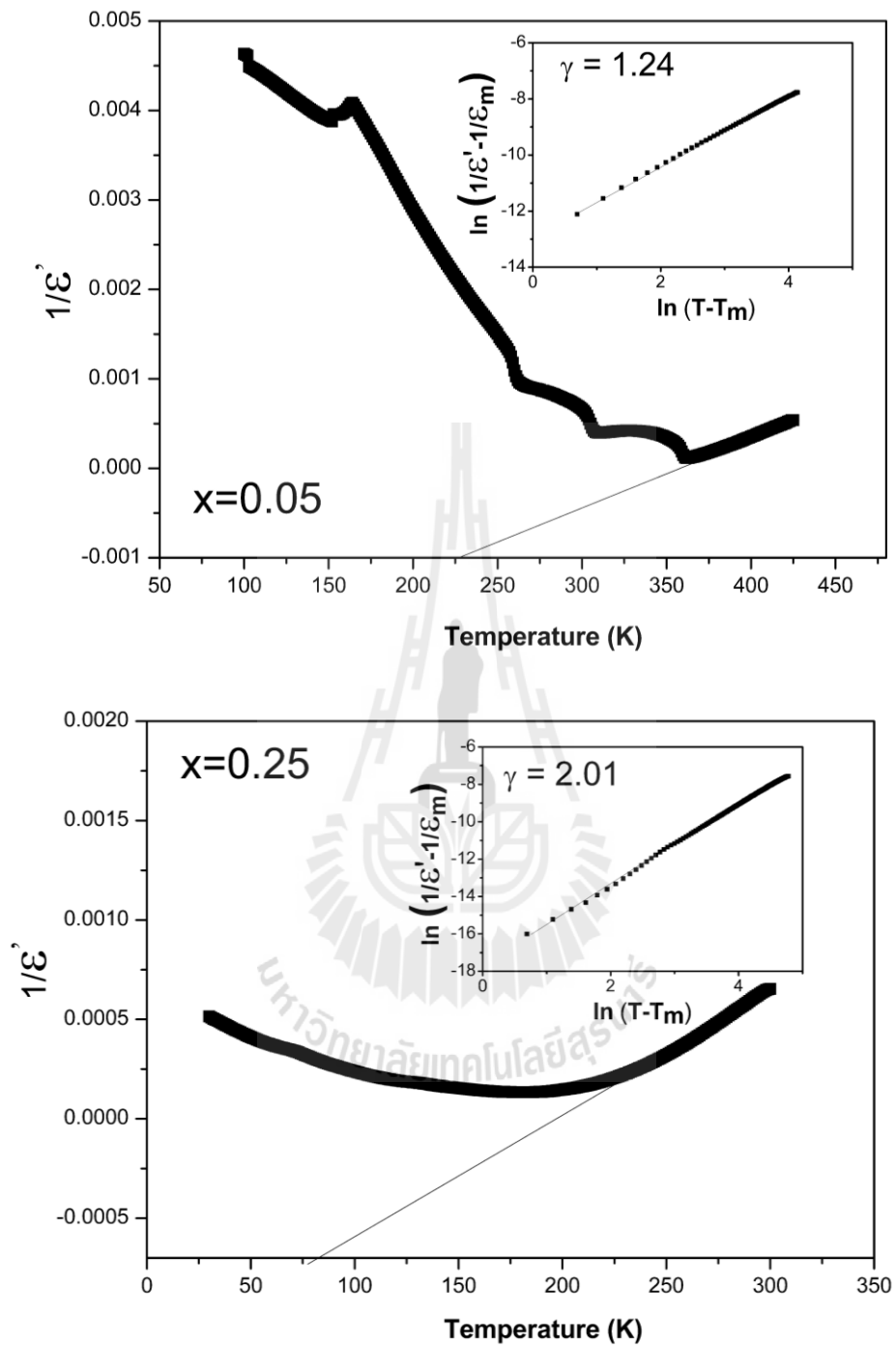


Figure 5.16 The inverse dielectric constant $1/\epsilon$ as a function of temperature at 100 kHz for $\text{Ba}(\text{Ti},\text{Sn})\text{O}_3$ symbols denote experimental data and solid line denotes fitting to the Curie-Weiss law. The insets show the plot of $\ln(1/\epsilon - 1/\epsilon_m)$ vs $\ln(T - T_m)$ for $\text{Ba}(\text{Ti},\text{Sn})\text{O}_3$ ceramics.

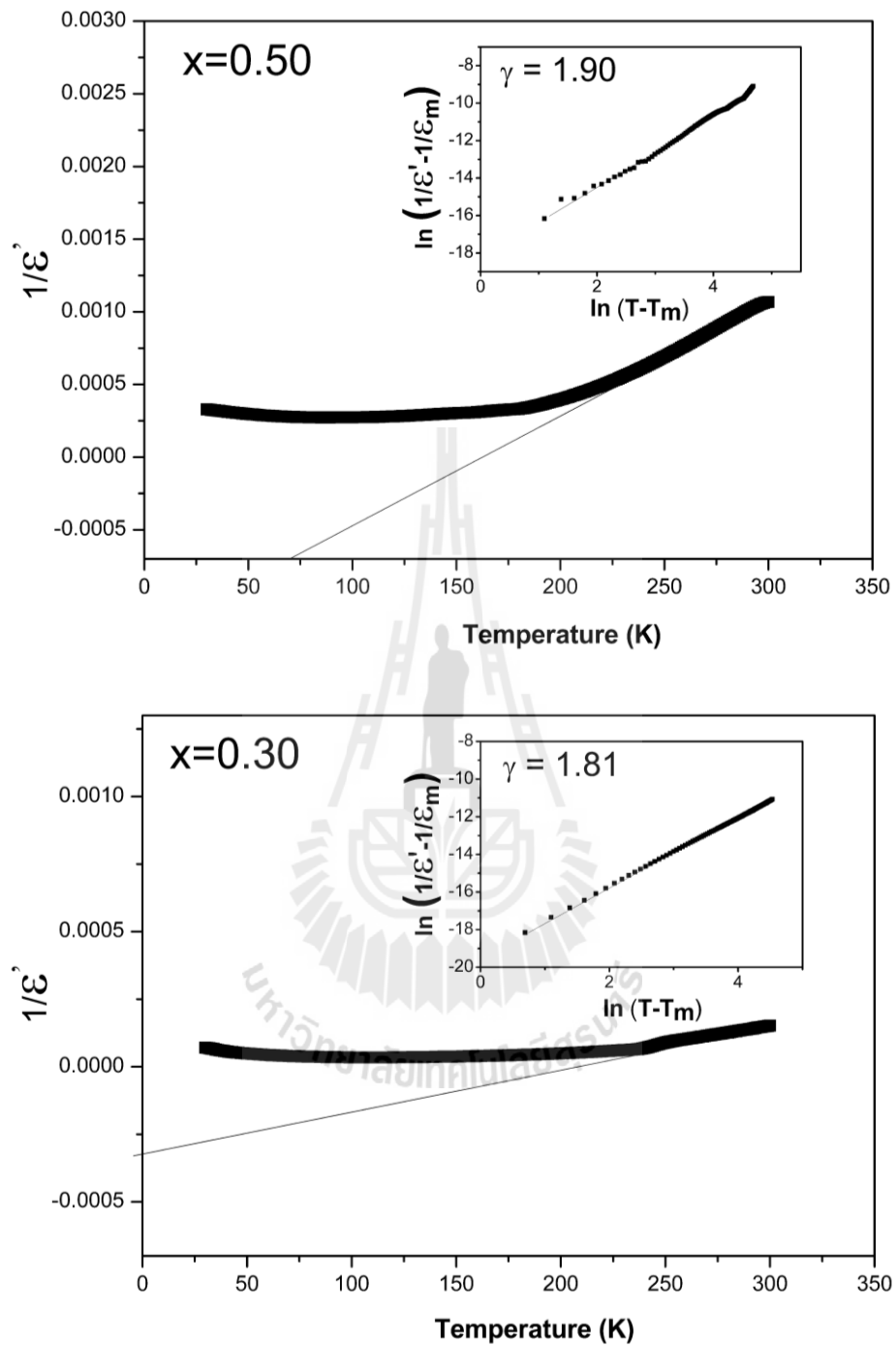


Figure 5.16 (Continued) The inverse dielectric constant $1/\epsilon$ as a function of temperature at 100 kHz for $\text{Ba}(\text{Ti},\text{Sn})\text{O}_3$ symbols denote experimental data and solid line denotes fitting to the Curie-Weiss law. The insets show the plot of $\ln(1/\epsilon - 1/\epsilon_m)$ vs $\ln(T - T_m)$ for $\text{Ba}(\text{Ti},\text{Sn})\text{O}_3$ ceramics.

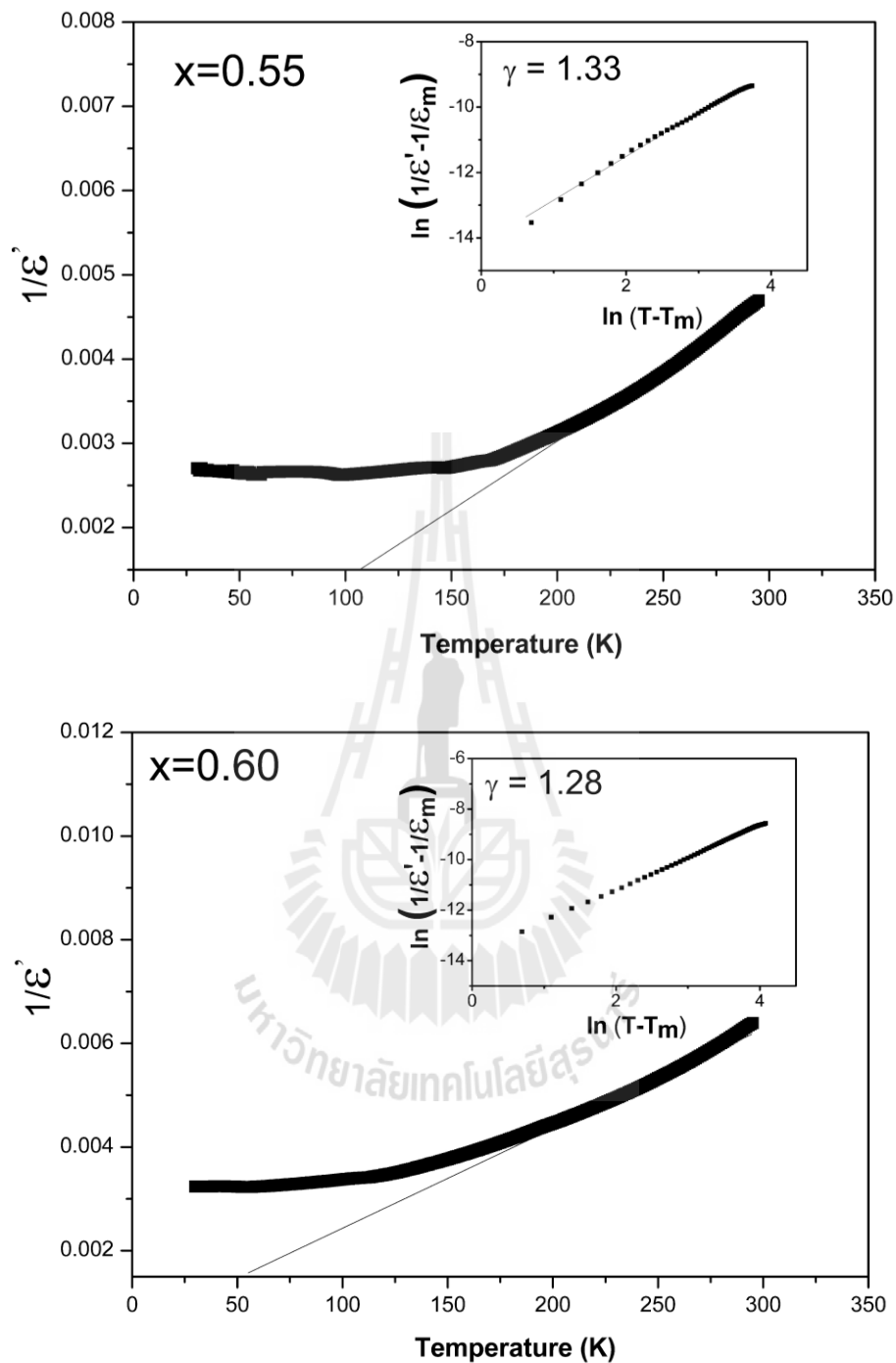


Figure 5.16 (Continued) The inverse dielectric constant $1/\epsilon$ as a function of temperature at 100 kHz for $\text{Ba}(\text{Ti},\text{Sn})\text{O}_3$ symbols denote experimental data and solid line denotes fitting to the Curie-Weiss law. The insets show the plot of $\ln(1/\epsilon - 1/\epsilon_m)$ vs $\ln(T - T_m)$ for $\text{Ba}(\text{Ti},\text{Sn})\text{O}_3$ ceramics.

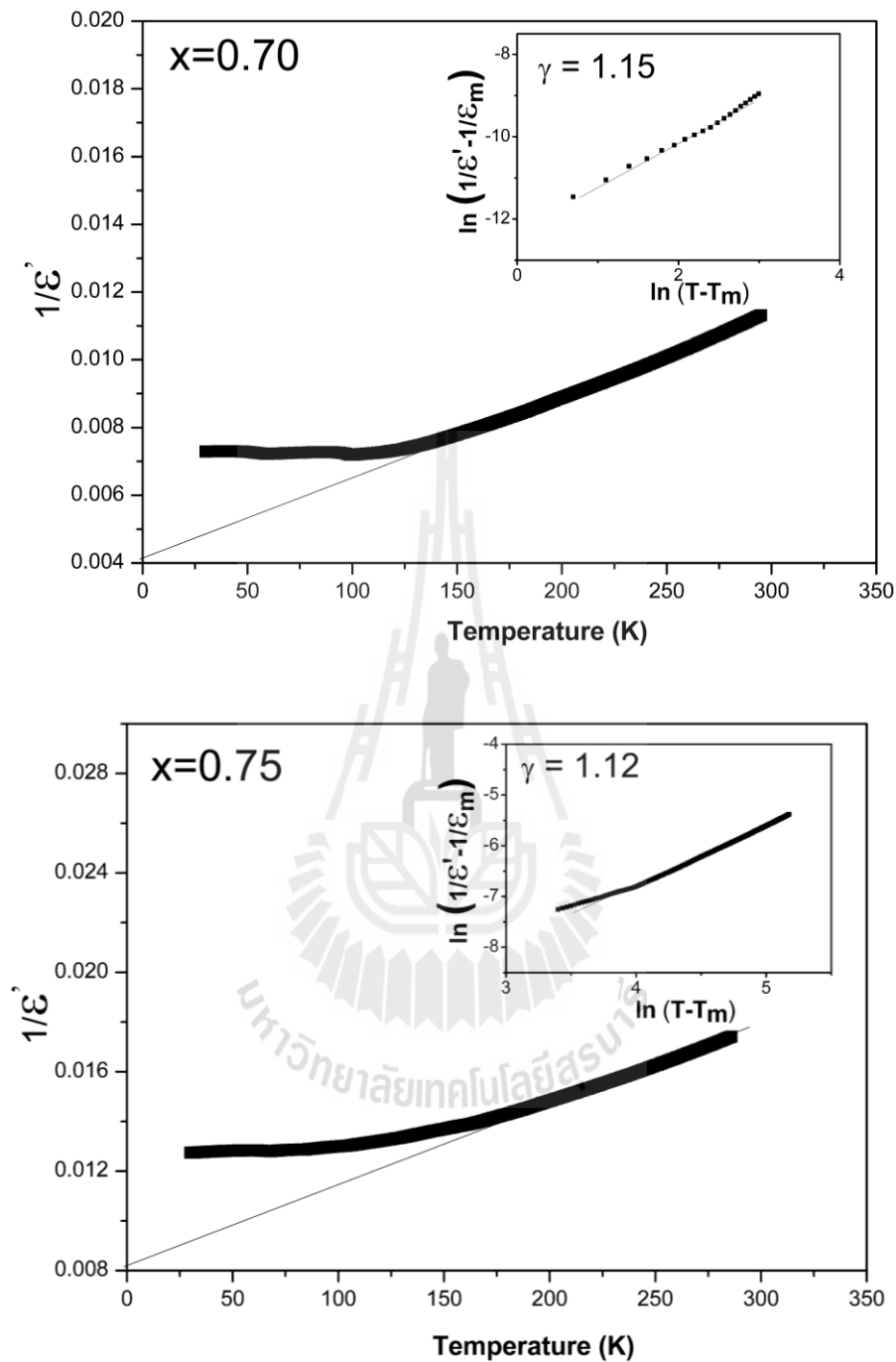


Figure 5.16 (Continued) The inverse dielectric constant $1/\epsilon$ as a function of temperature at 100 kHz for $\text{Ba}(\text{Ti},\text{Sn})\text{O}_3$ symbols denote experimental data and solid line denotes fitting to the Curie-Weiss law. The insets show the plot of $\ln(1/\epsilon - 1/\epsilon_m)$ vs $\ln(T - T_m)$ for $\text{Ba}(\text{Ti},\text{Sn})\text{O}_3$ ceramics.

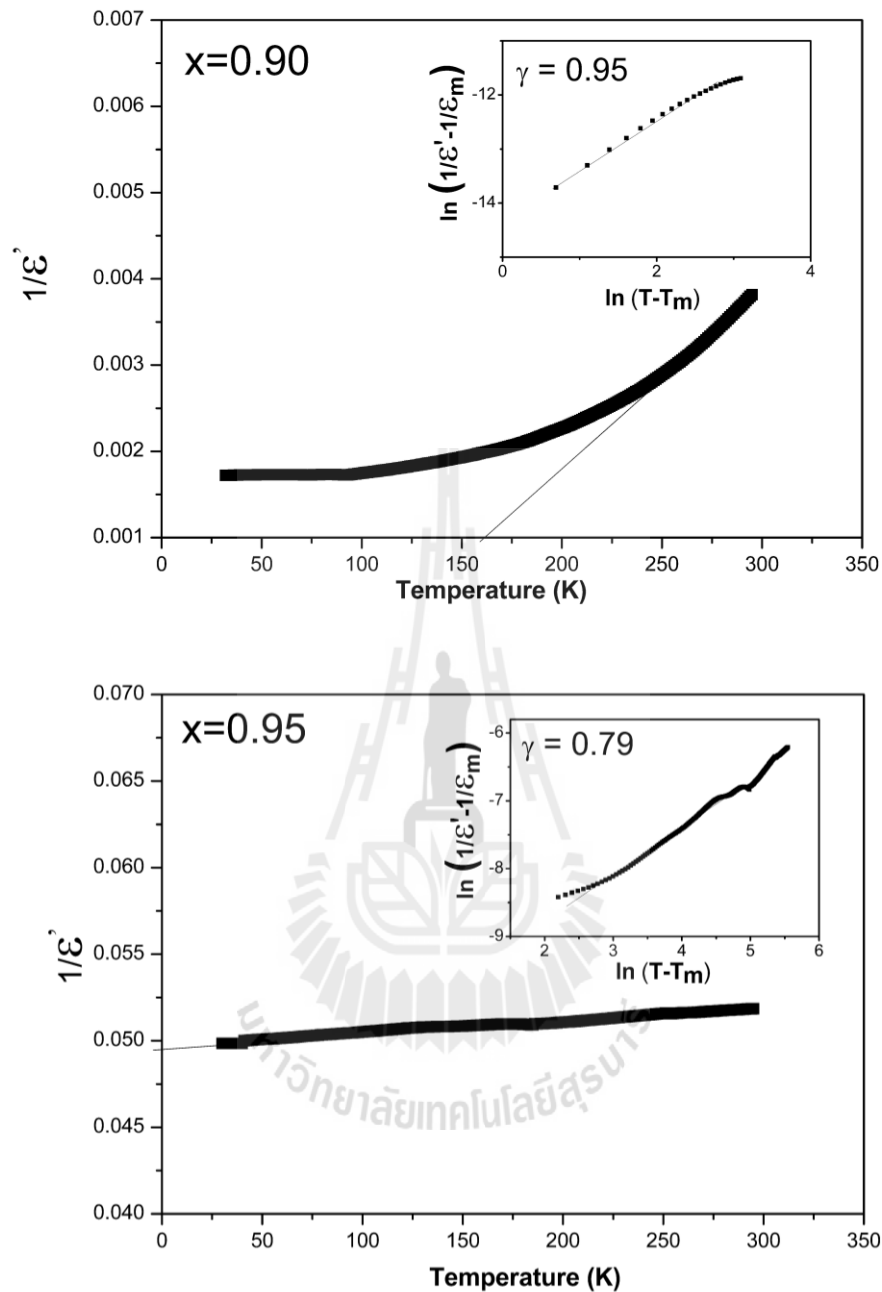


Figure 5.16 (Continued) The inverse dielectric constant $1/\epsilon$ as a function of temperature at 100 kHz for $\text{Ba}(\text{Ti},\text{Sn})\text{O}_3$ symbols denote experimental data and solid line denotes fitting to the Curie-Weiss law. The insets show the plot of $\ln(1/\epsilon - 1/\epsilon_m)$ vs $\ln(T - T_m)$ for $\text{Ba}(\text{Ti},\text{Sn})\text{O}_3$ ceramics.

Table 5.1 Calculated Curie constant and measured T_c from dielectric properties of Ba(Ti,Sn)O₃ compositions.

Composition	C (K)	T_c (K)
x=0.05	1.37×10^5	351.21
x=0.25	1.59×10^5	197.62
x=0.30	8.20×10^5	175.75
x=0.50	1.31×10^5	158.89
x=0.55	5.67×10^4	30.49
x=0.60	4.94×10^4	-15.53
x=0.70	4.08×10^4	-162.64
x=0.75	3.23×10^4	-309.89
x=0.90	4.80×10^4	113.27
x=0.95	1.33×10^5	-6591.76

Table 5.2 Degree of Relaxation γ , dielectric maxima Temperature and diffusivity of Ba(Ti,Sn)O₃ compositions.

Composition	γ	T_m (K)	δ_γ
x=0.05	1.24	362	12.05
x=0.25	2.01	181	41.98
x=0.30	1.81	109	99.68
x=0.50	1.90	89	139.27
x=0.55	1.33	34	59.46
x=0.60	1.28	54	302.77
x=0.70	1.15	100	365.68
x=0.75	1.12	68	278.85
x=0.90	0.95	32	4888.72
x=0.95	0.79	38	6491.52

5.7 Hysteresis

The polarization hysteresis data at room temperature for $\text{Ba}(\text{Ti},\text{Sn})\text{O}_3$ are shown in Figure 5.17. The characteristic of hysteresis loop showed the ferroelectric properties at $x = 0.05$. The area of hysteresis loop decreases to the slim loop of ferroelectric properties around $0.25 \leq x \leq 0.70$. When $0.25 \leq x \leq 0.50$, the hysteresis exhibited relaxor ferroelectric properties. And when $0.75 \leq x \leq 0.95$, the hysteresis exhibited a large dielectric loss which is more of the influence from the microstructure, not the local structure.

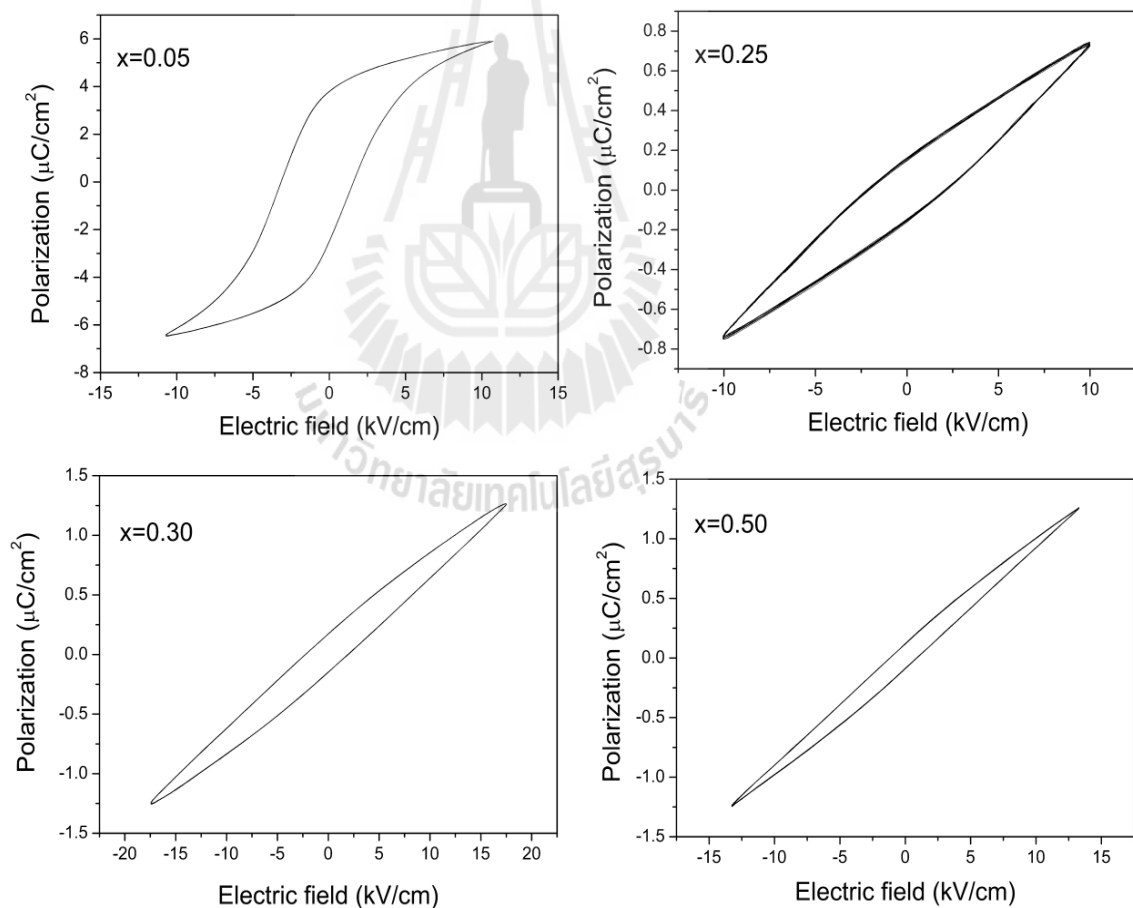


Figure 5.17 *P-E* hysteresis measurements on $\text{Ba}(\text{Sn}_x\text{Ti}_{1-x})\text{O}_3$ ceramics obtained at room temperature.

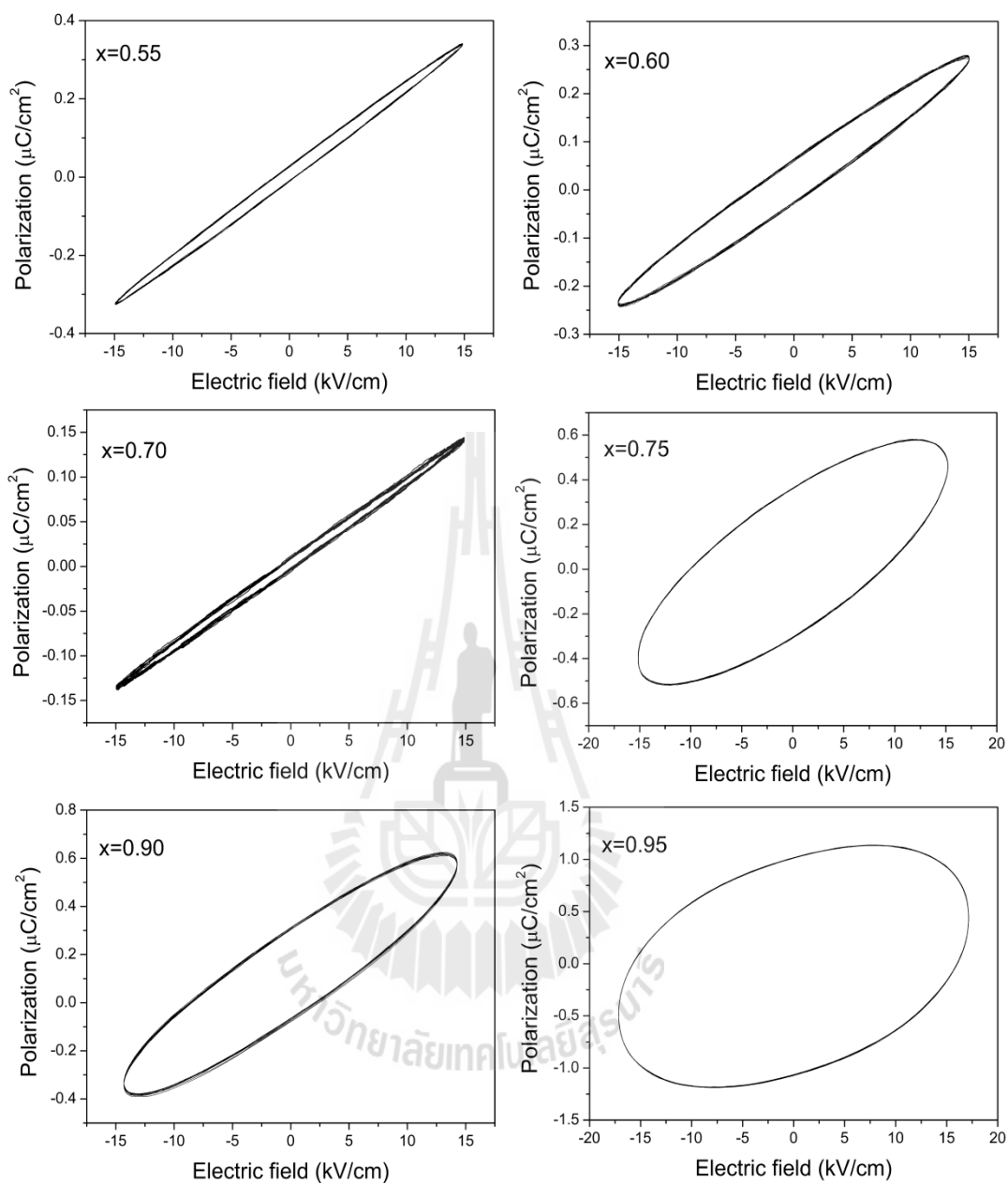


Figure 5.17 (Continued) *P-E* hysteresis measurements on Ba(Sn_xTi_{1-x})O₃ ceramics obtained at room temperature.

5.8 References

- Aydia, A., Khemakhem, H., Boudaya, C., Mühlh, R. V. and Simon, A. (2004). New ferroelectric and relaxor ceramics in the mixed oxide system $\text{NaNbO}_3\text{--BaSnO}_3$. **Sol. Stat. Sci.** 6: 333.
- Cai, W., Fan, Y., Gao, J., Fu, C. and Deng, X. (2011). Microstructure, dielectric properties and diffuse phase transition of barium stannate titanate ceramics. **J. Matt Sci: Matt Elec.** 22: 265.
- Cerneaw, M. and Manea, A. (2007). $\text{Ba}(\text{Ti}_{1-x}\text{Sn}_x)\text{O}_3$ ($x=0.13$) Dielectric Ceramics Prepared by Coprecipitation. **J. Am. Ceram. Soc.** 90: 1728.
- Hedin, L. and Lundqvist, S. (1970) Effects of Electron-Electron and Electron-Phonon Interactions on the One-Electron States of Solids. In Solid State Physics, Vol. Volume 23 (Eds, Frederick Seitz, D. T. and Henry, E.) Academic Press, pp. 1.
- Huang, C.-C. (2008). **Structure and Piezoelectric Properties of Lead-Free Bismuth-Based Perovskite Solid Solutions**. Oregon State University, Oregon State
- Levin, I., Cockayne, E., Krayzman, V., Woicik, J. C., Lee, S. and Randall, C. A. (2011). Local structure of $\text{Ba}(\text{Ti,Zr})\text{O}_3$ perovskite-like solid solutions and its relation to the band-gap behavior. **Phys. Rev. B.** 83: 094122.
- Levin, I., Krayzman, V. and Woicik, J. C. (2013). Local-structure origins of the sustained Curie temperature in $(\text{Ba,Ca})\text{TiO}_3$ ferroelectrics. **Appl. Phys. Lett.** 102: 162906.
- Maiti, T., Guo, R. and Bhalla, A. S. (2006). The evolution of relaxor behavior in Ti^{4+} doped BaZrO_3 ceramics. **J. Appl. Phys.** 100: 114109.

- Maiti, T., Guo, R. and Bhalla, A. S. (2008). Structure-Property Phase Diagram of $\text{BaZr}_x\text{Ti}_{1-x}\text{O}_3$ System. **J. Am. Ceram. Soc.** 91: 1769.
- Rehr, J. J. and Albers, R. C. (2000). Theoretical approaches to x-ray absorption fine structure. **Rev. Mod. Phys.** 72: 3.
- Vedrinskii, R. V., Kraizman, V. L., Novakovich, A. A., Demekhin, P. V. and Urazhdin, S. V. (1998). Pre-edge fine structure of the 3d atom K x-ray absorption spectra and quantitative atomic structure determinations for ferroelectric perovskite structure crystals. **J. Phys. Condens. Matter.** 10: 9561.
- Wei, X., Feng, Y., Hang, L. and Yao, X. (2004). Dielectric properties of barium stannate titanate ceramics under bias field. **Ceram. Int.** 30: 1401.
- Wei, X., Feng, Y., Wan, X. and Yao, X. (2004). Evolvement of dielectric relaxation of barium stannate titanate ceramics. **Ceram. Int.** 30: 1397.
- Wei, X. and Yao, X. (2007). Preparation, structure and dielectric property of barium stannate titanate ceramics. **Matt. Sci. Eng. B.** 137: 184.
- Yun Liua, R., Withersa, L., Weib, X. and Gerald, J. D. F. (2007). Structured diffuse scattering and polar nano-regions in the $\text{Ba}(\text{Ti}_{1-x}\text{Sn}_x)\text{O}_3$ relaxor ferroelectric system. **J. Sol. Stat. Chem.** 180: 858.

CHAPTER VI

STUDY OF PHASE INFORMATION AND DIELECTRIC PROPERTIES IN BARIUM TITANATE - BISMUTH ZINC TITANATE

6.1 Introduction

Recently, it has been found that $\text{BaTiO}_3\text{-Bi}(\text{Me})\text{O}_3$ (Me can be either a single trivalent cation or two cations with an average valence of +3 and occupy the octahedral sites) perovskites have high Curie transition temperature and excellent piezoelectric properties (Eitel *et al.*, 2001; Stringer *et al.*, 2006). Moreover, they are lead-free piezoelectric materials which are attractive due to the environmental concerns because of their environmental friendly characteristics.

It has been found that the $(1-x)\text{BaTiO}_3\text{-xBi}(\text{Zn}_{0.5}\text{Ti}_{0.5})\text{O}_3$ (BT-BZnT) compositions with $x = 0$ and 0.1 contain the tetragonal BT phase (Huang and Cann, 2008). For $x > 0.1$, those showed the rhombohedral or pseudo-cubic phase perovskite and also exhibit relaxor ferroelectrics like behavior. However, the exact MPB composition is difficult to determine. Although, the conventional study based on a typical X-ray Diffraction (XRD) measurement can show a strong global symmetry change, but cannot relate directly to the drastic change in the electrical properties. Interestingly, the X-ray Absorption Spectroscopy (XAS) technique can be used to investigate the local structure in various materials (Ravel *et al.*, 1998). The phase

transition of local structure can be pointed out which leads to the drastic change in the dielectric properties.

In this work, we focused our studies on the transition of global structure by XRD technique and probed the local structure information around the ferroelectrically-active Ti atom in BT-BZnT as a function of Bi(Ti,Zn)O₃ concentration, in hope to provide better understanding of how the local structure is related to the evolution of relaxor ferroelectric perovskite.

6.2 Experimental

(1-x)BaTiO₃-xBi(Zn_{0.5}Ti_{0.5})O₃ powders were prepared by our colleagues at Oregon State University, at USA via conventional solid state reaction method. The starting BaCO₃(≥99.9%), TiO₂(≥99.9%), ZnO(≥99%) and Bi₂O₃(≥99.5%) materials were weighed according to the composition (1-x)BaTiO₃-xBi(Zn_{0.5}Ti_{0.5})O₃ with $x = 0.05, 0.06, 0.07, 0.08, 0.09, 0.10, 0.11$ and 0.13 and mixed in ball mill for 24 h using an ethanol medium. After drying, the mixed powders were calcined at temperature of 950 °C for 12 h with 5°C/min heating/cooling rates. Sintering of the pellets was carried out between 1100-1300 °C for 4 h (Huang and Cann, 2008).

The phase formation and global structure of (1-x)BaTiO₃-xBi(Zn_{0.5}Ti_{0.5})O₃ were investigated by XRD patterns scanned in 2θ range of 20°-60° with 0.02° step and CuK_α radiation. The local structure was investigated by XAS measurements conducted at ambient temperature at the BL-8 of the Siam Photon Laboratory, Synchrotron Light Research Institute (SLRI), Thailand, (electron energy of 1.2 GeV, beam current 120-80 mA). The double crystal monochromator Ge(220) was used to monochromatized the X-ray beam for the Ti K-edge. The experiments were performed

in a fluorescence mode and the signals were collected by using the 13-component Ge-detector. XANES spectra for the Ti *K*-edge were measured for all compositions. The data were processed using the ATHENA program (Chandararak *et al.*, 2012).

The silver electrodes were sputtered on the BT-BZT ceramics for dielectric measurement. The HP4284 LCR meter was used to measure the dielectric constant and loss tangent from 100 Hz to 1 MHz in the temperature range of 150-425 K with a cooling rate of 2 K/min.

6.3 X-ray Diffraction

The XRD patterns of $(1-x)\text{BaTiO}_3-x\text{Bi}(\text{Zn}_{0.5}\text{Ti}_{0.5})\text{O}_3$ ceramics are shown in Figure. 6.1(a) for various solid solution compositions when $\text{Bi}(\text{Zn}_{0.5}\text{Ti}_{0.5})\text{O}_3$ added to BaTiO_3 . For $x \leq 0.07$, the peak splitting of the (200) reflection is observed and the tetragonal perovskite ($P4mm$) structure of the sample concluded. The tetragonal structure is decreased, as the BZT content increased, as reflected by the (200) peak splitting shown in Figure. 6.1(b) (Huang and Cann, 2008). For $0.08 \leq x \leq 0.13$, the samples exhibited pseudocubic or rhombohedral structure. The phase transition studies show that at $0.08 \leq x \leq 0.09$ the structure clearly changes from tetragonal to rhombohedral perovskite phases with increasing BZT concentration. The morphotropic phase boundary (MPB) between the tetragonal and rhombohedral phases was observed at a composition close to $x=0.09$. Figure 6.2 shows the lattice constant (solid line) and volume (dot line) as a function of x mol of $\text{Bi}(\text{Zn,Ti})\text{O}_3$. The lattice constant a is increasing and c is decreasing while x mol $\text{Bi}(\text{Zn,Ti})\text{O}_3$ increases until $x = 0.09$, and the lattice constant $a = c$ and phase finally transform into

rhombohedral structure. The unit cell volume is at the highest at $x=0.1$, where it starts showing the real relaxor region.

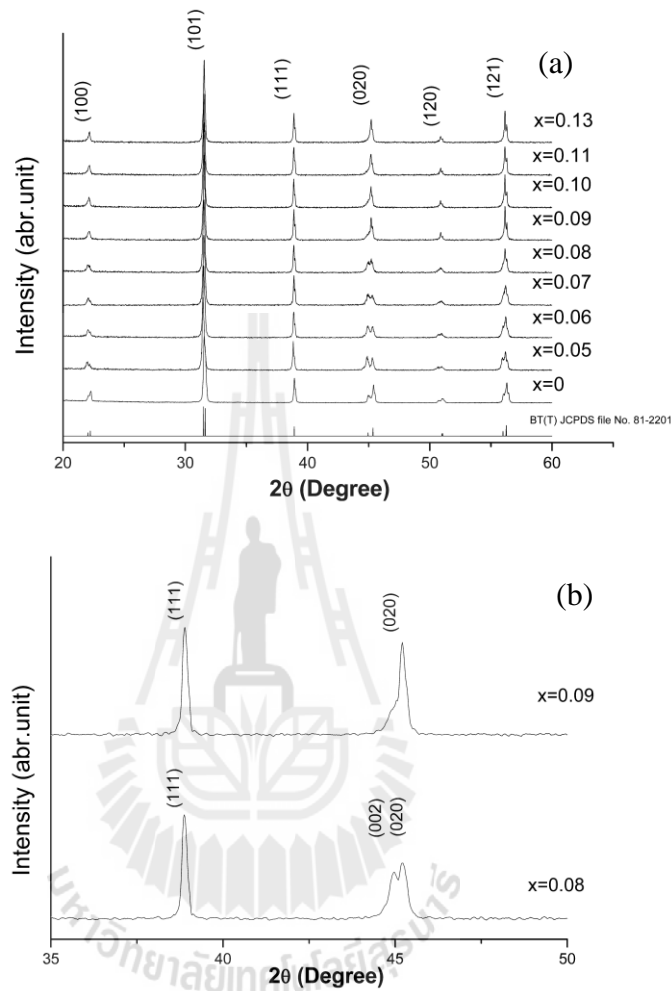


Figure 6.1 X-ray diffraction patterns of $(1-x)\text{BaTiO}_3-x\text{Bi}(\text{Zn}_{0.5}\text{Ti}_{0.5})\text{O}_3$ ceramics (a) all conditions (b) around phase transition $x=0.08$ and 0.09 .

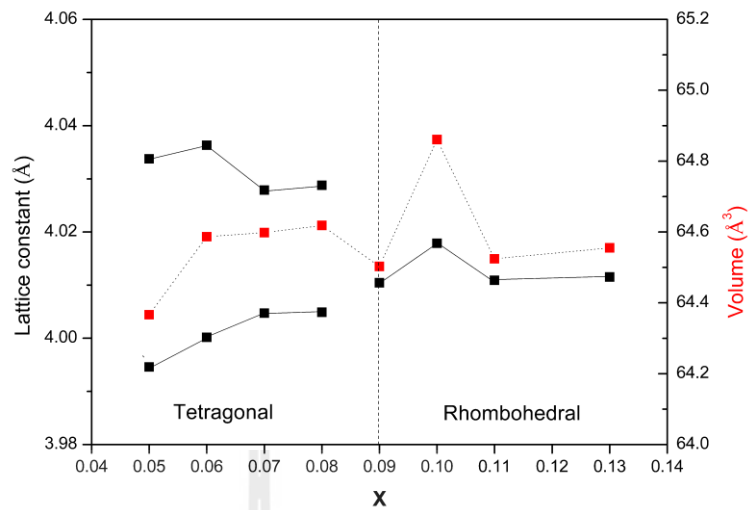


Figure 6.2 The lattice constant and unit cell volume as a function of x content of $(1-x)\text{BaTiO}_3-x\text{Bi}(\text{Zn}_{0.5}\text{Ti}_{0.5})\text{O}_3$ compositions.

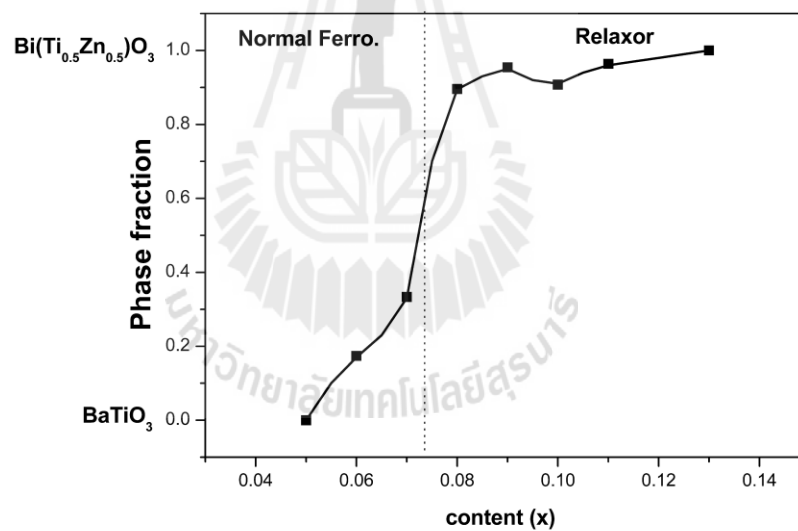


Figure 6.3 The phase fraction of $(1-x)\text{BaTiO}_3-x\text{Bi}(\text{Zn}_{0.5}\text{Ti}_{0.5})\text{O}_3$ from XRD patterns.

In addition, the phase fraction between BaTiO_3 and $\text{Bi}(\text{Zn}_{0.5}\text{Ti}_{0.5})\text{O}_3$ is obtained from linear combination of the integrated intensity of mean peak (110) of XRD patterns. The results show that the phase fraction suddenly increases around

$x=0.07-0.08$ which is corresponding to the phase transition of normal to relaxor ferroelectric. However, the result obtained here is not complete for determining the substitution information.

6.4 XANES results

6.4.1 Identification of Zn site in BiTiO_3

Generally, XANES measures the excitation of electrons K -levels to unoccupied bound states and is thus used to obtain information about the local arrangement of atoms around the absorbing atoms and the density of states of unoccupied states.

XANES spectra of Zn K -edge for Zn on Ti site in BiTiO_3 ($\text{Bi}(\text{Ti},\text{Zn})\text{O}_3$) and Zn on Bi site in BiTiO_3 ($(\text{Bi},\text{Zn})\text{TiO}_3$) were obtained using the FEFF8.2 codes follow models in Figure 6.4. The FEFF codes is using a full multiple scattering approach based on ab initio overlapping muffin-tin potentials. The muffin-tin potentials used in FEFF codes are self-consistent calculations with Hedin-Lundqvist exchange-correlation function (Hedin and Lundqvist, 1990). The results show that the measured XANES is clearly consistent with the calculation of Zn on Ti site and inconsistent with Zn at other lattice locations as show in Figure. 6.5.

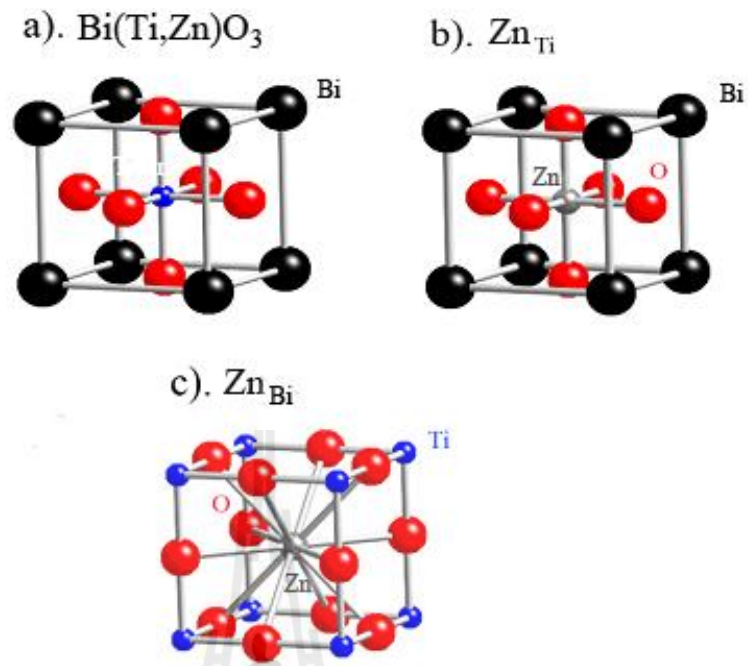


Figure 6.4 Model Perovskite crystal structure of $\text{Bi}(\text{Ti,Zn})\text{O}_3$. b–c schematic illustrations of Zn on Ti site, Zn on Bi site, respectively. Regions shown in c are shifted from that in a).

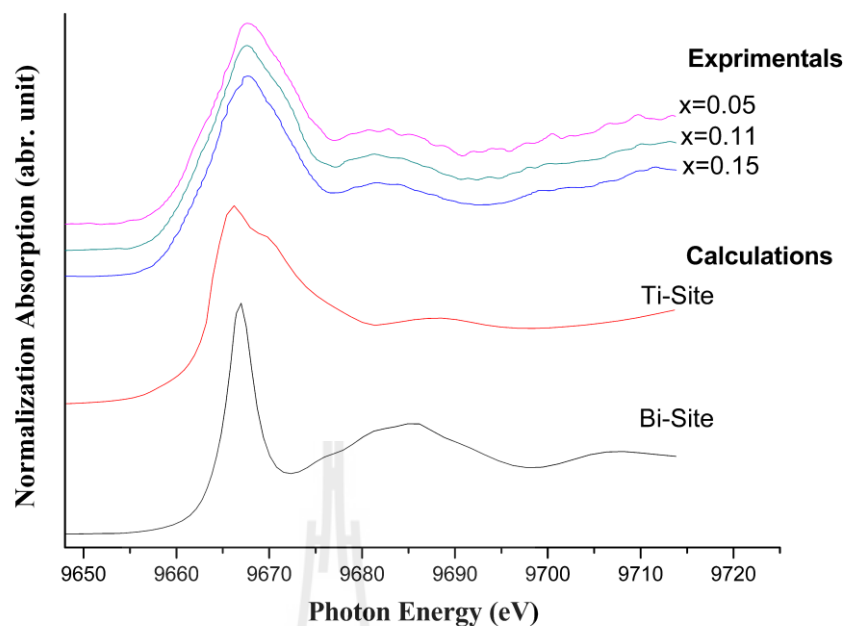


Figure 6.5 Present Zn *K*-edge XANES spectra of $(1-x)\text{BaTiO}_3-x\text{Bi}(\text{Ti}_{0.5}\text{Zn}_{0.5})\text{O}_3$ and calculation of Zn site for Zn on Ti site (Zn_{Ti} -red line), Zn on Bi site (Zn_{Bi} -black line).

6.4.2 XANES study on phase transition

The XANES is caused by the excitation of core electrons to unoccupied bound states and the spherical electron wave is scattering neighbor atom used to obtain information about the local arrangement of atoms around the absorbing atoms (Hedin and Lundqvist, 1970; Rehr and Albers, 2000). The intensity of peak A (I_A), which is caused by the Ti 1s electron transitions to the absorbing TiO_6 polyhedron 3d-originated unoccupied p-d hybrid orbitals of e_g -type symmetry. In Figure 6.6, local Ti off-centering is manifested in the Ti *K* pre-edge peak in X-ray absorption spectra (Ravel *et al.*, 1998). The integrated intensity of this peak is directly proportional to the mean-squared displacements of Ti (δ_{Ti}) off the instantaneous centers of oxygen

octahedral and is indirectly proportional to the lattice constants (Vedrinskii *et al.*, 1998; Levin *et al.*, 2013). The normalized Ti *K* pre-edge XANES spectra of $(1-x)\text{BaTiO}_3-x\text{Bi}(\text{Zn}_{0.5}\text{Ti}_{0.5})\text{O}_3$ ceramics are shown in Figure. 6.7. The integral intensity of peak A (I_A) decreases continuously, until the composition $x = 0.1$, and increases again because the Ti displacement decreases when close to rhombohedral phase and increases at real rhombohedral phase. Furthermore, the integral intensity of peak B (I_B) relates to the average of ratio Zn/Ti in the third shells which is decreasing while Zn occupied in the third shells of Ti core (Levin *et al.*, 2013). However, when $x > 0.1$, I_B increases because the ratio Zn/Ti is random by occupying in the third shells of Ti core or is in disorder relaxor region. Furthermore, while XANES spectra show starting difference in features for compositions $x = 0.09$, at $x \geq 0.1$ the spectra exhibit a clear change in features with the peak C; an indication of the change in local structure around Ti absorbing atom, corresponding to the phase transition from tetragonal to rhombohedral in XRD results.

The normalized Zn *K* edge XANES spectra of $(1-x)\text{BaTiO}_3-x\text{Bi}(\text{Zn}_{0.5}\text{Ti}_{0.5})\text{O}_3$ ceramics are shown in Figure. 6.8. The feature of Zn *K* edge XANES spectra does not change significantly hence the local structure. The Zn atoms substitute on B-site of perovskite structure, which correspond to the paraelectric region of the Zn atoms in oxygen octahedrals and indicates a cut off the normal ferroelectric regions. When the region of paraelectric phase increases, the polar nano region disperses in the paraelectric region and the interactions show relaxor ferroelectric behavior (Maiti *et al.*, 2006; Maiti *et al.*, 2008).

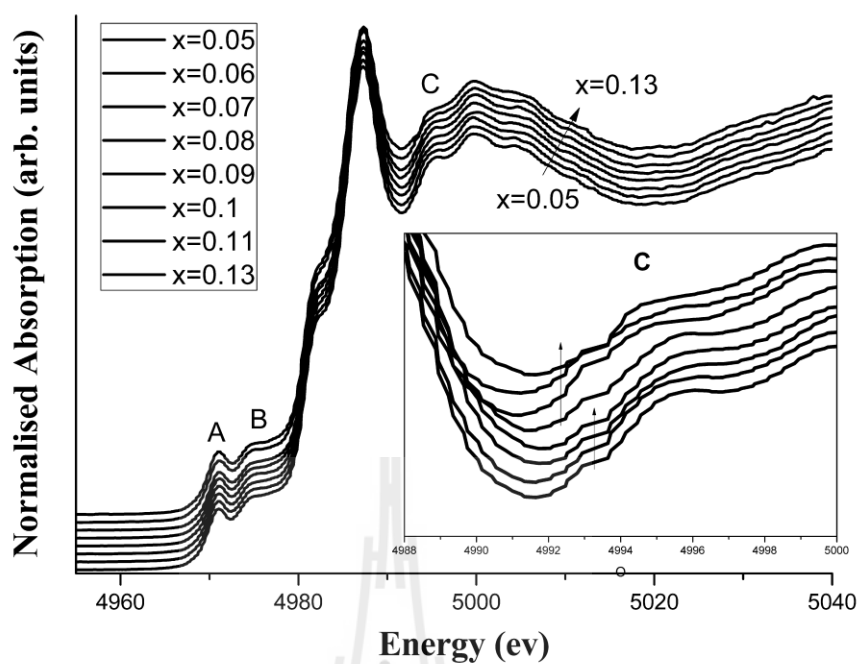


Figure 6.6 The normalized X-ray absorption Ti K-edge spectra of $(1-x)\text{BaTiO}_3-x\text{Bi}(\text{Zn}_{0.5}\text{Ti}_{0.5})\text{O}_3$, with $x = 0.05, 0.07, 0.09, 0.1, 0.11,$ and 0.13 .

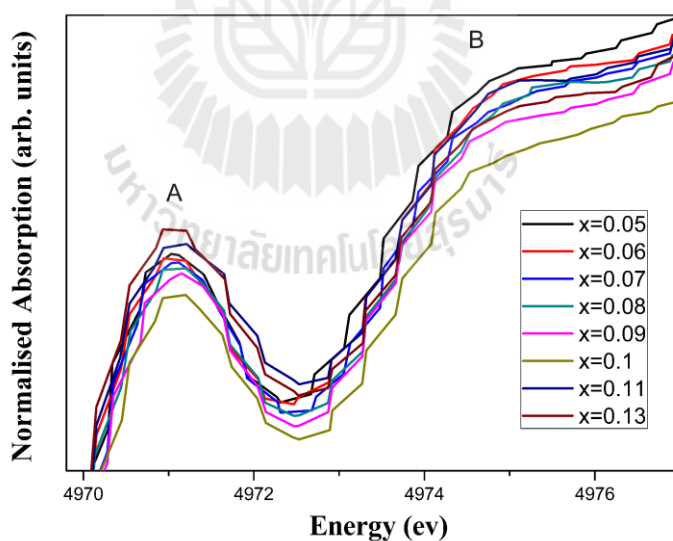


Figure 6.7 The normalized X-ray absorption Ti K pre-edge spectra of $(1-x)\text{BaTiO}_3-x\text{Bi}(\text{Zn}_{0.5}\text{Ti}_{0.5})\text{O}_3$, with $x = 0.05, 0.06, 0.07, 0.08, 0.09, 0.1,$ $0.11,$ and 0.13 .

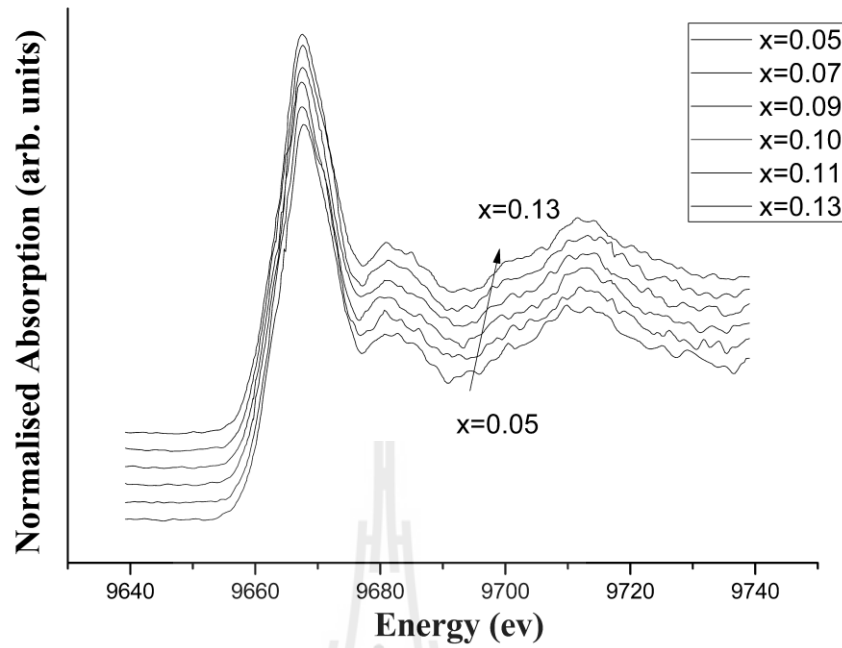


Figure 6.8 The normalized X-ray absorption Zn K-edge spectra of $(1-x)\text{BaTiO}_3-x\text{Bi}(\text{Zn}_{0.5}\text{Ti}_{0.5})\text{O}_3$, with $x=0.05, 0.07, 0.09, 0.1, 0.11,$ and 0.13 .

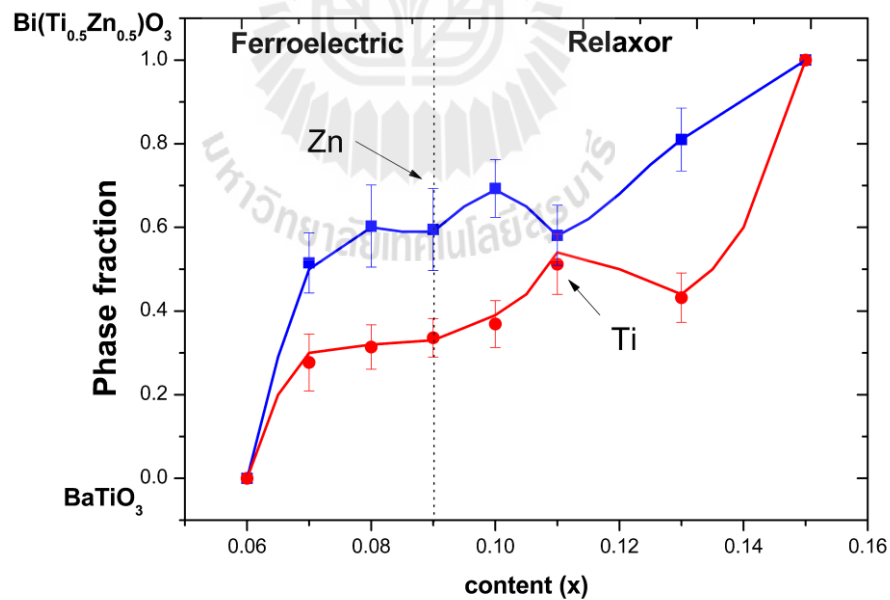


Figure 6.9 The phase fraction of Ti and Zn K-edge EXAFS in k-space in $(1-x)\text{BaTiO}_3-x\text{Bi}(\text{Zn}_{0.5}\text{Ti}_{0.5})\text{O}_3$ crystal.

In addition, we assume the mixture phase which is caused by the phase fraction between BaTiO_3 and $\text{Bi}(\text{Zn}_{0.5}\text{Ti}_{0.5})\text{O}_3$. Therefore, the phase fraction is obtained from a linear combination fit of BaTiO_3 and $\text{Bi}(\text{Zn}_{0.5}\text{Ti}_{0.5})\text{O}_3$ materials, (assuming that $x=0.05$ is BaTiO_3 with tetragonal structure and $x=0.15$ is $\text{Bi}(\text{Zn}_{0.5}\text{Ti}_{0.5})\text{O}_3$ with rhombohedral structure). As shown the Figure. 6.9, the results show that the phase fraction clearly separates between Ti and Zn atoms, indication of a composite material, not a solid solution. However, at around $x=0.11$ the phase fraction indicates a system with almost solid solution behavior.

6.5 EXAFS results

To process and enhance the EXAFS with the high k region, the plot $k^2X(k)$ is considered and windowed using a Hanning window $W(k)$. The EXAFS spectra were processed for information on local structure of Ti atom. In this work, the Ti K -edge EXAFS spectra can only be obtained up to photon energy of 250 eV above the absorption edge, due to the presence of Ba L_3 -edge. Therefore, EXAFS spectral fitting can only be performed up to the second shell; i.e. the first shell-oxygen octahedral and second shell of 8-fold coordinate, shown in Figure. 6.10.

The Ti K -edge EXAFS spectra did not show clearly the phase transition at $x = 0.08-0.09$. Therefore, the Ti K -edge EXAFS spectra can be changed to the normalized experimental EXAFS signal (χ) in function k , following Eq. (2.108), shown in Figure 6.11. However, at $x = 0.08-0.09$, $\chi(k)$ does not clearly present the phase transition of normal ferroelectric behavior to relaxor. In addition, $\chi(k)$ can be a Fourier transform (FT) in R-space, as shown in Figure 6.12. However, the phase transition cannot be

seen clearly. Therefore, it means that the local structure changes slightly from tetragonal to rhombohedral symmetry.

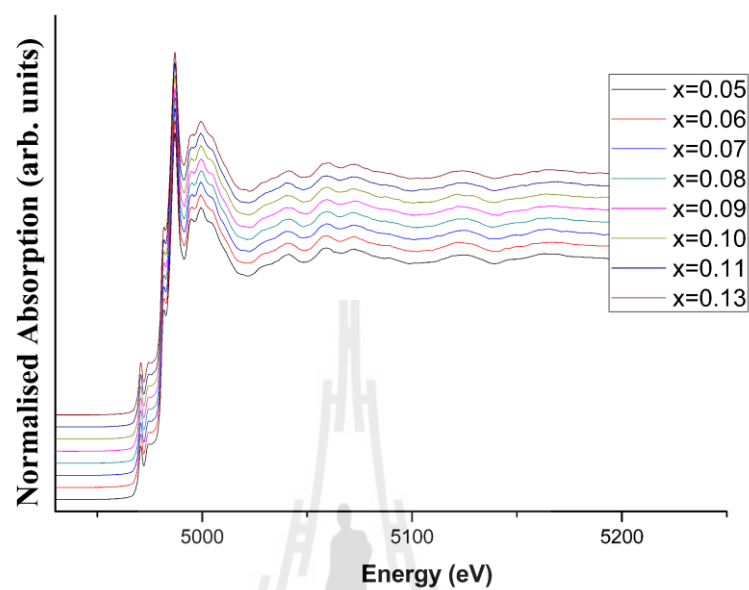


Figure 6.10 The EXAFS Fourier transform in E-space of $(1-x)\text{BaTiO}_3$ - $x\text{Bi}(\text{Zn}_{0.5}\text{Ti}_{0.5})\text{O}_3$ ceramics.

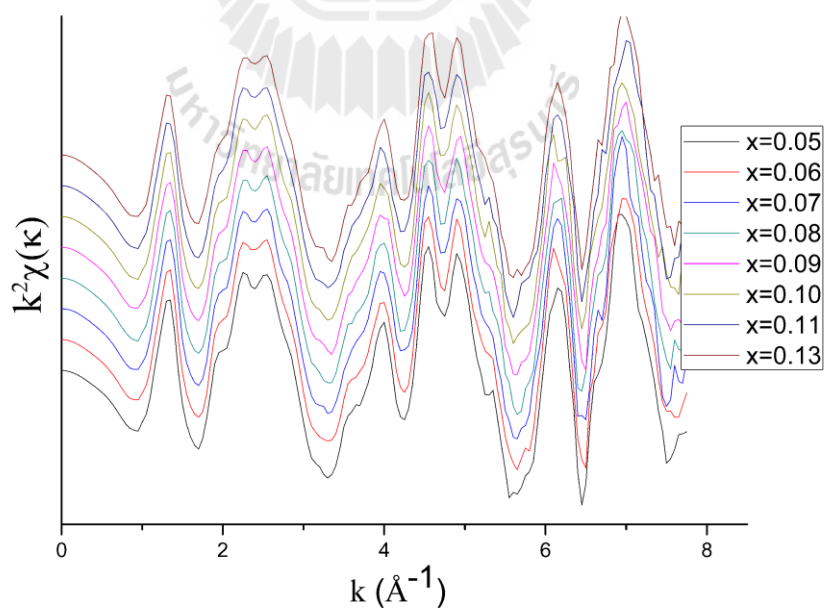


Figure 6.11 The EXAFS Fourier transform in k-space of $(1-x)\text{BaTiO}_3$ - $x\text{Bi}(\text{Zn}_{0.5}\text{Ti}_{0.5})\text{O}_3$ ceramics.

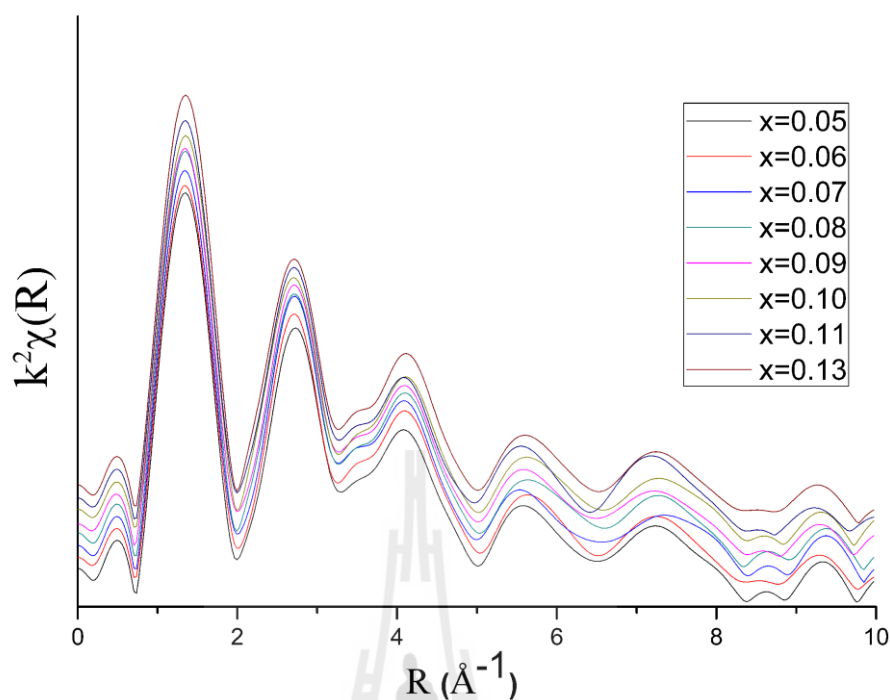


Figure 6.12 The EXAFS Fourier transform in R-space of $(1-x)\text{BaTiO}_3$ - $x\text{Bi}(\text{Zn}_{0.5}\text{Ti}_{0.5})\text{O}_3$ ceramics.

6.6 Dielectric permittivity

The dielectric constant and dielectric loss tangent ($\tan \delta$) at various frequencies for $(1-x)\text{BaTiO}_3$ - $x\text{Bi}(\text{Zn}_{0.5}\text{Ti}_{0.5})\text{O}_3$ compositions, with $x=0.05, 0.06, 0.07, 0.08, 0.09, 0.10, 0.11$ and 0.13 , are shown in Figure 6.13. The compositions with $0.05 \leq x \leq 0.07$ exhibit a normal ferroelectric behavior, and sharp peaks of dielectric constant as a function of temperature are observed. At $x=0.08$, the relaxor behavior and the broad peaks of dielectric constant as a function temperature start. A strong frequency dispersion is observed around the ϵ' and $\tan \delta$ peaks for $x \geq 0.09$ compositions or so called “relaxor like” behavior. With the increase in frequency, ϵ' decreases and the temperature of the maximum dielectric constant (T_m) shifts to

higher temperatures. In contrast, the dielectric loss tangent is increasing while the frequencies decreases, and similarly, the temperature with the maximum dielectric loss is shifted to higher temperatures. Furthermore, the dielectric constants decrease in the compositions with increased x . The dielectric loss tangent increases until $x=0.08$, but a few changes with frequencies are observed.



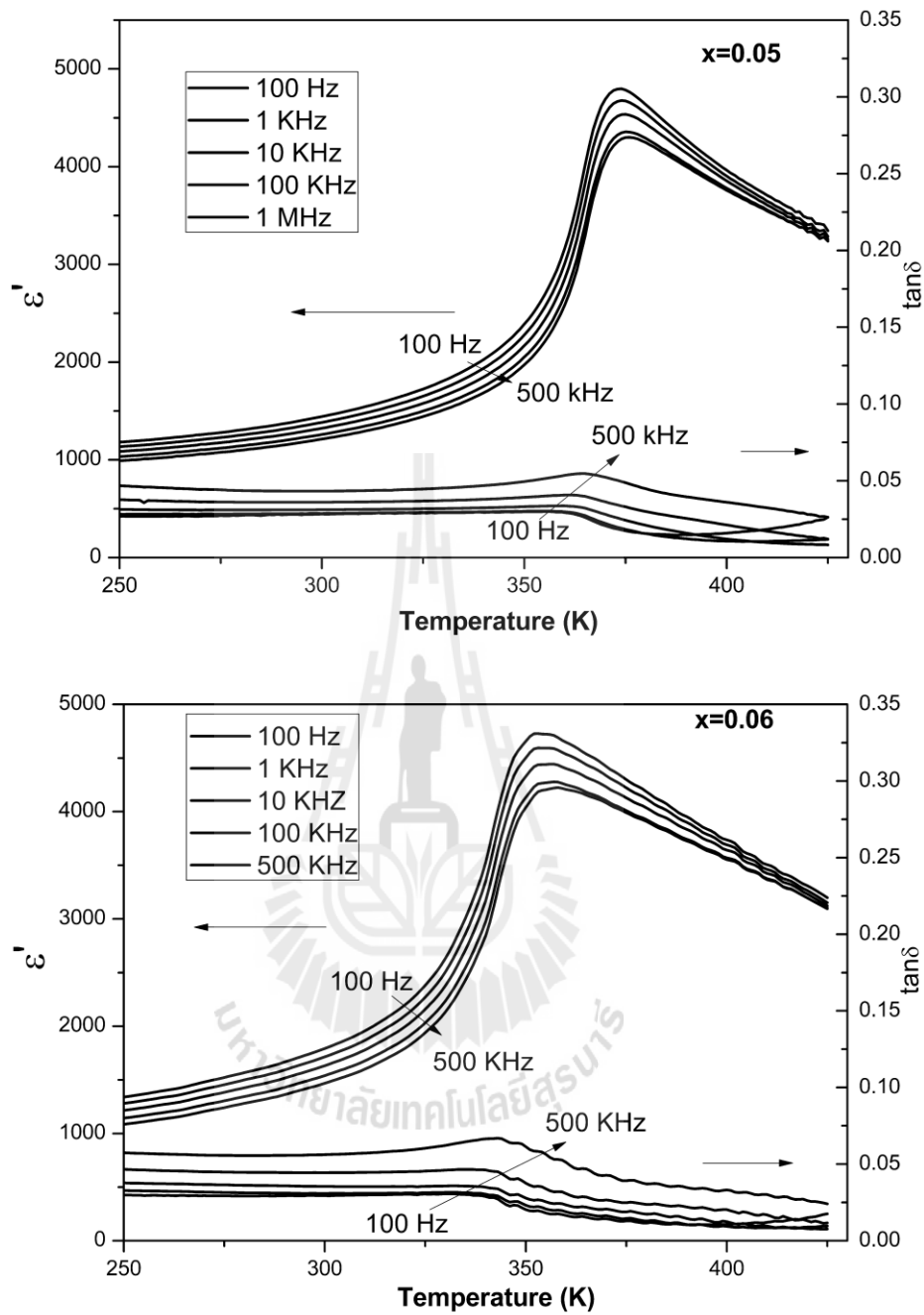


Figure 6.13 Temperature dependence of dielectric constant and loss tangent ($\tan\delta$) at various frequencies for $(1-x)\text{BaTiO}_3-x\text{Bi}(\text{Zn}_{0.5}\text{Ti}_{0.5})\text{O}_3$.

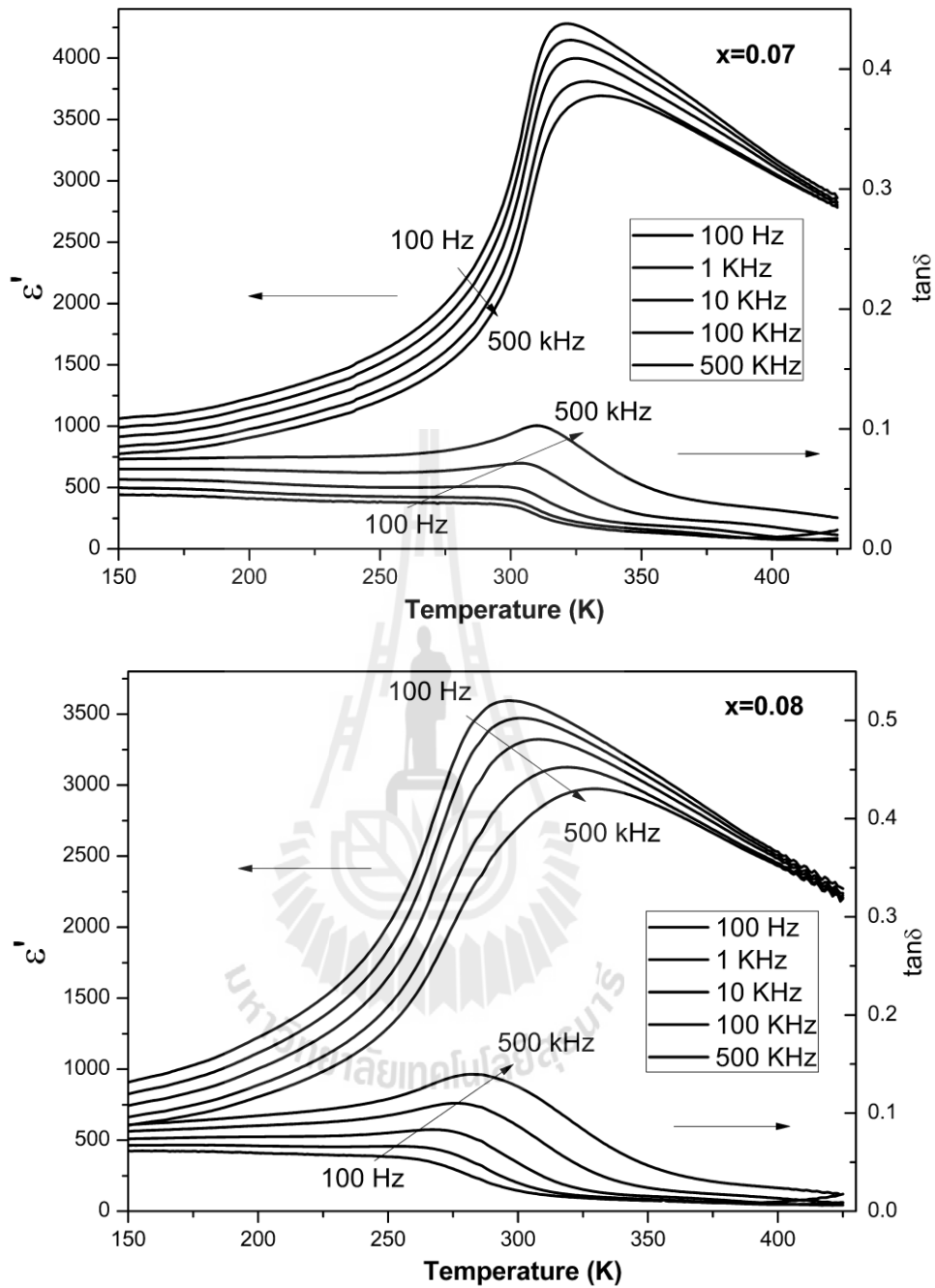


Figure 6.13 (Continued) Temperature dependence of dielectric constant and loss tangent ($\tan \delta$) at various frequencies for $(1-x)\text{BaTiO}_3-x\text{Bi}(\text{Zn}_{0.5}\text{Ti}_{0.5})\text{O}_3$.

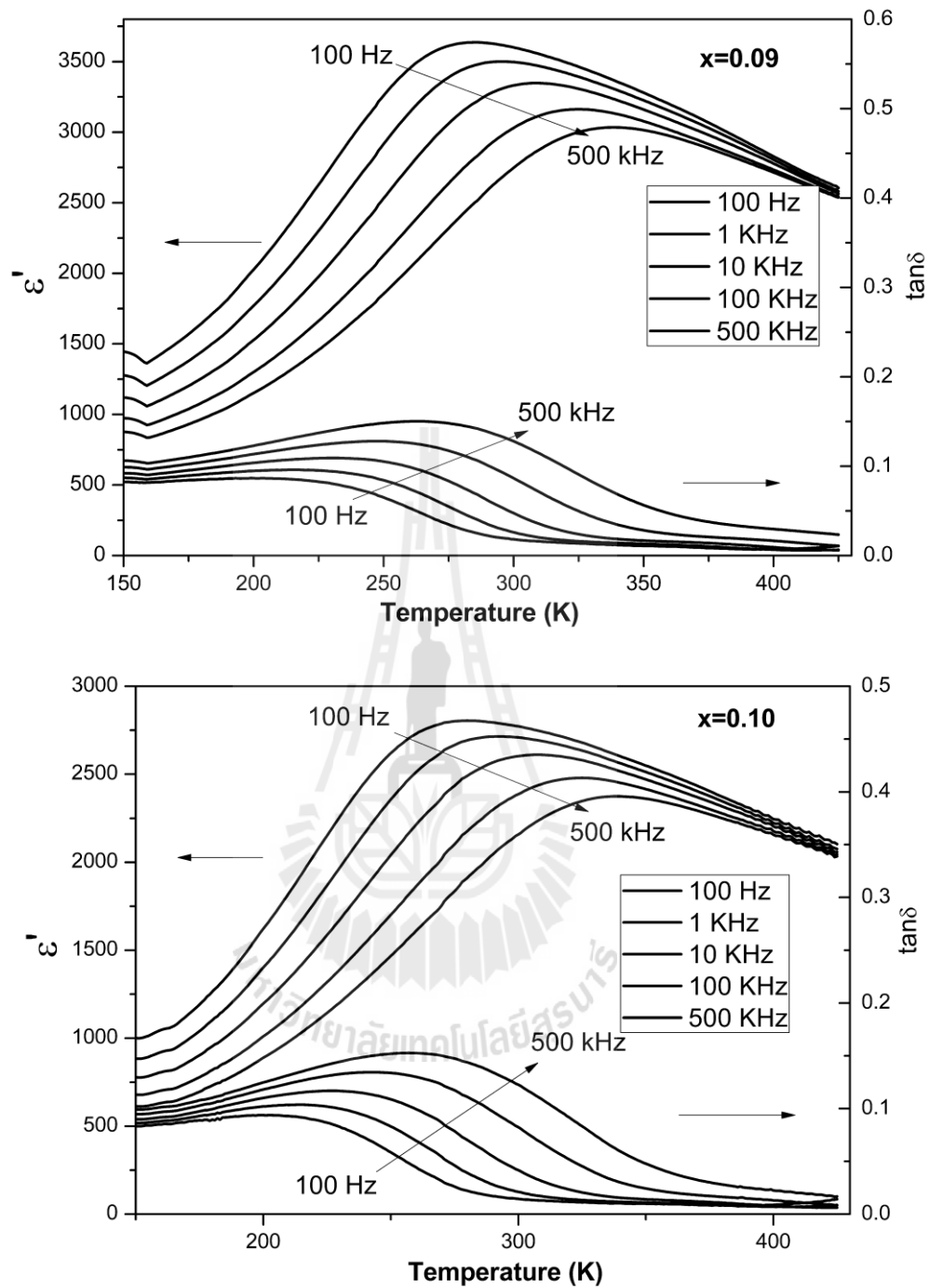


Figure 6.13 (Continued) Temperature dependence of dielectric constant and loss tangent ($\tan \delta$) at various frequencies for $(1-x)\text{BaTiO}_3-x\text{Bi}(\text{Zn}_{0.5}\text{Ti}_{0.5})\text{O}_3$.

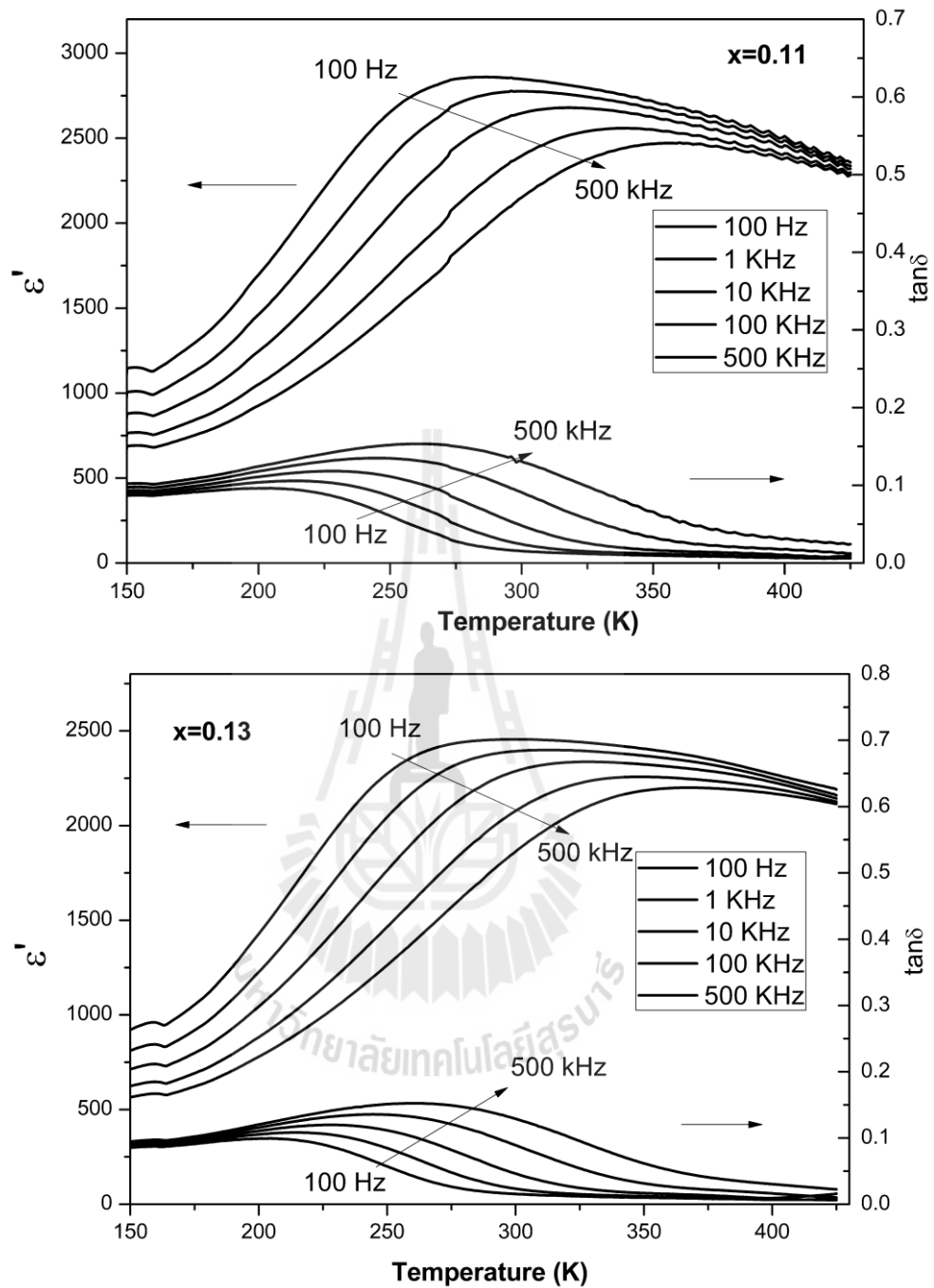


Figure 6.13 (Continued) Temperature dependence of dielectric constant and loss tangent ($\tan \delta$) at various frequencies for $(1-x)\text{BaTiO}_3-x\text{Bi}(\text{Zn}_{0.5}\text{Ti}_{0.5})\text{O}_3$.

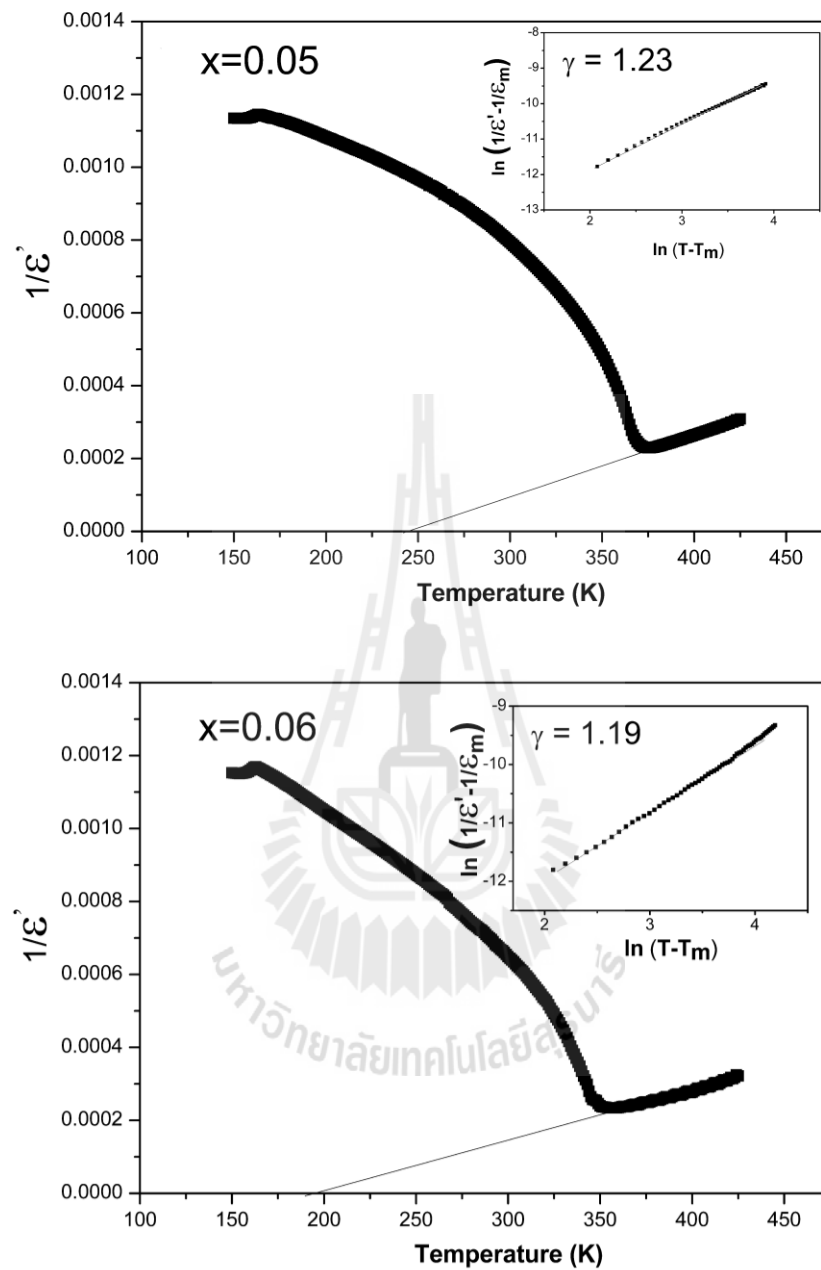


Figure 6.14 The inverse dielectric constant $1/\epsilon$ as a function of temperature at 100 kHz for $\text{Ba}(\text{Zr}_x\text{Ti}_{1-x})\text{O}_3$, symbols denote experimental data and solid line denotes fitting to the Curie-Weiss law. The insets show the plot of $\ln(1/\epsilon - 1/\epsilon_m)$ vs $\ln(T - T_m)$ for $(1-x)\text{BaTiO}_3 - x\text{Bi}(\text{Zn}_{0.5}\text{Ti}_{0.5})\text{O}_3$ ceramics.

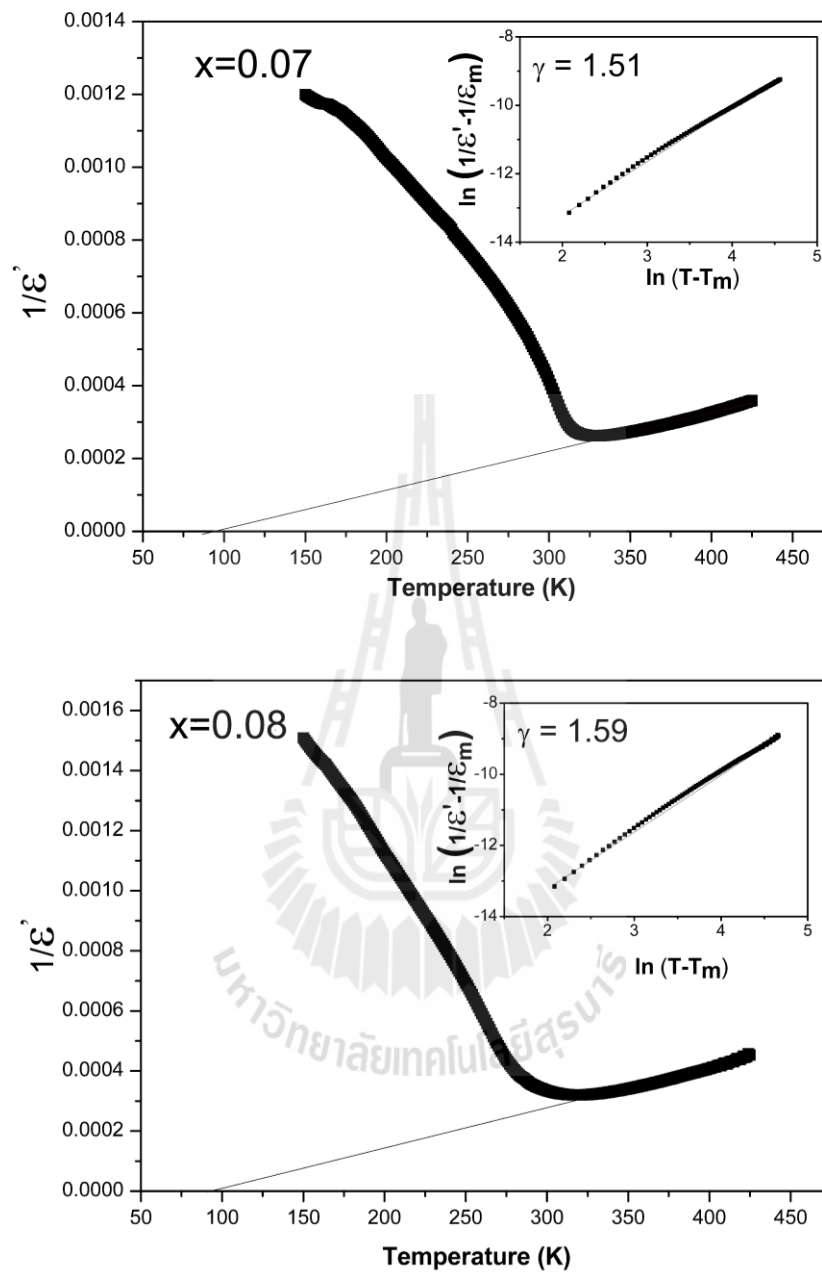


Figure 6.14 (Continued) The inverse dielectric constant $1/\epsilon$ as a function of temperature at 100 kHz for $\text{Ba}(\text{Zr}_x\text{Ti}_{1-x})\text{O}_3$, symbols denote experimental data and solid line denotes fitting to the Curie-Weiss law. The insets show the plot of $\ln(1/\epsilon - 1/\epsilon_m)$ vs $\ln(T - T_m)$ for $(1-x)\text{BaTiO}_3 - x\text{Bi}(\text{Zn}_{0.5}\text{Ti}_{0.5})\text{O}_3$ ceramics.

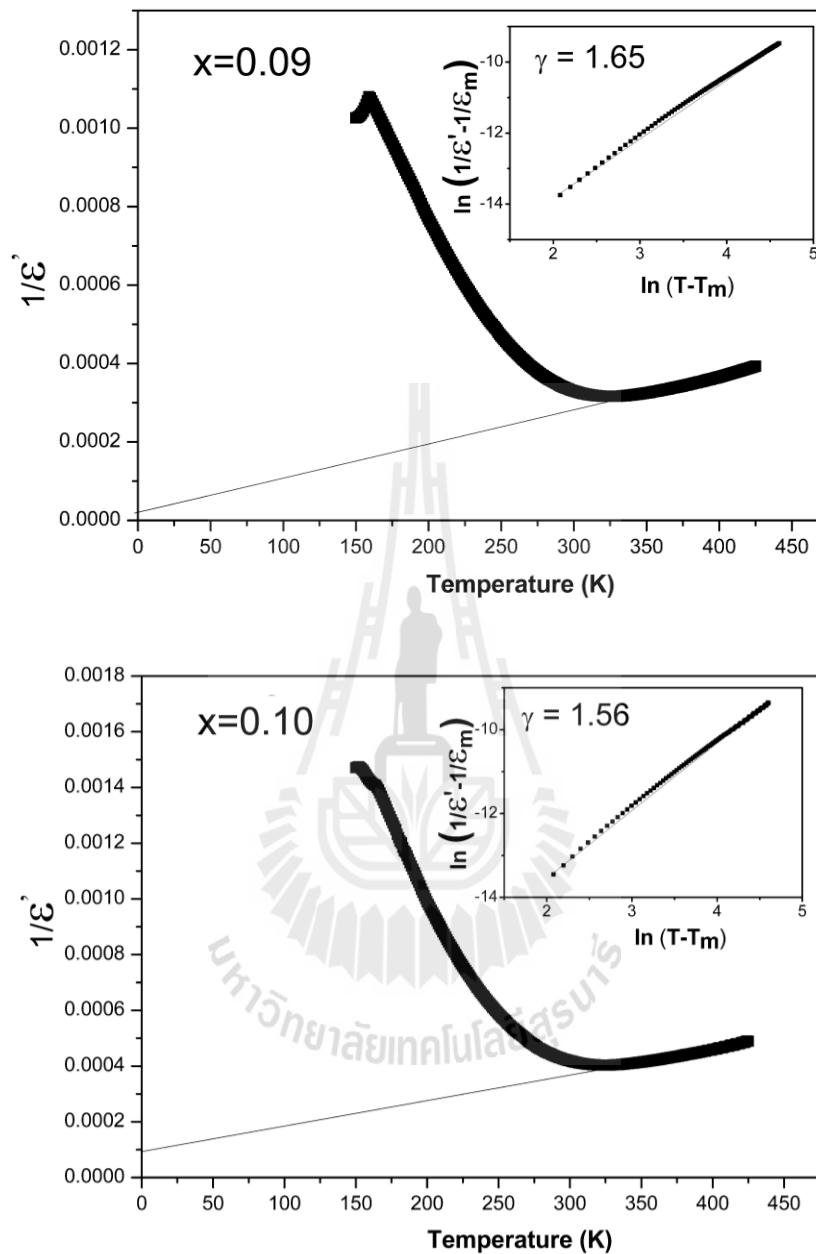


Figure 6.14 (Continued) The inverse dielectric constant $1/\epsilon$ as a function of temperature at 100 kHz for $\text{Ba}(\text{Zr}_x\text{Ti}_{1-x})\text{O}_3$, symbols denote experimental data and solid line denotes fitting to the Curie-Weiss law. The insets show the plot of $\ln(1/\epsilon - 1/\epsilon_m)$ vs $\ln(T - T_m)$ for $(1-x)\text{BaTiO}_3 - x\text{Bi}(\text{Zn}_{0.5}\text{Ti}_{0.5})\text{O}_3$ ceramics.

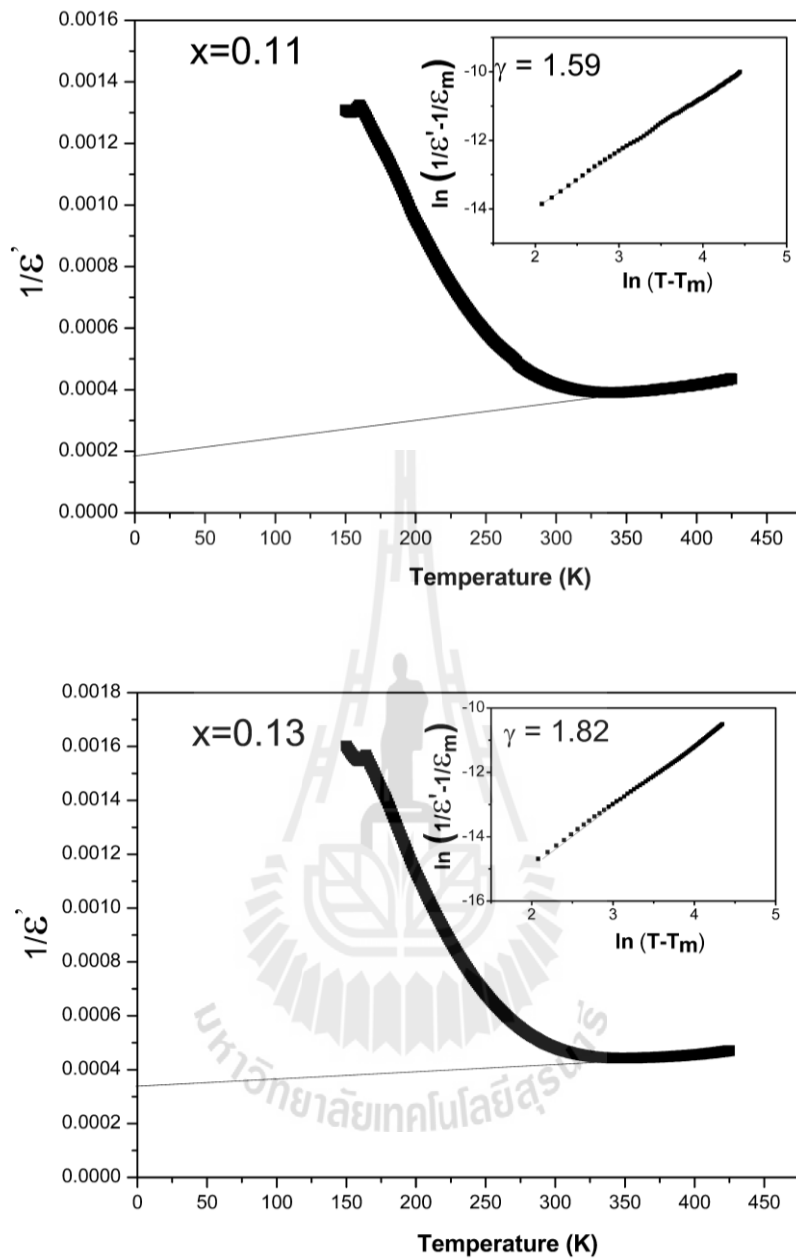


Figure 6.14 (Continued) The inverse dielectric constant $1/\epsilon$ as a function of temperature at 100 kHz for $\text{Ba}(\text{Zr}_x\text{Ti}_{1-x})\text{O}_3$, symbols denote experimental data and solid line denotes fitting to the Curie-Weiss law. The insets show the plot of $\ln(1/\epsilon - 1/\epsilon_m)$ vs $\ln(T - T_m)$ for $(1-x)\text{BaTiO}_3 - x\text{Bi}(\text{Zn}_{0.5}\text{Ti}_{0.5})\text{O}_3$ ceramics.

The Curie-Weiss law can explain a normal ferroelectric in the paraelectric region, following Eq. (2.64). Figure 6.14 shows the inverse dielectric constant as a function of temperature at 100 KHz. The linear fitting is observed in the paraelectric region or high temperature for all compositions. The fitting parameters Curie-Weiss constant and Curie temperature (as calculated) are shown in Table 6.1 (Maiti *et al.*, 2006). The results show that the Curie temperature decreases while the composition x increases. It is evident from the value of T_C that the compositions $x=0.05-0.08$ show the normal ferroelectric behavior. However, the values of T_C indicate nearly the relaxation behavior for $x=0.09-0.13$. Furthermore, the relaxor ferroelectric behavior in the high temperature region follows a modified Curie-Weiss law from Eq. (2.65). The value of δ_γ represents the degree of diffuseness for transition peaks. Both γ and δ_γ are determined from the slope and intercept $\ln(\epsilon'_{max}/\epsilon')$ versus $\ln(T - T_m)$, as shown in Figure. 6.14 for all compositions (Huang, 2008). In the Table 6.2, the value of γ is increasing while the composition x increases, indicating the relaxor behavior. For $x > 0.07$, the compositions exhibit the relaxation behavior until $x=0.13$, close to the ideal relaxor ferroelectric ($\gamma=2$). The value of δ_γ also increases because of the increasing relaxation. In addition, the transition temperature T_m decreases as x increases until $x=0.08$, indicating a destabilization of ferroelectric phase. For $x>0.08$, the transition temperature increases continuously within the rhombohedral phase field (Raengthon and Cann, 2011; Raengthon *et al.*, 2012).

Table 6.1 Calculated Curie constant and measured T_c from dielectric properties of $(1-x)\text{BaTiO}_3$ - $x\text{Bi}(\text{Zn}_{0.5}\text{Ti}_{0.5})\text{O}_3$ compositions.

Composition	C (K)	T_c (K)
x=0.05	5.90×10^5	243.72
x=0.06	7.21×10^5	196.04
x=0.07	9.41×10^5	92.99
x=0.08	7.45×10^5	94.62
x=0.09	1.11×10^5	-7.08
x=0.10	1.08×10^5	-95.48
x=0.11	1.91×10^5	-394.79
x=0.13	3.80×10^5	-1333.96



Table 6.2 Degree of relaxation γ , dielectric maxima temperature and diffusivity of $(1-x)\text{BaTiO}_3$ - $x\text{Bi}(\text{Zn}_{0.5}\text{Ti}_{0.5})\text{O}_3$ compositions.

Composition	γ	$T_m(\text{K})$	δ_γ
x=0.05	1.23	375	66.33
x=0.06	1.19	359	87.73
x=0.07	1.51	329	113.40
x=0.08	1.59	319	115.69
x=0.09	1.65	325	148.04
x=0.10	1.56	325	170.36
x=0.11	1.59	340	217.92
x=0.13	1.82	348	249.49

The process of relaxor ferroelectric is believed to be the presence of dynamic polar nano regions which are ever more active and are of fines scale in the vicinity of T_m in a classical relaxor system. Generally, the polar nanoregions (PNRs) exhibit a characteristic relaxation time (τ) in the local field configuration in its characteristic size. The separation of energy barrier switch to the polarization state decreases as the size of the PNRs decreases. The direction of a net polarization (P_s) fluctuates or becomes very dynamic with temperature while the barrier height becomes comparable to thermal energy (kT). Like the spin glass systems, the short-range interaction between the polar regions control the fluctuation of P_s , leading to its freezing at a characteristic temperature for below the T_m . The relaxation time (τ) in relaxor can be decribed by the Vogel-Fulcher relation (Maiti *et al.*, 2006; Maiti *et al.*, 2008; Maiti *et al.*, 2011),

$$\tau = \tau_0 \exp[E_a/k_B(T_m - T_{VF})] \quad (6.1)$$

where τ_0 is the pre-exponential factor, E_a is the activation energy for polarization fluctuations of an isolated cluster, T_m is the temperature at the maximum dielectric constant, k_B is the Boltzmann constant, and T_{VF} is the characteristic Vogel-Fulcher freezing temperature. The relaxation time depends on the temperature and can be well fitted with Vogel-Fulcher relation for composition $x=0.08-0.13$ (relaxor behavior only), as shown in Figure. 6.15. In the Table 6.3, the fitting parameters are summarized. With the increase in $\text{BiZn}_{0.5}\text{Ti}_{0.5}\text{O}_3$ content the freezing temperature is increased. The realistic increasing values of T_{VF} indicate the gradual evolution of polar-nano- egion-like relaxor behavior. Similarly, the activation energy decreases, with the evolution of the relaxor behavior and the energy corresponding to the thermal relaxation process also reduced. Therefore, the evolution of polar nano region or relaxor behavior in $(1-x)\text{BaTiO}_3-x\text{BiZn}_{0.5}\text{Ti}_{0.5}\text{O}_3$ materials enhances with the x in this system.

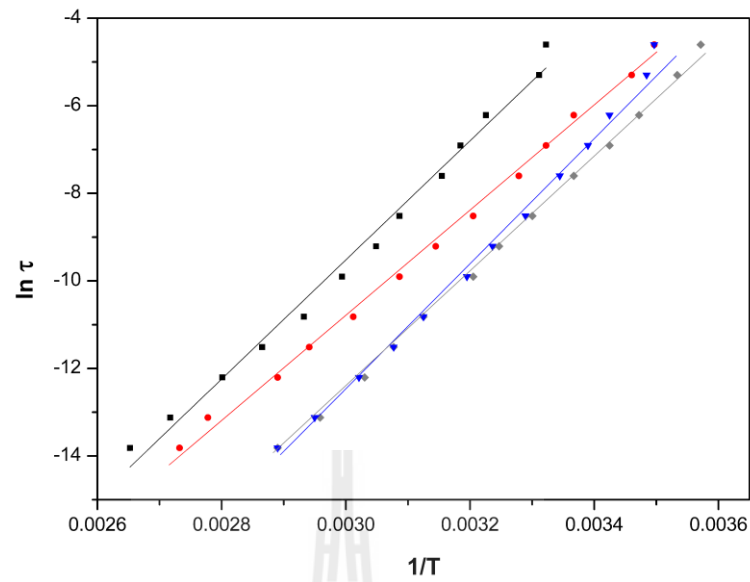


Figure 6.15 Temperature dependence of relaxation time for ceramics at 100 kHz, with $x = 0.05, 0.06, 0.07, 0.08, 0.09, 0.1, 0.11, \text{ and } 0.13$. Symbols denote experimental data and solid curve denotes fitting to the Vogel-Fulcher relation.

Table 6.3 Vogel-Fulcher temperature, activation energy E_a and exponent τ_0 as calculated from the Arrhenius plots of various $(1-x)\text{BT}-x\text{BZT}$ compositions.

Composition	Freezing temperature (T_{VF}) (K)	Activation energy (E_a) (eV)	Pre-exponential Factor (τ_0) (ps)
x=0.08	34	2.04	9.41×10^{-26}
x=0.09	51	1.27	1.90×10^{-13}
x=0.10	54	1.16	9.14×10^{-12}
x=0.11	65	1.03	6.15×10^{-9}
x=0.13	62	1.17	1.34×10^{-10}

6.7 Hysteresis

The polarization hysteresis data at room temperature for $(1-x)\text{BT}-x\text{BZnT}$ are shown in Figure 6.16. The remnant polarization (P_r) increased to $10.2 \mu\text{C}/\text{cm}$ and $11.3 \text{ kV}/\text{cm}$ for $0.05\text{BZnT}-0.95\text{BT}$ compared to pure BaTiO_3 . However, when more BZnT was added, the area of hysteresis loops decreased dramatically. The absence of clear hysteresis behavior for higher BZnT contents can be related to a decreased T_m as shown in Table 6.2. Although T_m increased for $x > 0.1$, the relaxor behavior due to rhombohedral symmetry and possibly degree of higher disorder in the structure resulted in the disappearance of hysteresis loop.

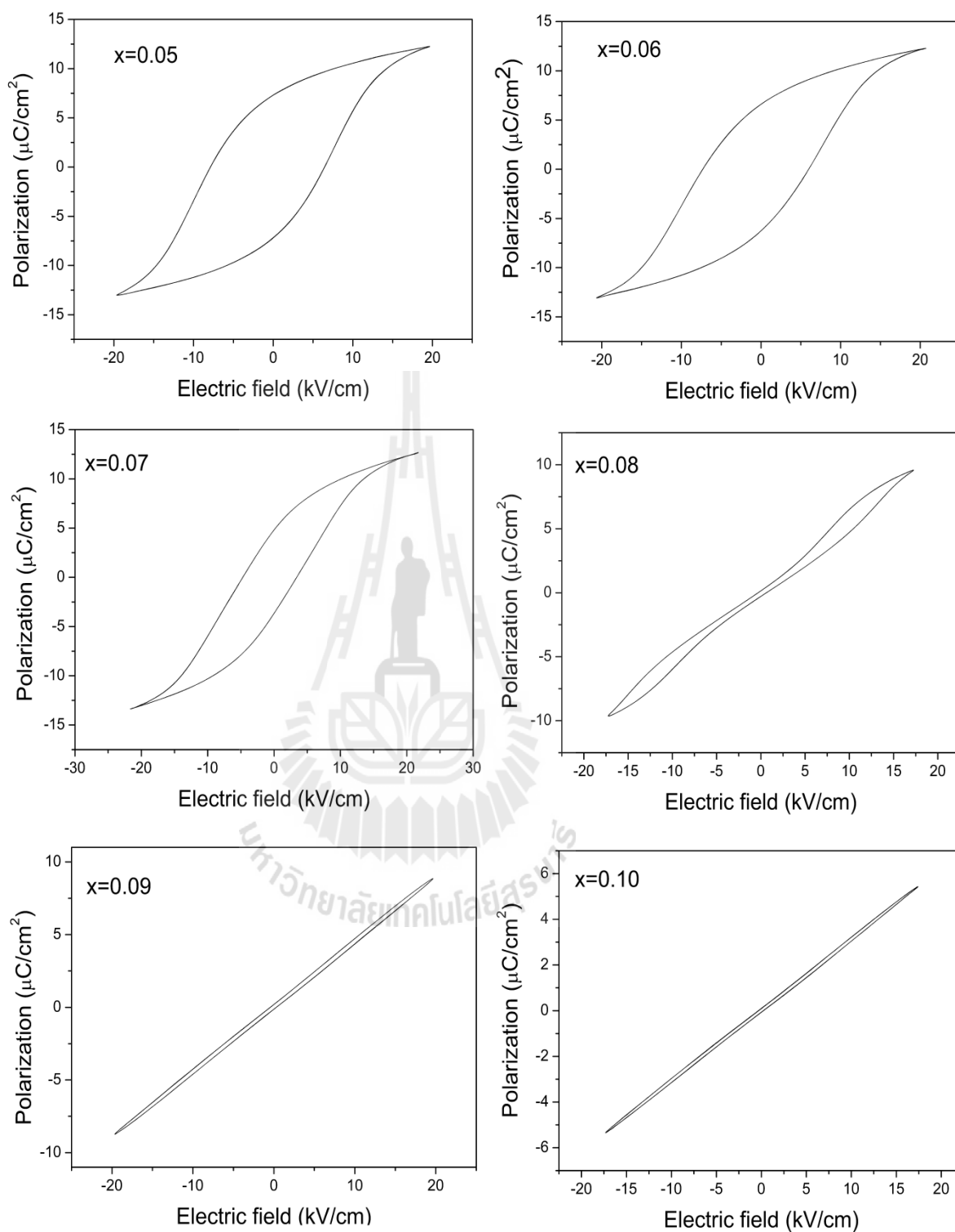


Figure 6.16 P - E hysteresis measurements on $(1-x)\text{BaTiO}_3-x\text{Bi}(\text{Zn}_{0.5}\text{Ti}_{0.5})\text{O}_3$ ceramics obtained at room temperature.

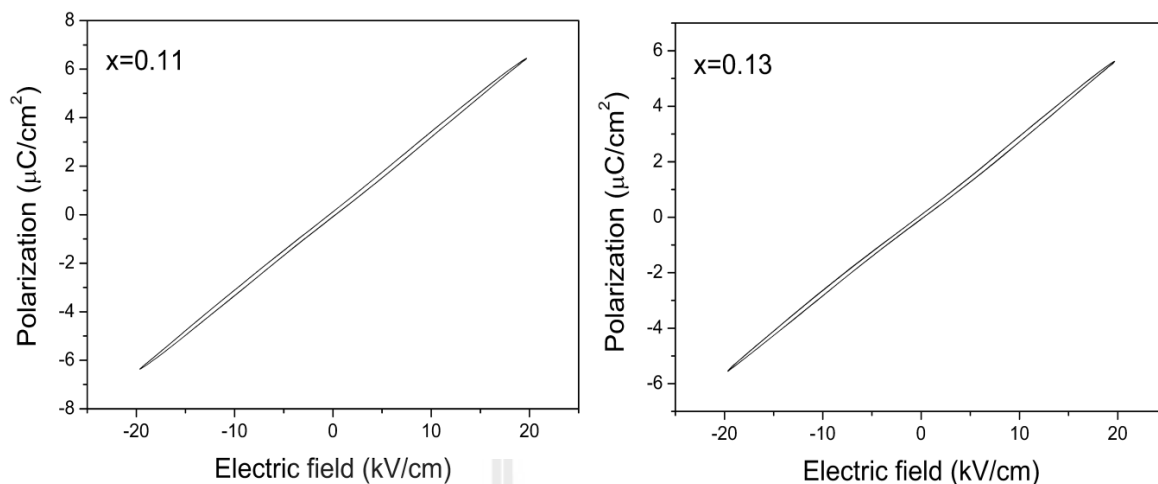


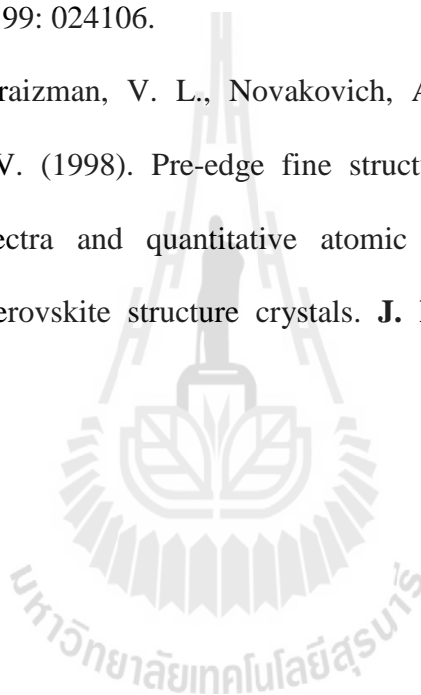
Figure 6.16 *P-E* hysteresis measurements on $(1-x)\text{BaTiO}_3-x\text{Bi}(\text{Zn}_{0.5}\text{Ti}_{0.5})\text{O}_3$ ceramics obtained at room temperature.

6.8 References

- Chandarak, S., Jutimoosik, J., Bootchanont, A., Unruan, M., Jantaratana, P., Priya, S., Srilomsak, S., Rujirawat, S. and Yimmirun, R. (2012). Local Structure of Magnetoelectric $\text{BiFeO}_3\text{-BaTiO}_3$ Ceramics Probed by Synchrotron X-Ray Absorption Spectroscopy. **J. Supercond. Nov. Magn.** 26: 455.
- Eitel, R. E., Randall, C. A., Shrout, T. R., Rehrig, P. W., Hackenberger, W. and Park, S.-E. (2001). New High Temperature Morphotropic Phase Boundary Piezoelectrics Based on $\text{Bi}(\text{Me})\text{O}_3\text{-PbTiO}_3$ Ceramics. **Jpn. J. Appl. Phys.** 40: 5999.
- Hedin, L. and Lundqvist, S. (1970) Effects of Electron-Electron and Electron-Phonon Interactions on the One-Electron States of Solids. **Solid State Physics.** 23 (Eds, Frederick Seitz, D. T. and Henry, E.) Academic Press, pp. 1.

- Hedin, L. and Lundqvist, S. (1990). Advances in Research and Application. **Solid State Phys.** 23: 1.
- Huang, C.-C. and Cann, D. P. (2008). Phase transitions and dielectric properties in $\text{Bi}(\text{Zn}_{1/2}\text{Ti}_{1/2})\text{O}_3$ - BaTiO_3 perovskite solid solutions. **J. Appl. Phys.** 104: 024117.
- Huang, C.-C. and Cann, D. P. (2008). Phase transitions and dielectric properties in $\text{Bi}(\text{Zn}_{1/2}\text{Ti}_{1/2})\text{O}_3$ - BaTiO_3 perovskite solid solutions. **J. Appl. Phys.** 104.
- Huang, C. C. (2008). **Structure and piezoelectric properties of lead-free bismuth-based perovskite solid solutions**. Ph.D.dissertation, Oregon StateUniversity.
- Levin, I., Krayzman, V. and Woicik, J. C. (2013). Local-structure origins of the sustained Curie temperature in $(\text{Ba},\text{Ca})\text{TiO}_3$ ferroelectrics. **Appl. Phys. Lett.** 102: 162906.
- Maiti, T., Guo, R. and Bhalla, A. S. (2006). The evolution of relaxor behavior in Ti^{4+} doped BaZrO_3 ceramics. **J. Appl. Phys.** 100: 114109.
- Maiti, T., Guo, R. and Bhalla, A. S. (2008). Structure-Property Phase Diagram of $\text{BaZr}_x\text{Ti}_{1-x}\text{O}_3$ System. **J. Am. Ceram. Soc.** 91: 1769.
- Maiti, T., Guo, R. and Bhalla, A. S. (2011). Evaluation of Experimental Resume of $\text{BaZr}_x\text{Ti}_{1-x}\text{O}_3$ with Perspective to Ferroelectric Relaxor Family: An Overview. **Ferroelectrics.** 425: 4.
- Raengthon, N. and Cann, D. P. (2011). Dielectric Relaxation in BaTiO_3 - $\text{Bi}(\text{Zn}_{1/2}\text{Ti}_{1/2})\text{O}_3$ Ceramics. **J. Am. Ceram. Soc.** 95: 1604.
- Raengthon, N., Sebastian, T., Cumming, D., Reaney, I. M. and Cann, D. P. (2012). BaTiO_3 - $\text{Bi}(\text{Zn}_{1/2}\text{Ti}_{1/2})\text{O}_3$ - BiScO_3 Ceramics for High-Temperature Capacitor Applications. **J. Am. Ceram. Soc.** 95: 3554.

- Ravel, B., Stern, E. A., Vadrinskii, R. I. and Kraizman, V. (1998). Local structure and the phase transitions of BaTiO₃. **Ferroelectric**. 206: 407.
- Rehr, J. J. and Albers, R. C. (2000). Theoretical approaches to x-ray absorption fine structure. **Rev. Mod. Phys.** 72: 3.
- Stringer, C. J., ShROUT, T. R. and Randall, C. A. (2006). Classification of transition temperature behavior in ferroelectric PbTiO₃-Bi(Me'Me'')O₃ solid solutions. **J. Appl. Phys.** 99: 024106.
- Vadrinskii, R. V., Kraizman, V. L., Novakovich, A. A., Demekhin, P. V. and Urazhdin, S. V. (1998). Pre-edge fine structure of the 3d atom K x-ray absorption spectra and quantitative atomic structure determinations for ferroelectric perovskite structure crystals. **J. Phys. Condens. Matter**. 10: 9561.



CHAPTER VII

STRUCTURE-PROPERTY RELATIONSHIP

Recently, extensive research efforts have been conducted on relaxor ferroelectrics. To describe the physical phenomena of relaxor ferroelectrics, several models; superparaelectric (Cross, 1987), “dipolar glass”(Viehland *et al.*, 1990), random field (Westphal *et al.*, 1992), etc, have been discussed.

In this work, the 3 BaTiO₃-based BZT, BST and BT-BZnT systems : were investigated. They all have relaxor properties. However, there are some slight differences in defect levels. Both BZT and BST have similar defect structure with substitution on B-site of ABO₃ perovskite but with different elements or ionic radii of substitution. In addition, BT-BZnT composites show similar effect to B-site substitution. Therefore, all systems can be relaxor ferroelectric materials. In this work, we investigated the gradual evolution of relaxation behavior in BT-BZT system. As the amount of BZT increases, the normal ferroelectric behavior of BT regions start breaking and generate the density of the nano-sized Ti oxygen-octahedral-rich polar regions in the Zn-rich matrix. In the classic A(B_xB_{1-x})O₃ ferroelectric relaxors such as PbMg_{1/3}Nb_{2/3}O₃ (PMN), the nano-sized cation ordered charged regions are distributed in a disordered matrix and lead to the well-known relaxor behavior (Maiti *et al.*, 2006). In this chapter, the relationship between structure and dielectric properties for all systems is formulated.

7.1 Global structure

The XRD results showed the global structure information around the phase transition of BZT, BST and BT-BZnT, as shown in Figure 7.1 for direct comparison. BZT do not exhibit a clear phase transition of normal ferroelectrics to relaxor and relaxor to polar cluster for $x=0.25-0.30$ and $x=0.70-0.75$. Similarly, XRD results of BST does not clearly show the phase information for $x=0.05-0.25$ and $x=0.50-0.55$, as shown as Figures 7.1a and 7.1b. However, the XRD results of BT-BZnT showed the phase transition between tetragonal to rhombohedral symmetry at around $x = 0.08 - 0.09$, as shown Figure 7.1c. It is possible that in case of BZT and BST the global structure distorts slightly. Therefore, XRD technique cannot observe such a small change very clearly. However, in the case of BT-BZnT, XRD technique can be used to observe clearly the phase transition. Since XRD technique observes overall structure in the system, if the structure does not change homogeneously in the whole system, XRD technique will not observe the change clearly. In contrast, it means that most of the global structures in BT-BZnT change to rhombohedral symmetry.

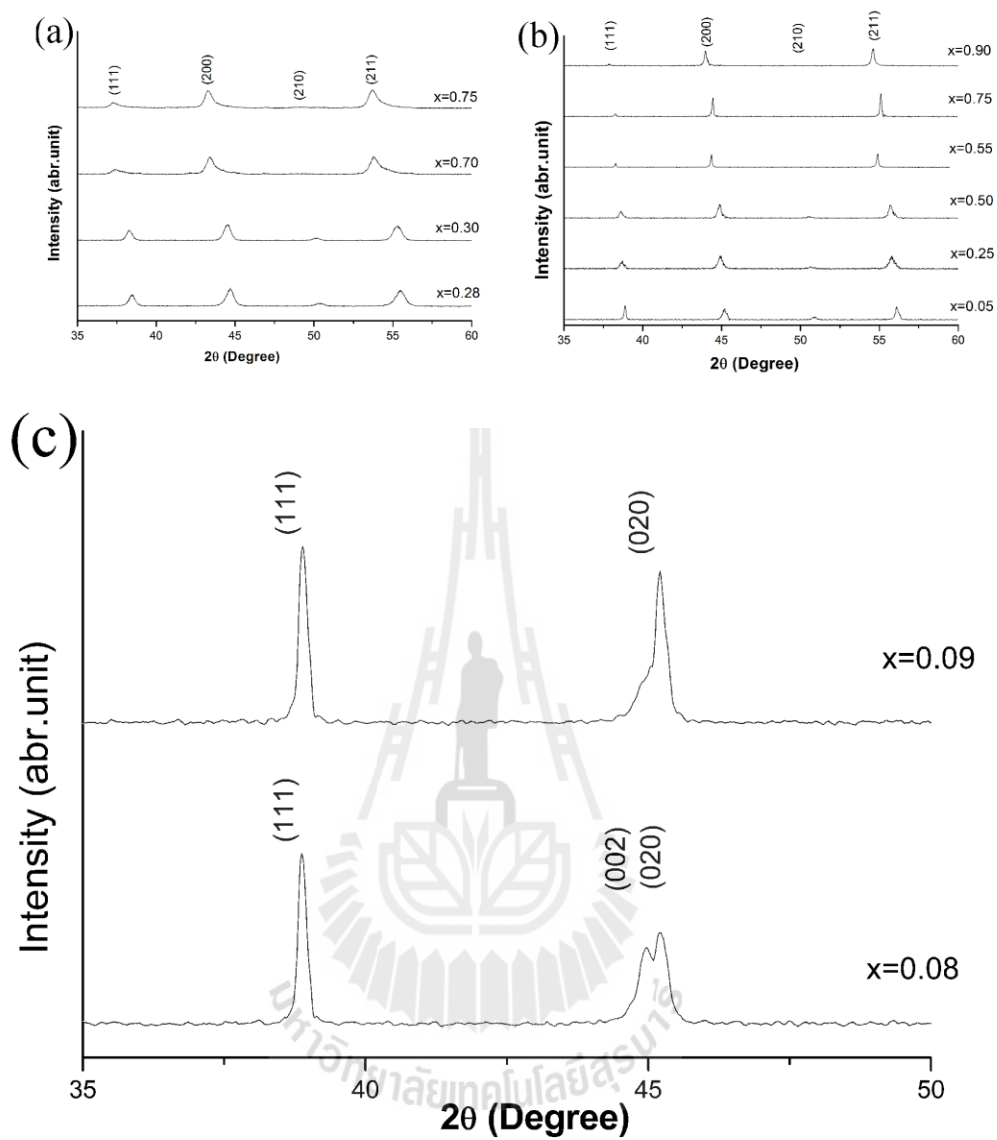


Figure 7.1 The XRD patterns at around phase transition (a) BZT (b) BST and (c) BT-BZnT

7.2 Local structure

The XAS results showed the local structure information around Ti and Zr for the phase transition of BZT, around Ti and Sn for BST and around Ti and Zn for BT-BZnT. In contrast to the XRD results, XAS results showed clearly the phase transition in BZT and BST systems. However, slight change in phase transition of BT-BZnT is observed, as shown in Figure. 7.2. This is possibly due to the local structure changes sensitively with bond length, and the bond length change slightly in BT-BZnT system. However, The phase fraction of Zn and Ti in BT-BZnT shows the presence of the composite material, not a solid solution. Both BZT and BST systems show clearer the phase transition than BT-BZnT system. Nevertheless, it is seen that XAS measurement is a powerful technique that can be used to observe the local site and surrounding atoms. Moreover, XANES results show electronic transitions which correspond with oxidation state and energy levels. Therefore, both XRD and XAS techniques provide a complementary observation of the crystal structure.

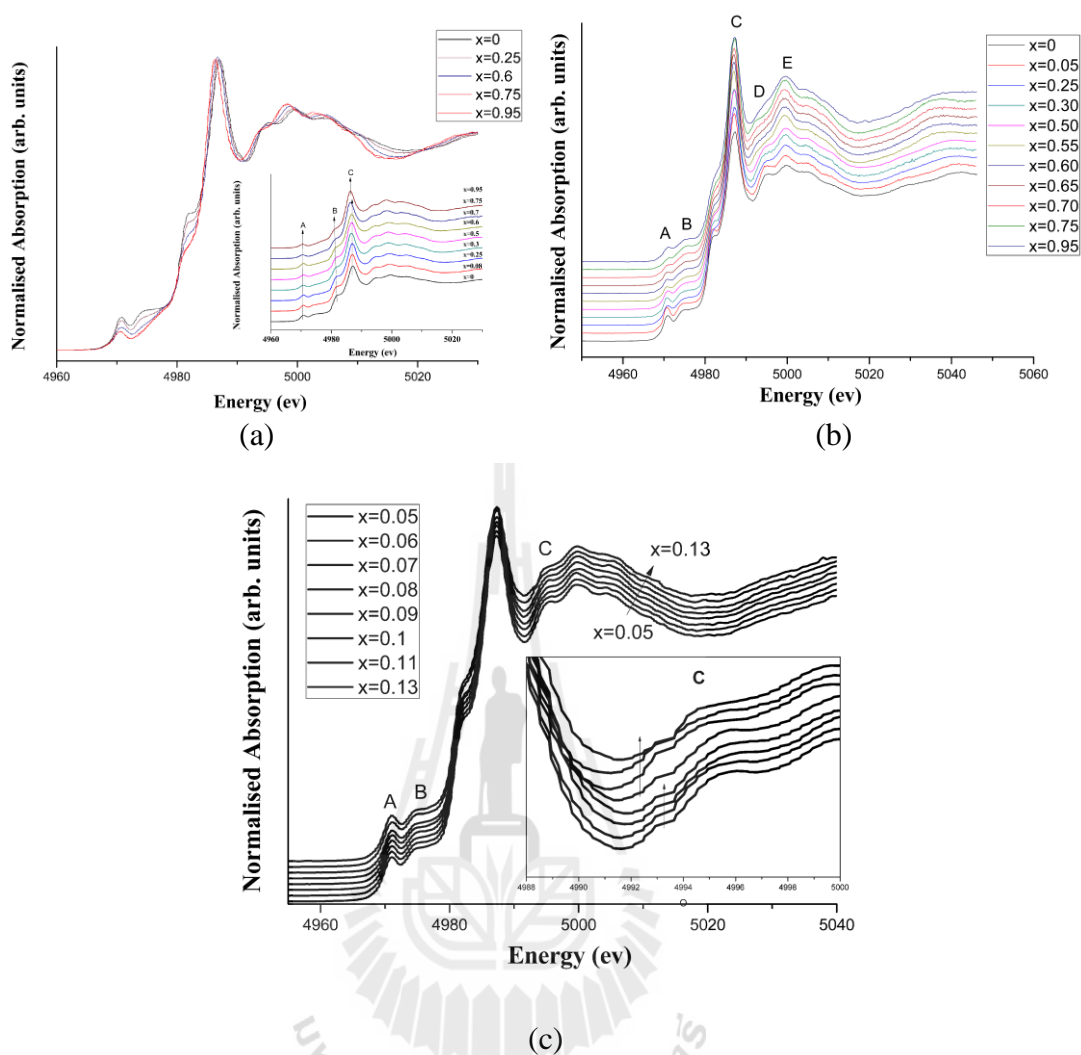


Figure 7.2 The normalized Ti K-edge XANES spectra (a) BZT (b) BST and (c) BT-BZnT

7.3 Dielectric properties

The dielectric permittivity indicates good capacitor and other electronic devices. Moreover, the temperature and frequency dependent dielectric permittivity can be used to determine a normal ferroelectric, relaxor, paraelectric, anti-ferroelectric and anti-paraelectric behaviors. BZT system exhibited the normal ferroelectric with shape peak of Curie temperature and T_m independent of frequencies at $x=0, 0.08$ and

0.25. The relaxor ferroelectrics have broad peak of Curie temperature and T_m dependent with frequencies around $0.28 < x < 0.70$. The polar cluster has a broad peak of Curie temperature and T_m dependent with applied electric field at $x < 0.75$. The XAS results corresponded well to dielectric properties. Therefore, we can understand better the local structure the change that can lead to the phase transition behavior as measured by dielectric properties. Similarly, BST system exhibited the normal ferroelectric at $x=0-0.05$ and relaxor at $x=0.25-0.5$, after then the polar cluster behavior exhibited. Since the ionic radii of Sn^{4+} is smaller than Zr^{4+} , the local structure in B-site or hole of oxygen octahedral is affected. On the other hand, BT-BZnT system exhibited the normal ferroelectric at $x=0-0.08$, and relaxor at $x \geq 0.09$. Zn^{2+} and Bi^{3+} are large atom in this system, employed to hold the box of unit cell perovskite in paraelectric phase with impact on unit cell of Ti atoms in central perovskite, which can change to rhombohedral structure. Moreover, both substitutions of Zr and Sn have impact on the stability of structure, and affect the decrease of Curie temperature. However, the substitution of Zn also affects the decrease of Curie temperature in tetragonal phase, but influences the increase of Curie temperature in rhombohedral phase.

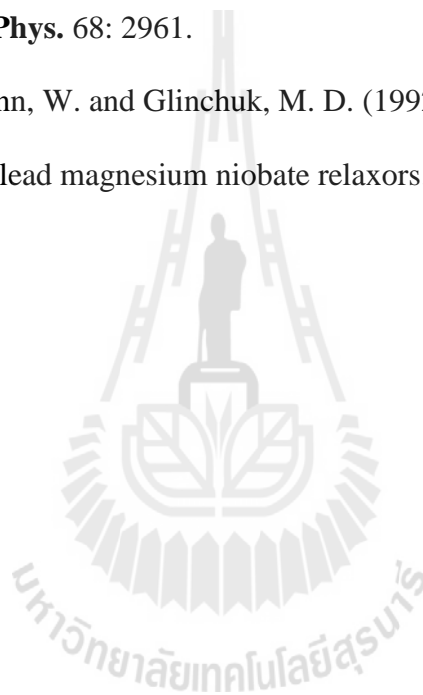
7.4 References

Cross, L. E. (1987). Relaxor ferroelectrics. **Ferroelectrics**. 76: 241.

Maiti, T., Guo, R. and Bhalla, A. S. (2006). The evolution of relaxor behavior in Ti^{4+} doped BaZrO_3 ceramics. **J. Appl. Phys.** 100: 114109.

Viehland, D., Jang, S. J., Cross, L. E. and Wuttig, M. (1990). Nonlinear Dielectric Response in Relaxor Ferroelectrics $(1-x)\text{Pb}(\text{Mg}_{1/2}\text{W}_{1/2})\text{O}_3-x\text{PbTiO}_3$ ($x=0.5$). **Jpn. J. Appl. Phys.** 68: 2961.

Westphal, V., Kleemann, W. and Glinchuk, M. D. (1992). Freezing of the polarization fluctuations in lead magnesium niobate relaxors. **Phys. Rev. Lett.** 68: 847.



CHAPTER VIII

CONCLUSIONS AND SUGGESTION

The global structural information was examined by X-ray Diffraction (XRD) techniques and Synchrotron X-ray Absorption Spectroscopy (XAS). In this work XAS technique was employed to investigate the local structure of the BaTiO₃-based relaxor ferroelectrics materials. The synchrotron XANES and EXAFS measurements were performed at the X-ray absorption spectroscopy beamlines (BL-8 and BL-5.2) of the Synchrotron Light Research Institute (SLRI, Thailand) for understanding the phase transition in the dielectric behavior which has a direct impact on centrosymmetric of perovskite structure.

In BZT system, the XRD results showed the *global* phase transition from tetragonal to cubic perovskite structure. However, the experimental and simulated XAS results, both in XANES and EXAFS regions, showed the *local* structural transition around Ti atom from *pseudo*-cubic to perfect cubic perovskite structure in Ba(Ti,Zr)O₃ or phase transition of relaxor ferroelectric to polar cluster.

In BST system, the *global* phase transition from tetragonal to cubic perovskite structure was observed by XRD results. However, the XRD results did not correspond to the dielectric properties. In addition, the experimental XAS results, both in XANES and EXAFS regions, showed the *local* structural transition around Ti atom from tetragonal to *pseudo*-cubic and *pseudo*-cubic to perfect cubic perovskite structure in

Ba(Ti,Sn)O₃ or phase transition of normal to relaxor ferroelectric and relaxor to polar cluster. Moreover, XANES spectra were confirmed by the simulated spectra.

In BT-BZnT system, the XRD results showed the *global* phase transition clearly from tetragonal to rhombohedral perovskite structure. In addition, the experimental XANES spectra result showed the starting *local* structural change which corresponded to phase transition from normal ferroelectric to relaxor behavior as seen from the dielectric properties.

This study has clearly shown an excellent agreement between the XRD and XAS techniques and the experimentally observed dielectric properties. It is suggested that a combination of XAS and other conventional techniques should also provide a powerful characterization tool for several smart materials, especially smart nano materials. In the future work, in BST system, we should synthesize the composition between $x=0.3-0.5$ because the phase fraction in relaxor region is not seen clearly. Moreover, we should investigate the local structure under various environments such as temperature, electric field, frequencies and pressure etc.



APPENDIX

APPENDIX

Conference and Presentations

Atipong Bootchanont, Muangjai Unruan, Jaru Jutimoosik, Saroj Rujirawat, Rattikorn Yimnirun “Synchrotron X-ray Absorption Spectroscopy Investigation of $\text{BaTi}_{1-x}\text{Zr}_x\text{O}_3$ ”, The 4th International Symposium on Functional Materials (ISFM2011), Sendai, Japan.

Atipong Bootchanont, Muangjai Unruan, Jaru Jutimoosik, Saroj Rujirawat, Rattikorn Yimnirun, Ruyan Guo, Amar Bhalla “X-ray Absorption Fine Structure Study of Phase Transition in $\text{Ba}(\text{Ti,Zr})\text{O}_3$ Perovskite”, The 8th Asian Meeting on Ferroelectrics (AMF-8), 19 December 2012, Ameri Hotel pattaya, Thailand.

Atipong Bootchanont, Saroj Rujirawat, Pinit Kidkhunthod, Rattikorn Yimnirun, “Identification of Sn Site in BaTiO_3 by Synchrotron X-ray Absorption Spectroscopy”, Siam Physics Congress SPC2013, Chaing Mai, Thailand.

Atipong Bootchanont, Saroj Rujirawat, Rattikorn Yimnirun, Ruyan Guo, Amar Bhalla “Local structure and evolution of relaxor behavior in BaTiO_3 - $\text{Bi}(\text{Zn}_{0.5}\text{Ti}_{0.5})\text{O}_3$ ceramics”, THE 3rd ACADEMIC CONFERENCE ON NATURAL SCIENCE FOR MASTER AND PhD STUDENTS FROM ASEAN COUNTRIES (CASEAN 2013), 11-15 November 2013, Phnom Penh, Cambodia.

Abstract submitted for International Symposium on Functional Materials 2011, Japan

X-ray absorption fine structure studies of perovskite $\text{BaTi}_{1-x}\text{Zr}_x\text{O}_3$

Atipong Bootchanont^{1,*}, Rattikorn Yimnirun¹, Muangjai Unruan¹,
Jaru Jutimoosik¹ and Saroj Rujirawat^{1,2,3}

¹School of Physics, Institute of Science, Suranaree University of Technology, Nakhon Ratchasima 30000, Thailand

²ThEP Center, CHE, 328 Si Ayutthaya Road, Bangkok 10400, Thailand
and

³Synchrotron Light Research Institute (Public Organization), Nakhon Ratchasima 30000, Thailand

*a.bootchanont@gmail.com

Barium zirconium titanate (BZT) is an important electronic ceramic material used in capacitors, piezoelectric, transducers and actuators. Recently some researchers have not observed structural carefully of relaxor behavior in Zr^{4+} doped BaTiO_3 by XRD studied, but X-ray Absorption spectroscopy (XAS) can be observed structure of material in angstrom-scale. The synchrotron XANES and EXAFS measurements were performed at the X-ray absorption spectroscopy beamline (BL-8) of the Synchrotron Light Research Institute (SLRI, Thailand). In this work, we investigated the change of the local atomic structure around titanium and zirconium ions of $\text{BaTi}_{1-x}\text{Zr}_x\text{O}_3$ ($x=0.1-0.5$) were prepared via the conventional solid state reaction method using XAS techniques. XANES and EXAFS spectra at the Ti *K-edge* and Zr *L-edge* were analyzed and compared by first principle calculation, will be explain the increase of Zr^{4+} doped BaTiO_3 affect to local structure, while information on the locally determined structures of the ferroelectric relaxor behavior compositions of $\text{BaTi}_{1-x}\text{Zr}_x\text{O}_3$ was also obtained.

Abstract submitted for the 8th Asian Meeting on Ferroelectrics, Thailand.

X-ray Absorption Fine Structure Study of Phase Transition in Ba(Ti,Zr)O₃ Perovskite

Atipong Bootchanont^{1,*}, Muangjai Unruan¹, Sujitra Chandarak¹

Jaru Jutimoosik¹, Saroj Rujirawat^{1,2} and Rattikorn Yimnirun¹

¹*School of Physics, Institute of Science, Suranaree University of Technology, Nakhon Ratchasima, 30000, Thailand*

²*Thailand Center of Excellence in Physics (THEP Center) Commission on Higher Education, Bangkok, 10400, Thailand*

In this work, BaTi_{1-x}Zr_xO₃ (x=0-0.95) were prepared via the conventional solid state reaction method and the change of the local atomic structure around titanium ions was investigated using XAS techniques at the X-ray absorption spectroscopy beam line (BL-8) of the Synchrotron Light Research Institute (SLRI, Thailand). The X-ray Absorption Near-Edge Structure (XANES) and Extended X-ray Absorption Fine Structure (EXAFS) spectra at the Ti *K-edge* were measured and compared with simulation done by FEFF program. The results showed that an increase of Zr content in BaTiO₃ affected the phase transition and local structure of BZT, while information on the locally determined structures of BaTi_{1-x}Zr_xO₃ was also obtained and discussed.

***Presenting author's email:** a.bootchanont@gmail.com

Abstract submitted for the Siam Physics Congress 2013, Thailand.

Siam Physics Congress SPC2013
Thai Physics Society on the Road to ASEAN Community 21-23 March 2013

Identification of Sn Site in BaTiO₃ by Synchrotron X-ray Absorption Spectroscopy

Atipong Bootchanont^{1,*}, Pinit Kidkhunthod², Saroj Rujirawat^{1,3}

and Rattikorn Yimnirun¹

¹*School of Physics, Institute of Science, Suranaree University of Technology,
Nakhon Ratchasima, 30000, Thailand*

²*Synchrotron Light Research Institute, Nakhon Ratchasima, 30000, Thailand*

³*Thailand Center of Excellence in Physics (ThEP Center) Commission on
Higher Education, Bangkok, 10400, Thailand*

*Corresponding author. E-mail: a.bootchanont@gmail.com

Abstract

In this work, Sn-doped BaTiO₃ (BSnT) samples were prepared via the conventional solid state reaction method. Synchrotron x-ray absorption near-edge structure (XANES) and extended x-ray absorption fine structure experiments were performed on Sn *L*₃-edge of Sn-doped BaTiO₃ samples and compared with XANES simulations by FEFF8.2 program. The results showed the measured Sn *L*₃-edge XANES were consistent with the XANES simulations of Sn on the Ti site in BT and inconsistent with Sn in the other sites. The good agreement between measured and calculated XAS results clearly indicated the Ti-site substitution of Sn in BaTiO₃ structure.

Keywords: X-ray absorption, XANES, and BaTiO₃.

Abstract submitted for the 3rd ACADEMIC CONFERENCE ON NATURAL SCIENCE FOR MASTER AND PhD STUDENTS FROM ASEAN COUNTRIES (CASEAN 2013), Cambodia.

Local structure and evolution of relaxor behavior in $\text{BaTiO}_3\text{-Bi}(\text{Zn}_{0.5}\text{Ti}_{0.5})\text{O}_3$ ceramics

Atipong Bootchanont^{*,a}, Saroj Rujirawat^{a,b}, Rattikorn Yimnirun^a, Ruyan Guo^c, Amar Bhalla^c

^{a)} School of Physics, Institute of Science, Suranaree University of Technology, and COE-NANOTEC-SUT on Advanced Functional Nanomaterials, Nakhon Ratchasima 30000, Thailand

^{b)} ThEP Center, CHE, 328 Si Ayutthaya Road, Bangkok 10400, Thailand

^{c)} Department of Electrical and Computer Engineering, College of Engineering, University of Texas at San Antonio, Texas 78249, USA

E-mail: a.bootchanont@gmail.com

In this work, we have studied the local structure relate to relaxor ferroelectric behavior of $(1-x)\text{BaTiO}_3\text{-}x\text{Bi}(\text{Zn}_{0.5}\text{Ti}_{0.5})\text{O}_3$ ($x=0.05\text{-}0.13$) ceramics. The evolution of relaxor behavior of $(1-x)\text{BaTiO}_3\text{-}x\text{Bi}(\text{Zn}_{0.5}\text{Ti}_{0.5})\text{O}_3$ (BT-BZT) solid solution respect to the increasing $\text{Bi}(\text{Zn}_{0.5}\text{Ti}_{0.5})\text{O}_3$ content in BaTiO_3 induce to the phase transition of tetragonal to rhombohedral structure, is analyzed by XRD technique. In addition, the local atomic structure of Ti atoms in BT-BZT was investigated by synchrotron x-ray absorption spectroscopy. Investigation of dielectric constant on various temperatures, exhibit the phase transition from normal ferroelectric to relaxor. The determination of evolution of polar regions in relaxor ferroelectricity with a characteristic cooperative freezing temperature follows Vogel-Fulcher relation on frequency dependence.

International Publications

1. **Atipong Bootchanont**, Jaru Jutimoosik, Sujittra Chandarak, Muangjai Unruan, Saroj Rujirawat, Rattikorn Yimnirun, Ruyan Guo and Amar Bhalla, “Investigation of Local Structure in BaTiO₃-BaZrO₃ System by Synchrotron X-ray Absorption Spectroscopy” **Ceramic International**, 0272-8842(2012).

2. **Atipong Bootchanont**, Narit Triamnak, Saroj Rujirawat, Rattikorn Yimnirun, David P. Cann, Ruyan Guo, and Amar Bhalla, " Local structure and evolution of relaxor behavior in BaTiO₃-Bi(Zn_{0.5}Ti_{0.5})O₃ ceramics" **Ceramic International** 40, 14555-14562(2014).

3. **Atipong Bootchanont**, Jaru Jutimoosik, Sujittra Chandarak, Muangjai Unruan, Pinit Kidkhunthod, Wantana Klysubun, Saroj Rujirawat, **Rattikorn Yimnirun**, Ruyan Guo and Amar Bhalla, Synchrotron X-ray Absorption Spectroscopy Study of Local Structure Transformation Behavior in Perovskite Ba(Ti,Zr)O₃ System" **Journal of Alloys and Compounds**, 616 430–435(2014).

4. Sujittra Chandarak, Jaru Jutimoosik, **Atipong Bootchanont**, Muangjai Unruan, Pongsakorn Jantaratana, Shashank Priya, Sutham Srilomsak, Saroj Rujirawat, Rattikorn Yimnirun, “Local Structure of Magnetoelectric BiFeO₃-BaTiO₃ Ceramics Probed by Synchrotron X-Ray Absorption Spectroscopy”, **Journal of Superconductivity and Novel Magnetism**, 26 : 455-461(2013).

5. Natkrita Prasoetsopha, Supree Pinitsoontorn, **Atipong Bootchanont**, Pinit Kidkhunthod, Pornjuk Srepusharawoot, Teerasak Kamwanna, Vittaya Amornkitbamrung, Ken Kurosaki, Shinsuke Yamanaka, “Local structure of Fe in Fe-doped misfit-layered calcium cobaltite: an X-ray absorption spectroscopy study”,

6.

J. Solid State Chemistry, 204, 257-265 (2013).

7. Supree Pinitsoontorn , Natkrita Prasoetsopha, Pornjuk Srepusharawoot, **Atipong Bootchanont**, Pinit Kidkhunthod, Teerasak Kamwanna, Vittaya Amornkitbamrung, Ken Kurosaki, and Shinsuke Yamanaka, “Local structure determination of substitutional elements in $\text{Ca}_3\text{Co}_{4-x}\text{M}_x\text{O}_9$ (M=Fe, Cr, Ga) using X-ray absorption spectroscopy”, **Physica Status Solidi A**, 1–8 (2014).

8. Narinthorn Wiriya, **Atipong Bootchanont**, Santi Maensiri, Ekaphan Swatsitang, “XANES analysis of $\text{Mn}_{1-x}\text{Co}_x\text{Fe}_2\text{O}_4$ nanoparticles prepared by hydrothermal method”, **Japanese Journal of Applied Physics** 53, 06JF09 (2014).

9. Narinthorn Wiriya, **Atipong Bootchanont**, Santi Maensiri, Ekaphan Swatsitang, “Magnetic properties of $\text{Zn}_{1-x}\text{Mn}_x\text{Fe}_2\text{O}_4$ nanoparticles prepared by hydrothermal method”, **Microelectronic Engineering**. 126, 1-8(2014).

10. Orapan Saensuk, Santi Maensiri, **Atipong Bootchanont** and Ekaphan Swatsitang, “Fabrication and magnetic properties of eletrospun $\text{Ni}_{1-x}\text{Cu}_x\text{Fe}_2\text{O}_4$ nanofiber”, **Microelectronic Engineering**. 126,158-164(2014).



Synchrotron X-ray absorption spectroscopy study of local structure transformation behavior in perovskite Ba(Ti,Zr)O₃ system



Atipong Bootchanont^{a,*}, Jaru Jutimoosik^a, Sujittra Chandarak^b, Muangjai Unruan^c, Pinit Kidkhunthod^d, Wantana Klysubun^d, Saroj Rujirawat^a, Rattikom Yimnirun^a, Ruyan Guo^e, Amar Bhalla^e

^aSchool of Physics, Institute of Science, Suranaree University of Technology, COE-NANOTEC-SUT on Advanced Functional Nanomaterials, Nakhon Ratchasima 30000, Thailand

^bDepartment of Materials Engineering, Faculty of Engineering and Architecture, Rajamangala University of Technology Isan, Nakhon Ratchasima 30000, Thailand

^cDepartment of Applied Physics, Faculty of Science and Liberal Arts, Rajamangala University of Technology Isan, Nakhon Ratchasima 30000, Thailand

^dSynchrotron Light Research Institute, Nakhon Ratchasima 30000, Thailand

^eDepartment of Electrical and Computer Engineering, College of Engineering, University of Texas at San Antonio, TX 78249, USA

ARTICLE INFO

Article history:

Received 3 June 2014

Received in revised form 22 July 2014

Accepted 22 July 2014

Available online 30 July 2014

Keywords:

Relaxor

Phase transition

Local structure

XANES

EXAFS

ABSTRACT

In this work, the change of the local atomic structure in BaTi_{1-x}Zr_xO₃ ceramics was investigated by synchrotron X-ray absorption spectroscopy technique. The X-ray Absorption Near-Edge Structure (XANES) and Extended X-ray Absorption Fine Structure (EXAFS) spectra at the Ti K-edge were measured and compared with simulated spectra. The results show that an increase of Zr content in Ba(TiZr)O₃ lattice structure affected significantly the phase transition behavior and the local structure surrounding the Ti absorbing atom. More importantly, the information on the locally determined structures and its relation to the phase transition characteristic from relaxor ferroelectric to polar clusters in Ba(TiZr)O₃ system were obtained and discussed.

© 2014 Elsevier B.V. All rights reserved.

1. Introduction

The prototypic ferroelectric barium titanate (BaTiO₃:BT), discovered in 1941 [1], exhibits ferroelectric behavior with high dielectric constant. Moreover, BT is lead-free perovskite material. Therefore, BT is environmental friendly and non-toxicity. However, dielectric properties of BT is lower than Pb(Zr,Ti)O₃ (PZT). In the recent years, it has been found that the substitution of Zr in BT or barium zirconium titanate (Ba(Zr,Ti)O₃ or BZT) has become one of the attractive candidates for various electronic devices.

The ferroelectric behavior is classified with spontaneous polarization dependent dielectric properties. Particularly, it is of great interest because barium zirconate (BaZrO₃:BZ) exhibits non-polar or paraelectric behavior, which does not have spontaneous polarization. It has been found that increasing Zr substitution into the Ti site in BaTiO₃ lattice can change the material to exhibit relaxor ferroelectric behavior [2–5]. If Zr is substituted into the Ti site in BaTiO₃ by more than 70 mol%, BZT exhibits polar clusters like behavior [2–4]. Moreover, the relaxor ferroelectric behavior is characterized with strong frequency-dependent dielectric

properties. It has been reported that, with the incorporation of Zr in BT, the rhombohedral to orthorhombic (T₁) and orthorhombic to tetragonal (T₂) phase transition temperatures increase, as compared to pure BT [2,3,6].

Recently, it has been reported that the Ba(Zr_xTi_{1-x})O₃ compositions with $x = 0$ and 0.005 contained the tetragonal BT phase [5]. With $x = 0.02$, the ceramic contained a mixture of the tetragonal and orthorhombic structures, whereas the $x = 0.04$ sample exhibited primarily the orthorhombic phase. For $x = 0.12$, the crystal structure then became cubic [5]. While it is clearly intuitive to expect the role of locally arranged lattice structure in determining the phase transition behavior and relevant properties of BZT material, the prior investigations usually employed only a global structural determination technique, such as X-ray Diffraction (XRD). In the present study, we employed the local structure sensitive Synchrotron X-ray Absorption Spectroscopy (XAS) technique to obtain the local structure information around the Ti atom in the ferroelectric region of Ba(Zr_xTi_{1-x})O₃ with hope to better understand how the local structure is related to the properties of ferroelectric transition.

2. Experimental

BaZr_xTi_{1-x}O₃ powders were synthesized by a conventional solid state reaction method. The materials were weighed according to BaZr_xTi_{1-x}O₃ composition with $x = 0.0, 0.08, 0.2, 0.3, 0.5, 0.6, 0.7, 0.75, 0.95$ and 1 from the starting BaCO₃

* Corresponding author.

E-mail address: a.bootchanont@gmail.com (A. Bootchanont).

($\geq 99.99\%$), TiO_2 ($\geq 99.96\%$) and ZrO_2 ($\geq 99.54\%$) powders, then ball milled in ethanol solution for 24 h for thorough mixing. The mixed powders were calcined at temperature of 1250°C for 2 h with $5^\circ\text{C}/\text{min}$ heating/cooling rates [7–11].

The global structure of $\text{Ba}(\text{Zr}_x\text{Ti}_{1-x})_2\text{O}_7$ was investigated by X-ray diffraction (XRD) method in 2θ range of 20 – 60° with 0.02° step and $\text{Cu K}\alpha$ radiation. The local structure was investigated at room temperature using Synchrotron X-ray Absorption Spectroscopy (XAS) measurements at BL-8 of the Siam Photon Laboratory, Synchrotron Light Research Institute (SLRI), Thailand (electron energy of 1.2 GeV and beam current 80 – 120 mA). The synchrotron X-ray beam with energy step of 0.20 eV was provided to excite the electrons in Ti K -edge. The Ti K -edge X-ray Absorption Near-Edge Structure (XANES) spectra for all compositions were obtained. The data were processed using the ATHENA program. The simulation was carried out using the FEFF8.2 program and qualitatively compared with XANES patterns obtained from the experiment. In addition, Extended X-ray Absorption Fine Structure (EXAFS) spectra were collected for some compositions and processed using the ARTEMIS program [7,12,13].

3. Results and discussion

3.1. XRD analysis

The XRD patterns of $\text{Ba}(\text{Zr}_x\text{Ti}_{1-x})_2\text{O}_7$ powders are shown in Fig. 1. It is seen that the global crystal structure, as determined by XRD, changes from tetragonal to cubic perovskite phases with increasing Zr concentration in BaTiO_3 lattice. The sample with $x=0$ (pure BT) shows the tetragonal perovskite phase, while the samples at $0.25 \leq x \leq 0.7$ exhibit the broad XRD peaks. The compositions with $x \geq 0.75$ also exhibit the broad peaks with the cubic perovskite structure. The standard tetragonal perovskite BaTiO_3 phase and cubic perovskite BaZrO_3 are also shown (matched with JCPDS file No. 81-2201 and 74-1299, respectively). The lattice constant of the cubic phase increases continuously with increasing Zr concentration. The XRD results show a noticeable change in the global structure across the compositional range studied. Fig. 2 displays the change in the lattice parameter with Zr content and corresponding electrical behavior in each region; i.e., normal ferroelectric ($0 \leq x \leq 0.27$), relaxor ferroelectric ($0.27 \leq x \leq 0.75$), and polar clusters ($x \geq 0.75$). In addition, the solid arrow line indicates a region of mixed tetragonal-orthorhombic perovskite phase ($0 < x < 0.12$), and a region of cubic perovskite symmetry ($x \geq 0.12$). However, the exact crystal symmetry is not clearly seen from the XRD study and the cubic structure region could also be identified as "pseudo-cubic".

3.2. XANES measurement and simulation

The normalized Ti K pre-edge XANES spectra of $\text{Ba}(\text{Zr}_x\text{Ti}_{1-x})_2\text{O}_7$ powders are shown in Fig. 3(a). Generally, XANES measures the excitation of core electrons to unoccupied bound states and is thus

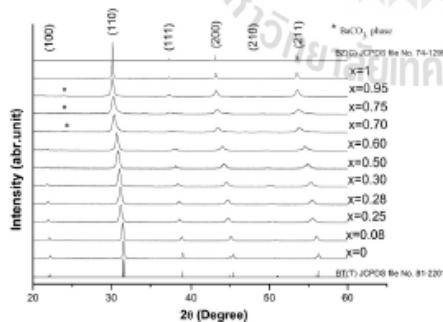


Fig. 1. X-ray diffraction patterns of $\text{Ba}(\text{Zr}_x\text{Ti}_{1-x})_2\text{O}_7$ powders for each composition at room temperature.

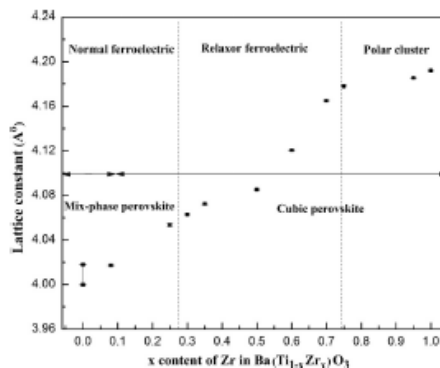


Fig. 2. Phase diagram of $\text{Ba}(\text{Ti}_{1-x}\text{Zr}_x)_2\text{O}_7$ compound as a function of Zr content, based on XRD at room temperature.

used to obtain information about the local arrangement of atoms around the absorbing atoms and the density of states of unoccupied states [14]. As seen in Fig. 3(a), the intensity of peak A (I_A), which is associated with both the quadrupole and the dipole $1s \rightarrow 3d$ transition of Ti, reflects the $3d$ – $4p$ hybridization for Ti. In addition, the intensity of peak B relates to the ratio of Zr/Ti in the third shell. In Fig. 3(b), local Ti off-centering is manifested in the Ti K pre-edge peak in X-ray absorption spectra [15]. The integrated intensity of this peak (Fig. 3(a)) is directly proportional to the mean-squared displacements of Ti (δ_{Ti}) off the instantaneous centers of oxygen octahedral (and is indirectly proportional to the lattice constants) following Eq. (1):

$$A = \gamma_2 (\delta_{\text{Ti}})^2 / 3 \quad (1)$$

where A is the integrated intensity or area of peak, γ_2 is an experimentally determined of constant using Ravel's method with an error bar of about $\pm 3\text{ eV}/\text{Å}^2$ [15] and δ_{Ti} is the mean-squared displacement of Ti ions from the center of oxygen octahedral [14–16]. This value δ_{Ti} is adopted as a reference for calculating local Ti off-centering from the pre-edge peak intensities in the solid-solution samples (Fig. 3(b)). The local value of δ_{Ti} in BZT, when Zr content is increasing decreases continuously until $x=0.5$, then increases in the relaxor ferroelectric region. After that, a drop at $x=0.75$ in paraelectric region is also larger than the expected change from the relaxor ferroelectric to polar cluster, and a local Ti off-center decreases. Furthermore, while XANES spectra indicate little difference in features for compositions with $0 \leq x \leq 0.7$, at $x \geq 0.75$ (Fig. 4), the spectra exhibit a significant change in features with the shift in the peak C to the left-hand side, indicating change in the local structure around Ti absorbing atom. For $x=0.95$ the features are similar to that of $x=0.75$. Moreover, according to Maiti et al. [3], it is found that the electrical behavior of $\text{Ba}(\text{Ti}_x\text{Zr}_{1-x})_2\text{O}_7$ at $x > 0.75$ changes from relaxor ferroelectric to polar clusters. This means that Ti atoms should move locally toward the center of oxygen octahedral or the isolated BT clusters do not communicate with each other and cannot switch themselves and respond collectively with the applied electric field. This shift in the location of Ti cannot be observed by XRD and several other conventional techniques for structural determination.

The XANES spectrum can be simulated using the unoccupied electronic states of the system, as described below. The X-ray absorbance $\mu(E)$ is given by Fermi's golden rule as

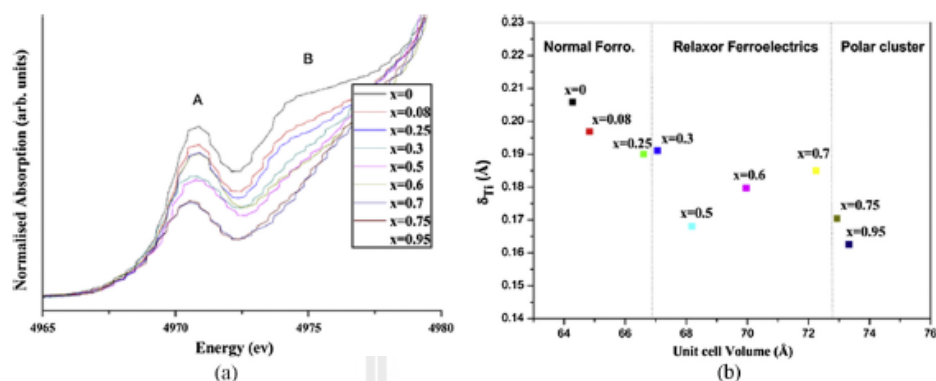


Fig. 3. (a) Normalized X-ray absorption Ti K pre-edge spectra of $\text{Ba}(\text{Zr}_x\text{Ti}_{1-x})_2\text{O}_7$ powders. (b) δ_{Ti} determined from the intensity of the pre-edge peak as a function of the unit-cell. The value of δ_{Ti} for $\text{Ba}(\text{Zr}_x\text{Ti}_{1-x})_2\text{O}_7$ was determined using the spectrum reported in Ref. [16].

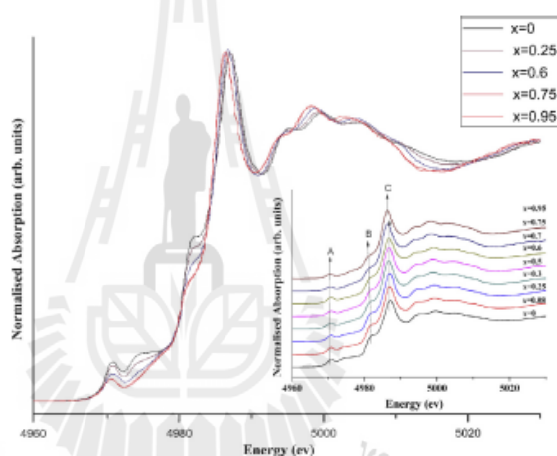


Fig. 4. Normalized X-ray absorption Ti K-edge spectra of $\text{Ba}(\text{Zr}_x\text{Ti}_{1-x})_2\text{O}_7$ powders for each composition at room temperature.

$$\mu(E) \propto \sum_f |D_{if}|^2 \delta(E_f - E_i + E), \quad (2)$$

where $|i\rangle$, $|f\rangle$, E_i , and E_f are the initial and final states and their energies, respectively; E are the photon energy and D dipole operator [17,18]. Simulated XANES spectra of Ti K-edge in Zr-deficient $\text{Ba}(\text{Ti,Zr})_2\text{O}_7$ and Zr-enriched $\text{Ba}(\text{Ti,Zr})_2\text{O}_7$ were obtained using the FEFF8.2 code. The FEFF code employs a full multiple scattering approach based on *ab initio* overlapping muffin-tin potentials. The muffin-tin potentials used in FEFF codes are self-consistent calculations with Hedin–Lundqvist exchange–correlation function [18,19]. It should be noted here first that, to simulate the XANES spectra of Ti, the structural model with Ti-off center in a rather perfect rhombohedral perovskite structure ($\alpha - \beta - \gamma = 89.96^\circ$) was used for the pseudo-cubic symmetry, while a nearly perfect cubic structural model ($\alpha - \beta - \gamma = 89.99^\circ$) with Ti moving toward the center was

used in the cubic symmetry case. The perfect rhombohedral ($\alpha - \beta - \gamma = 89.5^\circ$) and tetragonal ($\alpha - \beta - \gamma = 90^\circ$) perovskite structures were also calculated for comparison. The self-consistent calculation was performed in sphere radius of 4.2, 4.3, 4.4 and 4.5 Å, respectively, for rhombohedral and cubic structure around the absorber Ti K-edge in the system and the full multiple scattering calculations include all possible paths within a larger cluster radius of 6.0 Å.

The simulation of the XANES spectra of the BZT phase was subsequently carried out to investigate the feature around Ti absorbing atoms in BZT solid solution with the simulated and experimental results compared in Fig. 5. It is shown that the simulated spectra of the perfect rhombohedral and tetragonal perovskite structures are not in good agreement with the measurements. However, the simulated spectral features from the pseudo-cubic (or the rather perfect rhombohedral) structure

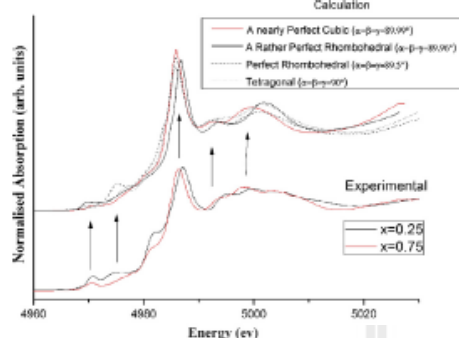


Fig. 5. Comparison of Normalized X-ray absorption Ti K-edge spectra of $\text{Ba}(\text{Zr}_x\text{Ti}_{1-x})\text{O}_3$ ($x=0.25$ and 0.75) with the simulated features of Ti K-edge XANES spectra of $\text{Ba}(\text{Zr,Ti})_2\text{O}_7$ -pseudo cubic (red-line), a nearly perfect cubic (black line), rhombohedral (dash-line), tetragonal perovskite (dot-line). (For interpretation of the references to color in this figure legend, the reader is referred to the web version of this article.)

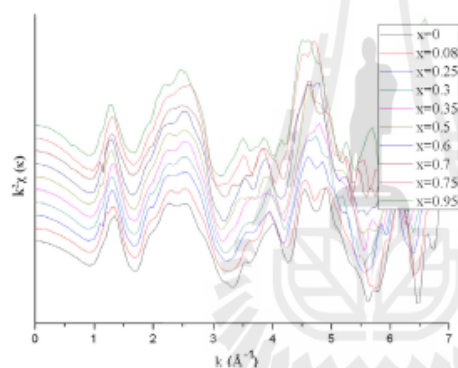


Fig. 6. The EXAFS Fourier transform in k -space of $\text{Ba}(\text{Ti,Zr})_2\text{O}_7$ powders.

$\text{Ba}(\text{Ti,Zr})\text{O}_3$ and a nearly perfect-cubic $\text{Ba}(\text{Ti,Zr})\text{O}_3$ are in good agreement with the experimental XANES spectra. This agreement between the experimental and simulated spectra indicates that for $\text{Ba}(\text{Ti,Zr})\text{O}_3$ compositions with lower Zr contents the local structure around Ti atom is in the pseudo-cubic symmetry (or the rather perfect rhombohedral model), even though the XRD results exhibit the (global) cubic perovskite structure. This new result is also consistent with the electrical properties which for $x \leq 0.7$ $\text{Ba}(\text{Ti}_{1-x}\text{Zr}_x)\text{O}_3$ ceramics exhibit ferroelectric characteristics with spontaneous polarization from local ionic distortion of Ti atoms. On the other hand, when $x > 0.7$, $\text{Ba}(\text{Ti}_{1-x}\text{Zr}_x)\text{O}_3$ ceramics show a polar cluster behavior with very small local spontaneous polarization; hence, the structure is close to perfect cubic perovskite, as observed in both XAS and XRD measurements.

3.3. EXAFS analysis

EXAFS spectra result from the back scattering of the spherical electron wave by the neighbors of the central absorbing atom, resulting in oscillations in the energy dependence of the absorption

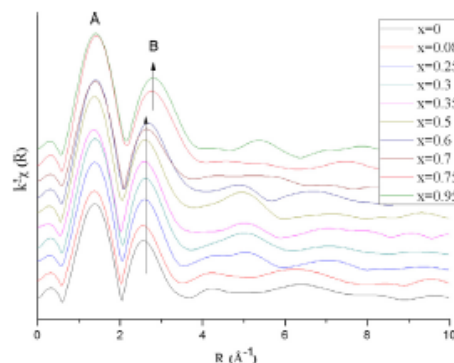


Fig. 7. The EXAFS Fourier transform in R -space of $\text{Ba}(\text{Ti,Zr})_2\text{O}_7$ powders.

coefficient $\mu(E)$ after the energy edge [17,18]. The normalized experimental EXAFS signal is

$$\chi(E) = [\mu(E) - \mu_0(E)] / \Delta\mu_0(E) \quad (3)$$

where μ_0 is the background absorption coefficient, $\Delta\mu_0(E)$ is the absorption edge jump, and k is the photoelectron wave number, given by $k = \sqrt{2m_e(E - E_0)}/\hbar$ with m_e is the electron mass and E_0 is the edge energy. $\chi(k)$ is obtained from the measured absorption coefficient, $\mu(E)$ by using the ATHENA program. E_0 is obtained by talking the first maximum of the derivative of $\mu(E)$ at the Ti K-edge 20,21,17. In general, $\chi(k)$ can be expressed by classical EXAFS equation as

$$\chi(k) = \sum_j \frac{S_0^2 N_j}{k R_j^2} |f_j^{\text{eff}}(k, R_j)| \sin [2kR_j + \varphi_j(k)] e^{-2\sigma_j^2 k^2} e^{-R_j/\lambda(k)} \quad (4)$$

where N_j is the degeneracy of path j , R_j its half-length, and its effective scattering amplitude. The Debye-Waller (DW) factor σ_j^2 is the standard deviation of the R_j distance distribution, assumed to be Gaussian. The DW factor takes into account both the thermal disorder and a possible small structural disorder. $\varphi_j(k)$ are the potentials of the absorbing site and scattering sites [17]. The other parameters are the photoelectron mean-free path $\lambda(k)$ and an overall amplitude factor S_0^2 , which is close to 1 and accounts for many-electron effects in the excited central atom. Note that Eq. (4) includes both single (back-) scattering (SS) and multiple scattering (MS) processes. For a SS path, N_j is simply the number of chemically identical atoms situated at a given distance R_j from the central atom. However, $\chi(k)$ can be a Fourier transform (FT) in R -space and expressed by

$$\chi(R) = \frac{1}{\sqrt{2\pi}} \int_0^\infty k^2 \chi(k) W(k) e^{i2kR} dk \quad (5)$$

To process and enhance the EXAFS within the high k region, the plot $k^2\chi(k)$ is considered and windowed using a Hanning window $W(k)$. The EXAFS spectra were processed, and information on local structure of the Ti atom via fitting with pseudo-cubic perovskite models of $\text{Ba}(\text{Ti,Zr})\text{O}_3$ in ARTEMIS program were obtained. In this work, the Ti K-edge EXAFS spectra can only be obtained up to photon energy of 250 eV above the absorption edge, due to the presence of Ba L_3 -edge. Therefore, EXAFS spectral fitting can only be performed up to the second shell; i.e. the first shell-oxygen octahedral and second shell of 8-fold coordination. Figs. 6 and 7 show the EXAFS Fourier Transform in k -space and R -space, respectively. For $x = 0.7$ – 0.75 , the trend of the peak B features change and correspond with XANES results and phase transition from relaxor to polar cluster.

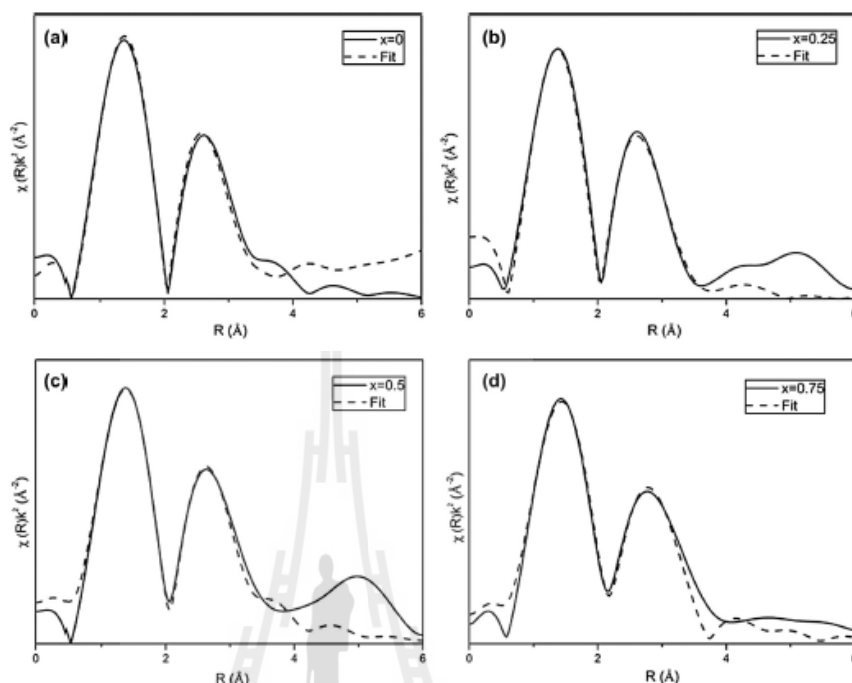


Fig. 8. Experimental and calculated (solid/dot) magnitude of EXAFS Fourier transform for (a) BaTiO_3 , (b) $\text{BaTi}_{0.75}\text{Zr}_{0.25}\text{O}_3$, (c) $\text{BaTi}_{0.50}\text{Zr}_{0.50}\text{O}_3$, and (d) $\text{BaTi}_{0.25}\text{Zr}_{0.75}\text{O}_3$. The k range used in the fit is from 2 to 5.7 \AA^{-1} for all data set.

Fig. 8 shows the EXAFS Fourier Transform and fitting for all the six samples. EXAFS data for $x \leq 0.7$ can be fit assuming the Ti ions occupy octahedrally coordinated B-sites in pseudo-cubic structure, the same condition used in XANES simulation. Each fit for the compositions with $x \geq 0.7$ was performed assuming the Ti ions occupy octahedrally coordinated B-sites in the perfect cubic structure. The model included single distances and their associated DW factors for the Ti–O and ($\times 6$), Ti–Ba ($\times 8$) coordination shells, respectively.

All single and significant double-scattering paths were also included. The refined structural parameters are summarized in Table 1, showing coordination numbers N , the bond length of Ti absorbing atoms within oxygen octahedral with 8-fold barium atoms and the Debye–Waller (DW) factor σ^2 . It is observed that with increasing Zr content in $\text{Ba}(\text{Ti,Zr})\text{O}_3$ system the local structure is closer to the perfect cubic symmetry, particularly at $x \geq 0.75$ with the pseudo-cubic (almost a perfect cubic) structure observed. This phase transition is likely the effect of temperature dependence in BaTiO_3 . While the temperature is increasing, the tetragonal perovskite structure of BaTiO_3 changes to cubic perovskite [14,22]. Similarly, when Zr content in $\text{Ba}(\text{Ti,Zr})\text{O}_3$ is increased, the structure at room temperature becomes disordered and when $x > 0.75$ the structure becomes that of BaZrO_3 .

3.4. Dielectric permittivity

The dielectric constant at 100 kHz on various temperatures for $\text{Ba}(\text{Zr}_x\text{Ti}_{1-x})\text{O}_3$ compositions (with $x = 0.08, 0.25, 0.28, 0.30, 0.35,$

Table 1

The structural parameters consisting of coordination numbers N , interatomic distances R and DW factors σ^2 obtained by fitting the EXAFS data of $\text{BaTi}_{1-x}\text{Zr}_x\text{O}_3$ ($x = 0.0, 0.25, 0.5, 0.75$).

Sample	Shell	N	R (Å)	σ^2
BaTiO_3	Ti–O ₁	1	1.4809(1)	0.003
	Ti–O ₂	1	2.2190(2)	0.003
	Ti–O ₃	4	1.8962(2)	0.003
	Ti–Ba ₁	4	3.3721(2)	0.005
	Ti–Ba ₂	4	3.4559(2)	0.005
$\text{BaTi}_{0.75}\text{Zr}_{0.25}\text{O}_3$	Ti–O ₁	1	1.4675(2)	0.003
	Ti–O ₂	1	2.2403(2)	0.003
	Ti–O ₃	4	1.8539(2)	0.003
	Ti–Ba ₁	4	3.3630(2)	0.003
	Ti–Ba ₂	4	4.1565(2)	0.003
$\text{BaTi}_{0.5}\text{Zr}_{0.5}\text{O}_3$	Ti–O ₁	1	1.9463(2)	0.008
	Ti–O ₂	1	1.9707(2)	0.008
	Ti–O ₃	4	1.9585(2)	0.008
	Ti–Ba ₁	4	3.3533(2)	0.0001
	Ti–Ba ₂	4	3.3675(2)	0.0001
$\text{BaTi}_{0.25}\text{Zr}_{0.75}\text{O}_3$	Ti–O	6	1.9718(1)	0.008
	Ti–Ba	8	3.4355(1)	0.0001

0.50, 0.75 and 0.95) are shown in Fig. 9. The temperature at maximum dielectric constant (T_m) decreases while Zr content increases in BaTiO_3 , indicating a destabilization of ferroelectric phase. In addition, $x = 0.08$ composition exhibits the sharp peak of normal ferroelectric behavior and shows the phase transition from

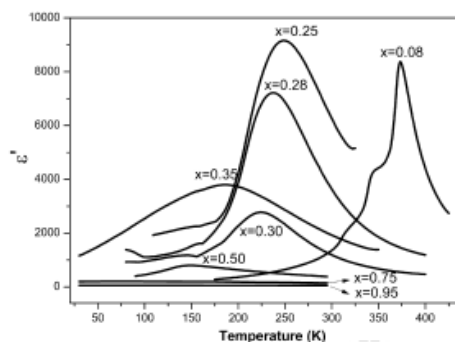


Fig. 9. The dielectric permittivity on a various temperature at 100 Hz for $x = 0.08, 0.25, 0.28, 0.30, 0.35, 0.50, 0.75$ and 0.96 .

rhombohedral to orthorhombic (T_1) about $T = 315$ K and orthorhombic to tetragonal (T_2) about $T = 340$ K, similar to pure BT. The composition with $x \geq 0.25$ exhibits the broad peak of relaxor ferroelectric behavior. For the composition with $x \geq 0.75$, very small dielectric permittivity value indicates that the Ti atoms move close to the center of oxygen octahedral. Therefore, the dielectric result confirms the Ti atoms behavior.

4. Conclusion

The structural information of $\text{Ba}(\text{Zr}_x\text{Ti}_{1-x})\text{O}_3$ materials was examined by X-ray Diffraction (XRD) and Synchrotron X-ray Absorption Spectroscopy (XAS) techniques. The XRD results show the global phase transition from tetragonal to cubic perovskite structure. However, the experimental and simulated XAS results, both in XANES and EXAFS regions, show the local structural transition around Ti atom from the pseudo-cubic to the perfect cubic perovskite structure in $\text{Ba}(\text{Ti,Zr})\text{O}_3$ or phase transition of relaxor ferroelectric to polar cluster. The results from this study are consistent with the observed electrical properties of the materials.

Acknowledgments

S.R. and R.Y. acknowledge support from COE-NANOTEC-SUT on Advanced Functional Nanomaterials. J.J. is grateful to SUT-Ph.D. scholarship from the Higher Education Research Promotion and National Research University Project of Thailand, Office of the Higher Education Commission and Suranaree University of Technology. AB is thankful for Ph.D. scholarship from the Science Achievement Scholarship of Thailand. Authors also acknowledge the support of INAMM/NSF program at UTSA.

References

- [1] H. Thurnauer, J. Deaderick, U.S. Patent No. 2,429,588, Oct. 21 filed, 1941.
- [2] T. Maiti, R. Guo, A.S. Bhalla, *J. Am. Ceram. Soc.* 91 (2008) 1769–1780.
- [3] T. Maiti, R. Guo, A.S. Bhalla, *Ferroelectrics* 425 (2011) 4–26.
- [4] F. Moura, A.Z. Simoes, B.D. Stojanovic, M.A. Zaghebe, E. Longo, J.A. Varela, *J. Alloys Comp.* 462 (2008) 129–134.
- [5] I. Levin, E. Cockayne, V. Krayzman, J.C. Woicik, S. Lee, C.A. Randall, *Phys. Rev. B* 83 (2008) 094122.
- [6] L. Eric Cross, *Ferroelectrics* 76 (1987) 241–267.
- [7] A. Bootchanont, J. Jitmoosik, S. Chandarak, M. Unruan, S. Rujirawat, R. Yimnirun, R. Guo, A. Bhalla, *Ceram. Int.* 39 (2013) 5579–5582.
- [8] J.Q. Qi, Y. Wang, W.P. Chen, L.T. Li, H.L.W. Chan, *J. Nano B* (2006) 959–963.
- [9] N. Binhayeenyi, P. Sukvisut, C. Thanachayanont, S. Muensit, *Mater. Lett.* 64 (2010) 305–308.
- [10] Z. Yu, C. Ang, R. Guo, A.S. Bhalla, *J. Appl. Phys.* 92 (2002) 3.
- [11] H. Kumpf, H. Modrow, *J. Phys. Chem.* 105 (2001) 3415–3421.
- [12] S. Chandarak, J. Jitmoosik, A. Bootchanont, M. Unruan, P. Jantarabana, S. Priya, S. Sriomsak, S. Rujirawat, R. Yimnirun, *J. Supercond. Novel Magn.* 26 (2013) 455–461.
- [13] I. Levin, V. Krayzman, J.C. Woicik, A. Tkachand, P.M. Vilarinho, *Appl. Phys. Lett.* 96 (2010) 052904.
- [14] R.V. Vedrinskii, V.L. Kraizman, A.A. Novakovich, Ph.V. Demekhin, S.V. Urazhdin, *J. Phys. Condens. Matter*, 10 (1998) 9561.
- [15] B. Ravel, E.A. Stern, R.I. Vedrinskii, V. Kraizman, *Ferroelectrics* 206 (1998) 407–430.
- [16] I. Levin, V. Krayzman, J.C. Woicik, *Appl. Phys. Lett.* 102 (2013) 162906.
- [17] C. Lahlhé, F. Hippert, J. Kreisel, M. Maglione, A. Simon, J.L. Hazemann, V. Nassif, *Phys. Rev. B* 74 (2006) 014106.
- [18] J.J. Rehr, R.C. Albers, *Rev. Mod. Phys.* 72 (2000) 3.
- [19] L. Hedin, S. Lundqvist, *Solid State Phys.* 23 (1969) 1.
- [20] Sang-Wook Han, *Int. J. Nano* 3 (2006) 2–3.
- [21] S. Limpijumnong, S. Rujirawat, A. Boonchun, *Appl. Phys. Lett.* 90 (2007) 103113.
- [22] M. Anicete-Santos, L.S. Cavalcante, E. Orhan, E.C. Paris, L.G.P. Simoes, M.R. Joly, I.L.V. Rosa, P.R. de Lucena, M.R.M. Santos, L.S. Santos-Junior, P.S. Pizani, E.R. Leite, J.A. Varela, E. Longo, *Chem. Phys.* 316 (2005) 260–266.

Available online at www.sciencedirect.com

ScienceDirect

Ceramics International 40 (2014) 14555–14562

CERAMICS
INTERNATIONALwww.elsevier.com/locate/ceramint

Review paper

Local structure and evolution of relaxor behavior in BaTiO₃–Bi(Zn_{0.5}Ti_{0.5})O₃ ceramics

Atipong Bootchanont^{a,*}, Narit Triamnak^b, Saroj Rujirawat^a, Rattikom Yimnirun^a,
David P. Cann^c, Ruyan Guo^d, Amar Bhalla^d

^aSchool of Physics, Institute of Science, and NANOTEC-SUT Center of Excellence on Advanced Functional Nanomaterials,
Suranaree University of Technology, Nakhon Ratchasima 30000, Thailand

^bDepartment of Materials Science and Engineering, Faculty of Engineering and Industrial Technology, Silpakorn University, Nakhon Pathom 73000, Thailand

^cMaterials Science, School of Mechanical, Industrial, and Manufacturing Engineering, Oregon State University, Corvallis, OR 97331, USA

^dDepartment of Electrical and Computer Engineering, College of Engineering, University of Texas, San Antonio, TX 78249, USA

Received 12 April 2014; received in revised form 12 June 2014; accepted 12 June 2014

Available online 20 June 2014

Abstract

In this paper, the local structure in relation to relaxor ferroelectric behavior of $(1-x)\text{BaTiO}_3-x\text{Bi}(\text{Zn}_{0.5}\text{Ti}_{0.5})\text{O}_3$ (with $x=0.05-0.13$) ceramics was studied. The evolution of phase transition from tetragonal to rhombohedral structure at room temperature in the BaTiO₃–Bi(Zn_{0.5}Ti_{0.5})O₃ (BT-BZT) solid solution with increasing Bi(Zn_{0.5}Ti_{0.5})O₃ content was analyzed by the conventional X-ray Diffraction (XRD) technique. Furthermore, the local atomic position of Ti atoms in the BT-BZT was investigated by the synchrotron X-ray Absorption Spectroscopy (XAS) technique. The XAS results indicated a change in local structure around the Ti absorbing atom, which corresponds with the phase transition from tetragonal to rhombohedral structure. Finally, the characteristic cooperative freezing temperature of the polar regions was determined to follow the frequency-dependent Vogel–Fulcher relation.

© 2014 Elsevier Ltd and Techna Group S.r.l. All rights reserved.

Keywords: Local structure; XANES; Relaxor; Phase transition

Contents

1. Introduction	14556
2. Experimental	14556
3. Results and discussion	14556
3.1. XRD analysis	14556
3.2. X-ray absorption near edge structure (XANES) measurement	14557
3.3. Dielectric behavior and phase transformation	14559
3.4. Curie–Weiss behavior	14559
3.5. Temperature dependence of the relaxation time	14559
4. Discussion	14561
5. Conclusion	14561
Acknowledgments	14562
References	14562

*Corresponding author.

E-mail address: a.bootchanont@gmail.com (A. Bootchanont).

1. Introduction

In recent years, it has been found that $\text{BaTiO}_3\text{-Bi(Me)O}_3$ perovskites (Me can be either a single trivalent cation or two cations with an average valence of +3 which occupy the octahedral sites) have high Curie transition temperature and excellent piezoelectric properties. Moreover, these lead-free piezoelectric materials are attractive due to their environmental friendly characters [1,2]. Interestingly, $(1-x)\text{BaTiO}_3\text{-xBi(Zn}_{0.5}\text{Ti}_{0.5}\text{)O}_3$ (or BT-BZT) compositions with $x=0$ and 0.1 have been found to contain the tetragonal BT phase [3]. For $x > 0.1$, rhombohedral or pseudo-cubic phase perovskite and relaxor ferroelectric like behavior have been observed. However, the exact morphotropic phase boundary (MPB) composition in BT-BZT system is difficult to determine. Although conventional studies based on X-ray Diffraction (XRD) show strong global symmetry change, such a conventional technique is not useful for investigating the integrate details associated with dramatic changes in the electrical properties of these materials. Interestingly, the X-ray Absorption Spectroscopy (XAS) technique can be employed to investigate the local structure in various materials [4]. The local structure change can be clearly related to the phase transition which leads to drastic changes in the dielectric properties.

In this work, we focused our studies on the transition of global structure by the XRD technique and probed the local structure information around the ferroelectrically-active Ti atom in the BT-BZT system as a function of Bi(Zn, Ti)O_3 concentration, in a desire to provide better understanding of how the local structure is related to the evolution of relaxor ferroelectric behavior in this complex perovskite system.

2. Experimental

$(1-x)\text{BaTiO}_3\text{-xBi(Zn}_{0.5}\text{Ti}_{0.5}\text{)O}_3$ powders were prepared by the conventional solid state reaction method. The starting BaCO_3 ($\geq 99.9\%$), TiO_2 ($\geq 99.9\%$), ZnO ($\geq 99\%$) and Bi_2O_3 ($\geq 99.5\%$) materials were weighed according to the composition $(1-x)\text{BaTiO}_3\text{-xBi(Zn}_{0.5}\text{Ti}_{0.5}\text{)O}_3$ (with $x=0.05, 0.06, 0.07, 0.08, 0.09, 0.10, 0.11$ and 0.13) and mixed in ball mill for 24 h using an ethanol medium. After drying, the mixed powders were calcined at temperature of 950 °C for 12 h with 5 °C/min heating/cooling rates. Sintering of the pellets was carried out between 1100 and 1300 °C for 4 h [3].

The phase formation and global structure of $(1-x)\text{BaTiO}_3\text{-xBi(Zn}_{0.5}\text{Ti}_{0.5}\text{)O}_3$ were investigated by X-ray diffraction (XRD) technique at room temperature using a 2θ scan range of 20°–60° with 0.02° step and $\text{CuK}\alpha$ radiation. The local structure was investigated by synchrotron X-ray Absorption Spectroscopy (XAS) measurements conducted at ambient temperature at the BL-8 of the Siam Photon Laboratory, Synchrotron Light Research Institute (SLRI), Thailand, with provided electron energy of 1.2 GeV and beam current 120–80 mA. The double crystal monochromator Ge(220) was used to select the energy of the X-ray beam for the Ti *K*-edge measurements. The experiments were performed in a fluorescence mode and the signals were collected by using the

13-component Ge-detector. The X-ray Absorption Near-Edge Structure (XANES) spectra for the Ti *K*-edge were measured for all compositions. The data were processed using the ATHENA program [4].

Next, silver electrodes were sputtered on the BT-BZT ceramics for dielectric measurements. A HP4284 LCR meter was used to measure the dielectric constant and loss tangent from 100 Hz to 1 MHz in the temperature range of 150–425 K with a cooling rate of 2 K/min.

3. Results and discussion

3.1. XRD analysis

The XRD patterns of $(1-x)\text{BaTiO}_3\text{-xBi(Zn}_{0.5}\text{Ti}_{0.5}\text{)O}_3$ ceramics are shown in Fig. 1(a) for various solid solution compositions. When $\text{Bi(Zn}_{0.5}\text{Ti}_{0.5}\text{)O}_3$ was added to BaTiO_3 with $x \leq 0.07$, the peak splitting of the (200) reflection is observed, an indication of the tetragonal perovskite (*P4mm*) structure in the BT-BZT system. It can also be seen that the

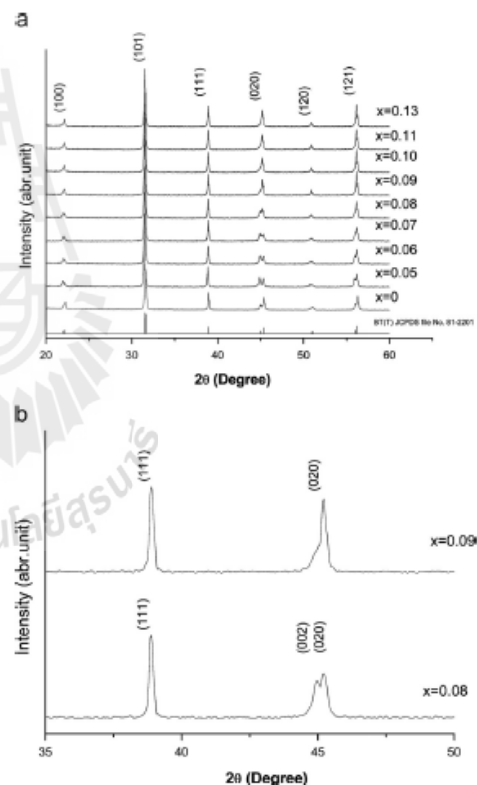


Fig. 1. X-ray diffraction patterns of $(1-x)\text{BaTiO}_3\text{-xBi(Zn}_{0.5}\text{Ti}_{0.5}\text{)O}_3$ ceramics.

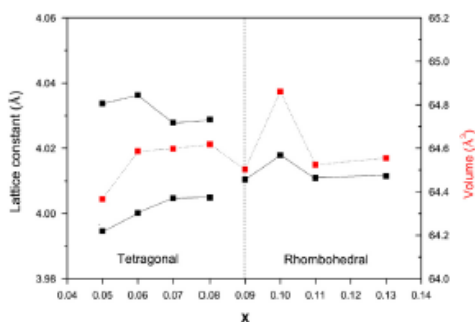


Fig. 2. The lattice constant and unit cell volume as a function of x content of $(1-x)\text{BaTiO}_3-x\text{Bi}(\text{Zn}_{0.5}\text{Ti}_{0.5})\text{O}_3$ compositions. (For interpretation of the references to color in this figure, the reader is referred to the web version of this article.)

tetragonality of the structure decreases, as the BZT content increases, as indicated by the reduction in the (200)–(020) peak separation shown in Fig. 1(b) [3]. For $0.08 \leq x \leq 0.13$, the samples exhibited pseudo-cubic or rhombohedral structure. It is also observed that at $0.08 \leq x \leq 0.09$ the structure clearly changes from tetragonal to rhombohedral perovskite phase with increasing BZT concentration. The possible MPB between the tetragonal and rhombohedral phases is observed at a composition close to $x=0.09$. Fig. 2 shows the lattice constant (black line) and volume (red line) as a function of $\text{Bi}(\text{Zn},\text{Ti})\text{O}_3$ content. The lattice constant a is increasing and c is decreasing with increasing $\text{Bi}(\text{Zn},\text{Ti})\text{O}_3$ content until $x=0.09$, when the lattice constant $a=c$ where the structure transforms into rhombohedral symmetry. The unit cell volume is the highest at $x=0.1$, where the relaxor region begins.

3.2. X-ray absorption near edge structure (XANES) measurement

XANES, a local probe technique that utilizes the processes of excitation of core electrons to unoccupied bound states where the photoelectron wavelength is on the order of the distance to the nearest neighbor, is used to obtain information about the local arrangement of atoms around the absorbing atoms [5,6]. The normalized Ti K -edge XANES spectra of $(1-x)\text{BaTiO}_3-x\text{Bi}(\text{Zn}_{0.5}\text{Ti}_{0.5})\text{O}_3$ ceramics are shown in Fig. 3(a). The intensity of peak A (I_A) is associated with the Ti $1s$ electron transitions to the absorbing TiO_6 polyhedron $3d$ -originated unoccupied p - d hybrid orbitals of e_g -type symmetry. In Fig. 3(b), local Ti off-centering is associated with the Ti K pre-edge peak in X-ray absorption spectra [7]. The integrated intensity of this peak is directly proportional to the mean-squared displacements of Ti (δ_{Ti}) from the instantaneous centers of oxygen octahedral and is indirectly proportional to the lattice constants [8,9]. The integral intensity of peak A (I_A) decreases continuously, until the composition $x=0.1$, and increases again because the Ti displacement decreases when it is close to rhombohedral phase and increases in the rhombohedral phase. Furthermore, the integral intensity

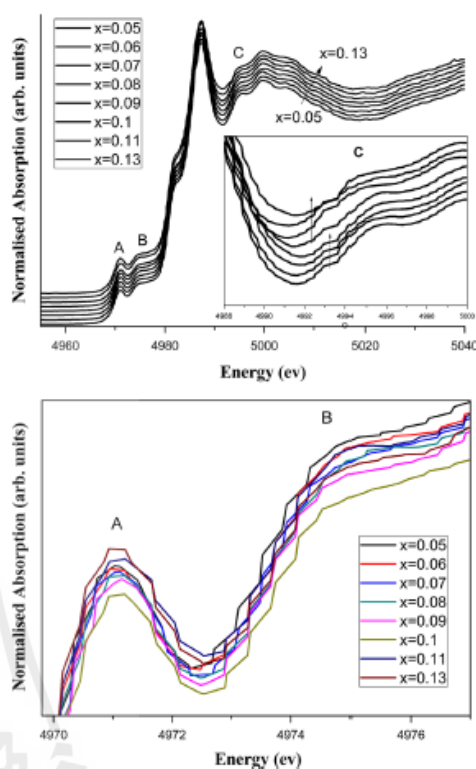


Fig. 3. (a) The normalized X-ray absorption Ti K -edge spectra (b) Ti K pre-edge spectra of $(1-x)\text{BaTiO}_3-x\text{Bi}(\text{Zn}_{0.5}\text{Ti}_{0.5})\text{O}_3$, with $x=0.05, 0.06, 0.07, 0.08, 0.09, 0.1, 0.11, \text{ and } 0.13$.

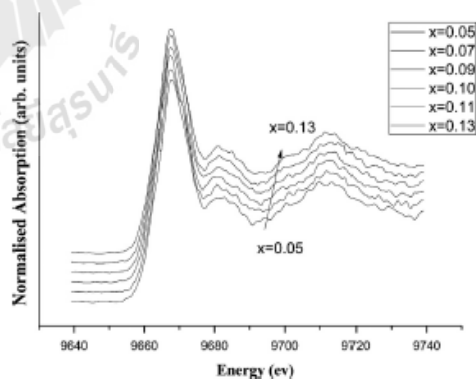


Fig. 4. The normalized X-ray absorption Zn K -edge spectra of $(1-x)\text{BaTiO}_3-x\text{Bi}(\text{Zn}_{0.5}\text{Ti}_{0.5})\text{O}_3$, with $x=0.05, 0.07, 0.09, 0.1, 0.11, \text{ and } 0.13$.

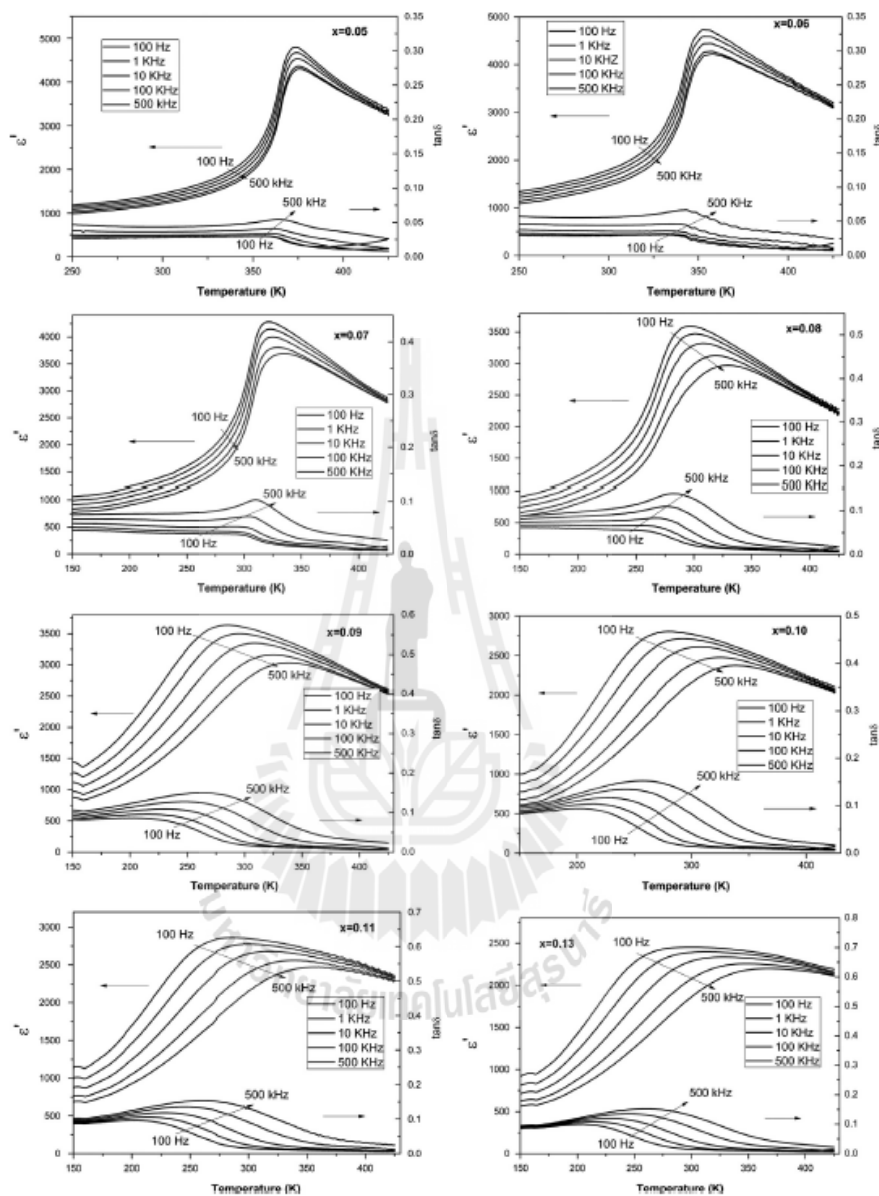


Fig. 5. Temperature dependence of dielectric constant and loss tangent ($\tan \delta$) at various frequencies for $(1-x)\text{BaTiO}_3-x\text{Bi}(\text{Zn}_{0.5}\text{Ti}_{0.5})\text{O}_3$, with $x=0.05, 0.06, 0.07, 0.08, 0.09, 0.1, 0.11$, and 0.13 (Arrows indicate the direction of increasing frequency).

of peak B (I_B) relates to the average of Zn/Ti ratio in the third shell, which is decreasing as Zn occupation increases in the third shell of Ti core [9]. However, when $x > 0.1$, I_B increases because the Zn/Ti ratio is random by occupied Ti core in the third shells or is in disorder relaxor region. Furthermore, while XANES spectra begin to exhibit different features for composition $x=0.09$, at $x \geq 0.1$ the spectra exhibit a clear change in features with the peak C; an indication of the change in local structure around Ti absorbing atom, corresponding to the phase transition from tetragonal to rhombohedral in XRD results.

The normalized Zn K-edge XANES spectra of $(1-x)$ BaTiO₃– x Bi(Zn_{0.5}Ti_{0.5})O₃ ceramics are shown in Fig. 4. The feature of Zn K-edge XANES spectra does not change significantly, neither does the local structure around Zn atoms. The Zn atoms substitute on B-site of perovskite structure with associated paraelectric properties which indicates a cut-off to the normal ferroelectric regions. When the paraelectric phase region increases, the polar nano-region disperses in the paraelectric region and the interactions result in the relaxor ferroelectric behavior [10,11].

3.3. Dielectric behavior and phase transformation

The dielectric constant and dielectric loss tangent ($\tan \delta$) at various frequencies for $(1-x)$ BaTiO₃– x Bi(Zn_{0.5}Ti_{0.5})O₃ compositions (with $x=0.05, 0.06, 0.07, 0.08, 0.09, 0.10, 0.11$ and 0.13) are shown in Fig. 5. The compositions with $0.05 \leq x \leq 0.07$ exhibit normal ferroelectric behavior and a sharp peak of dielectric constant as a function of temperature is observed. At $x=0.08$, the relaxor behavior and the broad peaks of dielectric constant as the function temperature are shown. A strong frequency dispersion is observed around ϵ' and $\tan \delta$ peaks for $x \geq 0.09$ compositions or so called “relaxor” like behavior. With an increase in frequency, ϵ' decreases and the maximum dielectric constant temperature (T_m) shifts to higher temperatures. In contrast, the dielectric loss tangent is increasing while the frequency decreases and the maximum dielectric loss temperature is shifted to higher temperatures. Furthermore, the dielectric constant decreases with the BZT content, while the dielectric loss tangent increases until $x=0.08$.

3.4. Curie–Weiss behavior

The Curie–Weiss law describes a ferroelectric in the paraelectric region, as

$$\frac{1}{\epsilon} = \frac{T - T_C}{C} \quad (1)$$

where T_C is Curie temperature and C is the Curie–Weiss constant [10]. Fig. 6 shows the inverse dielectric constant as the function of temperature at 100 KHz. The linear fitting is observed in the paraelectric region or high temperature for all compositions. The fitting parameters; i.e., the Curie–Weiss constant and Curie temperature are listed in Table 1 [10]. The results show that the Curie temperature decreases with the increasing BZT content. It is evident from the value of T_C that the compositions $x=0.05$ – 0.08 show the normal ferroelectric

behavior. However, the negative values of T_C (as would have been obtained from the graphs, but not shown here as it is physically impossible) clearly indicate the relaxation behavior for compositions $x=0.09$ – 0.13 . Furthermore, the relaxor ferroelectric behavior in the high temperature region follows the modified Curie–Weiss law [10–12],

$$\frac{1}{\epsilon} - \frac{1}{\epsilon_m} = \frac{(T - T_m)^\gamma}{2\epsilon_m \delta_\gamma} \quad (2)$$

where ϵ_m is the permittivity at T_m , γ is the degree of dielectric relaxation, $1 < \gamma < 2$; $\gamma=1$ corresponds to a normal ferroelectric phase transition. $\gamma > 1$ Represents relaxor-ferroelectric behavior transition. The value of δ_γ represents the degree of diffuseness for transition peaks. Both γ and δ_γ are determined from the slope and intercept $\ln(\epsilon'_{max}/\epsilon')$ versus $\ln(T - T_m)$, as shown in Fig. 6 for all compositions [13]. In Table 2, the value of γ , which increases as the BZT content increases, indicates relaxor behavior. For $x > 0.07$, the compositions exhibit the relaxation behavior until $x=0.13$, close to the ideal relaxor ferroelectric ($\gamma=2$). The value of δ_γ also increases as a result of the increased relaxation. In addition, the transition temperature T_m decreases as x increases until $x=0.08$ indicating a destabilization of ferroelectric phase. For $x > 0.08$, the transition temperature increases continuously within the rhombohedral phase field [14,15].

3.5. Temperature dependence of the relaxation time

The relaxor ferroelectric process is believed to be the presence of dynamic polar nano-regions which are ever more active and are of fines scale in the vicinity of T_m in a classical relaxor system. Generally, the polar nano-regions (PNRs) exhibit a characteristic relaxation time (τ) in the local field configuration in its characteristic size. The separation of energy barrier switch to the polarization state decreases as the size of the PNRs decreases. The direction of a net polarization (P_s) fluctuates or become very dynamic with temperature while the barrier height becomes comparable to thermal energy (kT). Like the spin glass systems, the short-range interaction between the polar regions control the fluctuation of P_s , leading to its freezing at a characteristic temperature far below the T_m . The relaxation time (τ) in relaxor has been described by the Vogel–Fulcher relation [10–12],

$$\tau = \tau_0 \exp[E_a/k_B(T_m - T_{VF})] \quad (3)$$

where τ_0 is the pre-exponential factor, E_a is the activation energy for polarization fluctuations of an isolated cluster, T_m is the temperature at the maximum dielectric constant, k_B is the Boltzmann constant, and T_{VF} is the characteristic Vogel–Fulcher freezing temperature. The relaxation time depends on the temperature and is well fit with Vogel–Fulcher relation for composition range, $0.08 \leq x \leq 0.13$ (relaxor behavior only), as shown in Fig. 7. The fitting parameters are summarized in Table 3. With the increase in BiZn_{0.5}Ti_{0.5}O₃ content, the freezing temperature is increased. The increasing values of T_{VF} indicate the gradual evolution of polar nano-region, the relaxor-like behavior. Similarly, the activation energy decreases with the

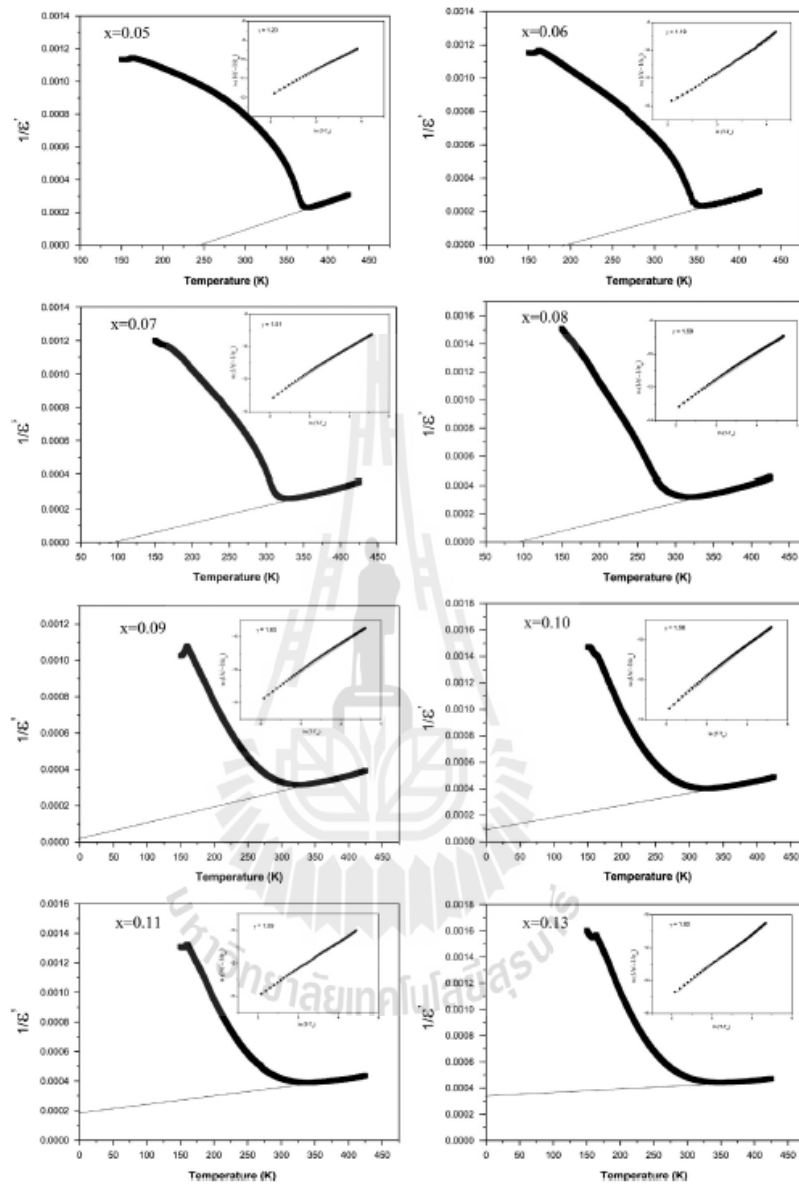


Fig. 6. The inverse dielectric constant $1/\epsilon'$ as a function of temperature at 100 kHz for $(1-x)\text{BaTiO}_3-x\text{Bi}(\text{Zn}_{0.5}\text{Ti}_{0.5})\text{O}_3$ with $x=0.05, 0.06, 0.07, 0.08, 0.09, 0.1, 0.11,$ and 0.13 . Symbols denote experimental data and solid line denotes fitting to the Curie-Weiss law. The insets show the plot of $\ln(1/\epsilon' - 1/\epsilon_\infty)$ vs $\ln(T - T_m)$ for $(1-x)\text{BaTiO}_3-x\text{Bi}(\text{Zn}_{0.5}\text{Ti}_{0.5})\text{O}_3$ ceramics.

Table 1
Calculated Curie constant and measured T_c from like dielectric properties of $(1-x)\text{BT}-x\text{BZT}$ compositions.

Composition	C (K)	T_c (K)
$x=0.05$	5.90×10^5	243.72
$x=0.06$	7.21×10^5	196.04
$x=0.07$	9.41×10^5	92.99
$x=0.08$	7.45×10^5	94.62
$x=0.09$	1.11×10^5	-7.08
$x=0.10$	1.08×10^5	-95.48
$x=0.11$	1.91×10^5	-394.79
$x=0.13$	3.80×10^5	-1333.96

Table 2
Degree of Relaxation γ , dielectric maxima temperature and diffusivity of like $(1-x)\text{BT}-x\text{BZT}$ compositions.

Composition	γ	T_m (K) at 100 MHz	δ_f at 100 MHz
$x=0.05$	1.23	375	66.33
$x=0.06$	1.19	359	87.73
$x=0.07$	1.51	329	113.40
$x=0.08$	1.59	319	115.69
$x=0.09$	1.65	325	148.04
$x=0.10$	1.56	325	170.36
$x=0.11$	1.59	340	217.92
$x=0.13$	1.82	348	249.49

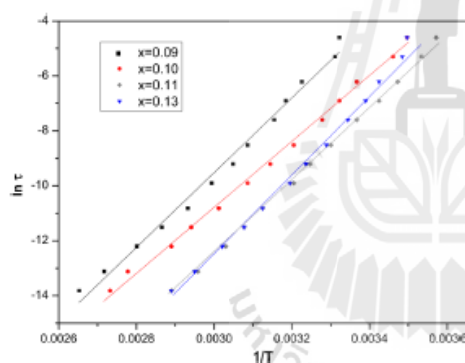


Fig. 7. Temperature dependence of relaxation time for ceramics at 100 MHz, with $x=0.05, 0.06, 0.07, 0.08, 0.09, 0.1, 0.11,$ and 0.13 . Symbols denote experimental data and solid curve denotes fitting to the Vogel-Fulcher relation.

Table 3
Vogel-Fulcher temperature, activation energy E_a and exponent n_0 as calculated from the Arrhenius plots of various $(1-x)\text{BT}-x\text{BZT}$ compositions.

Composition	Freezing temperature (T_{VF}) (K)	Activation energy (E_a) (eV)
$x=0.08$	34	2.04 (± 0.125)
$x=0.09$	51	1.27 (± 0.032)
$x=0.10$	54	1.16 (± 0.012)
$x=0.11$	65	1.03 (± 0.018)
$x=0.13$	62	1.17 (± 0.035)

evolution of the relaxor behavior and the energy corresponding the thermal relaxation process also reduces. Therefore, the evolution of polar nano-region or relaxor behavior in $\text{BaTiO}_3-x\text{Bi}(\text{Zn}_{0.5}\text{Ti}_{0.5})\text{O}_3$ materials enhances with BZT content in this system.

4. Discussion

In recent years, extensive research efforts have been conducted on relaxor ferroelectrics. To describe the physical phenomena of relaxor ferroelectrics, several models, superparaelectric [16], "dipolar glass" [17], random field [18], etc., have been discussed. In this work, we investigated the gradual evolution of relaxation behavior in the BT-BZT system. As the amount of BZT increases, the normal ferroelectric behavior of BT regions start breaking and generate the density of the nano-sized Ti oxygen-octahedral-rich polar regions in the Zn-rich matrix. In the classic $A(\text{B}_1\text{B}_{1-x})\text{O}_3$ ferroelectric relaxors such as $\text{PbMg}_{1/3}\text{Nb}_{2/3}\text{O}_3$ (PMN), the nano-sized cation ordered charged regions are distributed in a disordered matrix and lead to the well-known relaxor behavior [10].

In our work, XRD measurements show the global structure change, phase transition from tetragonal to rhombohedral symmetry. Although, XRD results indicate structural changes at temperature corresponding with peak in dielectric response, XRD cannot discern the evolution of local structure around B-site Ti and Zn atoms. Therefore, XAS measurements were utilized to determine the local structure. From the XANES results, in composition range $x < 0.09$, the increase of BZT content affects the polar regions, but it is not a disordered matrix on the local structure scale. However, the relaxor behavior begins at a critical composition $x=0.09$. For $x=0.1$, the local structure begins to exhibit the random occupation in the B-site sharing between BT and BZT, which corresponds to a disordered matrix. It can be hypothesized from the dielectric behavior that the amount of BZT > 0.09 is sufficient to build up a long-range polar disordered region that results in relaxor ferroelectric behavior in the BT-BZT system. The fits to the $x > 0.09$ data through the Vogel-Fulcher temperature dependent relaxation time suggests the evolution of relaxation time to mimic relaxors.

5. Conclusion

The structural information of $(1-x)\text{BaTiO}_3-x\text{Bi}(\text{Zn}_{0.5}\text{Ti}_{0.5})\text{O}_3$ ($x=0.05-0.13$) ceramics was examined by X-ray Diffraction (XRD) and synchrotron X-ray Absorption Spectroscopy (XAS) techniques. The XRD results show a clear global phase transition, tetragonal to rhombohedral at $x=0.09$. In addition, the experimental XANES spectra results indicate a slight local structural change around Ti atom at $x=0.09$ and a clear change with $x=0.10$, which corresponds to the phase transition from normal ferroelectric to relaxor behavior as observed from the dielectric constant vs T and f results. This investigation has demonstrated structural and electrical agreement among data from XRD, XAS and dielectric properties.

Acknowledgments

AB is thankful for Ph.D. scholarship from the Science Achievement Scholarship of Thailand and Suranaree University of Technology. RY and SR are grateful for financial support from NANOTEC-SUT Center of Excellence on Advanced Functional Nanomaterials. Authors also acknowledge the support of INAMM/NSF (#0844081) for hosting at UTSA.

References

- [1] R.E. Eitel, C.A. Randall, T.R. Shrout, P.W. Rehrig, W. Hackenberger, S.-E. Park, New high temperature morphotropic phase boundary piezoelectrics based on Bi(Me)O₃-PbTiO₃ ceramics, *Jpn. J. Appl. Phys. Part 1* 40 (2001) 5999.
- [2] C.J. Stringer, T.R. Shrout, C.A. Randall, Classification of transition temperature behavior in ferroelectric PbTiO₃-Bi(Me^{II}/Me^{III})O₃ solid solutions, *J. Appl. Phys.* 99 (2006) 024106.
- [3] C.-C. Huang, D.P. Cann, Phase transitions and dielectric properties in Bi(Zn_{1/2}Ti_{1/2})O₃-BaTiO₃ perovskite solid solutions, *J. Appl. Phys. Part 1* 104 (2001) 024117.
- [4] A. Bootchanont, J. Jitmoosik, S. Chandrak, M. Unruan, S. Rujirawat, R. Yimnirun, R. Guo, A. Bhalla, Investigation of local structure in BaTiO₃-BaZrO₃ system by synchrotron X-ray absorption spectroscopy, *Ceram. Int.* 39 (2013) S579–S582.
- [5] J.J. Rehr, R.C. Albers, Theoretical approaches to X-ray absorption fine structure, *Rev. Mod. Phys.* 72 (2000) 3.
- [6] L. Hedin, S. Lundqvist, Advances in research and application, *Solid State Phys.* 23 (1990) 1–181.
- [7] B. Ravel, E.A. Stern, R.I. Vedrinskii, V. Kraizman, Local structure and the phase transitions of BaTiO₃, *Ferroelectrics* 206 (1998) 407–430.
- [8] R.V. Vedrinskii, V.L. Kraizman, A.A. Novakovich, P.H.V. Demelhin, S.V. Urazhdin, Pre-edge fine structure of the 3d atom K X-ray absorption spectra and quantitative atomic structure determinations for ferroelectric perovskite structure crystals, *J. Phys. Condens. Matter* 10 (1998) 9561.
- [9] I. Levin, V. Krayzman, J.C. Woicik, Local-structure origins of the sustained Curie temperature in (Ba,Ca)TiO₃ ferroelectrics, *Appl. Phys. Lett.* 102 (2013) 162906.
- [10] T. Matü, R. Guo, A.S. Bhalla, The evolution of relaxor behavior in Ti4+ doped BaZrO₃ ceramics, *J. Appl. Phys.* 100 (2006) 114109.
- [11] T. Matü, R. Guo, A.S. Bhalla, Structure-property phase diagram of BaZr_{1-x}Ti_xO₃ system, *J. Am. Ceram. Soc.* 91 (2008) 1769–1780.
- [12] T. Matü, R. Guo, A.S. Bhalla, Evaluation of experimental resume of BaZr_{1-x}Ti_xO₃ with perspective to ferroelectric relaxor family: an overview, *Ferroelectrics* 425 (2011) 4–26.
- [13] C.C. Huang, Structure and piezoelectric properties of lead-free bismuth-based perovskite solid solutions, (Ph.D. dissertation), Materials Science Oregon State University, 2008.
- [14] N. Raengthon, T. Sebastian, D. Cumming, I.M. Reaney, D.P. Cann, BaTiO₃-Bi(Zn_{1/2}Ti_{1/2})O₃-BiScO₃ ceramics for high-temperature capacitor applications, *J. Am. Ceram. Soc.* 95 (11) (2012) 3554–3561.
- [15] N. Raengthonand, D.P. Cann, Dielectric relaxation in BaTiO₃-Bi(Zn_{1/2}Ti_{1/2})O₃ ceramics, *J. Am. Ceram. Soc.* (2011) 1–9.
- [16] L.E. Cross, Relaxor ferroelectrics, *Ferroelectrics* 76 (1987) 241.
- [17] D. Viehland, S.J. Jang, L.E. Cross, M. Wuttig, Nonlinear dielectric response in relaxor ferroelectrics (1-x)Pb(Mg_{1-x}W_{1-x})O₃-xPbTiO₃ (x=0.5), *Jpn. J. Appl. Phys.* 68 (1990) 2916.
- [18] V. Westphal, W. Kleemann, M.D. Ghinchik, Freezing of the polarization fluctuations in lead magnesium niobaterelaxors, *Phys. Rev. Lett.* 68 (1992) 847.

Available online at www.sciencedirect.com

SciVerse ScienceDirect

Ceramics International 39 (2013) S579–S582

CERAMICS
INTERNATIONALwww.elsevier.com/locate/ceramint

Investigation of local structure in BaTiO₃–BaZrO₃ system by synchrotron X-ray absorption spectroscopy

Atipong Bootchanont^{a,*}, Jaru Jutimoosik^a, Sujittra Chandarak^a, Muangjai Unruan^b,
Saroj Rujirawat^{a,c,d}, Rattikorn Yimnirun^{a,d}, Ruyan Guo^e, Amar Bhalla^e

^aSchool of Physics, Institute of Science, Suranaree University of Technology, Nakhon Ratchasima 30000, Thailand

^bRajamangala University of Technology Isan, Nakhon Ratchasima 30000, Thailand

^cThailand Center of Excellence in Physics (THEP Center) Commission on Higher Education, Bangkok 10400, Thailand

^dSynchrotron Light Research Institute (Public Organization), Nakhon Ratchasima, 30000 Thailand

^eDepartment of Electrical and Computer Engineering, University of Texas at San Antonio, TX 78249, USA

Available online 22 October 2012

Abstract

In this work, the global and local structures of Ba(Zr_xTi_{1-x})O₃ materials were investigated by X-ray Diffraction (XRD) and Synchrotron X-ray Absorption Spectroscopy (XAS) techniques, respectively. The Ba(Zr_xTi_{1-x})O₃ powders were prepared by a conventional solid state reaction method. The XRD study indicated that the global structure of the prepared material changed from pure tetragonal, to mixed tetragonal and cubic, and finally to pure cubic phase at high Zr content. Changes in the local structure around titanium atom were revealed using X-ray Absorption Near-Edge Structure (XANES) measurements, showing three regimes with different Ti off-center displacements, depending on Zr content in the material. A comparison between the measured and simulated XANES spectra also revealed the influence of different Zr/Ti ratios on the local structure around Ti atom.

© 2012 Elsevier Ltd and Techna Group S.r.l. All rights reserved.

Keywords: A. Calcination; B. Spectroscopy; C. X-ray method; C. BZT

1. Introduction

Barium zirconium titanate (Ba(Zr,Ti)O₃ or BZT) is an attractive candidate to replace lead-based materials for dynamic random access memories and electronic devices because of its environmental friendly constituent [1]. Since its recent widespread interest starting in the 1980s, most of the studies of BZT have focused mainly on the temperature and frequency dependence of the dielectric properties, the nature of phase transitions, and the ferroelectric relaxor behavior [2]. More specifically, researchers have found that increasing Zr substitution into Ti site in BaTiO₃ crystals can change the material to exhibit relaxor ferroelectric behavior [1–3]. A similar behavior can also happen in BaTiO₃–Bi(Ti,Zn)O₃ composite. BZT has been reported to exhibit the relaxor behavior in bulk forms with increasing Zr

content [2]. The relaxor ferroelectric behavior is classified with strong frequency-dependent dielectric properties. Interestingly, barium zirconate (BaZrO₃:BZ) possesses non-polar or paraelectric behavior, which cannot have spontaneous polarization; i.e. non ferroelectric. Additionally, a substitution of Zr⁴⁺ (ionic radius of 86 pm) with Ti⁴⁺ (ionic radius of 74.5 pm) exhibits several interesting features in the dielectric behavior of BaTiO₃ or BT [3]. It has been reported that with the incorporation of Zr in BT, the rhombohedral to orthorhombic (*T*₁) and orthorhombic to tetragonal (*T*₂) phase transition temperatures increase, as compared to pure BT [3]. In contrast, the tetragonal to cubic (Curie temperature, *T*_C) phase transition temperature decreases. Thus, when Zr concentration is less than 10 mol%, the BaZr_xTi_{1-x}O₃ system exhibits a pinched phase transition; i.e., all the above three phase transition temperatures (*T*₁, *T*₂, and *T*_C) are merged or pinched into a single diffuse phase transition. At around 27 mol%, Zr-doped BT ceramics exhibit a typical diffuse paraelectric to ferroelectric phase transition behavior,

*Corresponding author. Tel.: +668 49550910.

E-mail address: a.bootchanont@gmail.com (A. Bootchanont).

whereas Zr-riched compositions exhibit a typical relaxor-like behavior, in which T_C shifts to higher temperature with increase of frequency [3].

Recently, in $\text{Ba}(\text{Zr}_x\text{Ti}_{1-x})\text{O}_3$ system it has been found that the compositions with $x=0$ and 0.005 contained the tetragonal BT phase. With $x=0.02$, the ceramic sample contained a mixture of the tetragonal and orthorhombic structures, whereas the $x=0.04$ sample exhibited primarily the orthorhombic phase. For $x=0.12$, the crystal structure became cubic [4]. This investigation has also indicated that with increasing Zr content the electrical properties showed the transition from normal to relaxor ferroelectric behavior. However, a structural study based on a typical X-ray Diffraction (XRD) measurement did not show any strong global symmetry change, in contrast to the drastic change in the electrical properties. This is believed to be attributed to local (nano-scaled region) symmetry conversion within the material, undetected by the global-symmetry-based XRD measurement. Interestingly, the X-ray Absorption Spectroscopy (XAS) technique can be used effectively to investigate the local structure of materials. It is thus of great interest to employ the XAS technique to investigate the local structure within the $\text{Ba}(\text{Zr}_x\text{Ti}_{1-x})\text{O}_3$ system. In this article, we focused on the local structure information around the ferroelectrically-active Ti atom in $\text{Ba}(\text{Zr}_x\text{Ti}_{1-x})\text{O}_3$ and its characteristics as a function of Zr concentration in hope to provide better understanding of how the local structure is related to the normal to relaxor ferroelectric transition.

2. Experimental procedure

$\text{BaZr}_x\text{Ti}_{1-x}\text{O}_3$ powders were prepared by a solid state reaction method. The starting materials BaCO_3 , TiO_2 and ZrO_2 were weighed according to the composition $(1-x)\text{BaTiO}_3-x\text{BaZrO}_3$ with $x=0.0, 0.05, 0.1, 0.15, 0.2, 0.25, 0.3, 0.35, 0.4, 0.45, 0.5$ and 1.0. The raw materials were ball milled in ethanol for 24 h. After drying, the mixed powders were calcined at a temperature of 1250 °C for 2 h with 5 °C/min heating and cooling rates.

To investigate the phase formation and global structure of $\text{Ba}(\text{Zr}_x\text{Ti}_{1-x})\text{O}_3$, X-ray diffraction (XRD) patterns were scanned in 2θ range of 20°–60° with 0.02° step and CuK α radiation was used. To examine the local structure, X-ray Absorption Spectroscopy (XAS) measurements were conducted at ambient temperature at BL-8 of the Siam Photon Laboratory, Synchrotron Light Research Institute (SLRI), Thailand (electron energy of 1.2 GeV, beam current 120–80 mA). The double-crystal monochromator was operated with a pair of Ge (220) crystals for scanning the energy of the synchrotron X-ray beam with energy steps of 0.20 eV to excite the electrons in Ti K-edge. The experiments were performed in fluorescence mode and the signals were collected by using the 13-component Ge-detector. The X-ray Absorption Near-Edge Structure (XANES) measurements for the Ti K-edge were measured for all compositions. The data were processed using the ATHENA program. The

simulation was carried out using the FEFF8.20 program and compared with XANES patterns obtained from the experiment.

3. Result and discussion

The XRD patterns of $\text{Ba}(\text{Zr}_x\text{Ti}_{1-x})\text{O}_3$ powders are shown in Fig. 1. It is noticed that the crystal structure at room temperature changed from tetragonal to a mixture of tetragonal and cubic perovskite phases as Zr concentration increased. The sample with $x=0$ or pure BT shows tetragonal perovskite phase, while at $x=0.1$ ($\text{BaZr}_{0.1}\text{Ti}_{0.9}\text{O}_3$), a mixture of tetragonal perovskite BaTiO_3 (BT) phase and small amount cubic perovskite BaZrO_3 (BZ) phase occurred, which can be matched with JCPDS file no. 81-2201 and 74-1299, respectively. The cubic phase of BZ increased continuously with increasing value of x . When $x=0.2$, the small amount of solid solution BZT was observed and increased with further increase of x value. The tetragonal phase of BT disappeared when the Zr content exceeded 30 mol%. A mixture of three different phases (BT, BZ and BZT) was found at $0.2 \leq x \leq 0.35$. The XRD results have shown a clear change in the global structure across the compositional range studied.

The normalized Ti K-edge XANES spectra of $\text{Ba}(\text{Zr}_x\text{Ti}_{1-x})\text{O}_3$ powders obtained via XAS measurements are shown in Fig. 2(a). Generally, the XANES spectra show very similar features for all the compositions, with small variations observed at several peaks, an indication of changes in the local structure around Ti absorbing atom. XANES measures the excitation of core electrons to unoccupied bound states and is thus used to obtain information about the local arrangement of atoms around the absorbing atoms and the density of states of unoccupied states. As seen in Fig. 2(a), the intensity of peak A (I_A), which is associated with both the quadrupole and the dipole $1s \rightarrow 3d$ transition of Ti, reflects the $3d-4p$ hybridization for Ti and is

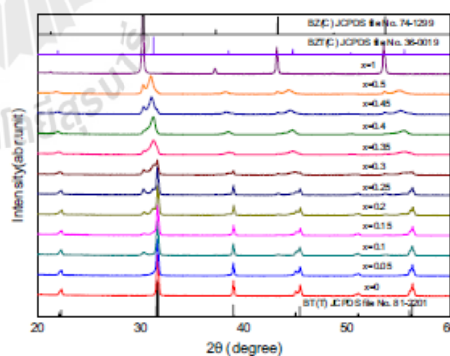


Fig. 1. X-ray diffraction patterns of $\text{Ba}(\text{Zr}_x\text{Ti}_{1-x})\text{O}_3$ powders.

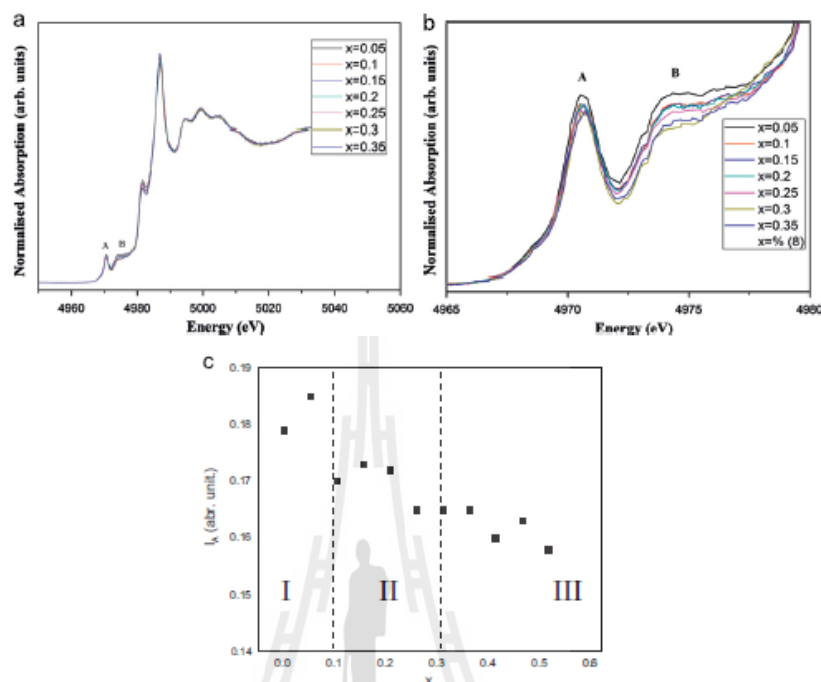


Fig. 2. (a) Normalized X-ray absorption Ti K-edge spectra of $\text{Ba}(\text{Zr}_x\text{Ti}_{1-x})\text{O}_3$ powders, (b) the variation of the pre-edge features of peaks A and B with Zr concentration in $\text{Ba}(\text{Zr}_x\text{Ti}_{1-x})\text{O}_3$, and (c) The intensity of peak A (I_A) of $\text{Ba}(\text{Zr}_x\text{Ti}_{1-x})\text{O}_3$ as a function of Zr concentration, showing three different regimes I, II, and III.

directly proportional to the displacements of Ti off-center of oxygen octahedra and is indirectly proportional to the lattice constants [5] following Eq. (1),

$$I_A = K(\Delta r^2)/3a^{5.5} \quad (1)$$

where K is a coefficient which depends neither on the atom displacements nor on the direction of the electric field, Δr^2 is the mean-square displacement of Ti ions from the center of oxygen octahedra and a is the average displacement of the oxygen octahedra [5].

The intensity of peaks A and B, as shown more clearly in Fig. 2(b), are examined with the local Zr/Ti ratio around the Ti absorbing atoms [5]. The intensity of peaks A and B were continuously decreased with increasing Zr concentration. The reduction step was observed at x between 0.05 and 0.1, which is consistent with the results of the X-ray powder diffraction patterns that showed the sample contained the dominant tetragonal BT phase at $x=0.0$ and 0.05 then the structures were changed to mixed phase between tetragonal BT and cubic BZ phases for $x \geq 0.1$. A reduction step was again found at x between 0.25 and 0.3, likely associated with very small amount of BT phase and coupled with an increase of a new BZT phase, as also

evident from the XRD results in Fig. 1. These two reduction steps were results of the difference in Ti off-center displacement in two ranges. The first range in the BT-riched compositions was attributed to the cubic BZ phase formation which forced the tetragonal unit cell of BT to deform to become more of a cubic unit cell and caused the decrease in the Ti off-center. The second range at x between 0.25 and 0.3 was caused by the competition of Ti off-center between the dominant BZT phase and small amount of BT phase. The intensity of peak A (I_A) is plotted as a function of Zr concentration in Fig. 2(c). The decrease of I_A with increasing Zr content can actually be divided into 3 regimes; i.e., I, II and III. Regime I comprises of two different phases: BT and BZ, in which the change of Ti off-center depends on cubic BZ phase, as described above. In Regime II, a combination of three different phases BT, BZ and BZT plays a role on Ti off-center displacement. Regime III comprises of a combination of BZT and BZ phases, in which I_A tends to decrease continuously. A decrease in Ti off-center in this part is affected by a unit cell distortion forced by BZ phase and by a different Zr/Ti ratio around Ti absorbing atoms within BZT itself.

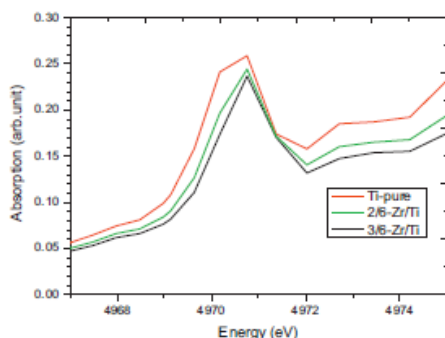


Fig. 3. Simulated pre-edge features of Ti K-edge XANES spectra of $\text{Ba}(\text{Zr}_x\text{Ti}_{1-x})\text{O}_3$ with different Zr/Ti ratio around the central Ti absorbing atom in the local perovskite BZT structure.

The simulation of the XANES spectra of BZT phase was subsequently carried out to investigate the Ti off-center and Zr/Ti ratio around Ti absorbing atoms in BZT solid solution and the simulated and the experimental results can be compared. Fig. 3 shows the simulated pre-edge feature of Ti K-edge XANES spectra of BZT with different Zr/Ti ratios. The simulation was performed with the FEFF8.20 program using partially nonlocal Dirac-Fock for core+HL for valence electron+a constant imaginary part exchange models.

In this study, only the nearest local Zr/Ti sites around the absorbing Ti were considered because the atoms that were further away from the Ti absorber atoms only slightly affected the amplitude of the scattering signal. Therefore, we considered the substitution of Zr into each site of the local Zr/Ti sites in the third shell, as shown in the inset of Fig. 3. The calculated result (shown in Fig. 3) showed the effect of replacing Ti with Zr on the local sites in the third shell. A decrease of the intensity of peak B in the pre-edge peak of Ti K-edge of BZT is observed. The intensity of peak B (at energy about 4972.5 eV) decreases with increasing amount of Zr ions occupying the nearest local Zr/Ti sites around the Ti absorbing ion. This calculated result shows a very good agreement with the experimental result. A direct comparison of the simulated and experimental results can be used to estimate the average amount of Zr occupying the nearest local Zr/Ti sites around the Ti absorbing atoms within the BZT material. However, it is also important to mention that the experimental XANES spectra obtained for BZT system in this present study are affected by several other factors; such as a contribution from Ti off-center from BT phase and different unit cell distortions from BT and BZ phases. Therefore, more

detailed investigations on single phase BZT material will be needed to examine the influence of Zr substitution in the local nearest Zr/Ti sites on the Ti off-center displacement in this novel material system.

4. Conclusion

The structural information of $\text{Ba}(\text{Zr}_x\text{Ti}_{1-x})\text{O}_3$ materials prepared by the solid-state reaction method was examined by X-ray Diffraction (XRD) and Synchrotron X-ray Absorption Spectroscopy (XAS) techniques. The XRD results showed the mixed phase of tetragonal BaTiO_3 , cubic BaZrO_3 , and $\text{Ba}(\text{Ti},\text{Zr})\text{O}_3$. Tetragonal BaTiO_3 phase disappeared when x exceed 0.3. Changes in the local structure around the titanium atom were revealed using X-ray Absorption Near-Edge Structure (XANES) measurements, showing three regimes with different Ti off-center displacements. A good agreement between the simulated result and the intensity of peaks A and B in the XANES spectra was related to the displacement of Ti off-center and the average amount of Zr/Ti ratio around the Ti absorbing atoms.

Acknowledgments

SC, MU, and RY acknowledge support for postdoctoral research fellowships from the Higher Education Research Promotion and National Research University Project of Thailand, Office of the Higher Education Commission and Suranaree University of Technology. AB is thankful for Ph.D. scholarship from the Science Achievement Scholarship of Thailand. Authors also acknowledge the support of INAMM/NSF Program at UTSA.

References

- [1] T. Matiti, R. Guo, A.S. Bhalla, Structure-property phase diagram of $\text{BaZr}_x\text{Ti}_{1-x}\text{O}_3$ system, *Journal of the American Ceramic Society* 91 (2008) 1769–1780.
- [2] Z. Yu, C. Ang, R. Guo, A.S. Bhalla, Dielectric properties of $\text{Ba}(\text{Ti}_{1-x}\text{Zr}_x)\text{O}_3$ solid solutions, *Materials Letters* 61 (2007) 326–329.
- [3] F. Mours, A.Z. Simoes, B.D. Stojanovic, M.A. Zaghetto, E. Longo, J.A. Varela, Dielectric and ferroelectric characteristics of barium zirconate titanate ceramics prepared from mixed oxide method, *Journal of Alloys and Compounds* 462 (2008) 129–134.
- [4] I. Levin, E. Cockayne, V. Krazzman, J.C. Woicik, S. Lee, C.A. Randall, Local structure of $\text{Ba}(\text{Ti},\text{Zr})\text{O}_3$ perovskite-like solid solutions and its relation to the band-gap behavior, *Physical Review B* 83 (2011) 094122.
- [5] R.V. Vedrinskii, V.L. Kraizman, A.A. Novakovich, Ph.V. Demekhin, S.V. Urazhdin, Pre-edge fine structure of the 3d atom K X-ray absorption spectra and quantitative atomic structure determinations for ferroelectric perovskite structure crystals, *Journal of Physics Condensed Matter: An Institute of Physics Journal* 10 (1998) 9561.

CURRICULUM VITAE

Name: Mr. Atipong Bootchanont

Education Background:

2005-2008 B.Sc. (Physics) Khon Kean University with scholarship from the Science Achievement Scholarship Programme of Thailand (SAST), Khonkean, Thailand.

2009-2014 Ph.D. (Physics) Suranaree University of Technology with scholarship from the Science Achievement Scholarship Programme of Thailand (SAST), Nakorn Ratchasima, Thailand.

Academic Experience:

1. Ph. D. Research at University of Texas at San Antonio, Texas, USA.
2. Research Assistant at Synchrotron Light Research Institute (Public Organization), Thailand.
3. Teaching Assistant at Laboratory, School of Physics, Suranaree University of Technology, Thailand.
4. Teacher of Science Classrooms in University-Affiliated School Project (SCiUS) at Suranaree University of Technology, Thailand.